The Dissertation Committee for Robin Singh
Certifies that this is the approved version of the following dissertation:

Multifunctional Foams and Emulsions for Subsurface Applications

APPROVED BY

SUPERVISING COMMITTEE:

Kishore Mohanty, Supervisor

David DiCarlo

Chun Huh

Navid Saleh

Kamy Sepehrnoori

Multifunctional Foams and Emulsions for Subsurface Applications

by

Robin Singh

Dissertation

Presented to the Faculty of the Graduate School of

The University of Texas at Austin

in Partial Fulfillment

of the Requirements

for the Degree of

Doctor of Philosophy

The University of Texas at Austin

December 2017

Dedication

Dedicated to my loving parents

Acknowledgements

I owe an enormous debt of gratitude to Dr. Kishore Mohanty for his constant support and guidance throughout my research. I was extremely fortunate to have him as my Ph.D. advisor. I am grateful to him for giving me the freedom to explore diverse research areas. He is truly inspirational and has been quite instrumental in shaping my professional and personal life. I wish to instill his three key qualities in my life: sincerity, humbleness, and compassion for others. It was my privilege to have worked under his guidance.

My deepest appreciation for my family who always encouraged me to pursue my dreams and aspirations. I am thankful to my mom and dad who are the best parents a son could have! I am grateful to them for their relentless prayers for my well-being. They have always been a source of inspiration to me and an epitome of hard work and perseverance. I am truly blessed to have their endless love and support. I thank my brother, Amit for his constant encouragement and guidance because of which I made it to IIT KGP (and then UT). I am thankful to my sister, Priyanka for her unconditional love and support throughout my life. I thank God for blessing me with such a wonderful and loving family.

I owe a great deal of gratitude to my wife, Donna for her love and emotional support during my Ph.D. journey. Her positive, cheerful, and caring nature has enabled me to achieve this milestone. Thank you, Donna, for everything, and especially for keeping me whole and sane through this process. UT will always remain a special place to me which brought us together. I am lucky to have you as my companion for life!

It was an honor to work with Professor Chun Huh on a research project in collaboration with Seoul National University. His energy and enthusiasm for research in

Abstract

Multifunctional Foams and Emulsions for Subsurface Applications

Robin Singh, PhD

The University of Texas at Austin, 2017

Supervisor: Kishore Mohanty

Foams and emulsions hold immense potential in assisting in the different stages of oil recovery processes such as enhanced oil recovery, drilling, and completion. This work is focused on developing robust, multifunctional foams or emulsions for subsurface applications, which offer unique advantages over conventional methods. The first half of the dissertation is focused on investigating novel foams stabilized using nanoparticles and/or surfactants to improve the gas enhanced oil recovery process. Gas flooding often has poor volumetric sweep efficiency due to viscous fingering, channeling, and gravity override. Foam is a promising tool to improve sweep efficiency in gas floods. It can reduce the mobility of gas by several orders of magnitude by increasing its apparent viscosity while keeping the liquid phase mobility unchanged.

For sandstone reservoirs, which are typically water-wet in nature, two different approaches of foam stabilization using nanoparticles were developed. In the first approach, synergistic stabilization of foams with a mixture of hydrophilic nanoparticles and an anionic surfactant was investigated. Foam stability experiments in bulk and porous media tests showed that adding hydrophilic nanoparticles to surfactant

formulations increases the foam stability. Microscopy revealed that nanoparticles are trapped in lamellae as well as at the Gibbs-Plateau borders. These nanoparticles act as physical barriers and retard the liquid drainage and the Ostwald ripening process. To fundamentally understand the role of nanoparticles in altering the foam dynamics in porous media, a high-pressure visualization experiment was performed in a 2D layered, heterogeneous porous media. This experiment showed that immiscible foams can result in significant incremental oil recovery of 25% to 34% OOIP (over waterflood). In the second approach, foam stabilized using in-situ surface-activated nanoparticles without any surfactant was explored as an EOR agent. The surface chemistry of the hydrophilic nanoparticles was tailored by adsorption of a small amount of short-chain surface modifiers to obtain surface-modified nanoparticles (SM-NP). Foam stabilization using these SM-NP was compared with that using a conventional surfactant to evaluate the potential of these SM-NP to act as an effective foaming agent.

Carbonate reservoirs, which are typically highly heterogeneous and oil-wet in nature, pose additional challenges for an effective foam EOR process. Crude oils are typically detrimental to foam stability. An oil-wet carbonate will have a thin oil film on the surface and thus foam lamellae stabilization is challenging. Therefore, wettability-alteration of rock matrix toward water-wet condition using a surfactant is required to favor the in-situ foam stability. This work demonstrated for the first time a synergistic approach of using foams with wettability-altering capabilities for oil-wet systems. It was shown that optimal surfactant formulations can not only alter the wettability of a carbonate core from oil-wet to water-wet conditions, but also can significantly increase the in-situ foam stability even in presence of crude oil.

The second half of the dissertation is focused on developing novel microencapsulation techniques using the concept of water-in-air powders for subsurface

applications. A facile, one-step method was reported to encapsulate micro- or nano-sized hydrophilic particles using silica nanoparticles. The encapsulated particles can be released based on an external stimulus, such as a change in pH of the external continuous phase. The use of this novel carrier system was demonstrated for the delayed release of PPG particles for conformance control. The application of this technology was then explored for microencapsulating highly concentrated acids (~10 wt.% HCl) for acid treatment of shales. The advantages of these novel acid-in-air powders over conventional acid-in-oil emulsions (which are typically used for shale acidization processes) were illustrated in terms of the thermal stability, corrosion inhibition efficiency, and shale surface reactivity.

Table of Contents

List of Tables

List of Figures

Chapter 1: Introduction

With the surging energy demand and consumption globally, there is an inevitable need to exploit the existing oil reserves efficiently. In the recent years, there is an increased interest in developing novel foams and emulsions to assist in the different stages of oil recovery processes. Several applications have been demonstrated in the field of enhanced oil recovery, drilling, completion, and stimulation in both conventional and unconventional reservoirs. This dissertation broadly focuses on three different areas for which novel foams/emulsions were developed—nanoparticle-stabilized foams in water-wet porous media, foams with wettability alteration in oil-wet carbonates, microencapsulation of particles or liquid using water-in-air powders (emulsions). The subsequent sections discuss the motivation for each area, the research objectives, and the dissertation outline.

1.1 MOTIVATION

1.1.1 Nanoparticle-Stabilized Foams in Water-Wet Porous Media

Gas flooding has been commercially applied as an enhanced oil recovery (EOR) technique for nearly 50 years. Based on a 2014 survey, U.S. CO_2-EOR projects alone provide 292,735 barrels of oil per day, which account for 38% of the U.S. output from EOR ("Worldwide EOR survey," 2014). This technique involves the injection of gas (e.g., hydrocarbon components like methane, ethane, and enriched-gases, and non-hydrocarbon components like carbon dioxide, nitrogen, and flue gas) into the oil reservoirs. These injected gases are immiscible, partially miscible, or completely miscible with the reservoir crude oil. One of the advantages of gas flooding is achieving better microscopic

displacement efficiency, which results in lowering of the residual oil saturation as compared to waterflood (Lake, 1989). However, the volumetric sweep efficiency is often very poor due to the inherent lower viscosity and density of the gas that leads to viscous fingering (Doorwar, 2015) and gravity override, respectively (Rossen, 1996). The other main technical issue is the channeling of gas through high permeability regions in heterogeneous reservoirs. These technical challenges result in an early gas breakthrough, poor sweep efficiency, and inefficient oil recovery.

Foam is a potential solution to alleviate these above-mentioned challenges associated with gas flooding (Kovscek et al., 1997; Rossen et al., 2010a). It can drastically reduce the gas mobility by several orders of magnitude by increasing the apparent viscosity of gas and trapping a large gas fraction inside the porous medium (Bernard and Jacobs, 1965). In the past, there have been several field tests, e.g., steam foam flood (Patzek, 1996a), foam-assisted water-alternating-gas injection (Blaker et al., 2002), carbon dioxide foam flood (Chou et al., 1992), and foam flood with a carbon dioxide-soluble surfactant (Mukherjee et al., 2016), in which foam was used to improve sweep efficiency. Conventionally, surfactants have been used to stabilize foam in field applications. However, surfactant-stabilized foams are not very stable under harsh reservoir conditions, such as high temperature, high salinity, and in the presence of crude oil. The other factors, such as surfactant adsorption on the rock matrix, surfactant-partitioning in crude oil, thermal degradation of surfactants under high temperature, pose further challenges toward economical field implementation of foam flooding (Jensen and Friedmann, 1987; Sharma et al., 2015; Ziegler and Handy, 1981). The use of nanoparticles can aid in mitigating some of these issues. They have the potential to stabilize foam under harsh conditions of temperature, salinity, the presence of crude oil. Moreover, these nanoparticles can be obtained cost-effectively from cheap raw materials like fly ash and silica (Lee et al., 2015;

2

Singh et al., 2015). Keeping this mind, in this work, two different approaches of foam stabilization using nanoparticles were explored for the water-wet system. In the first approach, foam stabilization using a mixture of nanoparticles and surfactants was investigated in bulk and porous media. To understand the effects of nanoparticle addition, high-pressure visualization of foam flow in layered and heterogeneous media was performed. In the second approach, foam stabilized by surface-modified nanoparticles in the absence of any surfactant was explored in bulk and water-wet porous media.

1.1.2 Foams with Wettability-Altering Capabilities in Oil-Wet Porous Media

Carbonate reservoirs account for more than 60% of the world's oil and 40% of the world's gas reserves (*World energy outlook*, 2006). These reservoirs are typically naturally fractured and highly heterogeneous. Unlike sandstone reservoirs, these are typically oil-wet in nature. (Chilingar and Yen, 1983; Roehl and Choquette, 2012), which poses additional challenges toward oil recovery. Secondary water-flood recovery in these reservoirs is poor as the water preferentially flows through the fractures; water does not spontaneously imbibe into the matrix because of its oil-wet nature. In such systems, the injectant fluid must overcome the negative capillary pressure barrier to invade the rock-matrix and displace oil. Moreover, this fluid must not channel through high-permeability regions, leaving the low-permeability regions uncontacted. Thus, the two major challenges for enhanced oil recovery in these carbonate reservoirs are—oil-wetness and heterogeneity. Foam is a potential solution to improve the sweep efficiency of these reservoirs. However, typically crude oils are highly detrimental to foam stability. An oil-wet carbonate will have a thin oil film on the surface and stabilization of foam lamellae in this condition is challenging. Wettability alteration of rock matrix toward water-wet using

3

optimal surfactant will favor in-situ foam stability. A stronger foam can then act as an effective fluid blocking agent and can divert injectant fluid (or foam) to new lower permeability regions. Thus, wettability alteration and foaming capabilities can act in synergy to effectively improve the sweep efficiency in the oil-wet system. Keeping this in mind, in this work, surfactant formulations were developed which could result in wettability alteration as well as strong in-situ foam in oil-wet carbonate systems. Bulk screening experiments were conducted to screen the optimal surfactants. The role of wetting nature of the rock matrix on in-situ foam stability was also studied.

1.1.3 Microencapsulation of Microparticles

Polymeric microparticles (such as preformed particle gel) swell under low salinity conditions and are typically used for conformance control in oil fields (Elsharafi and Bai, 2012), such as plugging fractures, channels, and thief zones. These particles are often referred to as "PPG" in the literature. Recently, PPG has been applied to improve the sweep efficiency of water flooding in fractured reservoirs (Elsharafi and Bai, 2012; Goudarzi et al., 2015). These particles can vary from micrometer to millimeter in size and can plug high permeability channels as well as fractures. It is an environmentally friendly material, which is typically not sensitive to reservoir mineral composition (Bai et al., 2007). Moreover, it overcomes some of the drawbacks of in-situ gelation process, such as gelation time and uncertainties associated with gelling because of segregation and temperature and pressure conditions for gelation. One of the challenges for using these particles is to prevent swelling in or near wellbore region during injection (Shi et al., 2011). Encapsulation of these particles and release far from well-bore are desirable. In this work, microencapsulation of these microparticles (PPG) to form water-in-air type

emulsion (powders) was explored. The controlled release of these particles based on external stimulus, such as a change in pH or surfactant addition in the carrier fluid, is also investigated.

1.1.4 Microencapsulation of Concentrated Acids

Acid treatment is a commonly used technique to improve the hydrocarbon production from tight carbonate reservoirs or calcite-rich shale reservoirs. Different types of acids are used during such stimulation processes that include hydrochloric acid (HCl), hydrofluoric acid (HF), nitric acid, acetic acid, and formic acid (Finšgar and Jackson, 2014). However, the most common acidizing agent is HCl at high concentration of 5-28% (Smith et al., 1978). A direct injection of concentrated acid is not desirable since it can cause excess surface reactions and result in matrix face dissolution. Therefore, retarded acid systems are often used for long-distance propagation of acid, creation of wormholes (in carbonates), and differential etching (in shale fractures). These include emulsified acids (acid-in-oil emulsions), foamed acids, polymer or surfactant-gelled acids, and solid encapsulated acids. However, there are several technical and operational challenges associated with these processes. Although emulsified acids have been successfully used in some fields, robust emulsion stability continues to be a challenge, and it requires additional additives and specialized equipment and expertise (Still et al., 2007). The solid encapsulated acids typically rely on the physical or chemical degradation of the surface coating for the release of acid. The precise control of required chemical conditions in the reservoir is difficult. Moreover, bulk scale production of these coated systems is prone to physical defects, which will lead to early release of acids. To mitigate some of these limitations of these conventional acid treatment processes, microencapsulation of

concentrated acids using nanoparticles by making water-in-air type emulsion (powders) was studied. The thermal stability, corrosion inhibition efficiency, and shale surface reactivity of these powders are compared with conventional acid-in-oil emulsions to illustrate the key advantages of the proposed process over conventional techniques.

1.2 RESEARCH OBJECTIVES

The major objectives of this dissertation are as follows:

- To investigate the synergistic stabilization of foams using a mixture of surfactant and hydrophilic nanoparticles in bulk and in porous media

- To perform high-pressure visualization of the fluid diversion via foams in heterogeneous media and understand the effect of hydrophilic nanoparticles on foam flow dynamics

- To develop foams with wettability-altering capabilities for oil-wet carbonates and to investigate the role of wetting nature on in-situ foam stability

- To perform microencapsulation of polymeric microparticles (PPG) using nanoparticles and to investigate the controlled release of particles using different external stimuli

- To perform microencapsulation of concentrated acids using nanoparticles for acid treatments of calcite-rich shales and compare their performance with conventional acid-in-oil emulsions

1.3 DISSERTATION OUTLINE

This dissertation is composed of seven chapters. Chapter 2 describes the fundamentals of foam flow in porous media. The different mechanisms of foam generation and coalescence in porous media are discussed. A detailed literature survey on foams

stabilized by nanoparticles with or without surfactants in the water-wet system is performed. The challenges and application of foam flow in oil-wet porous media are also discussed. Finally, the concept of microencapsulation and delayed release of particles/liquid using nanoparticles is discussed in detail. The application of this technology for conformance control and acid treatment is then described.

Chapters 3 and 4 focus on foam stability in bulk and water-wet porous media. Specifically, in Chapter 3, a comprehensive evaluation of synergistic stabilization of foam by a mixture of surfactant and nanoparticle is performed. Moreover, a visualization study of foam flow through a two-layer, heterogeneous model is presented. This study is the first-of-its-kind to visually demonstrate flow diversion due to nanoparticle-stabilized foam in a heterogeneous porous system. Flow phenomena, such as cross-flow between layers and foam phase separation, are discussed. Complementary experiments, such as static foam tests, vertical foam film test, and confocal laser scanning microscopy, are also performed to understand the effect of nanoparticle on foam stability.

In Chapter 4, foam stabilization using in-situ surface activated nanoparticles in the absence of any surfactant is investigated in bulk and water-wet porous media. The interfacial properties of the nanoparticles were modulated by attachment of short-chain surface modifiers, which render them partial hydrophobic. Foams were then stabilized by these surface-modified nanoparticles (SM-NPs) which have a tendency to adsorb at the air-water interface.

The previous two chapters focus on foam flow in water-wet porous media. In contrast, Chapter 5 presents a comprehensive study of foam flow in oil-wet porous media (carbonates). It presents a novel synergistic approach of using foams with wettability-altering capabilities to improve the tertiary oil recovery in the oil-wet heterogeneous systems. Complementary bulk experiments, such as contact angle experiments,

spontaneous imbibitions in a microchannel, and static foam tests, were performed to screen the optimal surfactant formulations.

In Chapters 6 and 7, a novel technique of microencapsulation using nanoparticles is demonstrated for different subsurface applications. In Chapter 6, a facile route to encapsulate hydrophilic microparticles or nanoparticles by preparing water-in-air powders stabilized by hydrophobic silica nanoparticles is presented. The encapsulated particles (dispersed in internal aqueous phase) do not interact with the external fluid (continuous phase) even at high temperatures. The encapsulated particles were released using an external stimulus, such as adding an external aqueous phase of a certain pH or a surfactant solution. This study is the first-of-its-kind that focuses on encapsulation and on a delayed-release of solid particles by making water-in-air powders. The application of this technique for targeted delivery of swelling agents, such as preformed-particle gel (PPG) was systematically studied.

Retarded acid systems, such as emulsified acids and polymer-gelled acids, are often used for stimulation of calcite-rich shale. Chapter 7 focuses on microencapsulation of highly concentrated acid (~10 wt.% HCl), which could be used as an alternative retarded acid system for shale acid treatments. The thermal stability, corrosion inhibition efficiency, and shale surface reactivity are compared with conventional acid-in-oil emulsions, which are typically used for shale acidization processes. Finally, Chapter 8 discusses the key conclusions and recommendations for future work.

Chapter 2: Literature Survey

2.1 INTRODUCTION

Gas flooding is one of the most widely used enhanced oil recovery (EOR) techniques (Taber et al., 1997). It consists of injection of a gas (e.g., hydrocarbon components like methane, propane and enriched-gases, and non-hydrocarbon components like carbon dioxide, nitrogen and flue gas) into oil reservoirs that have been typically waterflooded. In the U.S., CO_2-EOR projects alone provide 280,000 barrels of oil per day, which is 3% of the domestic oil production (Enick et al., 2012). If the gas is first or multi-contact miscible with the oil, the microscopic sweep efficiency is excellent in the region swept by the gas (Orr et al., 1982). However, the adverse mobility ratio due to the inherent low viscosity of gas leads to viscous fingering, leaving a part of the reservoir uncontacted (Lake and Venuto, 1990). Reservoir heterogeneity and gravity override also contribute to poor sweep efficiency (Koval, 1963).

Foam can be used to mitigate poor sweep problems associated with gas injection (Kovscek et al., 1994; Rossen et al., 2010b). The main mechanism by which foam reduces the gas mobility is by immobilizing or trapping a large fraction of the gas in the porous medium and by increasing the apparent viscosity of the gas (Hirasaki and Lawson, 1985). The concept of using foams as mobility control agents was first proposed by Boud and Holbrook in 1958. Since then, there have been several successful foam pilot tests in which surfactant and gases have been co-injected for mobility control (Patzek, 1996b). The subsequent sections will discuss the different phenomenon governing the foam flow dynamics in porous media.

9

2.2 FOAM FLOW IN POROUS MEDIA

In bulk, the foam is defined as a colloidal dispersion of gas bubbles in a continuous liquid phase (Schramm and Wassmuth, 1994). The foam morphology in a porous medium is quite different than in bulk. In porous media, the foam is a two-phase fluid system where some gas flow paths are made discontinuous by thin liquid films called lamellae (Hirasaki, 1989). These lamellae are typically stabilized by surfactants that are adsorbed at the interface. However, lamellae lack long-term stability. In porous media, continuous regeneration of these lamellae is an essential mechanism for foam transport. Figure 2.1 shows the basic morphology of foam flow in porous media.
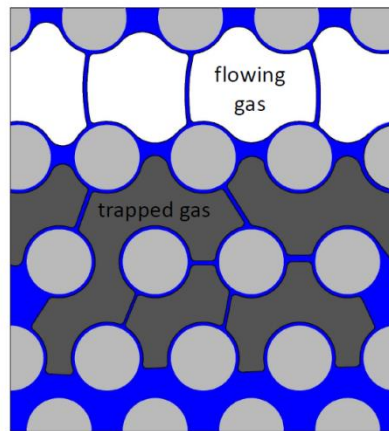
Figure 2.1: Schematic of foam flow in porous media showing the flow of free gas (white) and the trapped gas (grey) (Almajid and Kovscek, 2016)

2.3 FOAM PARAMETERS

Foams in bulk or porous media are typically characterized by two parameters: foam texture and foam quality.

2.3.1 Foam Texture

The bubble size distribution of the foam is often referred as the foam texture. Foam flow in porous media is strongly governed by foam texture. Ettinger and Radke (1992) were the first to quantify the role of bubble size in foam flow in porous media. They proposed a 1D population balance model where bubble sizes were calculated based on lamella creation and lamella decay processes. Several studies have shown that smaller bubbles (often referred as 'finer bubbles') lead to larger flow resistance during flow through porous media (Friedmann and Jensen, 1986; Kovscek and Radke, 1994).

2.3.2 Foam Quality

Foam quality is defined as the volume fraction of gas-phase dispersed in the liquid phase. The in-situ quality of foam flowing through porous media changes spatially as a function of time till a steady state is achieved. Therefore, most of the experimental studies report the injection foam quality, which can easily be calculated as the ratio of gas injection rate to the overall injection rate of gas and liquid.

2.4 MECHANISM OF FOAM GENERATION

The foams in porous media are essentially disconnected gas phases separated by thin liquid films known as lamellae. The foam generation and propagation depend on the continuous generation of these lamellae in the porous media. There are three main mechanisms for lamellae generation: snap-off, lamella division, and leave-behind. Recently, Liontas et al. (2013) proposed two new mechanisms of in-situ foam generation in microfluidic channels termed as bubble pinch-off. These mechanisms are discussed in the subsequent sections.

2.4.1 Snap-off

Snap-off is a mechanical process which involves the formation of new discontinuous gas bubbles as a large gas film passes a pore throat. It is typically considered as one of the most important mechanisms governing the foam formation (Morrow, 1990; Ransohoff and Radke, 1988). One of the important criteria for snap-off to occur is that the ratio of pore throat to the pore body is about 1:3 (Roof, 1970). Consider a liquid (blue)-filled water-wet pore throat and body system in which gas phase (white) under a pressure gradient invades from left as shown in Figure 2.2. For the gas phase to invade the pore throat, it must overcome the entry pressure (Figure 2.2a). If the capillary pressure is higher than this capillary entry pressure, the gas phase passes the pore throat resulting in the reduction in interfacial curvature. The gas phases start to rearrange itself and start to deposit liquid in the pore corners corresponding to the localized capillary entry pressure (Kovscek and Radke, 1996). The gradient in interfacial curvature results in further accumulation of liquid near pore neck, which eventually leads to snap-off process as depicted in Figure 2.2c. The newly formed gas bubble will remain stable only if the liquid phase has surface-active agents such as surfactants or surface-modified nanoparticles, which can stabilize the gas-water interface. In the absence of these agents, the gas bubble tends to coalesce and merge with the gas phase.
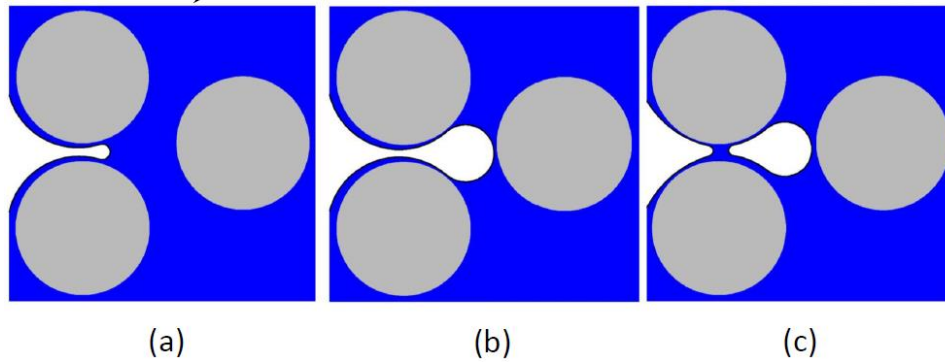
Figure 2.2: Schematic of snap-off mechanism: (a, b) gas phase invading the pore, (c) snap-off process (Almajid and Kovscek, 2016)

2.4.2 Lamellae division

Lamellae division is the process that involves the creation of new lamellae from an existing lamella (Figure 2.3a) when it is stretched to a branching point (Figure 2.3b). As opposed to the snap-off process, this process requires the presence of an existing lamella (formed by other mechanisms) in the system. One of the necessary criteria for lamella division to occur is that the bubble size must be equal to or greater than the size of the pore in porous media (Chambers and Radke, 1990). It is still debatable whether snap-off or lamella division is the dominant foam generation mechanism since literature could not arrive at any consensus. Gauglitz et al. (2002) reported that there exists a critical injection velocity or minimum pressure gradient ∇pmin, below which no foam is generated. They explained this behavior in terms of requirement of a minimum pressure gradient to mobilize the static gas bubbles (Figure 2.3a) across the branching point to create new bubbles (Figure 2.3b).
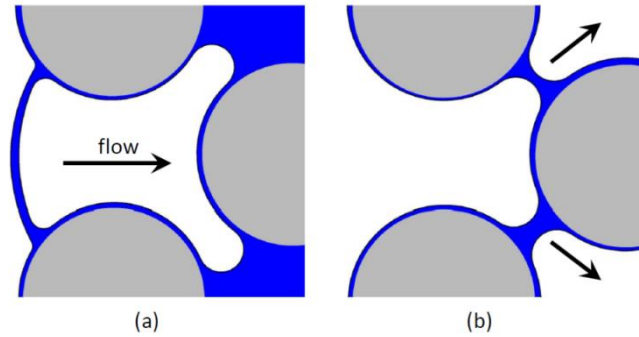
Figure 2.3: Schematic of lamella division mechanism: (a) flow of a gas bubble through a pore throat, (b) branching of lamella to create new lamellae (Almajid and Kovscek, 2016)

2.4.3 Leave-behind

The snap-off and lamellae-division results in the formation of disconnected gas bubbles, which reduces the gas mobility. Thus, these two mechanisms contribute to the formation of strong foam. On the contrary, the leave-behind mechanism does not create disconnected bubbles thus only results in weak foam. In this mechanism, two gas bubbles (white) invades the liquid (blue)-filled pore system (Figure 2.4a) and converge together and leave a liquid-lens behind (Figure 2.4b) which is parallel to the flow resulting in continuous-gas foam (Dicksen et al., 2002).
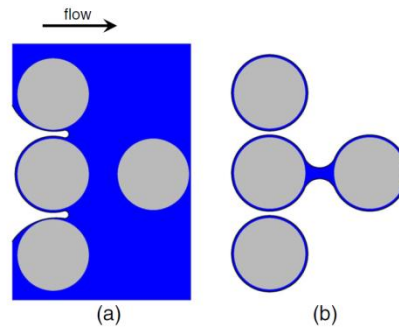
Figure 2.4: Schematic of leave-behind mechanism: (a) two gas bubbles invading liquid phase (blue), (b) creation of new lamella (Almajid and Kovscek, 2016)

14

2.4.4 Bubble pinch-off

Liontas et al. (2013) conducted foam flow experiment through a microfluidic constriction. The pre-generated foam was injected through the microfluidic device, and flow behavior of bubbles was observed using high-speed imaging. They reported two new pinch-off mechanisms of bubble generation. First, neighbor–wall pinch-off, which occurs when a bubble entering a constriction is pinched between a neighboring bubble and the curved wall of the constriction (Figure 2.5a). Second, the neighbor–neighbor pinch-off occurs when a bubble is pinched between two neighboring bubbles approaching the constriction (Figure 2.5b)

(a) Neighbor-wall pinch-off   (b) Neighbor-neighbor pinch-off
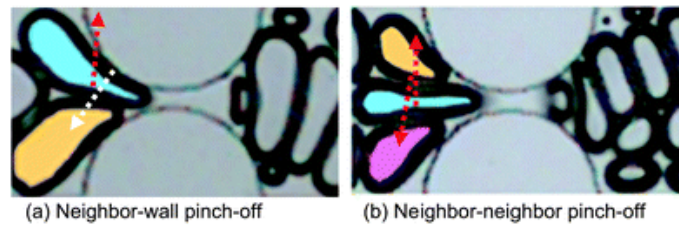
Figure 2.5: Bubble pinch-off mechanisms (Liontas et al., 2013)

2.5 MECHANISMS OF LAMELLA DESTRUCTION

The foam and emulsion stability vary from seconds to years. However, thermodynamically, these are always unstable (Bergeron, 1997). Chambers and Radke (1990) proposed two main mechanisms of lamellae destruction or coalescence: capillary suction and gas diffusion.

2.5.1 Capillary Coalescence

Thin lamellae in the foams are thermodynamically unstable. The stability of these lamellae is governed by the complex interplay of attractive and repulsive intermolecular

interactions. Capillary coalescence is one of the important mechanisms governing film destruction. An important concept to understand this phenomenon is disjoining pressure (Π). It was first introduced in the 1940 (Derjaguin, 1940). It is defined as the difference in the thermodynamic equilibrium state pressure applied to surfaces by separating interlayer and the pressure in the bulk phase. It is a function of film thickness with a positive value of Π implies net repulsive forces while a negative value implies net attractive forces. Figure 2.6 shows the typical behavior of disjoining pressure as a function of lamella thickness for a bulk foam system. In order to balance the disjoining pressure (Π), a higher capillary pressure is required. This disjoining pressure increases with the decrease in lamella thickness until it reaches a critical lamella thickness (h^c) as shown in Figure 2.6. Beyond this point, the lamella is no longer stable, and it breaks.
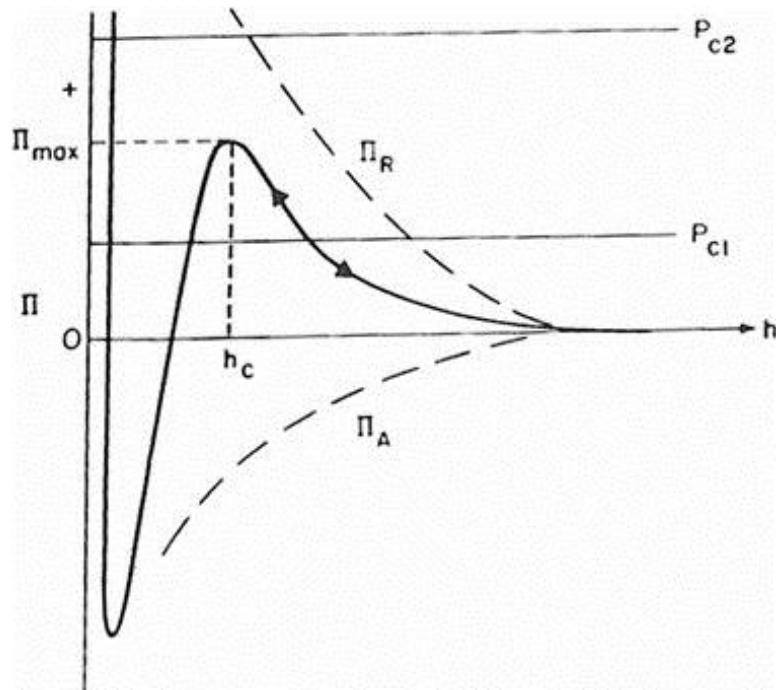
Figure 2.6: A typical disjoining pressure Π isotherm (solid line), resultant of attractive Π $_A$ and repulsive Π $_R$ contributions (dashed lines) (Chambers and Radke, 1990)

16

Analogous to the concept of critical disjoining pressure (above which the bulk foam lamella breaks), the foams in porous media are typically described using the concept of the limiting capillary pressure, P_c^*. Figure 2.7 shows the typical nature of P_c^* as a function of liquid saturation, S_w. As the fractional flow of gas increases, the liquid saturation decreases, and foam breaks abruptly at S_w^* corresponding to a P_c^*. Also, for a fixed water saturation (S_w^*), if the gas fractional flow increases, there is also an increase in bubble sizes as observed by Khatib et al. (1988)
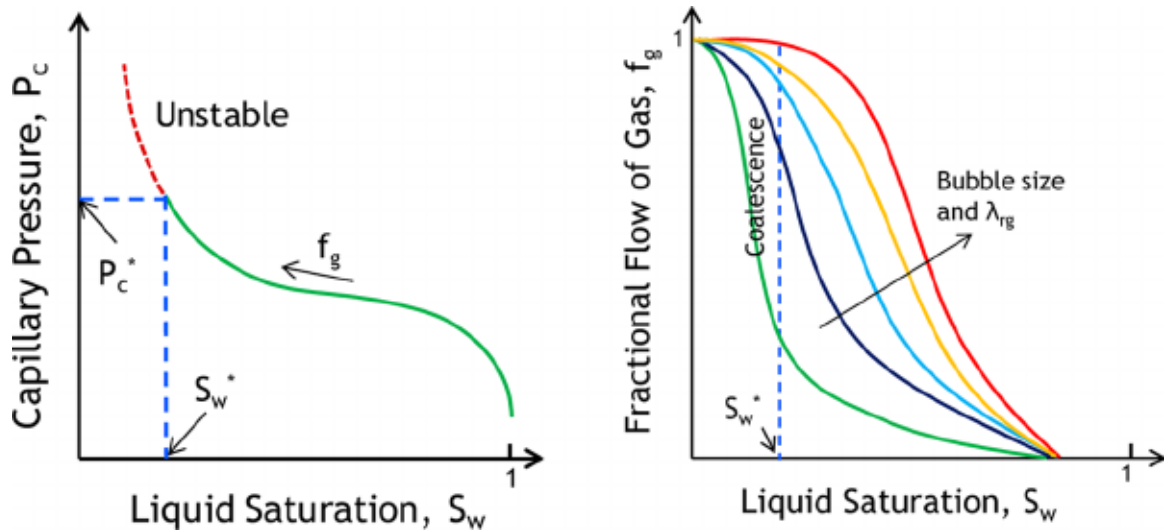
Figure 2.7: Plot of typical capillary pressure as a function of liquid saturation (left) and fractional flow of gas as a function of liquid saturation (Farajzadeh et al., 2015; Khatib et al., 1988a)

2.5.2 Gas Diffusion

The second mechanism of foam coalescence is gas diffusion. This mechanism is typically significant in bulk or static foam such as trapped foam in porous media. Based

on Young-Laplace equation, smaller bubbles have larger pressure and thus higher chemical potential as compared to larger bubbles. This potential gradient results in the mass transfer of gas from smaller bubbles to larger bubbles. Therefore, in bulk foams, larger bubbles will grow while smaller bubbles will shrink. This mechanism is often referred as Ostwald Ripening in bulk foam literature (Tcholakova et al., 2011).

2.5.3 Oil Detrimental Effect

Typically, oils are known to be detrimental to foam stability and generally considered as foam inhibiting or as antifoaming agents (Denkov, 2004a). Many researchers have reported this destabilizing effect of oil on foam stability in porous media (Jensen and Friedmann, 1987; Kuhlman, 1990). Understanding the phenomenon of foam-oil interactions is quite complex. However, a qualitative analysis can be done by investigating several parameters, which are dependent on surface energies of the system. Spreading coefficients (S), entering coefficients (E) and bridging coefficients (B) are three such parameters discussed below. The classical parameters, S and E, which are typically used in foam-oil interaction studies, were first derived by Harkins (1941).

2.5.3.1 Entering Coefficient (E)

The entering coefficient is given by the following expression:

$$E = \sigma_{w/g} + \sigma_{w/o} - \sigma_{o/g}$$

where, σ is the interfacial tension and the subscripts w, g, and o correspond to water, gas, and oil, respectively. A positive value of E indicated that in an oil-water-gas system oil will have a tendency to penetrate the gas-water interface from the aqueous side. Thus, the

foam-oil system is stable when entering coefficient, E is negative (Robinson and Woods, 1948).

2.5.3.2 Spreading coefficients (S)

The spreading coefficient is given by the following expression.

$$S = \sigma_{w/g} - \sigma_{w/o} - \sigma_{o/g}$$

A positive value of S indicates that in an oil-water-gas system, the oil will have the affinity to spread over the gas-water interface. Thus, thermodynamically, a negative value of spreading coefficient, S implies that foam will be stable in presence of oil (Harkins, 1941).

2.5.3.3 Bridging coefficients (B)

A negative value of S implies that oil will not spread at the gas-water interface. However, the oil can still act as an antifoaming agent by forming a lens at the interface. If the lens grows to form a bridge between two bubbles, it could result in bubble coalescence. In such cases, the bridging coefficient, B is positive. Note that a positive value of B is a necessary (not sufficient) condition for the oil to act as an antifoaming agent (Denkov, 2004a).

$$B = \sigma_{w/g}{}^2 + \sigma_{w/o}{}^2 - \sigma_{o/g}{}^2$$

2.5.3.4 Lamella Number (L)

Schramm and Novosad (1990) have suggested the parameter, lamella number, L, i.e.,

$$L = 0.15 * \frac{\sigma_{w/g}}{\sigma_{w/o}}$$

19

indicates whether oil can imbibe into foam lamellae. Based on the value of this number, foam has been classified into three types. L< 1, 1< L < 7 and L > 7, corresponds to Type A, B and C, respectively as shown in Figure 2.8. Type A foams represent the most stable foams, which do not interact with oil. They have both negative values for parameters E and S. Type B foams have negative S and positive E and are moderately stable. Oil interacts with foam lamellae but does not rupture them. Type C foams are unstable foam with both positive S and E. Oil tends to imbibe in these foams and ruptures the foam lamellae.

TYPE A

TYPE B

TYPE C

Ruptured lamella

— Direction of foam flow ➤
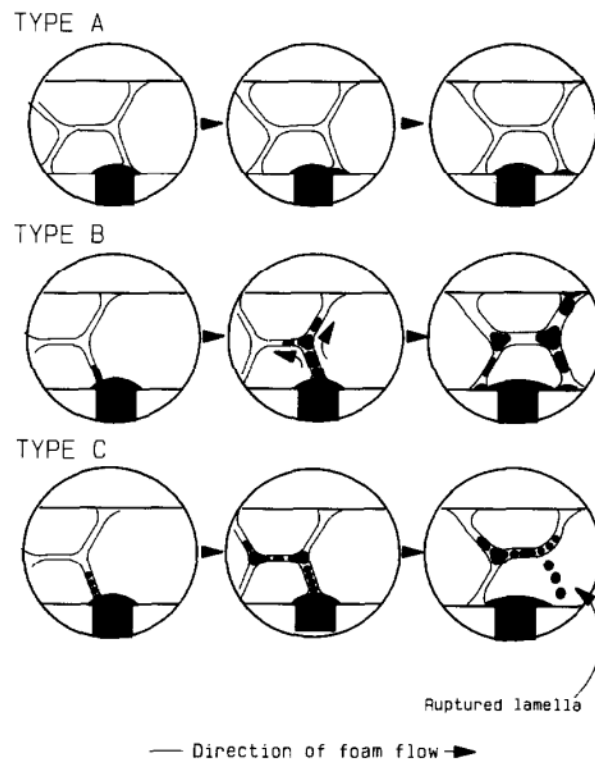
Figure 2.8: Schematic of expected foam-oil interaction based on lamella number
(Schramm and Novosad (1990)

20

2.6 FOAMING AGENTS

2.6.1 Surfactant

A surfactant is a surface-active molecule, which is amphiphilic in nature. It comprises of both hydrophilic portion ('head') and a hydrophobic portion ('tail') such as straight or branched hydrocarbon chains. The head comprises of functional groups that are cationic, anionic, zwitterionic or non-ionic in nature. Due to the amphiphilic nature, the surfactant can adsorb at the gas-water interface, which makes them an ideal candidate to stabilize strong foam. The adsorption of surfactant also lowers the interfacial tension between aqueous and gas/oil phase that assists in oil recovery process. When the surfactant concentration is low, the surfactant molecules in the bulk liquid phase are present in surfactant monomer form. However, above a certain surfactant concentration, the surfactant molecules aggregate to form spherical structures, which are known as micelles (Miller and Neogi, 1985). Depending on the degree of hydrophobicity (or hydrophilicity), the surfactant molecules partition in aqueous or gas/oil phase.

2.6.2 Nanoparticles

In the last decade, there is a recent surge in the research of nanomaterials for oilfield applications. It includes use of nanoparticle in Foam EOR (Emrani et al., 2017; Kim et al., 2016; Singh et al., 2015), nanofluid EOR (Hendraningrat et al., 2013; Zhang et al., 2014), hydraulic fracturing fluids (Barati et al., 2012), wettability alteration (Karimi et al., 2012a) and drilling fluids (Zakaria et al., 2012). One of the advantages of nanoparticles is that these could be modified with different functional groups to impart desirable characteristics for subsurface applications. These include foams/emulsion stabilizer (DiCarlo et al., 2011; Roberts et al., 2012), viscosifier (Ponnapati et al., 2011),

improved aqueous stability (Griffith and Daigle, 2017), and desired surface-wettability. It makes the nanoparticles quite lucrative for oilfield applications. Nanoparticles-stabilized foams offer several advantages over conventional surfactant-stabilized foams. The following subsections discuss the foam stabilized by surface-modified nanoparticles and surfactant-nanoparticles mixtures.

2.7 FOAMS STABILIZATION TECHNIQUES USING NANOPARTICLES

2.7.1 Surface-Modified Nanoparticles

Bulk foams or emulsions can be solely stabilized using colloidal particles with various surface chemistries (Alargova et al., 2004; Binks and Horozov, 2005a; Gonzenbach et al., 2006a; Saleh et al., 2005). Most of these particles were coated with surfactants, polymers, or polyelectrolytes to act as surface-active agents as they were not amphiphilic themselves. Alargova et al. (2004) achieved super-stabilized aqueous foams using synthesized polymer microrods in the absence of surfactants, which retained constant volume for days. These foam bubbles were sterically stabilized by the entangled rod-shape structures of the polymers. Saleh et al. (2005) reported generation of highly stable (> 6 months) oil-in-water emulsions stabilized by hydrophilic silica nanoparticles coated with polyelectrolyte anionic brush poly(styrenesulfonate) or PSS. Interestingly, the particle concentration used in this study was very low (~ 0.04 wt.%). Espinoza et al. (2010) demonstrated very stable supercritical CO_2-in-Water (C/W) foam generation in bead packs using hydrophilic silica nanoparticles, coated with polyethylene glycol (PEG). However, Worthen and coworkers (2012) showed that foams generated using partially hydrophobic silica nanoparticles in beadpacks were more stable than those with PEG-coated silica nanoparticles. Yu et al. (2012) investigated the effect of silica nanoparticle

structure and hydrophobicity on supercritical CO_2 foam behavior in glass beadpacks. The CO_2 bubble size decreased significantly with an increase in the hydrophobicity of silica nanoparticles. Mo et al. (2012) reported the effect of pressure, temperature, and rock samples on the performance of nanoparticle-stabilized CO_2 foam on residual oil recovery. The recovery over waterflood increased with the increase in pressure and decreased with the increase in temperature. Nguyen et al. (2014) studied C/W foams stabilized by partially hydrophobic silica nanoparticle in a microfluidic device. They observed a better sweep efficiency and smaller emulsion sizes in the case of nanoparticle foam flooding as compared to CO_2 flooding. In summary, SM-NPs can be used to stabilize foam, and several researchers have investigated these SM-NPs as foam stabilizers in bulk and in porous media.

2.7.2 Surfactant-Nanoparticles Mixture

Kam and Rossen (1999) theoretically demonstrated that solid particles could be used to stabilize foam without the presence of surfactants. Binks and Horozov (2005) tuned the contact angle of the silica nanoparticles quantitatively by varying the degree of controlled silanization. They were the first to experimentally report stable aqueous foams stabilized solely by silica nanoparticles with different degrees of hydrophobicity. Since then, several publications have explored such systems in detail (Martinez et al., 2008; Stocco et al., 2011, 2009). However, this technique is not versatile. It is restricted exclusively to silica nanoparticles as only these can provide abundant silanol groups which facilitate surface modification via silane treatment (Cui et al., 2013). Moreover, surface-modification of nanoparticles via chemical treatment tends to be expensive. In

such cases, altering the surface property of particles by in situ physisorption or chemisorption of surfactants or amphiphiles on their surfaces could be cost-effective.

Surface modification of nanoparticles via physiochemical interactions with surfactants has been shown to be a facile route for foam stabilization. Several researchers have investigated the potential of using the synergy between surfactant and nanoparticles to generate foam. Worthen et al. (2013a) reported the generation of viscous and stable CO_2-in-water foams with fine texture using bare silica nanoparticles and zwitterionic surfactants in beadpacks when neither of these species could stabilize foam independently. Cui et al. (2010) showed that non-surface active $CaCO_3$ nanoparticles can be surface activated via interaction with anionic surfactants leading to enhanced foamability in the bulk. The electrostatic interaction between the positive charges on particle surfaces and the negative charges of anionic surfactant head groups results in the monolayer adsorption of the surfactant at the particle-water interface. Table 2.1 and 2.2 summarize the nanoparticles-surfactant system used to stabilize foam/emulsion in bulk/micromodel and porous media, respectively.

Table 2.1: Nanoparticles-Surfactant systems used to stabilize emulsion in bulk or micromodel

Emulsion Type	Nanoparticles/ Polyelectrolyte	Surfactant	Gas/Oil	Media	References
Oil-in-water emulsion	Surface-active hydrophilic Si NP	Alkylpoly(oxyethylene) (Nonionic Surfactant)	Tricaprylin oil	Bulk	(Binks and Desforges, 2007)
Oil-in-water emulsion	Hydrophilic Si NP	CTAB (Cationic Surfactant)	Dodecane	Bulk	(Binks and Rodrigues, 2007)

Table 2.1, cont.

Oil-in-water emulsion	Hydrophilic Silica NP	Charged surfactants (lecithin or oleylamine)	Triglyceride oil (Miglyol®812)	Bulk	(Eskandar et al., 2007)
Foams	Hydrophilic Si NP	CTAB (Cationic Surfactant)	Air	Bulk	(Binks et al., 2008)
Foams	Hydrophilic Si NP	TTAB (Cationic Surfactant)	Air	Bulk	(Carn et al., 2009)
Foams	Octyl grafted silica NP	Triton X-100 (Nonionic Surfactant)	Air	Bulk	(Hunter et al., 2009)
Foams	$CaCO_3$ NP	SDS (Anionic Surfactant)	Air	Bulk	(Cui et al., 2010)
Foams	Silica NP	CTAB (Cationic Surfactant)	Air	Bulk	(Maestro et al., 2014)
Foams	Hydrophilic Silica NP	AOS/LAPB (Anionic/Zwitterionic)	CO_2	Micromodel	(Guo and Aryana, 2016)
Foams	Hydrophobic Silica NP	Ionic Surfactant	Air	Bulk	(Jiang et al., 2016)
Foams	Hydrophobic Silica NP	SDS (Anionic Surfactant)	CO_2	Bulk/ Micromodel	(S. Li et al., 2016)
Foams	Hydrophobic Silica NP	Sodium bis(2-ethylhexyl)sulfosuccinate (AOT)	CO_2	Bulk	(Zhang et al., 2016)
Foams	$CaCO_3$ NP	Food Emulsifiers	Air	Bulk	(Binks et al., 2017)
Foams	Fly Ash/ Fe NP	AOS-LAPB (Anionic/Zwitterionic)	CO_2	Micromodel	(Guo et al., 2017)
Foams	Hydrophilic Silica NP	CTAB (Cationic Surfactant)	CO_2	Bulk/ Micromodel	(Li et al., 2017)
O/W Emulsion	Hydrophilic Silica NP	Carboxyl betaine (Zwitterionic surfactant)	Toluene/ Decane	Bulk	(Liu et al., 2017)
Foams	Poly(sodium 4-styrenesulfonate)	CTAB (Cationic Surfactant)	Air	Bulk	(Schulze et al. 2017)

Table 2.1, cont.

Foams	Hydrophilic Silica NP	SDS (Anionic Surfactant)	Air	Bulk	(Vatanparast et al., 2017)
O/W Emulsion	Hydrophilic Silica NP	Tween 40 (Non-ionic Surfactant)	Decane	Micromodel	(K. Xu et al., 2017)
O/W Emulsion	Positively Charged Alumina NP	SDS (Anionic Surfactant)	Decane	Bulk	(M. Xu et al., 2017)
O/W Emulsion	CTAB (Cationic Surfactant)	Alkyl Polyoxyethylene Ether (Nonionic Surfactant)	Toluene/ Dodecane	Bulk	(Zhu et al., 2017)

In-situ surface activation of nanoparticles by adsorption of short-chain amphiphiles has been demonstrated as an effective method for foam stabilization in the bulk. Gonzenbach et al. (2006) demonstrated that inorganic colloidal particles can be partially hydrophobized with certain amphiphiles to produce ultra-stable wet foams, which could exhibit remarkable stability. Short-chain carboxylic acids, alkyl gallates, and alkylamines were used as amphiphiles, which had the tendency to anchor on the particle surfaces efficiently. The unique colloidal architecture, i.e., the sequential assembly of amphiphiles on the surface of the particle and on the particle at the air-water interface, was then proposed as a mechanism for long-term stability of foams (Figure 2.9). Liu and co-workers (2009) employed the same technique to obtain stable foams stabilized by hexylamine-modified laponite particles (Liu et al., 2009). They observed an increase in dilational viscoelastic modulus with an increase in hexylamine concentration, which they attributed to one of the mechanisms for increased bubble stability in these systems.

Table 2.2: Nanoparticles-Surfactant systems used to stabilize emulsion in porous media

Emulsion Type	Nanoparticles/ Polyelectrolyte	Surfactant	Gas	References
Foams	Hydrophilic Silica NP	Caprylamidopropyl betaine (Zwitterionic Surfactant)	CO_2	(Worthen et al., 2013b)
Foams	Partially Hydrophobic Silica NP	SDS (Anionic Surfactant)	N_2	(Sun et al., 2014a)
Foams	Partially Hydrophobic Silica NP	SDS (Anionic Surfactant)	N_2	(Sun et al., 2015)
Foams	Alumina NP	Lauryl amide sulfobetaine (Zwitterionic Surfactant)	N_2	(Wang et al., 2016)
Foams	Surface-modified Silica NP	Laurylamidopropyl betaine (Zwitterionic Surfactant)	CO_2	(Xue et al., 2016)
Foams	Polyelectrolyte complex nanoparticles	Surfonic N120 (Nonionic Surfactant)	CO_2	(Kalyanaraman et al., 2017)
Foams	Silica NP	Gemini (Cationic Surfactant)	N/A	(J. Wang et al., 2017)
Foams	Positively Charged Alumina NP	SDS (Anionic Surfactant)	N_2	(Yang et al., 2017)
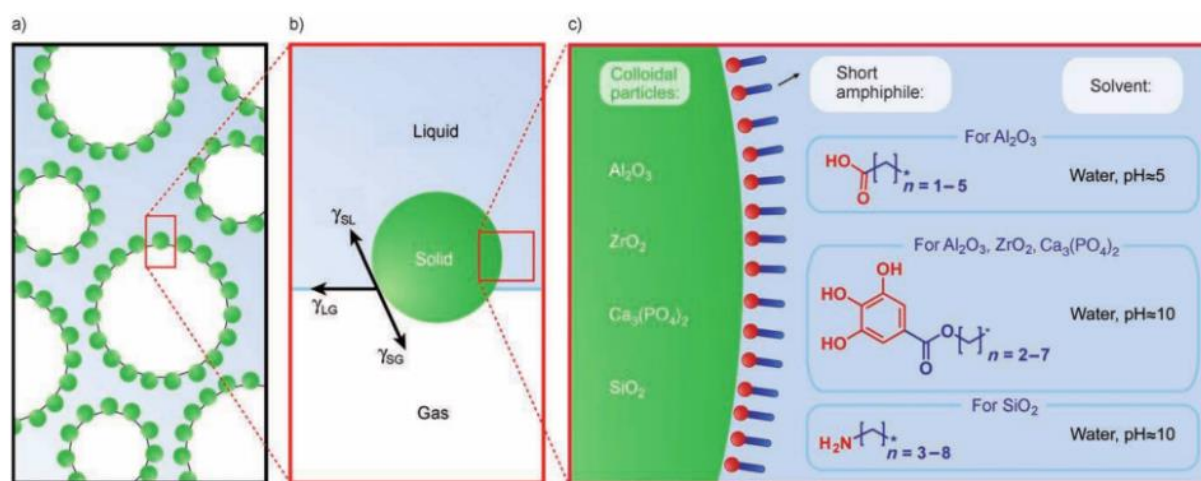
Figure 2.9: Sequential assembly of amphiphiles on the nanoparticle surface (Gonzenbach et al., 2006b)

2.8 FOAM STABILITY UNDER HARSH CONDITIONS

Foam stability under high-temperature and/or high-salinity (HTHS) conditions is challenging to achieve because of two main reasons. First, foam strength typically decreases with increase in temperature. This is because of reduction of liquid phase viscosity at higher temperatures, which expedites the liquid drainage process in foam lamellae. Second, the aqueous stability of surfactants limits their use under HTHS conditions. Several researchers have investigated novel surfactant-stabilized foams for HTHS conditions. Chen et al. (2015) reported CO_2-in-water (C/W) foam using a non-ionic surfactant with a high degree of ethoxylation. Similarly, Cui et al. (2016) studied Ethomeen C12 surfactant-stabilized C/W foam for HTHS applications in carbonates. This surfactant was only stable at lower pH (near 4) as it required complete protonation of C12 to be soluble. Xue et al. (2015) reported viscous C/W foams at a high salinity of 14.6% total dissolved solids (TDS) brine at 120 ºC using CO_2-soluble ionic surfactants. Recently, Alzobaidi et al. (2017) reported highly stable C//W foams of viscosity more than 100 cp using zwitterionic surfactants at 120 ºC. The high apparent viscosity of the foam was attributed to the viscoelastic nature of the surfactant. Such surfactant-stabilized foams could potentially be made more robust using nanoparticles with specific surface coatings.

However, colloidal stability of nanoparticles under high temperature and high salinity conditions is a challenge. According to the Derjaguin–Landau–Verwey–Overbeek (DLVO) theory, the sum of attractive van der Waals (vdW) forces and repulsive electrostatic forces dictate the stability of the nanoparticles (Israelachvili, 1985). The presence of high amount of monovalent and divalent ions screens the inherent charges on nanoparticles, which reduces the electrostatic repulsion between particles. The Debye length, which is a measure of the distance over which the electrostatic repulsion is felt in

the solution, decreases with an increase in salinity (Eslahian et al., 2014). For example, for a salinity of 150 mM, the Debye length is only 0.8 nm (Jiang et al., 2009). In such cases, nanoparticles aggregate due to the van der Waals forces (Elimelech et al., 2013). Moreover, if the nanoparticles are negatively charged, such as bare silica nanoparticles at pH 7, the presence of oppositely charged ions such as Ca^{2+} could result in interparticle bridging, which expedites nanoparticle aggregation (Wuelfing et al., 2001).

Several approaches can be adopted to stabilize nanoparticles under harsh conditions. One such approach is steric stabilization that involves grafting macromolecules or ligands on the nanoparticle surface (Alzobaidi et al., 2017b; Worthen et al., 2016; Yang and Liu, 2010). The presence of these ligands results in steric hindrance, which reduces the probability of two nanoparticles to collide or interact. Additionally, the ligands should have the ability to solvate under the given harsh conditions in aqueous media. Such ligands can provide steric stabilization to the core nanoparticles (Napper, 1983).

2.9 MECHANISMS FOR FOAM STABILITY BY SURFACTANT-NANOPARTICLE MIXTURE

2.9.1 Particle Detachment Energy

The energy required to detach a particle of radius R from the interface depends on the contact angle θ and surface tension γ_{aw} of the interface (Binks and Lumsdon, 2001). If the particle size is small (< few microns), gravity and buoyancy effects can be neglected. The amount of energy required to move the particle from the interface to the bulk solution is given by:

$$E = \pi R^2 \gamma_{aw} (1 - |\cos \theta|)^2$$

For contact angle, $\theta < 30°$ (highly hydrophilic particle) or $\theta > 150°$ (highly hydrophobic particle), this detachment energy would be quite low which implies that these particles cannot stabilize foam (as per this theory). For a contact angle close to 90° and a particle of diameter 10 nm, this detachment energy is quite large (in the absence of surfactants), and it is of the order of 10^3 kT. The large energy associated with attachment implies that once the nanoparticle is brought to the interface, it would be irreversibly adsorbed on the interface and will provide robust foam stability (Binks, 2002). The presence of surfactant reduces this energy by approximately half because the surface tension decreases from ~72 dyne/cm to ~30 dyne/cm (Eastoe and Dalton, 2000). This hypothesis suggests that highly hydrophilic particles do not stabilize interfaces (but they can by other mechanisms, as discussed below). Note that the above expression of detachment energy is valid for particles with size of order of nanometers or bigger. Since the derivation of this expression assumes a continuum fluid phase rather the effect of individual water molecules, this expression should be avoided for particles of the order of angstroms (Å). Smaller particles such as surfactants are typically governed by Brownian motion and their detachment energy is comparable to the thermal energy $k_B T$ (Z. Wang et al., 2017).

2.9.2 Maximum Capillary Pressure for Coalescence

In the absence of nanoparticles, the foam films are flat, and the capillary pressure P_c is balanced by the disjoining pressure in the foam film. When the capillary pressure exceeds a threshold pressure, P_c^{max} the film ruptures (Denkov et al., 1992). In the presence of nanoparticles, the films do not have to be flat. Nanoparticles have the potential to provide a steric barrier in the thinning of foam films and thus play a major role in

retarding coalescence of foam bubbles. Kaptay (2006) has derived an expression for the maximum capillary pressure by analyzing a single hexagonal layer of particles between two bubble films, i.e.,

$$P_c^{max} = \beta \frac{2\gamma_{aw}}{R} \cos \theta$$

where, β is a theoretical packing parameter, γ_{aw} is the air-water interfacial tension, and R is the particle radius. As the radius decreases, the maximum capillary pressure the film can experience without rupturing, increases. Figure 2.10 shows a spherical particle that bridge between two bubble films with a contact angle θ. If this angle is greater than 90º, the positive capillary pressure in the film adjacent to the particles will cause drainage of the liquid away from a particle and will cause dewetting of the films to format a hole (Figure 2.10 a). However, for contact angle < 90º, as in the present case of hydrophilic nanoparticles, after an initial drainage; a critical film thickness is achieved and the film will become planar. Further drainage causes the capillary pressure to draw liquid towards the particle and thus stabilize the film by bridging (Figure 2.10 b) (Pugh, 1996). This theory explains how foam films can be stabilized by bridging of hydrophilic nanoparticles.
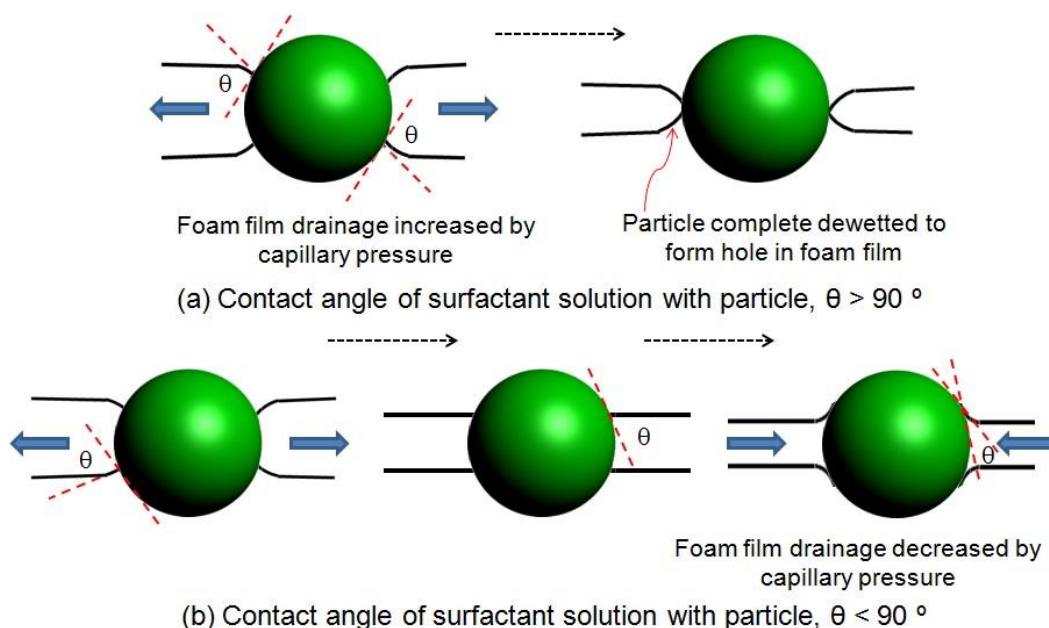
Figure 2.10: Bridging particle behavior in a foam (a) hydrophobic (b) hydrophilic particles

2.9.3 Kinetics of Film Drainage

Horozov (2008) has suggested three possible ways hydrophilic particles can be incorporated into liquid films: (a) a monolayer of bridging particles, (b) a bilayer of closed-pack particles, and (c) a network of particle aggregates inside the film. Figure 2.11 illustrates these three cases in foam films. The particles (surfactant molecules or nanoparticles) are forced to attain an orderly arrangement within a thinning inter-bubble film, resulting in stepwise thinning of the film. This stratification process slows down the liquid drainage and provides additional foam stability in conjunction with the disjoining pressure. The driving force for the particle exhibiting stepwise thinning is the chemical potential gradient of the particle at film periphery, where particle leaves the interface, and a vacancy is formed at its place (Kralchevski et al., 1990) . Johonnott (1906) was first to show this behavior in foam film studies using surfactants at high concentrations. Sethumadhavan et al. (2004, 2001) reported the stratification behavior of silica

nanoparticles resulting in film stability. This tendency of an orderly arrangement of particles was reported to decrease significantly as the polydispersity of nanoparticles increased.
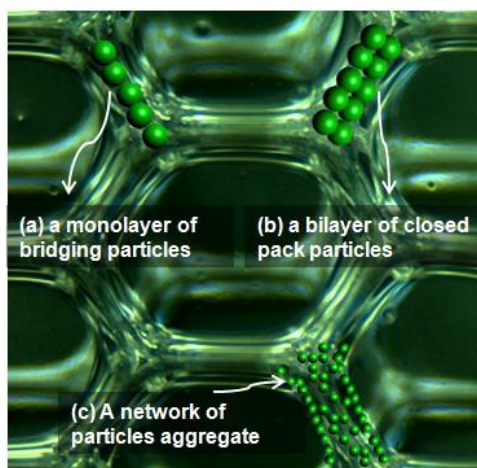
Figure 2.11: Three possible mechanism of liquid film stabilization using nanoparticles

2.10 MECHANISMS FOR FOAM STABILIZED BY IN-SITU SURFACE ACTIVATED NP

The term "in-situ" here refers to "in the localized reaction mixture," which is commonly used in chemistry literature and does not imply "inside the porous medium". This technique relies on the selection of a suitable surface modifier that can attach itself to the nanoparticle surface via either electrostatic interaction or ligand-exchange reaction. The surface modifier requires hydrophilic groups that can attach to the hydrophilic nanoparticle surface and short chain hydrophobic groups that can render the surface partially hydrophobic. The short-chain ensures the high solubility of surface modifiers in the water and prevents phase separation. Unmodified nanoparticles are typically inherently highly hydrophilic (θ close to 0). Thus, they did not show any affinity towards air-water interface and E is quite low (for the case of R = 10 nm and γ_{aw} = 72 dyne/cm), as shown

in Figure 2.12 (left). However, surface modification by anchoring modifiers on the surface renders them partially hydrophobic. The obtained surface-modified nanoparticles have positive affinity towards the air-water interface and are able to stabilize foam. The detachment energy also increases significantly; in the order of 10^3. Figure 2.12 (right) illustrates this mechanism, showing air bubbles stabilized by nanoparticles (green spheres), which are coated with modifiers (black molecules). The term "energy window" in the caption refers to detachment energy of particles with a range of contact angles corresponding to the shaded region.
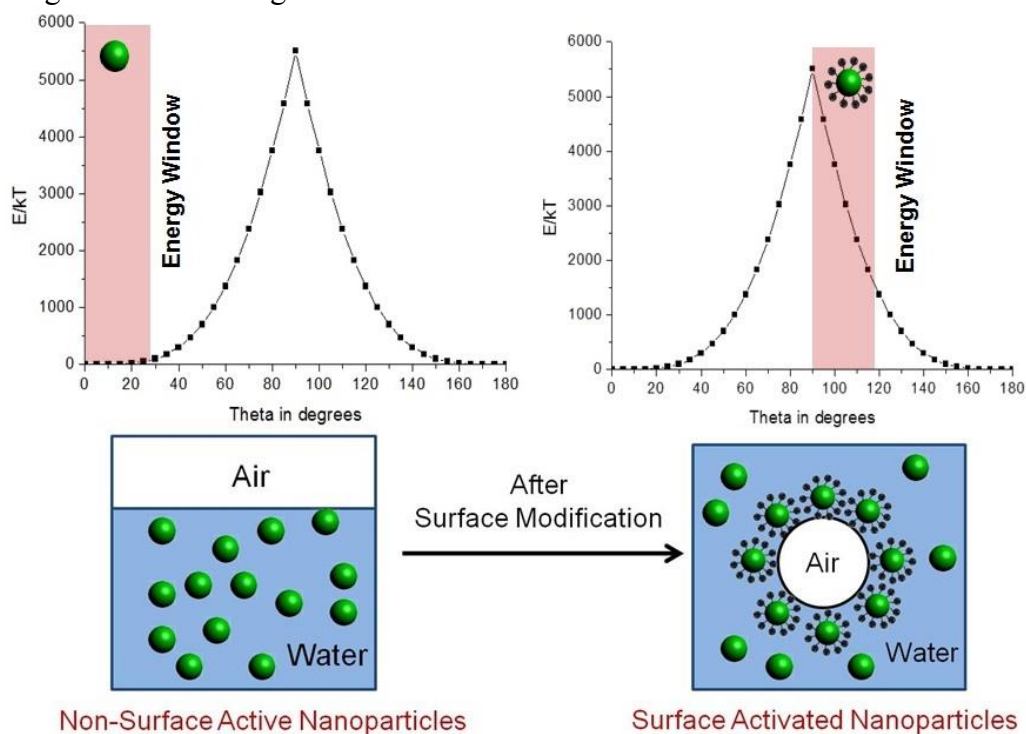
Figure 2.12: Mechanism of foam stabilization using surface-activated nanoparticles

2.11 FOAMS WITH WETTABILITY ALTERATION

Carbonate reservoirs are typically naturally fractured, highly heterogeneous and oil-wet (Chilingar and Yen, 1983; Roehl and Choquette, 2012). Secondary water-flood

recovery in these reservoirs is poor because water preferentially flows through the fractures; water does not spontaneously imbibe into the matrix because of its oil-wet nature. In such systems, the injectant fluid must overcome the negative capillary pressure barrier to invade the rock-matrix and displace oil. Moreover, this fluid must not channelize through high-permeability regions, leaving the low-permeability regions uncontacted. Thus, the two major challenges for enhanced oil recovery in these carbonate reservoirs are – oil-wetness and heterogeneity.

2.11.1 Definition of Wettability

Wettability is the relative adhesion of two fluids to a solid surface. In the context of two immiscible fluids in porous media, wettability is the tendency of one fluid to adhere to the interstitial surface of the porous media in the presence of the other fluid (Donaldson and Alam, 2013). It is a fundamental physical property of the reservoir that affects several parameters such as fluids distribution, relative permeabilities, capillary pressure, and residual oil saturation (Anderson, 1987). Wettability is typically characterized with contact angle. The four different wettability states are water-wet, fractional-wet, mixed-wet, and oil-wet. In a water-wet system, a majority of the rock surface is wet by water. The aqueous phase occupies the smaller pores, and the oil phase occupies the larger pores. A thin water film exists on the wall surface. A rock surface with contact angle (measured through the aqueous phase) less than 75º is considered as water-wet (Treiber and Owens, 1972). In a fractional-wet system, the wetting characteristic of the pore surfaces is quite heterogeneous with preferential wetting of oil or water is randomly distributed throughout the pore surfaces (Brown and Fatt, 1956). The random distribution of different minerals results in such wettability state. In a mixed-wet system,

the smaller pores of the rock are water-wet in nature, while the larger pores are oil-wet in nature (Salathiel, 1973). This state is formed when the crude oil has surface-active compounds such as naphthenic acids, and it displaces the connate water to reside in larger pores. The crude oil eventually displaces the water film on the surface to make it oil-wet. The wetting states—fractional-wet and mixed-wet—are often referred together as neutral-wettability. A contact angle of 75º to 105º is typically assigned to this neutral-wettability state. In the oil-wet system, in contrast to the water-wet case, the oil phase resides in the smaller pores with the aqueous phase in larger pores. Oil phase exists as a continuous phase with thin film adhering to the rock surface. A contact angle > 105º is assigned as an oil-wet system.

2.11.2 Wettability Alteration Techniques

Wettability is a function of rock mineralogy, fluid composition, saturation history, and reservoir temperature. It can be altered from oil-wet to water-wet using different surfactants such as anionic surfactants (Seethepalli et al., 2004; Sharma and Mohanty, 2013), cationic surfactants (Austad et al., 1998; Strand et al., 2003), or non-ionic surfactants (Alvarez et al., 2014; Gupta and Mohanty, 2010). The selection of a suitable surfactant is typically governed by specific reservoir oil composition, mineralogy, temperature, brine composition (Adibhatla and Mohanty, 2008; Mohan et al., 2011). Wettability can also be altered thermally (Kim and Kovscek, 2013; Schembre et al., 2006), by low salinity water injection (Mahani et al., 2015; Tang and Morrow, 1997), or by modified-brine injection (Shariatpanahi et al., 2011). Studies have reported alkaline flooding for wettability alteration (Ehrlich and Wygal, 1977; Leach et al., 1962; Najafabadi et al., 2008).

The success of a wettability-altering process in an oil-wet carbonate system strongly relies on the contact area between the injectant fluid and the matrix. More contact area ensures effective wettability alteration of the matrix surface as well as oil recovery by spontaneous imbibition. Channeling of the injectant fluid in a heterogeneous carbonate reservoir could adversely affect the oil recovery. Foam is a potential solution to mitigate the poor sweep efficiency in heterogeneous reservoirs (Kovscek et al., 1994; Rossen et al., 2010b). The application of foams in carbonates reservoir has additional challenges compared to sandstone reservoirs. These are discussed in detail in the subsequent sections.

2.11.3 Foams in Oil-Wet System

Foam propagation in porous media is strongly influenced by its wettability and foam strength is typically reduced in oil-wet/intermediate-wet rocks (Schramm and Mannhardt, 1996). As discussed previously, there are three main mechanisms of foam generation in porous media–leave-behind, snap-off, and lamella division (Mast, 1972; Ransohoff and Radke, 1988). Snap-off, however, is one of the most common and primary mechanisms of foam propagation (Falls et al., 1988; Holm, 1968). Snap-off occurs in water-wet pores when a meniscus passes through a narrow throat into an adjacent large pore body, resulting in disconnection of the non-wetting phase. Yu and Wardlaw (1986) reported that for surfaces with contact angle (with respect to aqueous phase) greater than 70°, snap-off does not occur in throats. This implies that foam propagation in an oil-wet system strongly relies on its wettability alteration to water-wet. Sanchez and Hazlett (1992) investigated foam flow in the oil-wet bead (silanated) packs using alpha-olefin sulfonate as a foaming agent. They proposed that foam generation in the initially oil-wet medium was a result of wettability alteration of the medium from hydrophobic to

37

hydrophilic state. Haugen et al. (2012) conducted foam flow experiments in fractured, oil-wet limestone cores. They observed that in-situ foam generation in the fractures via co-injection of gas and surfactant was inefficient and pre-generated foam injection for large pore volumes (>100 PVs) was necessary to recover oil.

Typically, crude oils are known to be detrimental to foam stability and are generally considered as foam-inhibiting or antifoaming agents (Denkov, 2004a). Several studies have reported this destabilizing effect of oil on foam stability in porous media (Irani and Solomon, 1986; Kuhlman, 1990). The foam strength of anionic surfactants in the presence of crude oil can be boosted by the addition of surface-active additives such as betaines (Basheva et al., 2000). Theoretically, this synergy can be evaluated in terms of molecular interaction parameters, which is a measure of interaction between surfactant molecules in the adsorbed layers and in the micelles (Rosen and Zhu, 1984). (Li et al., 2012) demonstrated that tertiary alkaline/surfactant/foam (ASF) processes could recover a significant amount of oil in a layered, 2D heterogeneous sandpack that was preferentially oil-wet. They showed that the addition of lauryl betaine to the surfactant formulation made the blend a good foaming agent with and without the presence of crude oil in the sandpacks.

2.12 MICROENCAPSULATION OF PARTICLES

2.12.1 Background

Microencapsulation is an active field of research with applications in drug delivery (Wang et al., 2006), food science and biotechnology (Nazzaro et al., 2012), material science (Brown et al., 2003), textile industry (Zhao et al., 2016), and oilfield applications (Gupta and Kirk, 2009). Emulsification is one of the common techniques for

microencapsulation (Lee et al., 2001; Morita et al., 2000). Typically, the emulsions are stabilized using surfactant molecules. However, surface-active colloidal particles can also act as sole stabilizers for foams (Binks and Horozov, 2005a; Gonzenbach et al., 2006a) and emulsions (Binks and Lumsdon, 2001; Ikem et al., 2008). The concept of particle-stabilized colloids dates back more than a century, when Ramsden (Ramsden, 1903) and Pickering (Pickering, 1907) reported their pioneering work. These particle-stabilized colloids are often referred as Pickering emulsions. In such emulsions, the solid particles could irreversibly adsorb at the interface and provide long-term stability against coalescence compared to conventional surfactant-stabilized emulsions (Binks, 2002). The presence of a dense shell of solid particles around the droplet act as a physical barrier, which allows the emulsion to sustain severe surrounding conditions such as high concentrations of dispersed phase or presence of electrolytes (Aveyard et al., 2003). These unique properties make these particle-stabilized emulsions effective for controlled delivery applications (Frelichowska et al., 2009; Simovic and Prestidge, 2007; Tikekar et al., 2013).

2.12.2 Concept of Water-in-Air Powders

In particle-stabilized emulsions, the wettability of the particles, characterized by contact angle θ (measured through water phase), strongly governs the emulsion curvature. For an air-water-particle system, hydrophilic particles ($\theta < 90º$) are likely to stabilize an air-in-water emulsion (aqueous foam) while, conversely, hydrophobic particles ($\theta > 90º$) are likely to stabilize a water-in-air powder. Binks and Murakami, (2006) showed that water-in-air powder can be produced by blending water and highly hydrophobic silica nanoparticles ($\theta > 90º$) at a high shear rate (Figure 2.13). In such powders, the liquid

droplets are completely encapsulated by self-assembled nanoparticles, which impart them free-flowing property similar to a dry powder. Such water-in-air powders are often referred to as 'dry water' in the literature (Saleh et al., 2011). This concept of dry water was first introduced in 1968 (Dieter et al., 1968). Since then, very few studies (Carter et al., 2011; Forny et al., 2007; Wang et al., 2008) have focused on utilizing this technique for technical applications. Wang et al. (2008) showed that dry water could be used for CO_2 or methane storage by forming clathrate hydrate. Forny et al. (2007) performed a comprehensive study on the operating conditions required for dry water formation. They demonstrated that these water-rich powders could be produced on an industrial scale. Carter et al. (2011) reported the formation of complex tri-phasic oil-in-water-in-air emulsion system, which allows to compartmentalize both oleophilic and hydrophilic phases on a micrometer scale.
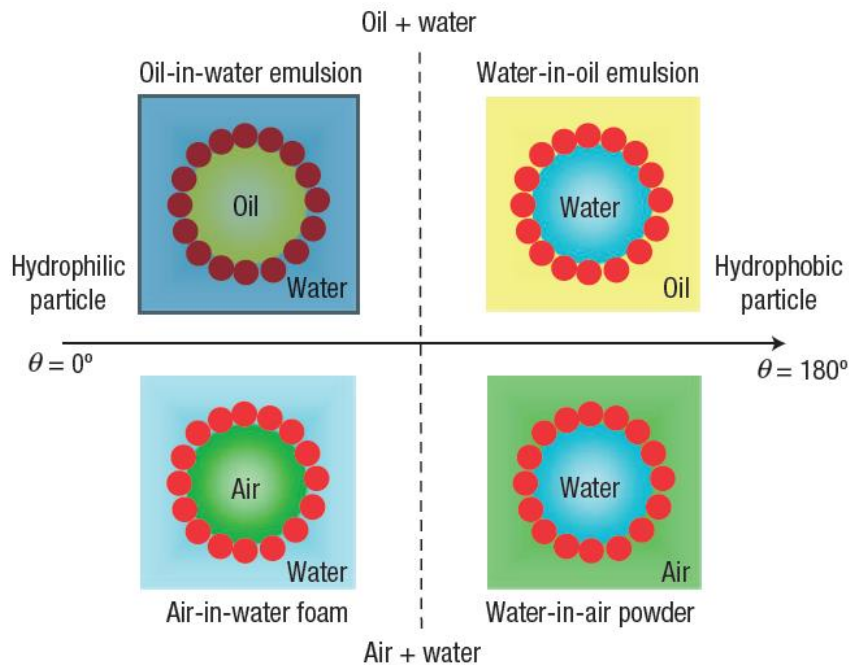
Figure 2.13: The different emulsion-types based on the wetting nature of the particles stabilizing the interface (Binks and Murakami, 2006)

40

2.12.3 Encapsulated PPG for Conformance Control

Most of the reservoirs are heterogeneous in nature. The sweep efficiency of injection fluid in such reservoir is typically poor. As discussed earlier, the foams are one of the techniques to improve the sweep. Other techniques include the use of gel treatment to improve the conformance control. Such treatments have been successfully applied in several mature fields (Liu et al., 2006; Pritchett et al., 2003). Preformed particle gel (PPG) has proven to be effective in conformance control application in oil fields (plugging fractures, channels, and thief zones). It is a temperature-resistant and salt-tolerant particle that swells under low salinity conditions. Recently, it has been applied to improve the sweep efficiency of water flooding in fractured reservoirs. These particles can vary from micron to mm in size and can plug high permeability channels as well as fractures (Imqam et al., 2015). It is an environmentally friendly material, which is typically not sensitive to reservoir minerals. Moreover, it overcomes some of the drawbacks of in-situ gelation process such as gelation time and uncertainties associated with gelling because of segregation, temperature, and pressure conditions for gelation. One of the challenges of using these particles is to prevent swelling in or near wellbore region during injection. The encapsulation and delayed release of PPG particles can mitigate these issues. In this work, a comprehensive study was performed to develop microencapsulated PPG microparticles. The release of these particles was then studies based on the external stimuli conditions.

2.13 MICROENCAPSULATION OF ACIDS

2.13.1 Shale Stimulation

Shale gas production has grown tremendously with the advent of modern hydraulic fracturing and directional drilling technologies. Its contribution to total gas production is expected to rise from 34% in 2011 to 50% in 2040 indicating the important role shale gas would play in U.S. energy future (Outlook, 2001). Before these technologies, the production from the shale basins was not considered economically viable. The low natural permeability of the shale limited the total production. The hydraulic fracturing (HF) relies on the injection of non-reactive fracturing fluids such as slick water or polymeric solutions to create fractures which increase the contacted reservoir surface area and the stimulated reservoir volume (Guo et al., 2014). These fracturing fluids are injected with proppants, which maintain the fracture conductivity after fracture closure. However, there are some technical challenges associated with proppant-based HF. Notably, proppants, such as sand, tend to settle vertically near the wellbore before the fracture closure resulting in an uneven proppant distribution (Tong et al., 2017; Tong and Mohanty, 2016). In addition to primary fractures, HF process connects to several natural and stimulated micro-fractures whose fracture apertures are in the order of 0.01 to 1 mm. These microfractures remain inaccessible to the proppants due to smaller aperture size as well as due to slow proppant transport, and hence are susceptible to fracture closure.

2.13.2 Acid Treatment in Calcite-Rich Tight Rocks

Acid treatment during or after hydraulic fracturing is an approach to improve HF (Grieser et al., 2007). This process relies on the injection of reactive fracturing fluids, such as concentrated acids, which create non-uniform surface etching on the fracture surface.

These injected fluids can penetrate both the natural and the induced micro-fractures. The conductivity of these fractures (without any proppants) is retained by the non-uniform etching/roughness even after fracture closure. Several studies have recommended the combination of proppant HF and acid HF for effective reservoir stimulation (Bale et al., 2010; Li et al., 2013). Although the concept of acid HF is relatively new, other acid treatment technologies, such as downhole acidic scale removal and matrix acidizing, are well-established and have been widely implemented (N. Li et al., 2016). The concept of matrix acidizing dates back to 1895, where concentrated HCl was used to stimulate the matrix of carbonate reservoirs (Williams et al., 1979).

2.13.3 Challenges of Acid Treatment

One of the technical challenges associated with the implementation of acid treatment in either carbonate reservoirs or carbonate-rich shale reservoirs is the high reactivity of the acidizing fluids. It leads to the face dissolution. In the case of carbonate matrix, worm holes are preferred over face dissolution (Wei et al., 2017). In the case of shale, differential/uneven etching of the fracture face is preferred over the uniform bulk dissolution of shale and mud creation. Therefore, retarded acid systems are often used for the long-distance propagation of acid and creation of wormholes (in carbonates) and differential etching (in shale fractures). Retarded acid systems include emulsified acids (acid-in-oil emulsions), foamed acids, polymer or surfactant-gelled acids, and solid encapsulated acids (Cairns et al., 2016; Nasr-El-Din et al., 2000; Taylor and Nasr-El-Din, 2003). The acid-in-oil emulsions method is one of the most commonly adopted technique and offers greatest chemical retardation (Kalfayan, 2007). These emulsions are typically stabilized by a surfactant. The presence of strong acidic conditions (pH ~1) and harsh

reservoir conditions (high temperature and high salinity) poses challenges to not only emulsion stability, but also to the aqueous stability of the surfactant.

Another common technique to retard the acid reaction is to use the solid encapsulated system. It relies on physical or chemical degradation of the surface coating for the release of acid. The precise control of required chemical conditions in the reservoir is difficult. Moreover, bulk scale production of these coated systems is prone to physical defects, which will lead to early release of acids. For example: Burgos et al. (2004) reported a field trial of acid fracturing using encapsulated citric acid. The acid was coated with vegetable oil, which prevented mixing with aqueous carrier fluids. The system relies on melting of coating above 180 ºF in reservoir and crushing during fracture closure. Similarly, Nasr-El-Din et al. (2009) reported a field trial of injection of the precursor of lactic acid in the form of solid beads. These beads hydrolyze in the presence of water and produce in-situ lactic acid. One of the reported operational challenges encountered during the implementation was that not all the beads were hydrolyzed due to an insufficient amount of water as most of the water was leak-offed in the formation after the fracture closure. In this work, a comprehensive study was performed to microencapsulate the acids using the hydrophobic silica nanoparticles to form acid-in-air powders. The encapsulated acid could be released via external stimuli such as mechanical pressure during fracture closure. Complementary experiments such as thermal stability tests, corrosion tests, and shale topography study were performed to elucidate the key advantages of these microencapsulated acid powders over conventional acid-in-oil emulsions.

Chapter 3: Foam Stabilized by Surfactant-Nanoparticle Mixture in Water-Wet Porous Media

3.1 INTRODUCTION

Surfactant stabilized foams have been used in the past for vertical conformance and mobility control in gas enhanced oil recovery processes. Lack of stability of these foams often limits their application. The goal of this study is to investigate the synergistic effects of using a blend of silica nanoparticles (NP) and anionic surfactants on foam stability in both bulk and porous media. First, stability of static foams was studied using surfactants and surfactant-NP mixtures with and without the presence of a crude oil. Second, the foam lamellae were studied by fluorescence microscopy and confocal laser scanning microscopy. Third, mobility of foams was measured by co-injecting the surfactant or surfactant-NP solutions with nitrogen gas through a Berea sandstone core at a fixed foam quality (gas fraction by volume). Fourth, oil displacement experiments were conducted in Berea cores using these foams. Finally, a high-pressure visualization study was performed where flow dynamics of these foams through a two-layer, heterogeneous sandpack were investigated.

3.2 METHODOLOGY

3.2.1 Material

Anionic surfactant Bioterge AS-40, a C_{14-16} alpha-olefin sulfonate, (39% active) was obtained from Stepan Co. The nanoparticles used in this study were aqueous dispersions of silica nanoparticles, Nyacol DP 9711, as provided by Nyacol Nano

---

This chapter is based on: (Singh and Mohanty, 2015, 2017a). Dr. Mohanty supervised the project.

Technologies, Inc. The mean diameter of these particles was 20 nm. Fluorescent silica nanoparticles(FL-NP), obtained from 3M, were used for fluorescence microscopy. These primary silica particles were 5 nm in diameter and polyethylene glycol (PEG) coating brings the particles to a nominal diameter of 10 nm. Berea sandstone cores were used in foam flow, retention, and core flood experiments. Crude oils (A, B and C) were obtained from a reservoir. The properties of these crude oils are tabulated in Table 3.1. The viscosity was measured using an ARES Rheometer. Sodium Chloride (>99% pure, Fisher Chemical), Nitrogen (research grade, Matheson, USA) were used as received. Blue food color (McCormick) was used to visualize the displacement of brine in foam flow experiments. Sand (US Silica) of two different mesh sizes- 100-120# and 40-70# were used to prepare heterogeneous sand packs. The viscosity was measured using an AR-G2 rheometer from TA instruments.

Table 3.1: Properties of the crude oils

Crude Oil	Density	Viscosity at 25 ºC	Acid Number
	gm/cm^3	cp	mg KOH/gm oil
A	0.773	9	2.45
B	0.887	382	1.72
C	0.830	36.2	4.91

3.2.2 Aqueous Stability of Nanoparticles

The silica nanoparticles, Nyacol DP 9711 has proprietary coating, which makes them hydrophilic in nature. The size of the nanoparticles was characterized using a Transmission Electron Microscope (TEM). A droplet of nanoparticle dispersion was taken on a Formvar-coated copper grid and was analyzed using FEI Tecnai TEM operating at 80kV. The mean diameters of primary particles were found to be 20 nm via image

analysis using Image J software. The TEM image is shown in Figure 3.1. The particle hydrodynamic diameters in the aqueous dispersions were characterized via dynamic light scattering (DLS) technique using the Delsa™ Nano analyzer without any pH adjustment and at room temperature. Ultra-pure water with resistivity greater than 18.2 megaohm-cm was used to prepare brine solutions. The stock solution of 2 wt.% nanoparticles was first prepared. This stock solution was used to prepare six samples containing varying concentration of NaCl (1, 2, 4, 6, 8, 10 wt %) and 0.5 wt.% nanoparticles. The seventh sample has 0.5 wt.% nanoparticles in API brine (8 wt.% NaCl and 2 wt.% $CaCl_2$). Figure 3.2 shows these samples after 2 weeks of preparation. The sample solutions were clear and no precipitation was observed. Table 3.2 shows measured hydrodynamic diameter of the nanoparticles for these samples. The mean values were between 24.9-35.5 nm for different salinities indicating no particle aggregation. These values from DLS analysis are slightly larger than that from TEM which was expected as DLS measures the hydrodynamic diameter and is biased towards larger particles in the suspensions (Cumberland and Lead, 2009a; Diegoli et al., 2008).
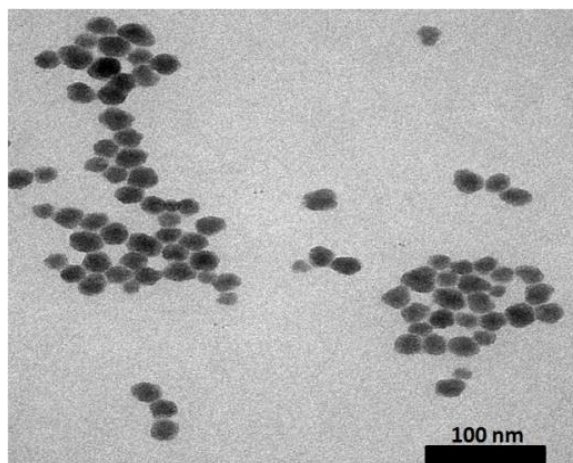
Figure 3.1: TEM image of surface modified-silica nanoparticles.

Figure 3.2: Samples containing 0.5 wt.% NP and 1, 2, 4, 6, 8, and 10 wt.% NaCl, and API brine (from left to right)

Table 3.2: Diameter of nanoparticles measured using DLS

Sample	Diameter in nm (by DLS)
0.5 wt.% NP in 1 wt.% NaCl	28.6 ± 7.7
0.5 wt.% NP in 2 wt.% NaCl	24.9 ± 6.9
0.5 wt.% NP in 4 wt.% NaCl	28.0 ± 7.4
0.5 wt.% NP in 6 wt.% NaCl	30.3 ± 8.0
0.5 wt.% NP in 8 wt.% NaCl	31.5 ± 8.1
0.5 wt.% NP in 10 wt.% NaCl	29.1 ± 8.1
0.5 wt.% NP in API Brine	35.5 ± 8.8

3.2.3 Preparation of Nanoparticles Dispersion

The stock solution of 1 wt.% Bioterge (BT) surfactant was first prepared. Samples were prepared by diluting this stock solution. Aqueous dispersion samples were prepared by incorporating silica nanoparticles with varying concentrations of 0, 0.1, 0.3, and 0.5 wt.%, each having 0.5 wt.% surfactant and 1 wt.% sodium chloride. The dispersion was

stirred for 12 hr to ensure mixture homogeneity. Table 3.3 shows the diameter and the zeta potential (both measured using Delsa™ Nano analyzer) of the nanoparticle dispersion with and without surfactant. As we can see from this table, presence of surfactant does not cause any particle agglomeration suggesting that surfactant, Bioterge can be used in combination of the nanoparticles.

Table 3.3: Properties of nanoparticle dispersions

Sample	Diameter in nm (by DLS)	Zeta Potential in mV
0.5 wt.% NP +1wt.% NaCl	28.6 ± 7.7	-3.87 ± 2.56
0.5 wt.% BT + 0.5 wt.% NP +1wt.% NaCl	28.3 ± 8.2	-4.34 ± 1.93
0.5 wt.% FL-NP + 1 wt.% NaCl	15.3 ± 6.6	-3.47 ± 2.86
0.5 wt.% BT +0.5 wt.% FL-NP + 1 wt.% NaCl	16.1 ± 7.3	-3.98 ± 3.21

3.2.4 Interfacial Tensions (IFT)

The IFT between oil-brine, oil-air, and brine-air systems were measured via pendant droplet analysis using Ramé-Hart goniometer. The droplet (of brine/oil) was held for sufficient time (>5 min) to allow it to equilibrate with air/liquid phase. The axisymmetric shape analysis of the droplet was performed by DROPimage Advanced software, which measures the IFT by fitting the drop profile with Young-Laplace equation. Ten measurements were performed 5 s apart and the mean and standard deviations of these measurements were calculated.

3.2.5 Foamability and Static Foam Tests

Preliminary foam tests were conducted by shaking 5 mL of these samples vigorously for 10 times in test tubes and the macroscopic foam textures were observed at the room temperature. In case of foam shake tests in presence of crude oil, 0.5 mL oil was initially added to samples before vigorous mixing. Static foam tests were conducted in a similar method as reported in the literature (Vikingstad et al., 2006). 100 mL of each sample was then taken in a graduated glass cylinder (diameter: 4 cm, length: 30 cm). Air was injected from the bottom and static foam was generated. The cylinder was always sealed from the top using a rubber cork (with a small outlet port for venting air) to avoid any evaporation. The height of the foam (above the liquid phase) was monitored as the time progressed. In foam tests in the presence of crude oils, first the foam was generated by dispersing the air and then oil (2 mL) was introduced in the bulk liquid phase from the bottom using a thin tube.

3.2.6 Vertical Foam Film Tests

Zhang (2004) performed this test to study effect of hardness on foam stability. A similar method was adopted in this study to study the effect of nanoparticles on foam stability. The foam drainage behavior was visualized by making foam in a small, vertically-oriented, optical glass cell (4 x 12 x 48 mm; Produstrial, Fredon, NJ). A small amount of nanoparticle dispersion (0.5 mL) was injected into the cell and foam was generated by dispersing air from the bottom using a syringe. The time-dependent foam morphology was observed using a Nikon microscope equipped with a high-resolution camera. Images were recorded every 30 seconds using Image Pro software and lamella width was measured after sufficient drainage time. Similar experiments were conducted using the dispersion of fluorescently tagged-nanoparticles. Images of foam texture were

captured both in visible as well as UV light. All these measurements were done at the room temperature.

3.2.7 Confocal Laser Scanning Microscopy (CLSM)

CLSM is a powerful tool which has been often used in the literature to study nanoparticles in foam films (Murray et al., 2011; Zou et al., 2013). CLSM was performed with Leica SP2 AOBS Confocal Microscope using the 10X dry (HC PL APO 0.40NA CS) objective lens operating in fluorescence mode. Samples containing 0.5 wt % surfactant and 0.3 wt.% of fluorescently tagged-nanoparticles were used. The nanoparticles were excited with 488 nm wavelength laser. In order to visualize the low-quality foam (disconnected bubbles), a small amount of sample was placed in the welled slide and air was dispersed using a syringe to make foam. A cover slip was then placed on top of the slide to seal it. The bottom of the sample was then scanned at room temperature. For imaging the high-quality foam (connected bubbles), similar procedure was adopted as in the case of vertical foam film tests. A small amount of sample was taken in rectangular glass cell (4 x 12 x 48 mm; Produstrial, Fredon, NJ) and foam was generated by dispersing air using a syringe. The glass cell was then placed horizontally after sealing it and the middle section of sample was scanned under the microscope. The resolution of the imaging was 200 microns for both the above cases.

3.2.8 Oil-Free Foam Flow Experiments in Cores

The cores were dried at 90 ºC for 24 h in an oven and were laminated with FEP shrink wrap tubing (Geophysical Supply Company, Houston, TX). These were then placed in a Hassler-type core holder (Phoenix, Houston, TX) with a confining pressure of 1500

psi. The brine porosity and permeability of the cores were then determined using standard methods (Peters, 2012). Figure 3.3 shows the experimental schematic. Two Series-D syringe pumps from Teledyne ISCO (Lincoln, NE) were used in the setup, which are capable of low injection rates (as low as 0.001cc/min). The apparatus was built to co-inject nitrogen gas and surfactant or surfactant-NP blends through a sandpack (0.6 inch diameter and 6 inch long) to ensure proper mixing and foam generation. The pre-generated foam was then injected from the top of the core in the core holder. The effluent from the core went to a high-pressure view cell. The downstream pressure of the experiment was maintained by a backpressure regulator installed after the view cell operating at 100 psi. The pressure drops across various sections of the core were measured using Rosemount differential pressure transducers. All connections were made with stainless steel Swagelok fittings. At the end of this experiment, several pore volumes of brine were flushed through the core to remove the foam and the backpressure was intermittently depressurized and pressurized several times to remove the trapped gas. Finally, the brine permeability was measured. Similar procedure was adopted by Simjoo et al. (2012) during their studies of immiscible foam flow in porous media.

3.2.9 Nanoparticle Transport and Retention in Porous Media

The experiment setup was designed to quantify the amount of nanoparticle retention in the porous medium. The setup was similar to Figure 3.3 except the sandpack and view-cell was removed. Silica nanoparticle concentration in the effluent was measured by inductively coupled plasma−optical emission spectrometer (ICP-OES) by following the method described in Wang et al. (2012). The calibration curve for different nanoparticle dispersion standards was found to be linear (R^2=0.9998).

3.2.10 Oil Displacement Experiments in Cores

The experimental setup was similar to Figure 3.3 except the view cell was removed to lower the dead volume of the setup to accurately measure the oil recovery. The cores were first fully saturated with brine; brine porosity and permeability were measured. These core properties are tabulated in Table 3.4. The cores were then flooded with filtered crude oil (at least 2.5 PV) from the top at a constant pressure of 750 psi at room temperature until the brine production stopped. The initial oil saturation was determined by mass balance. The whole setup was pressurized with a back-pressure of 100 psi. The brine flood was conducted at 1ft/day for 2 PV until no oil was produced. Then, it was flooded with brine at 5 ft/day to minimize capillary end effects. The cores were then pre-flushed with 1 PV of surfactant or surfactant-NP blend to avoid any adsorption of surfactant while foam flooding. Nitrogen gas and surfactant or surfactant-NP blend were then co-injected through sand pack to make foam. This pregenerated foam was then injected into the core from the top for more than 7 PV. Oil recovery and pressure drops were monitored at each step.

Table 3.4: Properties of the cores used

Experiments	Length	Diameter	Porosity	Permeability	Initial Oil Saturation
Foam flow	29.36 cm	2.52 cm	23.5 %	357 mD	0 %
Retention	30.27 cm	2.50 cm	22.3 %	313 mD	0 %
Coreflood-1	30.30 cm	2.47 cm	21.3 %	383 mD	64 %
Coreflood-2	30.30 cm	2.49 cm	22.9 %	315 mD	63.8 %
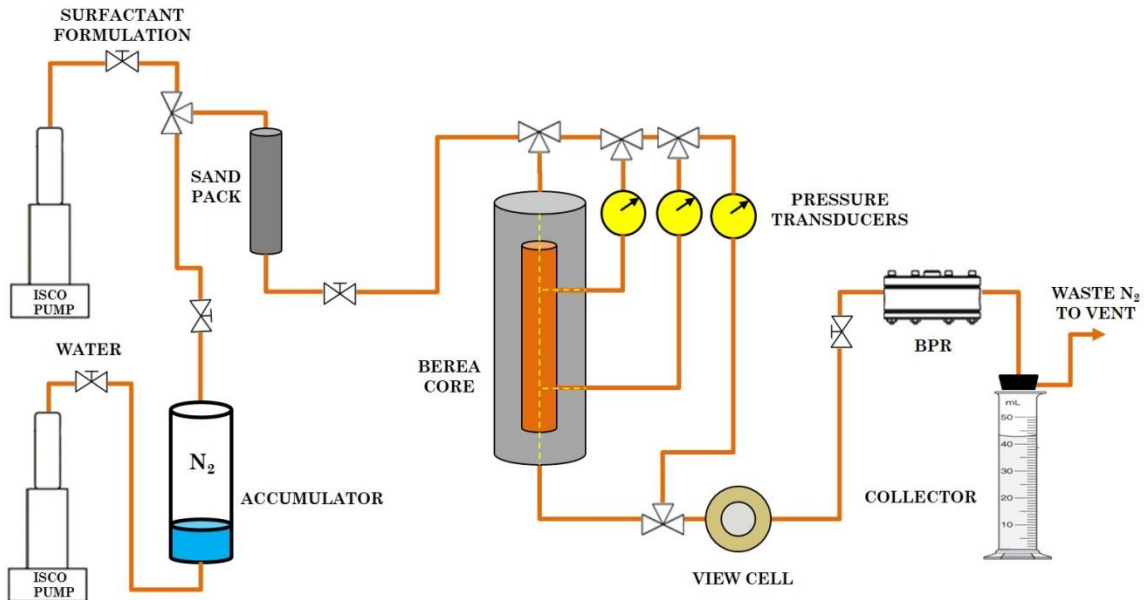
Figure 3.3: Schematic of the apparatus for foam flow experiments and corefloods

3.2.11 Preparation of 2D Heterogeneous Sandpack

An in-house sandpack holder made of stainless steel was fabricated with one face made of a transparent acrylic plate (thickness: 0.75 inch) for visualization. Chemical-resistant O-rings (McMaster-Carr) were used to provide sealing between acrylic and steel face under high pressure. The dimension of the interior of the holder was 5.4 inch * 2.9 inch * 1 inch. There were three injection ports on the left side and three production ports on the right side, as shown in Figure 3.4. Stainless steel screens (400 mesh) were welded on these ports to prevent sand flow. The holder was packed with two layers of silica sand: the top layer using 40-70 mesh and the bottom layer using 100-120 mesh. The permeability and the porosity of the system was measured to be 14 Darcy and 30%, respectively. The permeability of the top layer was 22.6 Darcy while that of the bottom

layer was 3.8 Darcy. The layer permeability was measured by flowing water through a 1D tube (1 ft long; 1 inch in diameter) packed with each sand-type at a time.

3.2.12 Oil-Free Foam Flow Experiments in 2D Sandpacks

Foam flow experiments were conducted to investigate the dynamics of foam flow in a heterogeneous porous medium, first in the absence of crude oil. Foams were stabilized by either a surfactant or a surfactant-nanoparticle blend. Petrophysical properties such as porosity and permeability of the sandpack were determined before performing the vacuum saturation with blue-dyed brine at the room temperature. Figure 3.4 shows the experimental schematic. Two series-D syringe pumps from Teledyne ISCO (Lincoln, NE) were used in the setup, which are capable of low injection rates (as low as 0.001 cc/min). The apparatus was built to co-inject nitrogen gas and aqueous (brine/surfactant/surfactant-nanoparticle blend) solution through a sandpack (0.6-inch diameter and 6-inch long) to ensure proper mixing and foam generation. The pre-generated foam was then injected through the three ports on the left side of the heterogeneous sandpack. The downstream pressure of the experiment was maintained by a back-pressure regulator (Equilibar, NC and Swagelok, OH) at 110 psi which was installed downstream of the sandpack. The pressure drop across the 2D sandpack was measured using Rosemount differential pressure transducers. An automated data acquisition system (LabView, National Instruments) was used to record the pressure. The experiment was performed at room temperature. The displacement of dyed-brine by injection fluid was captured using a Supereyes® microscope. The image processing was performed using the ImageJ/Fiji software to calculate the sweep efficiency (fraction of the area that is non-blue) as a function of time. For transient analysis, each image was first cropped into two parts —

upper layer and the bottom layer. Each image was first converted to an 8-bit image and then a binary image using the threshold function in the ImageJ. It resulted in black [rgb = (0, 0, 0)] and white [rgb = (255, 255, 255)] colors corresponding to the swept and the unswept region, respectively. The 'plot profile' function was then used to track the average foam front. This function takes an average of the rgb values at yz-planes for every x.
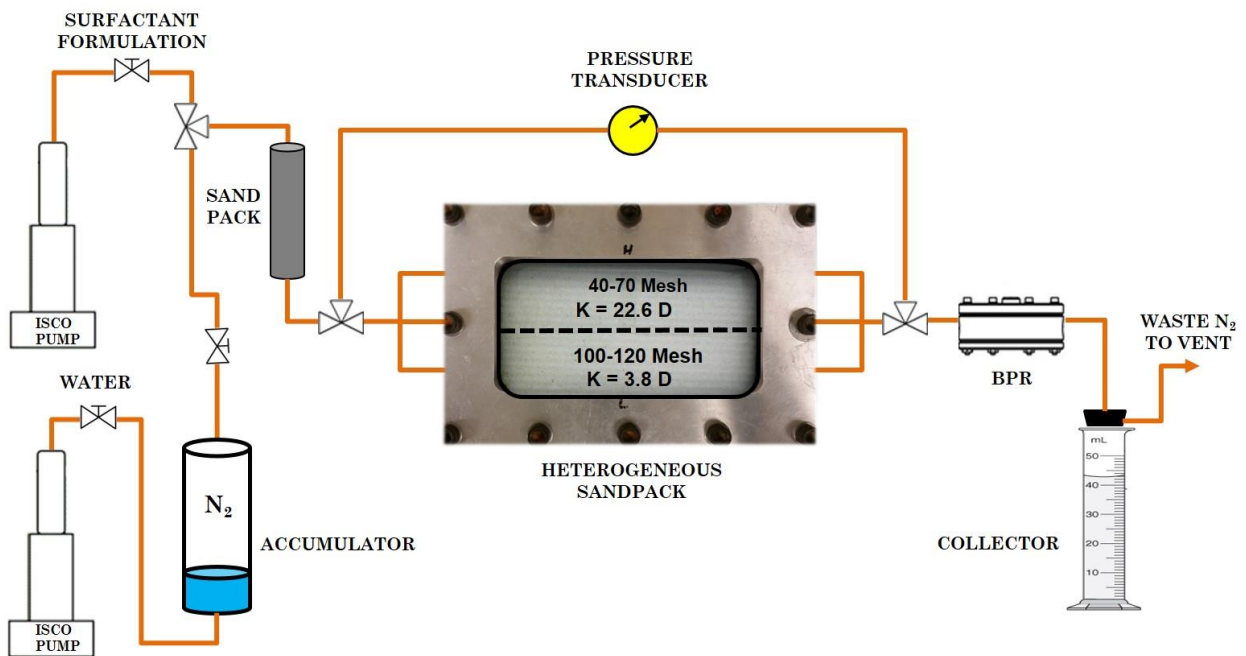
Figure 3.4: Schematic of the apparatus for foam flow and oil displacement experiments

3.2.13 Oil Displacement Experiments in 2D Sandpacks

The objective of oil displacement experiments was to visualize foam flow behavior in the presence of a crude oil in a heterogeneous system. The same experimental setup was used as in the case of oil-free foam flow experiments and the experiment was performed at

room temperature. Conventionally, in such experiments, the oil saturation is performed by displacing the brine-saturated porous media with crude oil at a constant high pressure. However, due to the high permeability contrast (6:1) in the present system, it was not possible to achieve high initial oil saturation using this technique. Therefore, the initial oil saturation was achieved by vacuum saturation, which resulted in 100% initial oil saturation for every case. The whole setup was then pressurized with a back-pressure of 110 psi. The brine flood was then conducted at 10 ft/D for 4 PV until no oil was produced. Nitrogen gas and surfactant or surfactant-NP blend were then co-injected through sand pack to make foam at 80% quality (volume fraction of gas). This foam was injected into the two-layer sand pack at an average interstitial velocity of 4 ft/d. This pre-generated foam was injected through the three ports on the left side of the heterogeneous sandpack for more than 18 PV. Oil recovery and pressure drops were monitored at each step. The oil displacement was captured using a Supereyes® microscope.

3.3 RESULTS AND DISCUSSION

3.3.1 Foamability and Foam Sensitivity to Crude Oil

Basic shake test was performed using 0.5 wt.% of surfactant in 1 wt.% NaCl brine with varying nanoparticle concentrations from 0 to 0.5 wt.%. The foam drainage behavior was not studied in these experiments and only the macroscopic foam behavior was observed. Figure 3.5 shows that these samples achieved maximum foam height indicating good foaming tendency in the absence of oil. No visual differences were observed (by naked eye) in the macroscopic foam texture with increasing nanoparticles concentration in the surfactant solution. This experiment was then repeated in the presence of crude oil. Before mixing the solution, 0.5 mL crude oil was added to the solution. Three crude oils

(A, B and C) were used in this test. Figure 3.6 shows the foam morphology at time t=0 min formed using 0.5 wt.% of surfactant solution (with no nanoparticles) in the presence of these crude oils.
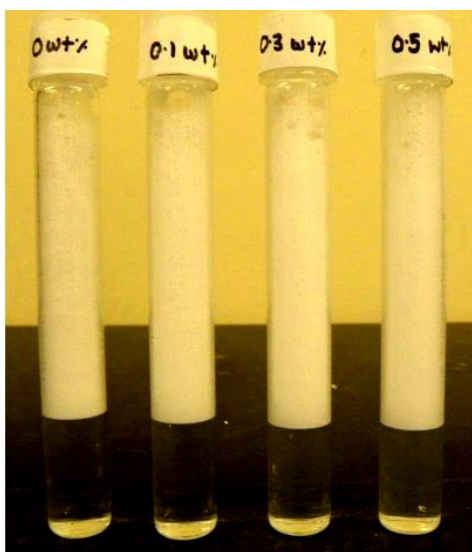
Figure 3.5: Foam morphology with 0.5 wt.% surfactant at 0, 0.1, 0.3, and 0.5 wt.% nanoparticle concentrations (from left to right)

It was seen that foam volume decreased drastically for the case of crude oil A indicating that foam was not stable with this crude oil. Oil was instantaneously drained to the bulk solution rupturing the foam lamellae showing no retention ability of oil within a lamella. For the case of crude oil B and C, foam volume was retained at the maximum at time, t=0 min and even for longer duration (> 8 h) as shown in Figure 3.6. In both of these samples, oil was seen distinctly inside the foam lamellae indicating the tendency of oil to imbibe into the lamella without rupturing it. Thus, the foam was more stable even in the presence of crude oil B and C as compared to the case of crude oil A. This test was repeated with samples having 0.5 wt.% surfactant and 0.3 wt.% nanoparticles and the same macroscopic foam behavior was observed.

58

Figure 3.6: Foam morphology with 0.5 wt.% surfactant in the presence of oil at time (a)
t=0 minute (left); (b) t=8 hr (right)

It can be seen that foam behaves differently with different crude oils. Typically, oils are known to be detrimental to foam stability and generally considered as foam inhibiting or antifoaming agents (Denkov, 2004b). Many researchers have reported this destabilizing effect of oil on foam stability in porous media (Friedmann and Jensen, 1986; Irani and Solomon, 1986; Kuhlman, 1990). Understanding the phenomenon of foam-oil interactions are quite complex, however a qualitative analysis can be done by investigating several parameters which are dependent on surface energies of the system. Spreading coefficients (S), entering coefficients (E) and bridging coefficients (B) as discussed in Chapter 2.

Table 3.5 shows the measured interfacial tensions of oil-gas-surfactant systems for the three crude oils. The presence of nanoparticles (used in this study) did not alter the surface tension values significantly, so the values of the parameters S, E, L and B would be the same for the case of the oil-gas-surfactant-NP system. Figure 3.6 shows, after 8 hr

foams were not stable with crude oil A (μ = 9 cp) and were quite stable with crude oils B (μ = 382 cp) and C (μ = 36.2 cp). Thus, foam sensitivity to crude oil revealed that lighter crude oils are more destabilizing to foams than heavier oils. The calculated values of spreading coefficients, entering coefficients, lamella number, and bridging coefficients are listed in Table 3.6. Results show that spreading coefficients, entering coefficients and bridging coefficients are positive for all the three crude oil systems. Thus, these parameters were not reliable in predicting the stability of the foam-oil system. Lamella number predicted crude oil system A to be of type C and crude oils B and C to be of type B, which is consistent with the macroscopic observation of these foams. However, the criterion based on Lamella number implies that a low oil-surfactant water tension system cannot form stable foam, which is not true (Li et al., 2012).

Table 3.5: Interfacial tension data for the three oils

System	Interfacial Tension (mN/m)		
	Oil A	Oil B	Oil C
Oil-Gas	21.31 ± 0.06	22.16 ± 0.04	20.73 ± 0.06
Oil-Surfactant	0.08 ± 0.02	4.03 ± 0.01	2.35 ± 0.04
Air-Surfactant	31.69 ± 0.09	31.69 ± 0.09	31.69 ± 0.09

Table 3.6: Calculated parameters based on interfacial data

Parameters	Oil A	Oil B	Oil C
Spreading Coefficient (S)	10.3 ± 0.17	5.4 ± 0.14	8.61 ± 0.19
Entering Coefficient (E)	10.4 ± 0.17	13.5 ± 0.14	13.31 ± 0.19
Lamella Number (L)	59.4 ± 0.11	1.2 ± 0.10	2.02 ± 0.13
Bridging Coefficient (B)	550.1 ± 0.34	529.2 ± 0.28	579.9 ± 0.38

3.3.2 Static Foam Tests

Static foam tests were carried out with nanoparticles dispersed in 0.5 wt.% surfactant with varying concentrations from 0.1 - 0.5 wt.% and foam height decay was compared with that of 0.5 wt.% surfactant alone. The decay of foam height was monitored with time. The results are plotted in Figure 3.7. Half-life, which is the time it takes for the foam to decay to half of its original height, can be seen from the plot. Half-life of foams generated using surfactants alone without nanoparticles was about 48 hr. As the concentration of nanoparticles was increased to 0.1 wt.%, half-life increased to 68 hr. The synergistic effects on foaming of surfactant-nanoparticle system became more pronounced when nanoparticles concentration was increased to more than 0.3 wt.%. The foam heights remained almost constant for days (>4 d). The mechanisms behind this synergy and enhanced bulk foam stability by combination of surfactant and nanoparticles are studied in the subsequent sections.

These foam tests were then repeated in the presence the crude oil A, B, and C using 0.5 wt.% surfactant with and without nanoparticles at the room temperature. The nanoparticle concentration used in these cases was 0.3 wt.%. Foams were first generated and then 2 mL crude oil was introduced from the bottom using a fine tube. Macroscopic foam-oil interactions and foam height were observed with time. Figure 3.8 shows the foam height decay profile in the presence of crude oil A as well as foam-oil interaction at the oil interface. The image was captured just after the introduction of oil into the foam system. As seen in the preliminary foam tests, crude oil A was quite detrimental to foam. As soon as the oil came in contact with the foam, it resulted in rupturing of the lamellae, which cause rapid decay of foam with time. The half-life in this case was only 24 min for both surfactant and surfactant-NP blend. No additional stabilization of foam was observed due to presence of nanoparticles as the deleterious effect of oil on foam dominated the foam

61

decay. The half-life in the absence of crude oil was of the order of days (> 48 h) and in presence of crude oil A only of the order of min (24 min).
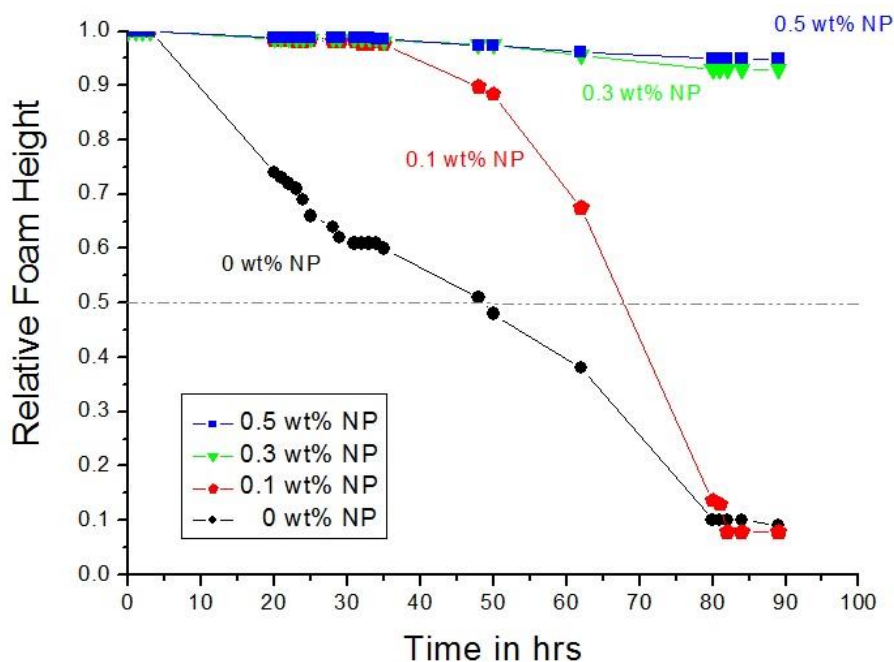
Figure 3.7: Static foam tests with 0.5 wt.% surfactant and varying nanoparticle concentration at 25 ºC

In case of crude oils B and C, there was no detrimental effect on the foam. The oil did not rupture the lamellae on contact, which resulted in longer half-lives. The additional stability of foam was observed in surfactant-nanoparticle blends as compared to surfactant alone as evident from longer half-lives. The half-life increased from 15 h to 22 h for the case of crude oil B (Figure 3.9); it increased from 10 h to 14 h for the case of crude oil C (Figure 3.10).
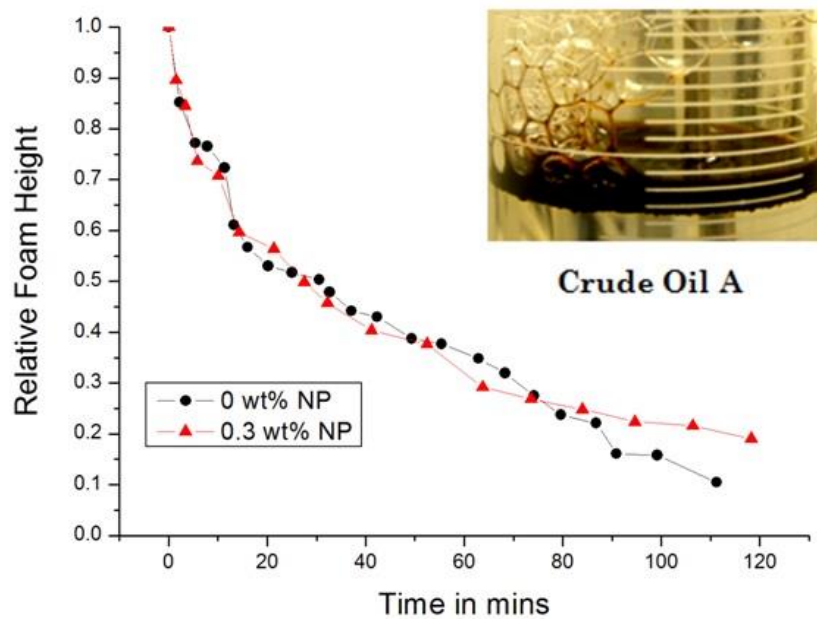
Figure 3.8: Static foam tests with crude oil A at 25 ºC
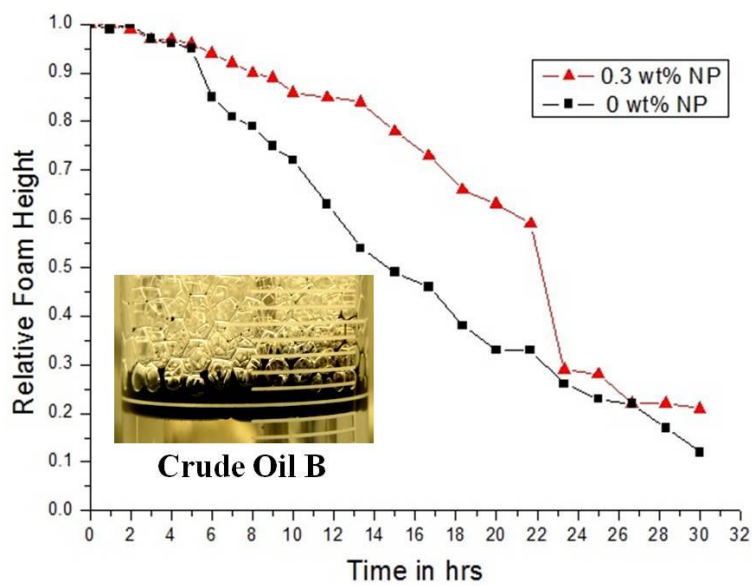
Figure 3.9: Static foam tests with crude oil B at 25 ºC
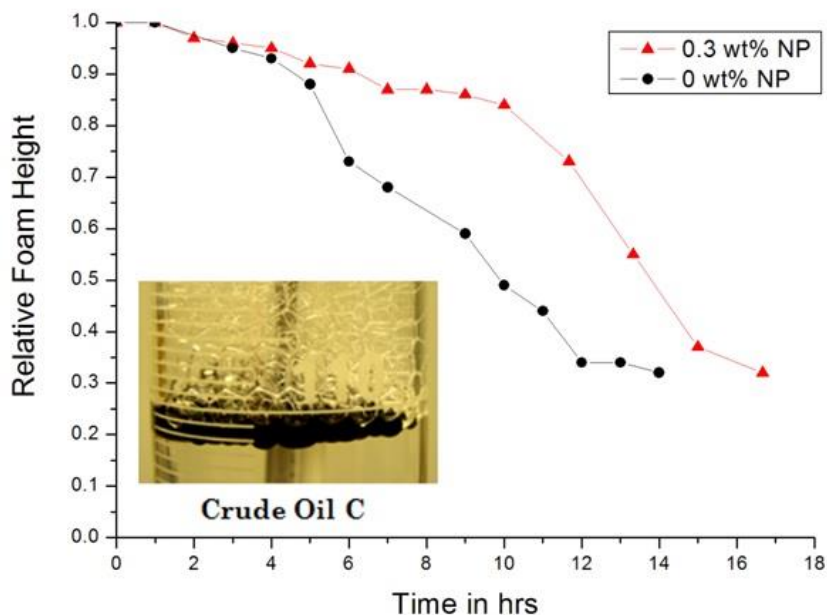
Figure 3.10: Static foam tests with crude oil C at 25 ºC

3.3.3 Vertical Foam Films Tests

Foam was generated in the optical glass cell using 0.5 wt.% surfactant solution with and without nanoparticles. The concentration of nanoparticles in the former case was 0.3 wt.%. The bubbles were formed between the parallel walls of foam cells spanning both sides. The typical bubble structure can be considered as polygonal prisms. A Gibbs-Plateau border is formed when three neighboring bubbles meet at one edge. The foam morphology was observed using a high-resolution microscope. After allowing sufficient drainage time of 30 min, the images of foam were captured. Figure 3.11 shows the foam structure for surfactant and surfactant-NP blend, respectively. The typical lamella width in surfactant case was found out to be about 340 microns, while for the blend it was 472 microns. The experiment was repeated several times to check for reproducibility and

64

results were consistent within a variation of ± 20 microns. The thicker lamella width for the surfactant-NP blend case indicates a retarded drainage process.
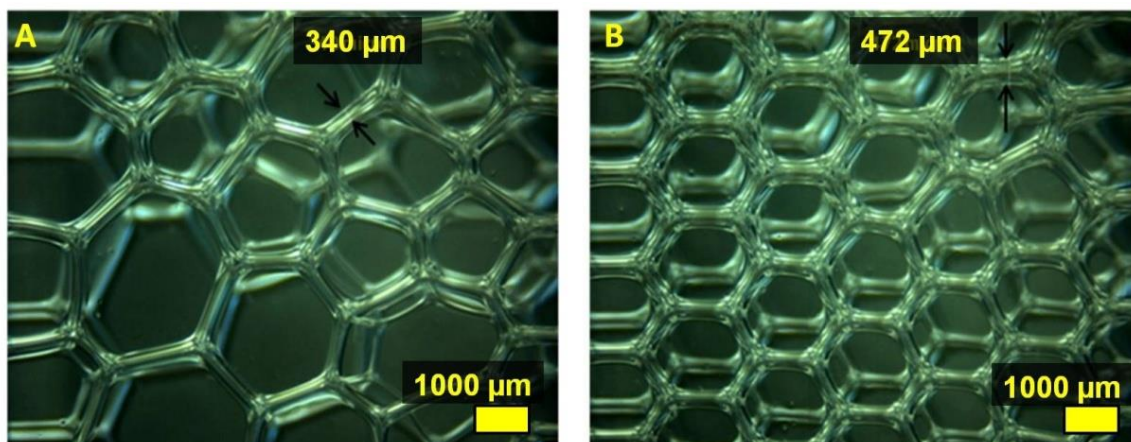
Figure 3.11: Vertical foam films made using (A) 0.5 wt.% surfactant (left) and (B) 0.5 wt.% surfactant and 0.3wt.% NP (right) (Scale Bar is 1000μm)

To fundamentally understand the mechanism of enhanced foam stability and thicker lamella width for the case of surfactant-NP blend, fluorescently-tagged nanoparticles (FL-NP) were used. Foam was generated using 0.5 wt.% surfactant with 0.3 wt.% FL-NP in the foam cell. The foam drainage behavior was observed using a vertical-stage microscope. Figure 3.12 shows the foam structure after 30 min of drainage in visible light and in UV light. From the front view of vertical films, the cross-section of the horizontal plateau border, which is perpendicular to the foam cell can be seen. The locations of the nanoparticles, i.e., fluorescence, can be easily seen from the image captured in the UV light. The fluorescence in the Gibbs-Plateau border and the lamellae in between the bubbles indicate nanoparticle trapping in these regions. These nanoparticles present a physical barrier in the drainage of free liquid and retard the coalescence process.
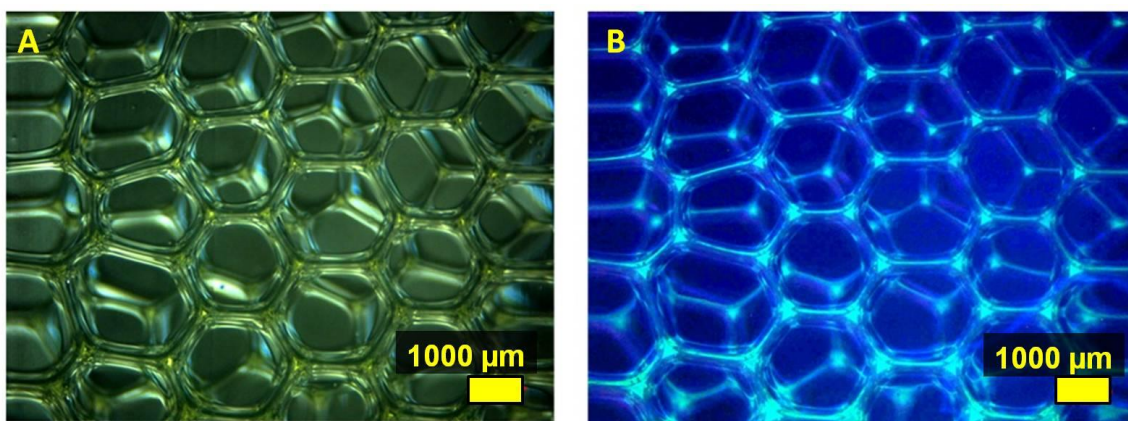
Figure 3.12: Vertical foam films made using FL-NP; Image captured in (A) visible light (B) UV light (Scale Bar is 1000μm)

3.3.4 Confocal Laser Scanning Microscopy (CLSM)

To investigate the mechanisms by which nanoparticles enhance surfactant-stabilized foam, CLSM was performed using hydrophilic, fluorescently-tagged silica nanoparticles (FL-NP). A mixture of AOS surfactant (0.5 wt.%) and FL-NP (0.3 wt.%) was placed in a glass vial and was hand-shaken for 30 seconds to generate foam with a fine texture. A small amount of this foam was transferred to a slide with a well and CLSM was performed. In this experiment, since the resolution was in the order of microns, it was not possible to resolve individual NP size. However, the microscope can detect the fluorescence emitted from the FL-NP and thus could be used to track the nanoparticles' location in the foam phase. Figure 3.13 A, B, and C show the fluorescence image, bright field image and merged image, respectively, of a weak foam sample. Since the nanoparticles concentration was relatively high (0.3 wt %), they (green) could be seen surrounding the bubbles and dispersed in the continuous liquid phase. Figure 3.13 D, E, and F show the fluorescence image, bright field image and merged image, respectively of

the strong foam sample. Silica-nanoparticles (green) could be observed surrounding the air-water interface as well as the plateau border. These nanoparticles form three-dimensional networks that enhance the stability of the bubbles. Similarly, Figure 3.14a shows one of the 2d-stack image acquired during the experiment. The yellow fluorescent color indicates the presence of the nanoparticles around the bubbles (black region). These nanoparticles can be seen present uniformly in the bulk liquid phase with no special affinity to the air-water interface due to their hydrophilic nature. A 3d reconstruction of the images was performed using a series of such 2D image stacks (Figure 3.14b). A similar 3d reconstruction of the inverted image shows the different bubbles present in the mapped cuboid (Figure 3.14c). It can be seen that these nanoparticles form a physical barrier all-around the air-bubble. These closely-packed nanoparticles act a 'colloidal armor' which retard the bubble coalescence and coarsening process. In the literature, several experimental studies have reported this phenomenon where particle-stabilized bubbles are stable (against collapse) for days or weeks as compared to surfactant-stabilized bubbles that collapse in order of hr (Du et al., 2003; Kostakis et al., 2007; Subramaniam et al., 2006). Note that in the static foam tests and CLSM, bulk foam stability was studied. In the subsequent sections, foam stability in porous media will be investigated.
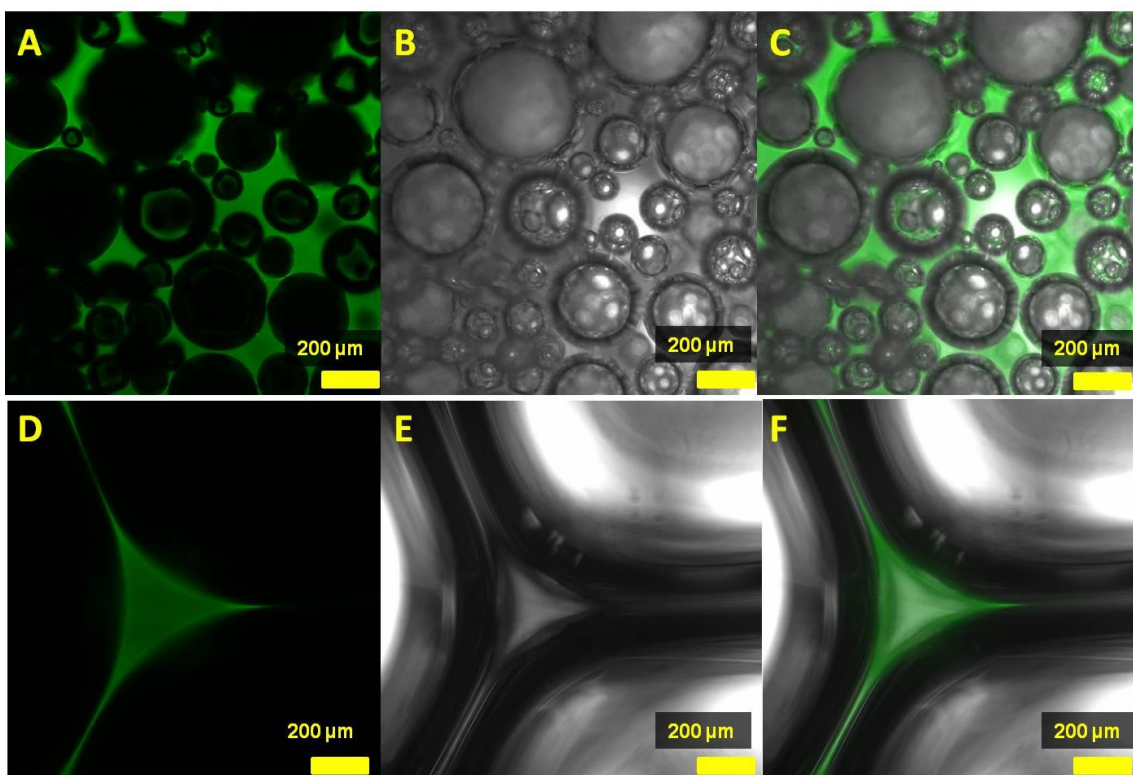
Figure 3.13: Confocal microscopy images of foam stabilized by 0.5 wt.% surfactant and 0.3 wt.% of fluorescently tagged nanoparticles. (A, D) Fluorescent image showing nanoparticles (green), (B, E) Bright field image, and (C, F) Merged Image (Scale bar is 200 microns)
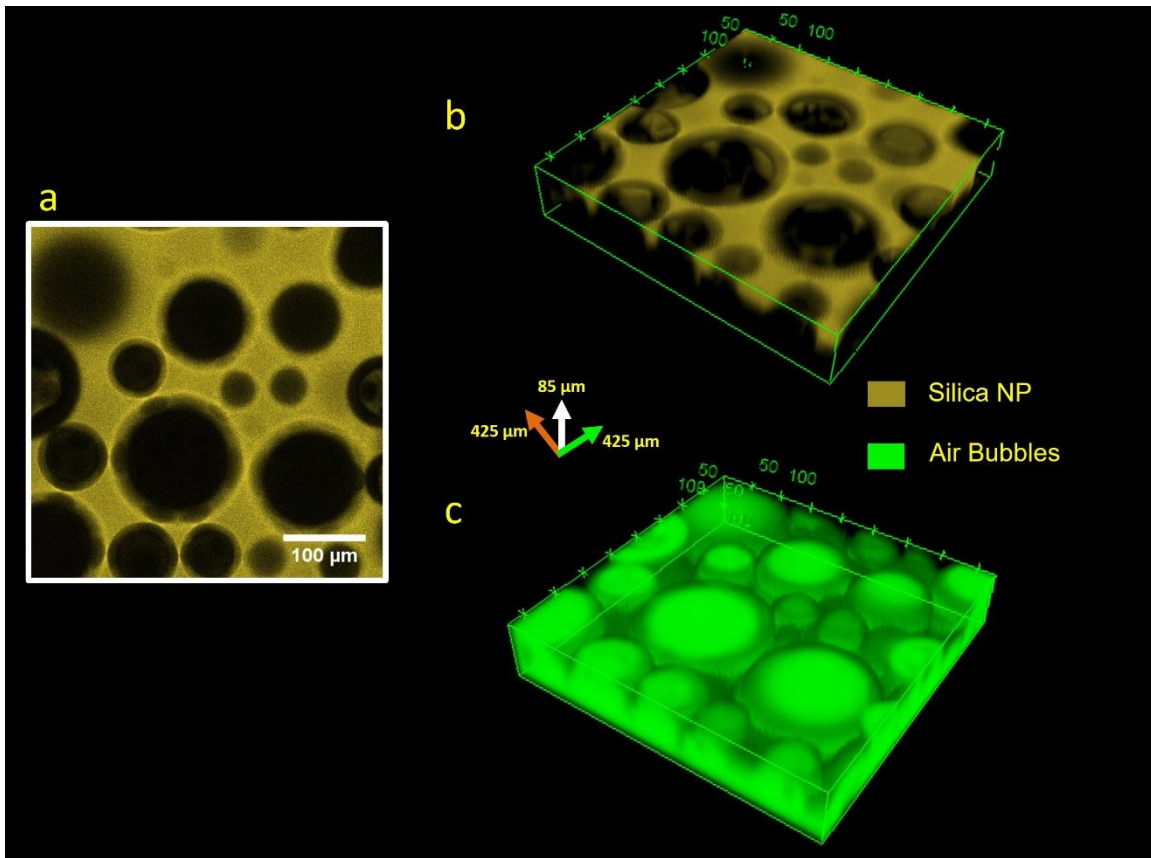
Figure 3.14: Confocal laser scanning microscopy images of foams stabilized by 0.5 wt % surfactant and 0.3 wt % FL-NPs: a) 2D stack image showing nanoparticles (yellow) and air bubbles(black) ; b) 3d reconstructed image showing nanoparticles (yellow); c) 3d reconstructed image showing air bubbles (green)

3.3.5 Oil-Free Foam Flow Experiments in Cores

Foam flow experiments were conducted in 1-ft long Berea sandstone cores using 0.5 wt.% surfactant with varying nanoparticle concentrations from 0.1 wt.% to 0.5 wt.% as foaming agents. The pressure drop profiles across different sections of the cores were monitored. The macroscopic foam texture of effluent coming out of the core was visualized using the view-cell installed at the downstream end of the core. The flow rates in these experiments were maintained at 4 ft/d to achieve a large enough pressure drop

which can be measured accurately. All these experiments were performed at the room temperature and with a back-pressure of 100 psi.

First, the surfactant pre-flush was conducted to saturate the core with surfactant and avoid any surfactant adsorption during foam flooding. Steady state pressure drop was measured after 3 PV of injection, which was very low (about 0.1 psi). After the surfactant pre-flush, nitrogen gas and surfactant solution (without nanoparticles) were co-injected into the sandpack to generate foam at 4 ft/day and with a quality of 80%. This pre-generated foam was injected from the top of the core for at least 5 PV to achieve a steady state pressure drop. Figure 3.15 shows the pressure drop obtained for this case and high-pressure foam texture as seen in the view cell after the steady state. The pressure drop has many fluctuations, but the average pressure drop in the steady state was about 9.7 psi. The average bubble diameter, measured from the foam texture, was about 910 microns.
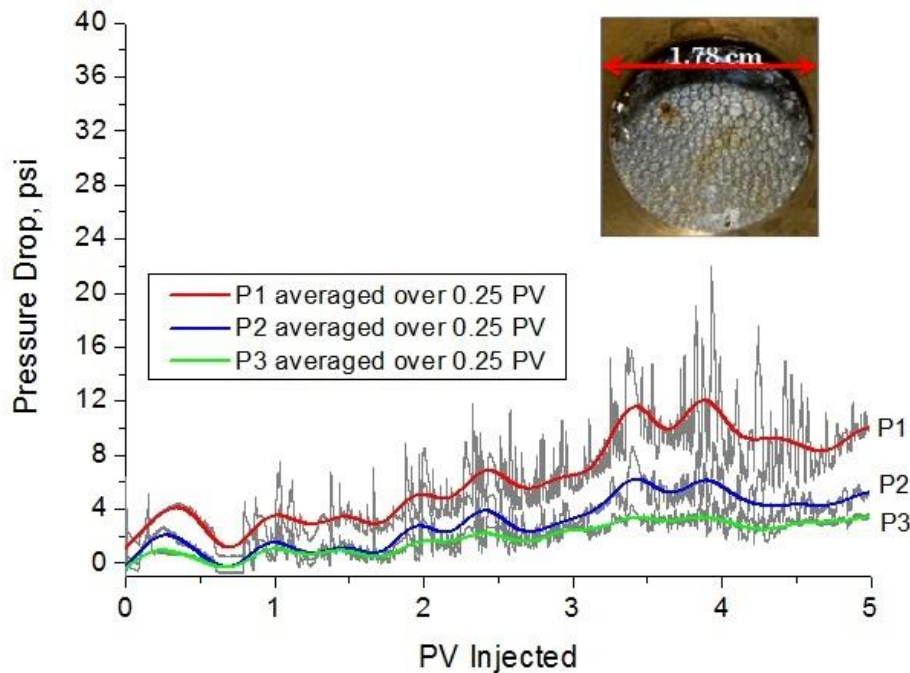
Figure 3.15: Pressure drop profile for the injection of pre-generated foam made by co-injecting nitrogen and 0.5 wt.% surfactant through a sandpack
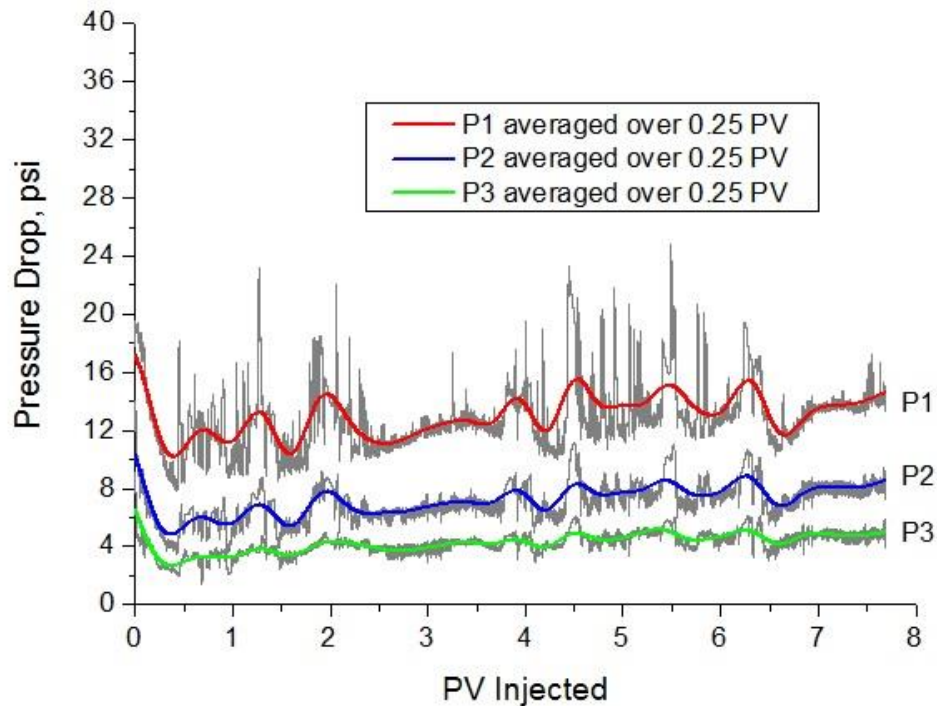
Figure 3.16: Pressure drop profile for the injection of pre-generated foam made by co-injecting nitrogen and 0.5 wt.% surfactant with 0.1 wt.% nanoparticle through a sandpack

In the subsequent steps, nanoparticle concentration was varied from 0.1 wt.% to 0.5 wt.% in the injection fluid while keeping the same surfactant concentration (0.5 wt %). Flow rate was kept at 4 ft/day with 80% quality throughout the experiments. Steady state pressure drops were typically achieved after 8 PV of co-injection. Figure 3.16 shows the pressure drop profile when 0.1 wt.% of nanoparticles was used. The average steady state pressure drop was about 13.7 psi, which is slightly more than the case with no nanoparticles indicating a stronger foam. Then nanoparticle concentration was raised to 0.3 wt.% in the injection fluid. Figure 3.17 shows the pressure drop profile and the steady state foam texture. Steady state pressure drop in this case was 17.4 psi. It can be seen that the foam in this case consists of fine textured bubbles. The average bubble diameter was

71

found to be 330 microns, which is smaller than those for the NP-free surfactant case. Large pressure drop achieved in this case is due to finer in-situ bubble texture stabilized by surfactant-nanoparticle system. With 0.5 wt.% concentration of NP, the steady-state pressure increased to 21.5 psi.
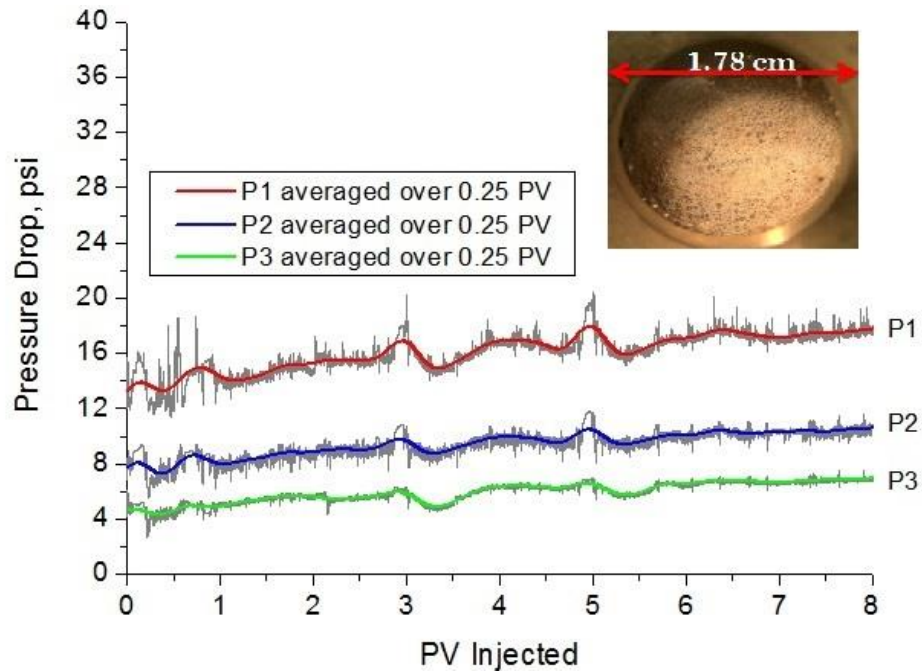
Figure 3.17: Pressure drop profile for the injection of pre-generated foam made by co-injecting nitrogen and 0.5 wt.% surfactant with 0.3 wt.% nanoparticle through a sandpack
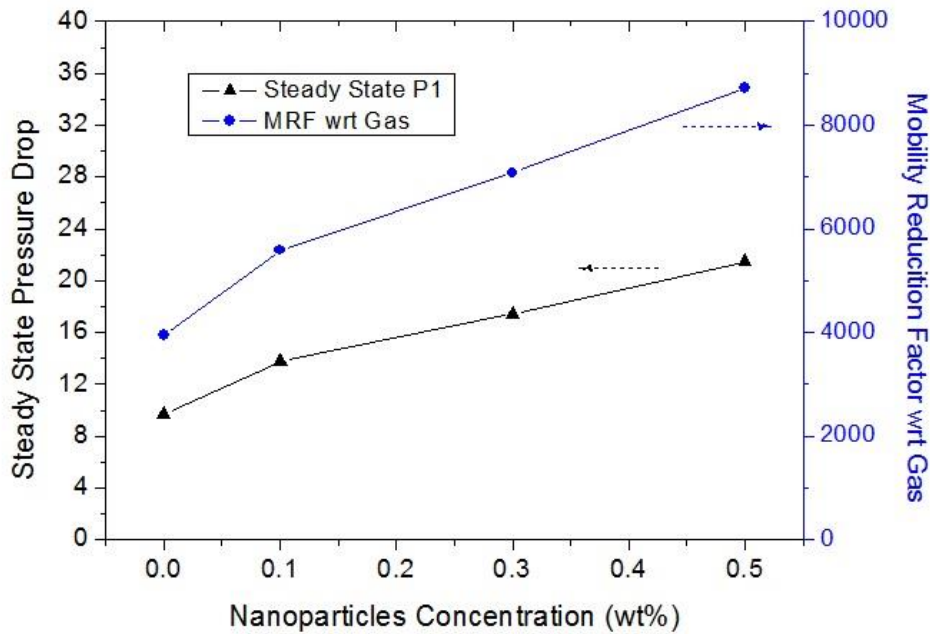
Figure 3.18: Steady state pressure drops (left axis) and mobility reduction factors (right axis) achieved using varying concentrations of nanoparticles

Mobility reduction factor (MRF) is defined here as the ratio of the pressure drop across the core due to foam flow and the pressure drop due to single phase gas flow at the same flow rate. Figure 3.18 is the plot of steady state pressure drops and mobility reduction factors achieved for varying concentrations of nanoparticles. As the nanoparticle concentration increases from 0 wt.% to 0.5 wt.%, the MRF increases from 4000 to 8700. At the end of the experiment, the core was cleaned as described in the methodology section and brine permeability was measured. It was found to be 335 mD which was close to the initial value of 357 mD suggesting minimal permeability damage. Small reduction in permeability was expected due to some trapped gas in the core that could not be removed by brine flushing and rapid pressurization-depressurization cycles.

3.3.6 Nanoparticle Transport and Retention in Porous Media

In order to quantify the nanoparticle retention, the term Nanoparticle Recovery, R_{NP} was calculated which is used in the recent literature (Caldelas et al., 2011; Murphy, 2012). It refers to the ratio of amount of nanoparticles recovered to the amount of nanoparticles injected in the system. The quantity of nanoparticles recovered was calculated by integrating the area under the effluent history using the trapezoidal approximation. The ratio of this quantity with pore volumes of nanoparticles injected multiply by injected nanoparticle concentration gives the R_{NP}. Murphy[61] reported retention data of Nyacol (DP 9711) nanoparticles, which were used in the present study, in the Boise sandstone. He reported R_{NP} of 96% and 95% when injected concentration was 2.84 wt.% and 1.5 wt.%, respectively. In the present study, the Nanoparticle Recovery for a mixture of 0.5 wt.% surfactant and 0.5 wt.% nanoparticles in the Berea sandstone was measured at the similar conditions as used in above foam flow experiments. First, 4 pore volumes (PV) of the above mixture (in 1wt.% NaCl brine) was injected in the Berea core (previously saturated with brine) at 4ft/day. Second, 4 PV of brine was then injected at same flow rate to flush the system. Effluent samples were taken at each 0.1 PV at each step. These samples were analyzed using ICP-OES. Figure 3.19 shows the plot of effluent history with x-axis showing the PV injected and the y-axis showing dimensionless concentration, C_D which is the nanoparticle concentration of the effluent normalized by nanoparticle concentration of the injected fluid. Nanoparticle recovery, R_{NP} was calculated using this plot and was found to be 99.57%. This result along with the data available in the literature shows that nanoparticles used in this study has very low retention in the porous medium and has the potential of long-distance propagation without causing permeability damage.
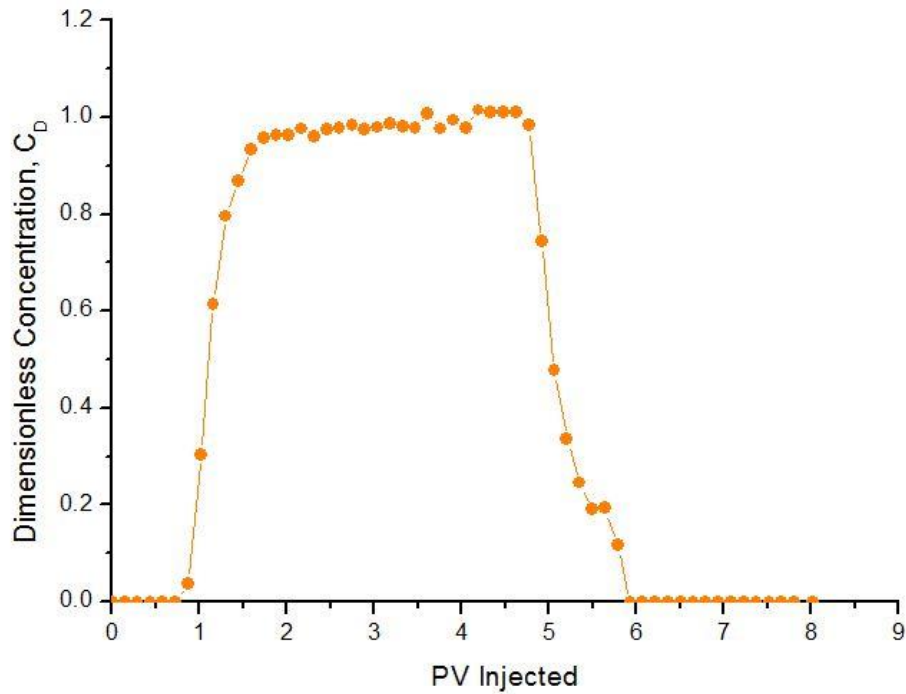
Figure 3.19: Effluent history of nanoparticles

3.3.7 Oil Displacement Experiments in Cores

Core Flood 1 was conducted in a Berea core with the crude oil C. The initial oil saturation was 64 %. Figure 3.20 shows the injection scheme, cumulative oil recovery and overall pressure drop across the core. Brine flood was conducted at 1 ft/day to mimic the waterflood at a typical field rate. It was continued for 2 PV until no oil was produced. The waterflood oil recovery was 54.4 %OOIP (original oil in place) and oil saturation was reduced to 29.2 %. The pressure drop during water flood was between 1-3 psi. Then, brine was injected at 5 ft/day for another 1 PV to minimize the capillary end, if any. The pressure drop increased to 7.4 psi as the flow rate was increased 5 times. No oil was recovered during this stage implying no significant capillary end effects. Before

75

conducting the foam flood, the core was pre-flushed with 0.5 wt.% surfactant solution for 1 PV at 1 ft/day to avoid any surfactant adsorption during foam flooding. No oil was recovered during surfactant injection as the surfactant does not lower the IFT sufficiently (IFT ~ 2.3 mN/m) to mobilize residual oil. The pressure drop during pre-flush was almost constant at 1.1 psi. Then, co-injection of 0.5 wt.% of surfactant solution and nitrogen gas was started with a quality of 80% at 1ft/day. Since there is some dead volume before the core as explained earlier, the pressure drop increase due to in-situ foam generation was delayed by about 0.7 PV. The additional oil recovery for first 3.5 PV of co-injection over waterflood was 9.3% OOIP. No significant amount of oil was produced after 3.5 PV of injection, but the co-injection was continued for another 4.5 PV to observe the foam mobility in the presence of residual oil. The average pressure drop continued to grow and reached about 9 psi at the end of experiment. The ultimate cumulative oil recovery was 63.7 %OOIP and final oil saturation was 23.2%.

The second core flood (Core Flood 2) was conducted in another Berea core with the same procedure as the previous core flood except with both surfactant and nanoparticles. The initial oil saturation in this case was 63.8%. The cumulative oil recovery (%OOIP) and overall pressure drop are shown in Figure 3.21. The core was flooded with brine for 2 PV at 1 ft/day which reduced the oil saturation to 29.8% and resulted in 53.3 %OOIP oil recovery. The pressure drop during this stage was low (~ 2 psi). Then, the core was flooded with brine for 1 PV at 5 ft/day. No additional oil was recovered implying negligible capillary end effects. The pressure drop increased to about 10.5 psi at the flow rate of 5 ft/day. Then, the core was pre-flushed with an aqueous solution of 0.5 wt.% of surfactant and 0.3 wt.% nanoparticle for 1 PV. No oil was recovered during this stage. Co-injection of 0.3 wt.% nanoparticle in 0.5 wt.% surfactant solution and nitrogen gas was then started at 1ft/day with 80% quality. The additional oil

recovery over water flood after 3.5 PV of injection was 10.6 %OOIP. The co-injection was continued for another 4.5PV. The pressure drop in this core flood went to around 9.8 psi at the end of the experiment.
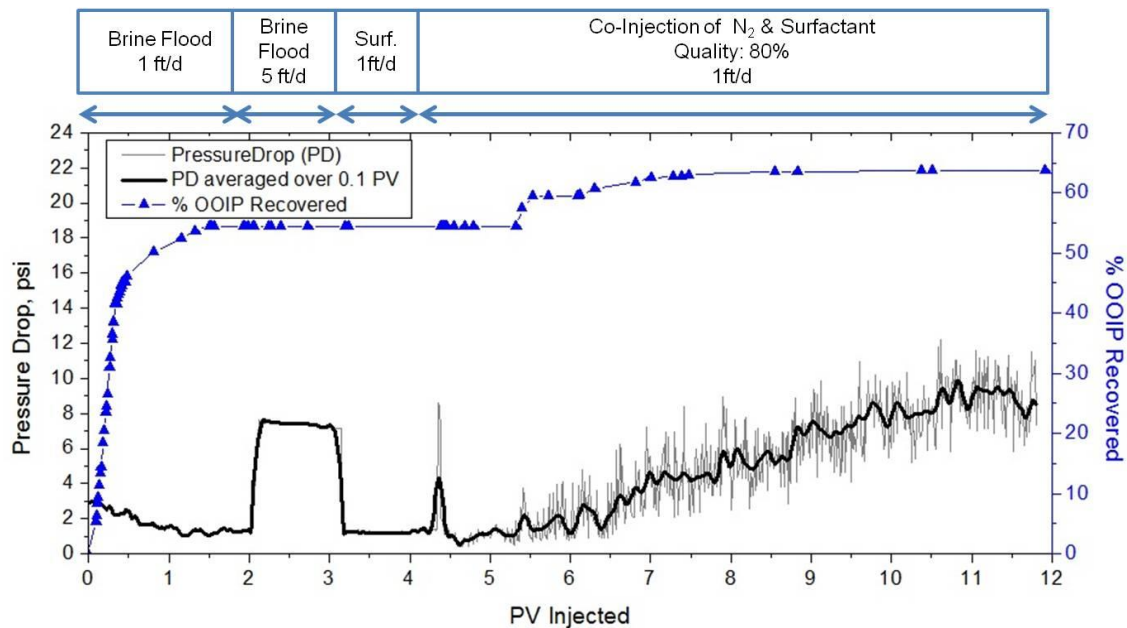
Figure 3.20: Pressure drop profile (left axis) and cumulative oil recovery (right axis) for the Core Flood 1

The objective of these oil displacement experiments in water-wet cores was to investigate the potential of displacing waterflood residual oil by immiscible foams stabilized by surfactant or surfactant-NP blends. These experiments showed that these foams can reduce the residual oil by about 10 %OOIP. This is significant considering that the gas is immiscible with the oil. In water-wet systems, immiscible foam can increase the trapped gas saturation which decreases the residual oil saturation resulting in additional oil recovery. Moreover, they can reduce the gas mobility significantly. It should be noted, the cores used in the corefloods were only one inch in diameter and were quite homogenous;

thus, there was no scope to improve the volumetric sweep efficiency. Similar oil displacement experiments in heterogeneous and 3D media could address this issue. Therefore, further oil-free foam flow experiments and oil displacement experiments were performed in 2D heterogeneous sandpack. The results of these experiments are discussed in subsequent sections.
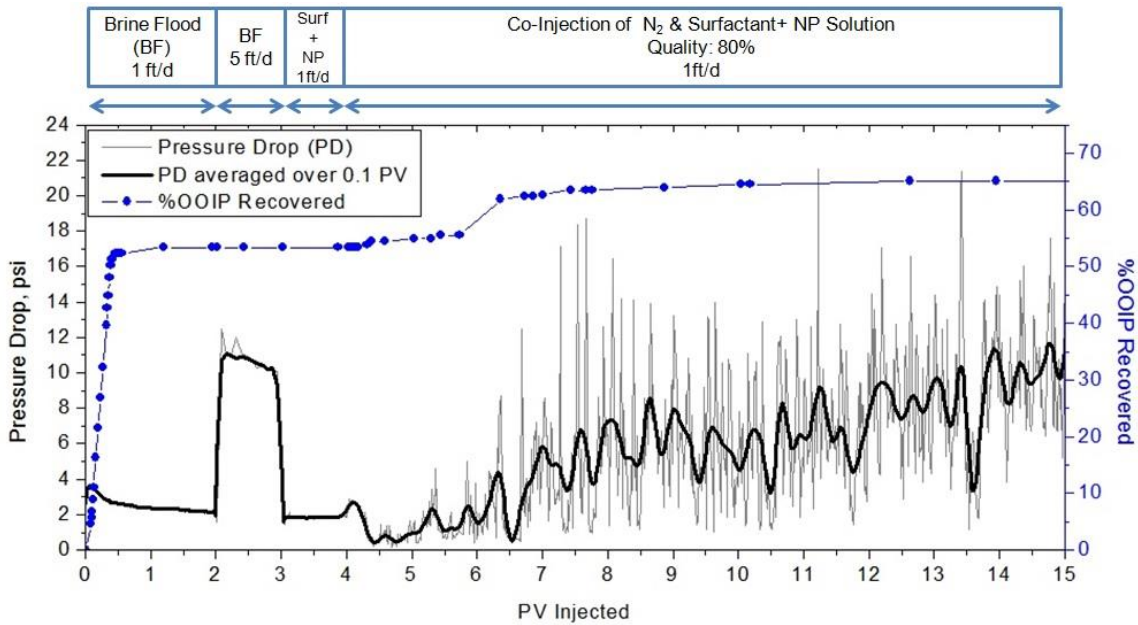
Figure 3.21: Pressure drop profile (left axis) and cumulative oil recovery (right axis) for the Core Flood 2

3.3.8 Oil-Free Foam Flow Experiments in 2D Sandpacks

The objective of foam flow experiments was to investigate the foam rheology in the absence of oil and to visualize the displacement of water by foam in the two-layer model. The layered sandpack was first fully saturated with blue-dyed water (1 wt % NaCl) by flushing several pore volumes of this fluid. First, a base case was performed in which

only brine (1 wt % NaCl) was injected as the displacing fluid at 10 ft/D. Figure 3.22 shows the displacement profile as a function of PV injection. The upstream dead volume was equal to 0.09 PV. The reported pore volumes of injection in this chapter are after correcting for this dead volume. The injected brine first swept the top layer and a breakthrough was observed in the top layer before it started sweeping the bottom layer. It is to be noted that mobility ratio is 1 for this case. The pressure drop in this case was very low (0.04 psi). The system was again flushed with 20 PV of blue-dyed brine (1 wt % NaCl) to displace the colorless brine before starting the next experiment.

Second, AOS surfactant solution (0.5 wt.%) and nitrogen gas were co-injected at 80% quality. Initially, the in-situ generated foam mixes with the initially 100% water saturated layers. The presence of excess water results in low-quality (less gas fraction by volume), weak foam. The dilution of surfactant at the foam front further weakens the foam. Some of the foam broke down to release gas. Due to a large permeability at the top, significant vertical permeability of the system and the lower density of gas (compared to brine), severe gas channeling was observed from the top of the upper layer. (Since there was no overburden pressure on the sandpack, a high permeability channel of width less than 1 mm was present on the top of the upper layer. The channeling was not visible in the displacement profile but was verified by visual inspection of the gas coming out from the outlet.). The gas breakthrough was observed in less than 0.1 pore volume (PV) of foam injection. Even after 1 PV of foam injection, the sweep efficiency was poor and minimal sweep was observed in the low-permeability layer. The initial mobility ratio, M (ratio of mobility of gas to the mobility of the displaced phase) in this case was high compared to the first case of brine flood where M was 1. Therefore, initially sweep efficiency of brine flood was better than that of foam flood. After 1 PV of foam injection, as foam strength increased (and mobility ratio decreased) it started diverting fluid to the low permeability

(lower) layer. Note that at this stage, foam had not swept the upper layer completely, but it had started to sweep the bottom layer (as opposed to the brine case). This (sweeping of the low permeability layer before total sweep of the high low permeability layer) is one of the fundamental differences between the sweeping mechanism of foam flooding as compared to any other single-phase injection such as brine, polymer, or surfactant flood. A sweep efficiency of 100% was achieved after 3.75 PV injection. The pressure drop increased from 0.04 psi to 9.3 psi at the end of the experiment. This increase in pressure drop is an indication of strong in-situ foam presence in the system. The resistance factor (RF) which is the ratio of pressure drop due to single-phase brine injection to the pressure drop due to foam injection at the end of experiment was 232.

After the experiment, the system was flushed with 20 PV of methanol to break the foam completely. It was followed by an injection of more than 30 PV of brine (4 wt.% NaCl) to flush the methanol. The system was intermittently pressurized and depressurized to remove any trapped gas from the system. The system was again flushed with 20 PV of blue-dyed brine (1 wt % NaCl) to displace the colorless brine before starting the next experiment. To ensure complete removal of the colorless brine, the salinity of the effluent was measured using a handheld analog refractometer which came out to be 1 wt.% NaCl (equal to blue-dyed brine). The pressure drop across the sandpack was measured for blue-dyed brine injection at 10 ft/D and it was equal to the initial pressure-drop of brine flood which suggested that no foam is trapped in the system.

The sweep improvement due to foam injection is a strong function of the surfactant formulation. The foaming tendency of the formulation could be increased by either increasing surfactant concentration, adding foam boosters such as zwitterionic surfactants or surface-modified nanoparticles (Sun et al., 2014b) or polymers (Pei et al., 2010). This work is focused on utilizing the synergy between surfactants and hydrophilic nanoparticles

in stabilizing foams. Therefore, a blend of 0.5 wt.% AOS surfactant and 0.3 wt.% NP was prepared. This blend was co-injected with nitrogen gas at 80% quality. Figure 3.23 and 24 shows the comparison of pressure drop and sweep efficiency for the three cases, respectively. For 1 PV of injection – the sweep efficiency of the blend case was better than that of the surfactant case (Figure 3.22). It suggests that stronger foam was created faster in the blend case. A 100% sweep efficiency was achieved in about 3 PV for the case of blend foam compared to 4 PV for the case of surfactant foam. The pressure drop in this case at the end of 10 PV was about 18.2 psi which is 1.95 times the surfactant case, suggesting that the high resistance factor was achieved due to nanoparticles. The RF in this case was 455. Thus, this experiment shows the synergistic interactions of surfactant and nanoparticles in stabilizing foam in a two-layered system. The transient foam flow analysis is discussed in the discussion section.

3.3.9 Oil Displacement Experiments in 2D Sandpacks

Flood 1 was conducted with the surfactant AOS as the foaming agent. The porosity and permeability of the two-layer sandpack were 30% and 14 Darcy, respectively. The sandpack was vacuum-saturated with crude oil which resulted in the initial oil saturation of 100%. Figure 3.25 shows the injection schedule, cumulative oil recovery (secondary y-axis) and overall pressure drop (primary y-axis) across the sandpack. Brine flood was conducted at 10 ft/d to mimic a waterflood in a reservoir. It was continued for more than 4 PV until no oil was produced. The waterflood oil recovery was 46 %OOIP (original oil in place) and oil saturation was reduced to 54%. The pressure drop during water flood was very low (0.17 psi).
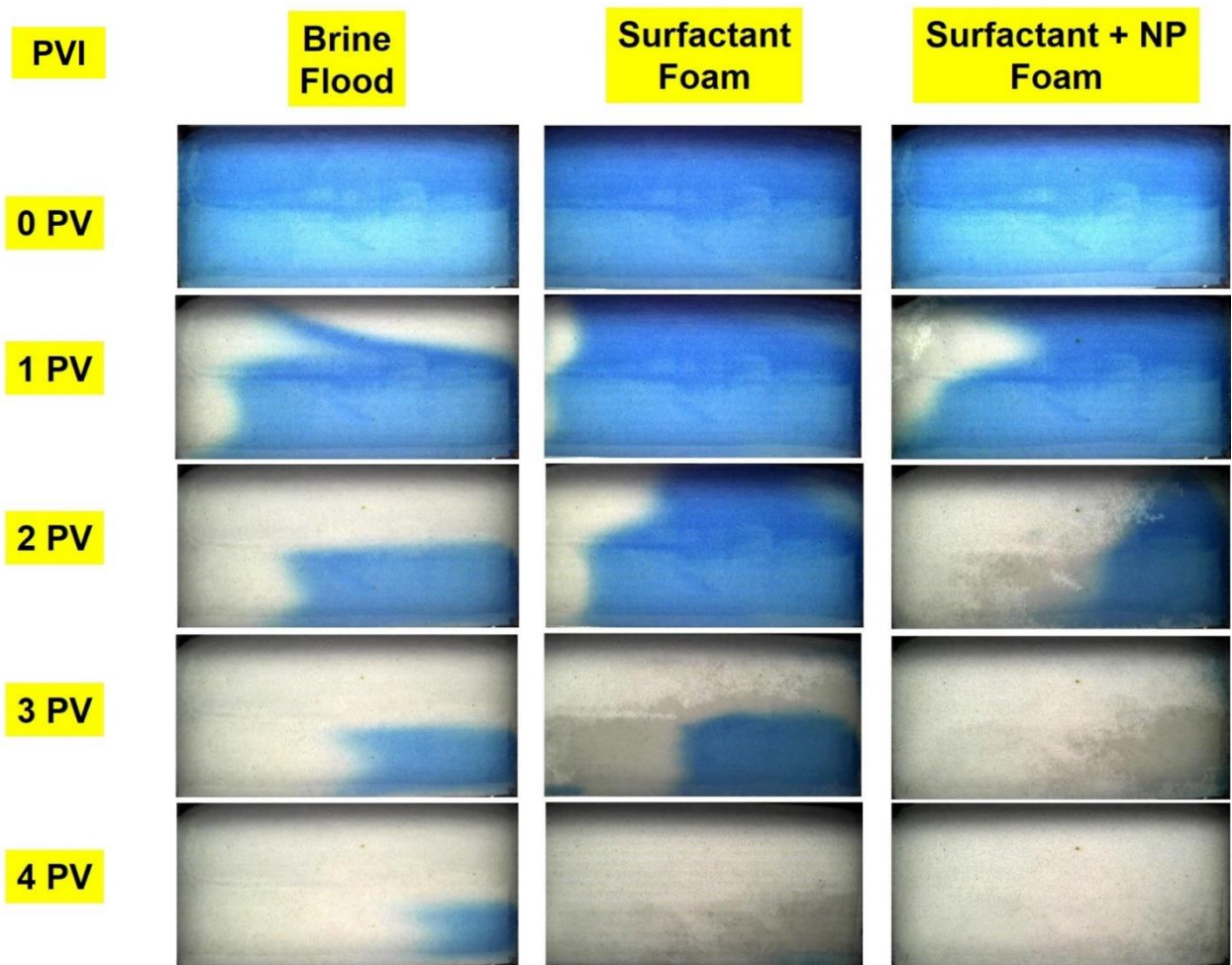
Figure 3.22: Displacement profile at different pore volumes of injection (PVI)
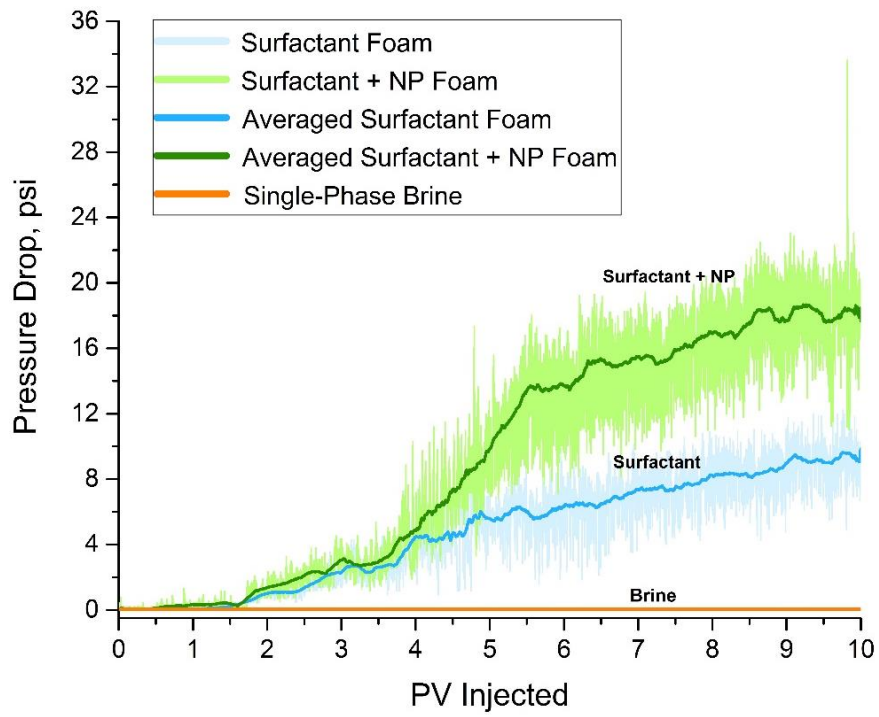
Figure 3.23: Pressure drop profiles during foam flow experiments
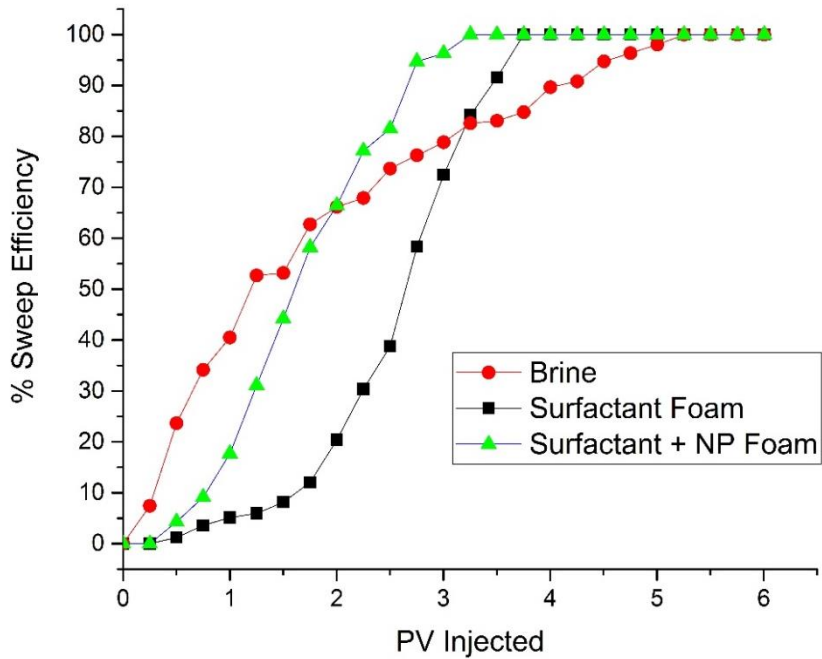
Figure 3.24: Plot of sweep efficiency as a function of pore volumes (PV)

Figure 3.26 shows the oil distribution during foam flooding at different pore volumes of injection. Water flood swept only the top high-permeability layer, leaving all the oil in the bottom low-permeability layer. (Figure 3.26A) It is interesting to note that at this stage adopting any other tertiary recovery process such as gas flooding, surfactant flooding or polymer flooding will result in channeling of injection fluid in the top layer. However, foam has the capability to divert flow from high permeability region to low permeability region. Therefore, this water flood was followed by a foam flood. AOS surfactant solution (0.5 wt.%) and nitrogen gas were coinjected with a quality of 80% at 4 ft/D. Figure 3.26B shows the foam flow diversion from the high-permeability layer to the low-permeability layer. Foam flood increased the oil recovery by 17% within the first 4.5 PV. The oil recovery almost plateaued after 8 PVI, which is in agreement with the observed oil distribution (Figures 26C, 26D, 26E) in which no substantial sweep efficiency was achieved between 6 to 14 PV. The remaining oil slowly came out primarily due to crossflow of oil from the low-permeability to the high-permeability region as seen in Figures 26D and 26E. The pressure drop started to increase after 1.5 PV of foam injection and reached a value of 4 psi (compared to 0.17 psi for waterflood). The ultimate cumulative oil recovery was 71.1 %OOIP, the incremental oil recovery by foam was 25.1 %OOIP and the final oil saturation was 28.9 %. It took 23 PV to reach this state.
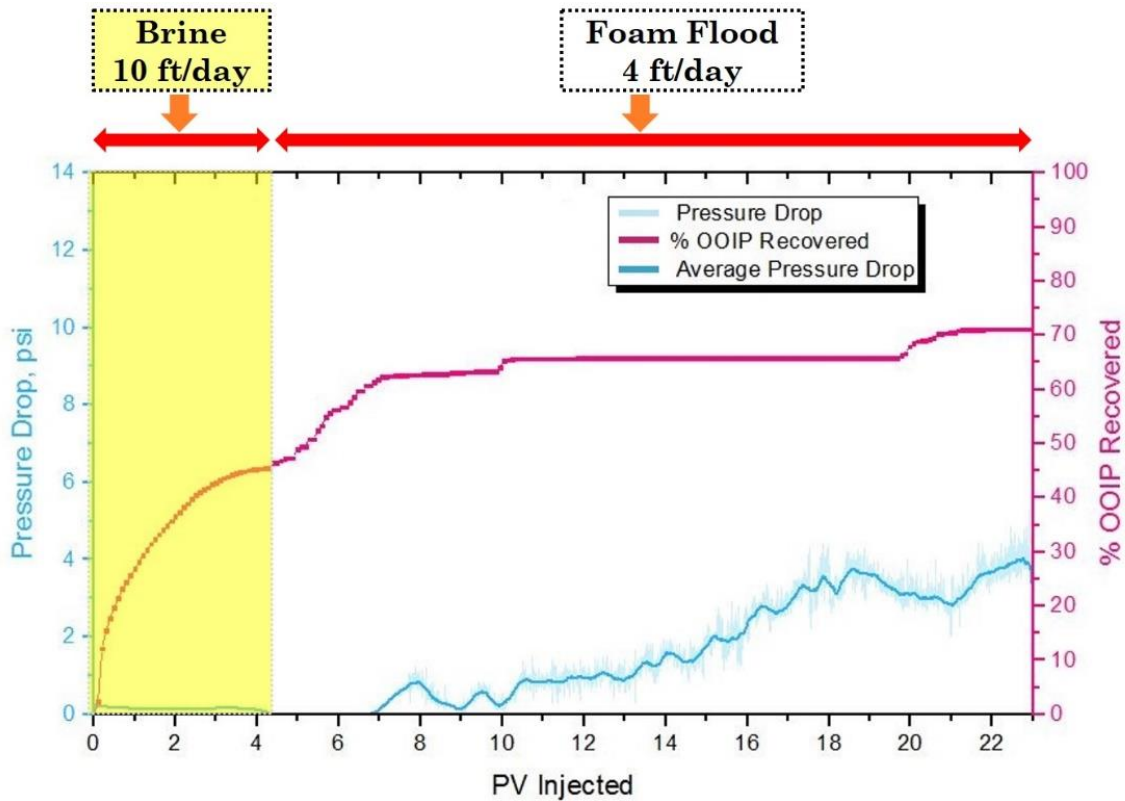
Figure 3.25: Pressure drop profile (cyan, left axis) and cumulative oil recovery (pink, right axis) for Flood 1

Flood 2 was conducted with a blend of surfactant (AOS) and nanoparticles as the foaming agent. The sandpack holder was again packed with clean oil-free sand. The same porosity and permeability of the system were achieved as in the previous flood. The sandpack was then vacuum-saturated with crude oil resulting in the initial oil saturation of 100%. Figure 3.27 shows the injection procedure, cumulative oil recovery (secondary y-axis) and overall pressure drop (primary y-axis) across the sandpack. Similar to Flood 1, first a brine flood was conducted at 10 ft/D. It was continued for more than 4 PV until oil production significantly slowed down. The waterflood oil recovery was 45 %OOIP and oil saturation was reduced to 55% which is similar to the Flood 1 result. Then, a surfactant-nanoparticle blend (0.5 wt.% AOS + 0.3 wt.% NP) and nitrogen gas was coinjected with a

85

quality of 80% at 4 ft/D. Figure 3.26 shows the comparison of oil distribution due to foam flooding at different pore volumes (PV) of injection for the surfactant case (left) and the blend case (right). Foam flow diversion can be seen from the high-permeability layer to the lower one (Figure 3.26H). Foam flood increased the oil recovery to 62 %OOIP within the first 4.5 PV. A close to 100% sweep was observed in about 10 PV (compared to 18 PV for surfactant foam case). Note that a large amount of oil still came out even after 10 PVI. The reason for this is that even if the foam/gas sweeps a certain region, it has non-zero residual oil saturation which could be further reduced by foam. This left-behind oil in the swept region could not be seen by the eye. The pressure drop started to increase after 1 PV of foam injection and reached a value of 5 psi (compared to 0.17 psi for waterflood). The oil recovery in the blend case increased continuously as opposed to the case of surfactant foam which almost plateaued after 10 PVI. The higher oil recovery in this case could be attributed to better microscopic as well as volumetric sweep efficiency due to stronger in-situ nanoparticle-stabilized foam. The ultimate cumulative oil recovery (after 22 PV) was 79.4 %OOIP; incremental oil recovery by foam was 34.4 % and final oil saturation was 20.6 %.

| Foam PVI | Surfactant Foam | Surfactant-NP Foam |
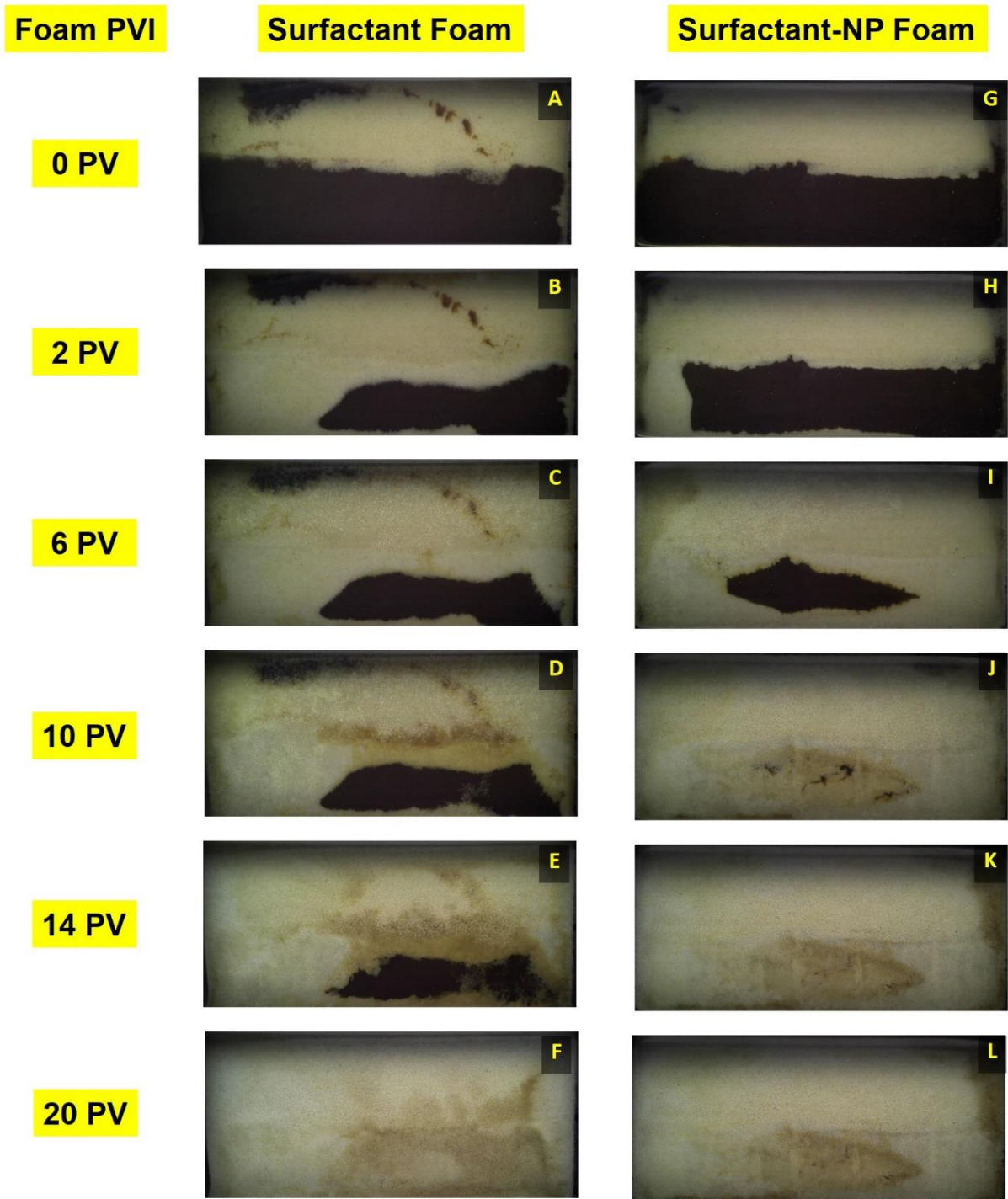
Figure 3.26: Oil distributions during Flood 1 (left) and Flood 2 (right) at different pore volumes of foam injection (PVI)
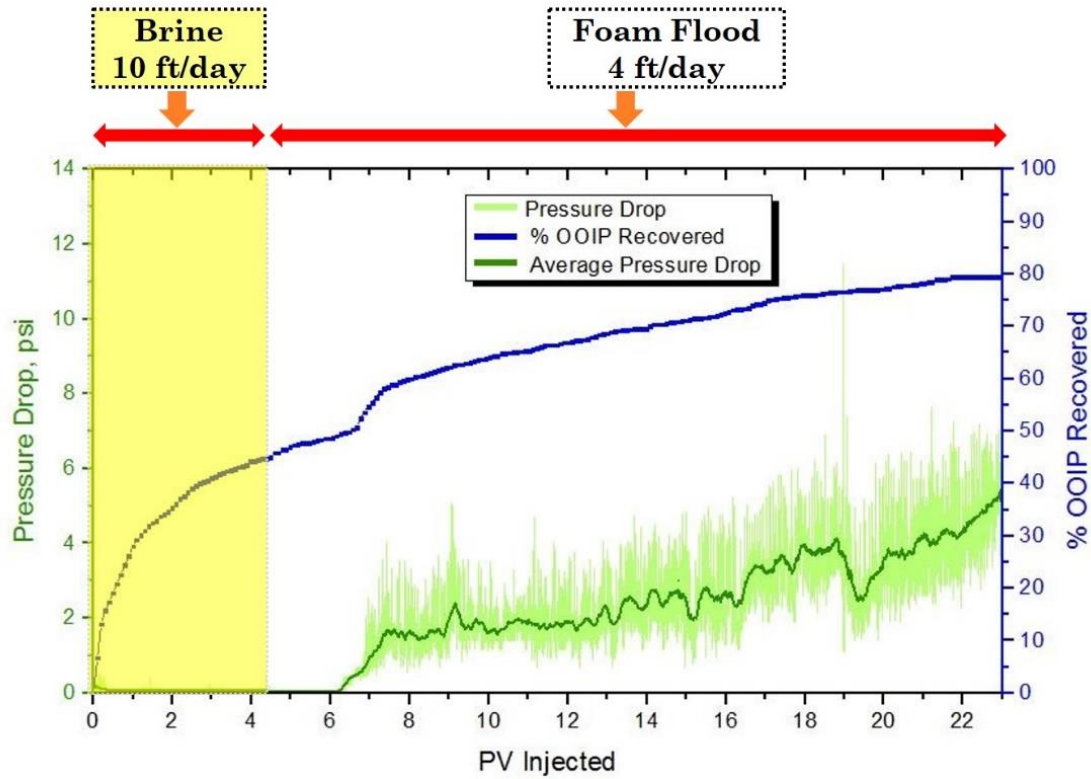
Figure 3.27: Pressure drop profile (green, left axis) and cumulative oil recovery (blue, right axis) for Flood 2

3.3.10 Discussion

3.3.10.1 Effect of Nanoparticles

An image analysis was performed on the pictures of transient foam flow in the absence of oil. Figure 3.28 shows the foam front profiles in the surfactant and surfactant-np cases. The different plots correspond to different pore volumes of injection. The x-axis represents the normalized spatial horizontal length along the sandpack. The y-axis represents the unswept fraction in the yz-plane at any x. Figure 3.28 shows that, for the case of surfactant, up to 2.5 PV of foam injection the foam fronts in the top (Figure 3.12A) and bottom layer (Figure 3.28B) move at different speeds with the foam front in the

bottom (low-permeability) layer lagging. For the same 2.5 PV of foam injection in the case of the blend, foam fronts move at the same speed (Figure 3.28C, 28D). This shows that due to the presence of nanoparticles, stronger in-situ foam was generated in the top layer which effectively diverted foam in the low permeability region faster. The presence of nanoparticles increases the in-situ foam strength in both high and low permeability layers (but disproportionately) which result in an effective sweep. The other implication of these results is that foam in a heterogeneous system where layers are in capillary contact tends to self-regulate its mobility in each layer. Similar observations have been reported in the literature (Bertin et al., 1999).
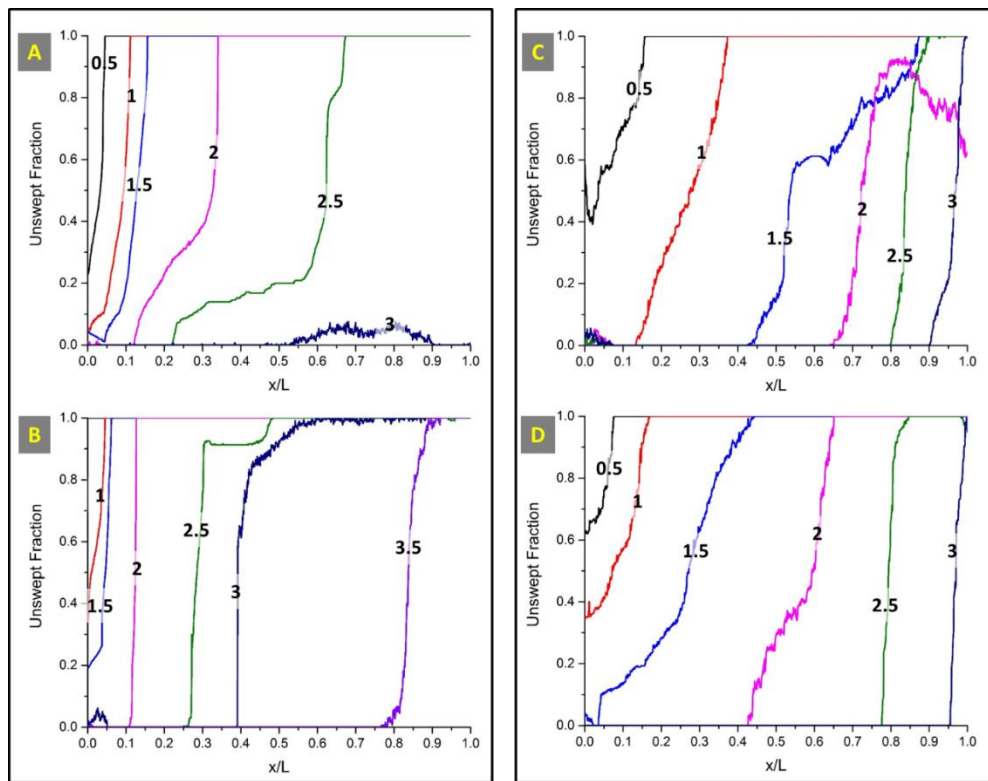
Figure 3.28: Sweep profiles in the top (A, C) and bottom layers (B, D) of sandpack during foam flow experiments at different pore volumes (labeled on curves) for: surfactant foam case (left); surfactant-np blend foam case (right)

3.3.10.2 Foam Phase Separation

Khatib et al. (1988) introduced the concept of limiting capillary pressure, P_C^* for foam in porous media. It is the capillary pressure above which foam collapses abruptly. It is analogous to critical disjoining pressure in bulk foam above which lamellae collapse (Aronson et al., 1994). P_C^* is a function of surfactant type and concentration, salt concentration, gas flow rate, and porous media permeability (Khatib et al., 1988b). In the present heterogeneous layered system, both layers will have different P_C^*. Literature data suggests that limiting capillary pressure increases with a decrease in permeability (Farajzadeh et al., 2015). Therefore, the layer with higher value of P_c^* (bottom low-permeability layer in this case) will draw water from the layer with lower value of P_c^* (upper high-permeability layer) (Rossen and Lu, 1997). This phenomenon was visualized in the foam flow experiments during foam injection where the surfactant solution entered the low-permeability region first followed by the foam. Figure 3.29 shows the displacement profile at 3.2 PV of surfactant foam injection. Based on the color, it can be seen that it is the liquid fraction of the foam that initially enters the low-permeability region, which is later followed by foam. This suggest that capillary crossflow in the present case weakens the foam in the high-permeability layer particularly near the boundary of abrupt permeability contrast. Thus, this phenomenon works antagonistically towards improving the flow diversion due to foam. These observations suggest that special care must be taken during foam simulation in layered system such as optimal grid-size selection to capture this effect near the boundary. Foam phase separation in such systems is one of the key mechanisms and the assumption that foam will stay as a homogeneous "foam" phase should not be made in simulations. This also implies that surfactant solution segregated from the foam also contributes toward sweeping the oil from the bottom low-permeability layers in Flood 1 and Flood 2 (in conjunction with the foam). However, the

contribution in oil recovery from this surfactant solution was also attributed to foam flooding as this phenomenon occurs only due to foam plugging in the top high-permeability layer. Mere surfactant solution injection without any foam will not sweep the bottom layer and will result in channeling from the top layer as observed for the case of brine injection (Figure 3.22).
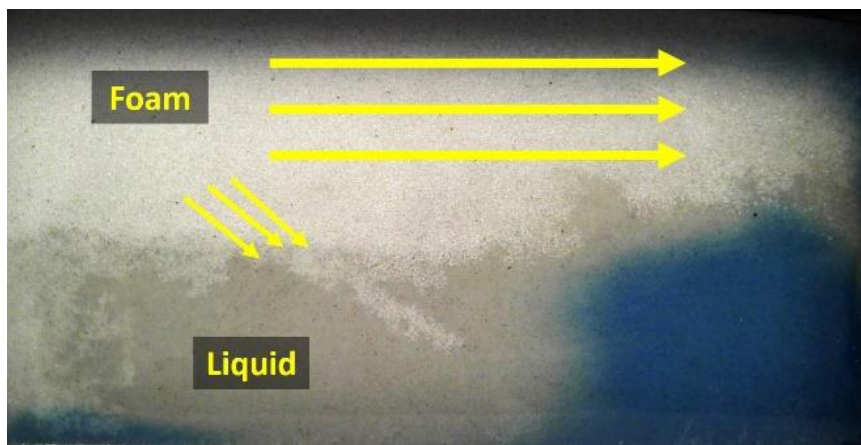
Figure 3.29: Foam phase separation during foam flow experiment

3.3.10.3 Crossflow

Two types of cross-flow behavior were distinctly observed during foam (both surfactant and blend case) flood in the oil displacement experiments. The first cross-flow type was observed in which foam diversion happens from the high-permeability layer to the low-permeability layer as shown in Figure 3.30. This flow diversion is due to the fact that foam strength increases in high-permeability layer more than that in lower-permeability layer(Bertin et al., 1999; Casteel and Djabbarah, 1988). This selective mobility reduction is a known attribute of foam flow in heterogeneous porous system

which helps to improve the volumetric sweep (Heller, 1994). The second type of cross-flow was the flow of oil from the low-permeability layer to the high-permeability layer, as shown in Figure 3.30B. If the permeability contrast is significant, it is easier for oil to flow out through the upper layer than the lower layer. Simulations should capture both cross-flow behaviors.
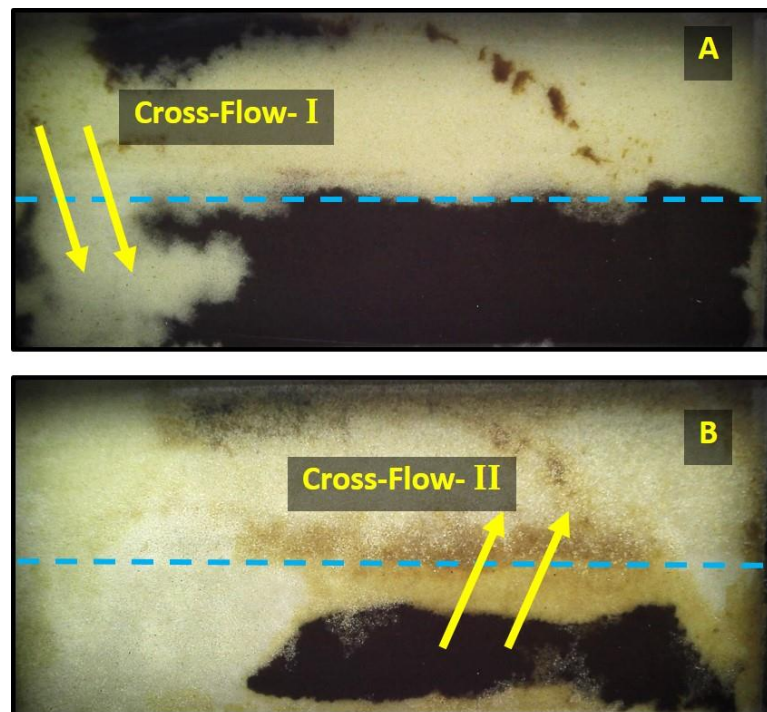
Figure 3.30: Two types of cross-flow mechanisms observed during oil displacement experiments

3.4 CONCLUSIONS

In this study, the effect of nanoparticle-surfactant blends on foam performance in both bulk and porous media was evaluated systematically. The following conclusions can be drawn from this work:

- Static foam tests indicate stabilization effect of nanoparticles on surfactant-nanoparticle foam stability in the absence of crude oil. An increase in half-lives of foam was observed with increasing nanoparticle concentrations. The foam height remained almost constant for days (>4 d) when the nanoparticles concentration was more than 0.3 wt.%.

- Vertical foam film tests and confocal laser scanning microscopy elucidated that nanoparticles are trapped in the plateau border as well as lamellae, which retard liquid drainage and bubble coalescence.

- The classification of foams based on lamella number was found to be in agreement with the macroscopic foam-oil interaction behavior. The spreading, entering, and bridging coefficients were found to be unreliable parameters to estimate foam-oil stability.

- As the concentration of nanoparticles increased, the mobility reduction factor (MRF) of surfactant-nanoparticle foam in a Berea core increased up to a factor of two.

- Core flood in a sandstone core with a reservoir crude oil showed that immiscible foams using surfactant or surfactant-nanoparticle blend can increase the oil recovery (over water flood) by about 10% of the original oil in place (OOIP).

- Despite the presence of a permeability contrast (6:1), which is favorable of channeling of gas through high permeability region, foam was effective in diverting fluid to low-permeability region irrespective of the presence of crude oil.

- Foam flow experiments showed that the liquid fraction of the foam is first diverted to the low-permeability layer followed by the whole foam. It suggests that foam cannot be always treated as a homogeneous "foam" phase during foam flow in a heterogeneous system.

- Foam flood in heterogeneous sandpacks with a reservoir crude oil showed that incremental oil recovery of 25% to 34% OOIP (over waterflood) using immiscible foams. Foams stabilized by surfactant-nanoparticle blend outperform surfactant-stabilized foam by 9% OOIP.

- Two different types of cross-flow between the low-permeability layer and the high-permeability layer were identified as key mechanisms governing oil-displacement process during foam flooding process.

These conclusions indicate that nanoparticles could be potentially used for boosting the foam performance of surfactant-stabilized foam. Such foams may be able to provide mobility and conformance control in miscible and immiscible gas displacements. Moreover, this synergy between nanoparticle and surfactant in foam stabilization can potentially be used to minimize the surfactant usage and maximize the foam propagation distance in subsurface applications.

Chapter 4: Foams Stabilized by Surface Activated Nanoparticles in Water-Wet Porous Media

4.1 INTRODUCTION

The objective of this chapter is to explore the foam stabilization via in-situ surface activation of nanoparticles in the bulk and porous media. Previous studies have focused on foam stabilized by either nanoparticle with different degrees of surface modification or by surfactant-nanoparticle mixtures (such as in Chapter 3), but not by in-situ surface-lyophobization of nanoparticles. The surface chemistry of the hydrophilic nanoparticles was tailored by adsorption of a small amount of short chain surface modifiers to obtain surface-modified nanoparticles (SM-NP). Foams were then created in-situ by co-injecting SM-NP solution and nitrogen gas through Berea sandstone at a fixed quality, and mobility reduction factors were measured. Water floods and subsequent foam floods were conducted in Berea cores saturated with a crude oil using SM-NP solution and surfactant as foaming agents. The methodology and results are described in the following sections.

4.2 METHODOLOGY

4.2.1 Materials

Alumina coated silica nanoparticles, Ludox® CL, was supplied by Sigma-Aldrich. Figure 4.1 illustrates the surface configuration of these nanoparticles, showing the core silica with alumina surface coating. The size of the nanoparticles was characterized using a Transmission Electron Microscope (TEM). A FEI Tecnai TEM operating at 80 kV was used. The mean diameters of primary particles were found out to be 20 nm. The TEM

This chapter is based on: (Singh and Mohanty, 2016a). Dr. Mohanty supervised the project.

95

image is shown in Figure 4.2. Non-ionic surfactant Triton CG-110, an alkyl polyglucoside (60% active), and anionic surfactant Bioterge AS-40, a C14-16 alpha-olefin sulfonate (39% active), was obtained from The Dow Chemical Company and Stepan Company, respectively. Ultra-pure water with resistivity greater than 18.2 megaohm-cm was used to prepare brine solutions. Berea sandstone cores were used in foam flow and oil displacement experiments. Crude oil was obtained from a reservoir, and it had a viscosity of 30 cp at 25 ℃. Propyl Gallate (Sigma-Aldrich), Sodium Chloride (99%, Fisher Chemical), Nitrogen (research grade, Matheson, USA) were used as received.
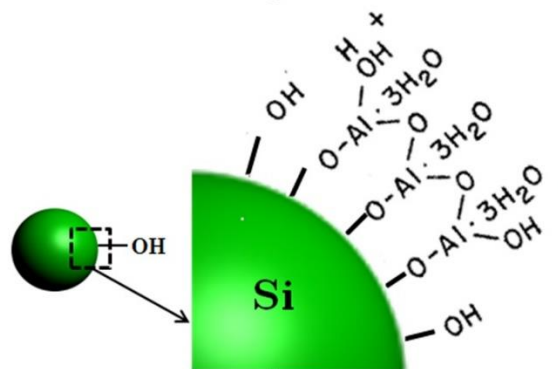
Figure 4.1: Sketch of alumina coated silica nanoparticle

4.2.2 Preparation of Nanoparticles Dispersion

The stock solution of 5 wt. % of Ludox® CL nanoparticles was first prepared using ultra-pure water. Samples were prepared by diluting this stock solution. A surface modifier, propyl gallate (PG) was added slowly to these samples with continuous magnetic stirring to avoid any local particle coagulation. Samples containing 1 wt.% of nanoparticles with varying concentrations of PG (0.05 wt. %, 0.075 wt. %, and 0.1 wt. %) were prepared. Surface modified nanoparticles are called SM-NP here. These samples

were stirred for 48 hr to ensure mixture homogeneity and reaction equilibrium. These mixings were performed at room temperature and at their normal pH without any adjustment. The zeta potential and hydrodynamic particle diameters of these aqueous dispersions were characterized using the Delsa™ Nano analyzer.
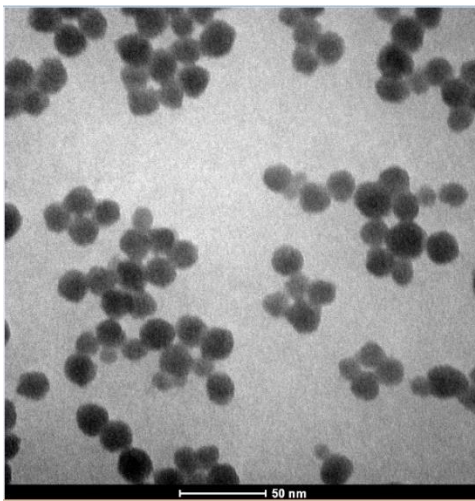
Figure 4.2: TEM image of 1 wt.% nanoparticles (Scale bar is 50 nm)

4.2.3 Foamability and Static Foam Tests

Preliminary foam tests were conducted by Bartsch shake test in which 15 mL of these samples were vigorously shaken for 10 times in test tubes, and the macroscopic foam textures were observed. To visualize the texture in detail, the bubble samples were placed on the microscope slides, and images were recorded using a Nikon microscope equipped with a high-resolution camera. Image J software was used to analyze these images and determine bubble size distribution. 20 mL of each sample was then taken in a graduated cylinder (diameter: 1 cm, length: 20 cm) at the room temperature. The apparatus consisted of a transparent cylinder made of acrylic with a stainless steel sparging frit (pore

size 2 μm) at the bottom, which was used to disperse air. Both ends of the cylinder had Swagelok fittings, which prevented evaporation. Air was injected from the bottom, and static foam was generated. The height of the foam (above the liquid phase) was monitored as a function of time.

4.2.4 Foam Flow Experiments

Berea sandstone cores were used for these experiments. Cylindrical cores, 1" or 1.5" diameter and 1 ft long, were drilled from the block. Berea is oil-free outcrop rock, so no pre-cleaning was required. The cores were dried at 90 ºC for 24 hr in an oven and were laminated with FEP shrink wrap tubing (Geophysical Supply Company, Houston, TX). These were then placed in a Hassler-type core holder (Phoenix, Houston, TX) with a confining pressure of 1500 psi. Petrophysical properties like air porosity and permeability of the cores were then determined. Figure 4.3 shows the experimental schematic. Two Series-D syringe pumps from Teledyne ISCO (Lincoln, NE) were used in the setup which are capable of low injection rates (as low as 0.001cc/min). The apparatus was built to co-inject nitrogen gas and SM-NP solution through a sandpack (0.6- inch diameter and 6-inch long) to ensure proper mixing and foam generation. The pre-generated foam was then injected at the top of the core. The downstream pressure of the experiment was maintained by a back-pressure regulator (Equilibar, NC) installed after the coreholder. The pressure drops across the core were measured using Rosemount differential pressure transducers. All connections were made with stainless steel Swagelok fittings.
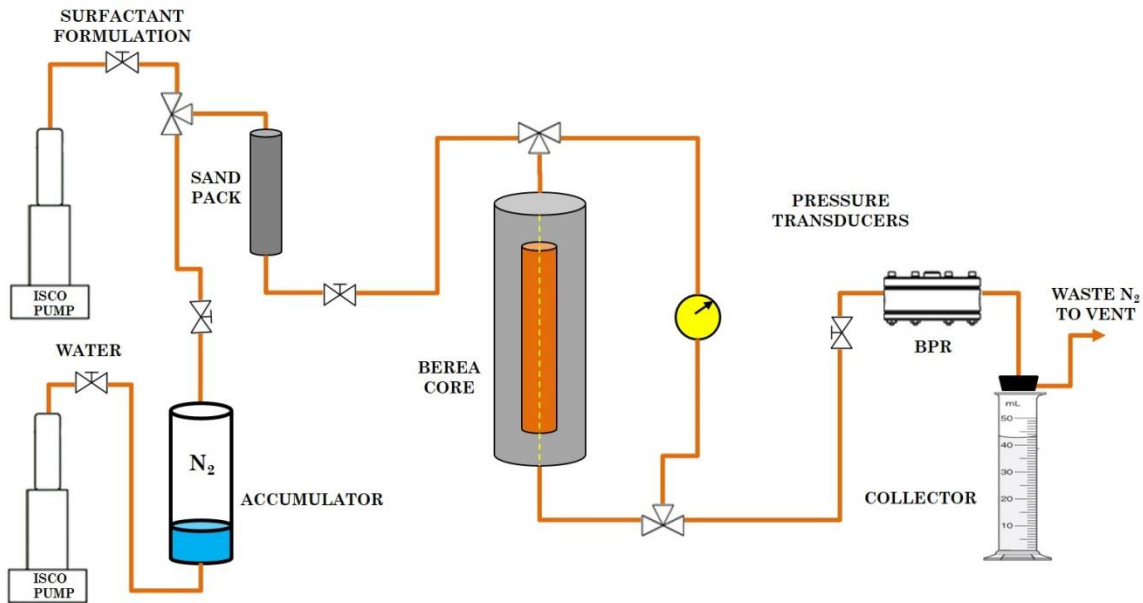
Figure 4.3: Schematic of the setup for foam flow experiments and corefloods

4.2.5 Oil Displacement Experiments

Coreflood experiments were conducted to investigate the foam behavior of SM-NP solution in the presence of crude oil as compared to that with a surfactant. The objective was focused on studying foam rheology and microscopic sweep efficiency of foam. Since the cores used in these experiments were 1" in diameter and were quite homogeneous, volumetric sweep efficiency improvement was not an important factor here. The experimental setup was similar to that described in Figure 4.3. The brine porosity and permeability of the cores were determined. The cores, fully saturated with brine, were then flooded with filtered crude oil (at least 2.5PV) from the top at a constant pressure of 750 psi at room temperature until no brine was produced. The initial oil saturation was determined by mass balance. The whole setup was pressurized with a back-pressure of

100 psi. The brine flood was conducted at 1ft/day for 2 PV until no oil was produced. Then, it was flooded with brine at 5 ft/day to minimize capillary end effects. The cores were then pre-flushed with 1 PV of surfactant or SM-NP solution to avoid any adsorption of surfactant while foam flooding. Nitrogen gas and the surfactant or SM-NP solution were then co-injected through sand pack. This pre-generated foam was then injected into the core from the top for more than 7 PV. Oil recovery and pressure drops were monitored at each step.

4.3 RESULTS AND DISCUSSION

4.3.1 Surface Hydrophobization of Nanoparticles

In a surfactant-free system, particle adsorption at the air-water interface is a necessary condition for foam stabilization solely by particles. The foam stability is mainly governed by the interfacial property of the particle — the contact angle (θ). In their experimental work, Binks and Horozov (2005) showed that highly hydrophilic and highly hydrophobic particles tend to destabilize foam. Thus, proper tuning of the contact angle of particles is required to get stable foam. Therefore, the first objective was to make the nanoparticle surface partially hydrophobic. This was achieved by anchoring short chain surface modifier, PG to the particle surface. The nanoparticle's surface is primarily covered by –OH2+ groups which are the potential sites for surface modifier attachment. The positive zeta potential of these nanoparticles confirms the presence of these –OH2+ groups. PG, which has multiple hydroxyl groups, can attach to these –OH2+ groups via ligand-exchange reactions. After this reaction, the –OH2+ groups on the particle surface are replaced by PG's hydroxyl group as shown in Figure 4.4.
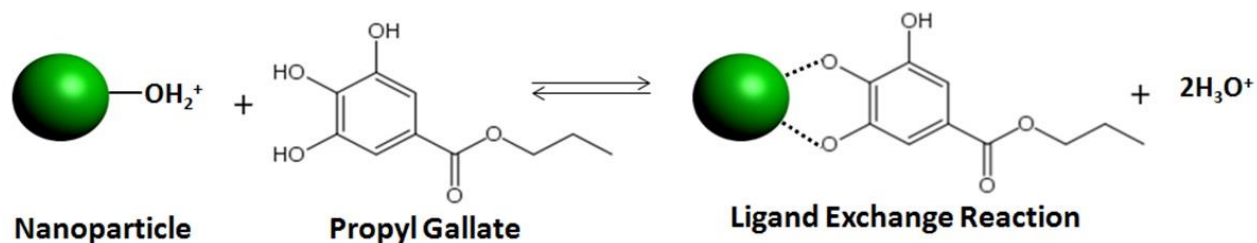
Figure 4.4: Ligand-exchange reaction between nanoparticle and propyl gallate

It is to be noted that the attachment via ligand-exchange reactions is quite strong than mere electrostatic interactions between the oppositely charged particle and modifier's functional groups (Hidber et al., 1997). This attachment reaction is also independent of the charge of the nanoparticles, and it can occur even if the particle surface is negatively charged at a different pH (Gonzenbach et al., 2006b). The reduction in zeta potential of SM-NP solutions with an increase in surface modifier concentration confirmed the attachment reaction as shown in Table 4.1.

Table 4.1: Zeta potential of the SM-NP with different initial surface modifier
concentration

Nanoparticle Concentration (wt. %)	Surface Modifier Concentration (wt. %)	Zeta Potential of SM-NP (mV)
1	0	32.84
1	0.05	23.78
1	0.075	17.14
1	0.1	13.39

4.3.2 Foamability and Bubble Texture

Preliminary foam tests were conducted by shaking 15 mL samples vigorously for 10 times in test tubes, and the macroscopic foam textures were observed. Figure 4.5 shows the resulting foam for t = 0 min, 30 min and 240 min. Sample A had 1 wt % of

101

nanoparticles, sample B had 0.05 wt % PG, and sample C had a mixture of 1 wt.% nanoparticles and 0.05 wt % PG which was magnetically stirred for 24 hr. Sample A did not show any foaming tendency since it had only hydrophilic nanoparticles. Sample B showed some initial foaming, but the foam collapsed in a few min. However, sample C formed a strong foam with a fine texture that remained stable for a long time (t > 240 min). This basic foam test substantiated the fact that foam stabilized solely by nanoparticles are possible if the surface of the nanoparticle is partially hydrophobic.
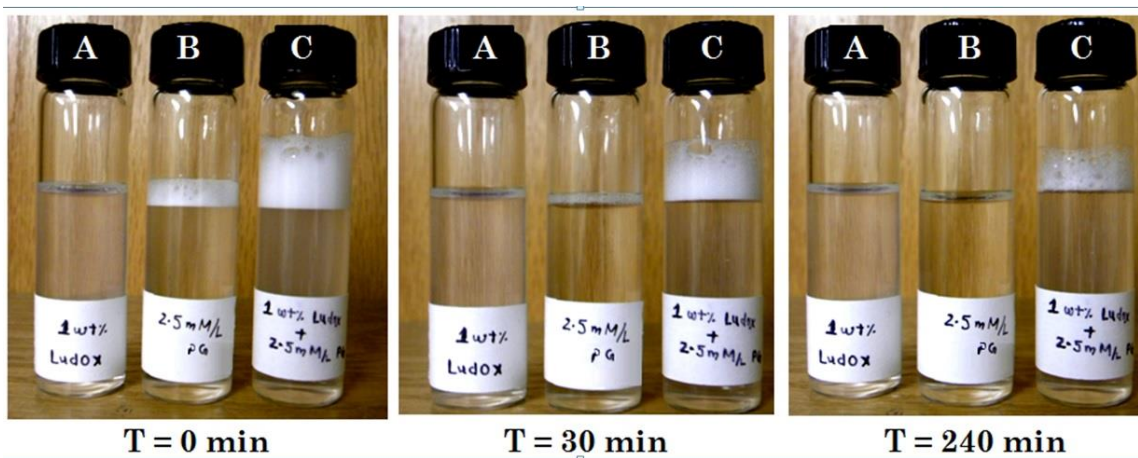
Figure 4.5: Foamability at three different times (A) 1 wt. % NP, (B) 0.05 wt. % PG, (C) 1 wt. % NP + 0.05wt.% PG

Figure 4.6 (top) shows the optical micrographs of the foam stabilized by different samples. Quantitative analysis of these images was performed using the corresponding threshold images, as shown in Figure 4.6 (bottom), to estimate average bubble radius, Ravg. A non-ionic surfactant, Triton CG-100 which is considered a good foaming agent was used as a base case to compare the foam texture of the SM-NP stabilized foam. Large

bubbles were observed for the case of the surfactant (Figure 4.6A) where the Ravg was found out to be 84 microns. Figures 4.6B, C and D show the texture of foam stabilized by SM-NP with the initial surface modifier concentrations of 0.05 wt.%, 0.075 wt.%, and 0.1 wt.%, respectively. Relatively finer bubbles were observed for these three cases, and R_{avg} were calculated to be 51 microns, 32 microns, and 38 microns, respectively. Smaller bubbles indicate stronger foam which was the result of retarded coalescence of bubbles due to adsorption of SM-NP on the air-water interface.

4.3.3 Static Foam Test

Static foam tests were conducted using SM-NP with varying concentration of initial surface modifier concentration. The decay of foam height was monitored with time. These experiments were conducted at the room temperature. Figure 4.7 shows the plot of relative foam height versus the decay time in hr. Half-life, which is the time it takes for the foam to decay to half of its original height, can be determined from the plot. The half-life of the foam for SM-NP with initial modifier concentration — 0.05 wt %, 0.075 wt % and 0.1 wt % was found out to be 11 hrs, 23hrs, and 34 hrs, respectively. The large magnitude of the half-lives indicated stable foam formation stabilized by SM-NP. As the concentration of surface modifier increased, half-lives increased considerably suggesting increased affinity of SM-NP to the air-water interface. The macroscopic foam texture observed (by naked eyes) in these three cases were quite similar and were characterized by very fine bubbles. Figure 4.7 shows the foam morphology for the case of SM-NP with 0.1 wt.% surface modifier concentration.
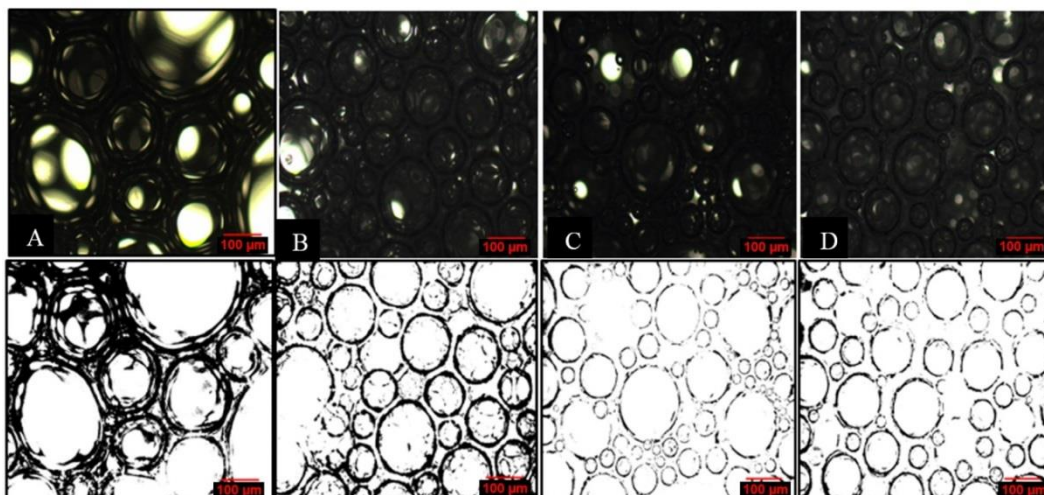
Figure 4.6: Optical micrographs of foam stabilized by: (A) 0.5 wt % Triton CG-100, (B) 1 wt % NP + 0.05 wt % PG, (C) 1 wt.% NP + 0.075 wt.% PG, (D) 1 wt.% NP + 0.1 wt.% PG (Scale Bar is 100 μm)
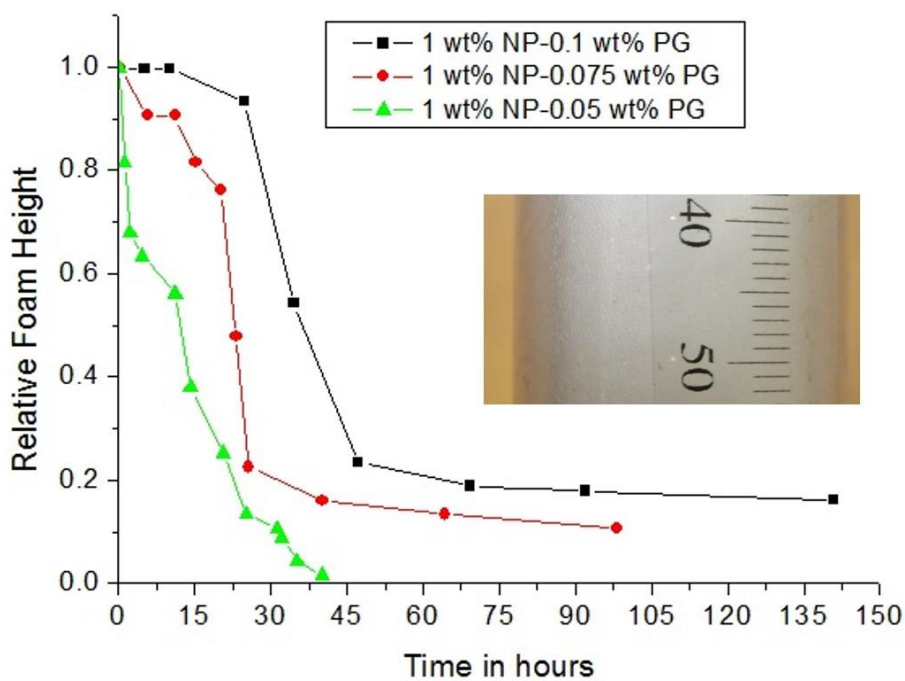
Figure 4.7: Static foam tests of different samples

4.3.4 Mechanisms for Foam Stabilized Solely by SM-NP

The key mechanisms responsible for foam stabilization by nanoparticle-system such as particle detachment energy, the maximum capillary pressure of coalescence, and kinetics of film drainage are explained in detail in Chapter 2. In this chapter, the concept of in-situ hydrophobization of nanoparticles for foam stabilization was focused. The term "in-situ" here refers to "in the localized reaction mixture" which is commonly used in chemistry literature and does not implies "inside the porous medium." This technique relies on the selection of suitable surface modifier that can attach itself to the nanoparticles surface via either electrostatic interaction or ligand-exchange reaction. The surface modifier should have hydrophilic groups that can attach to the hydrophilic nanoparticle surface and specifically short chain hydrophobic groups that can render the surface partially hydrophobic. The short chain ensures high solubility of surface modifiers in the water and prevents phase separation. In this work, the degree of surface modification of nanoparticles was controlled by varying the concentration of the surface modifier (0.05 wt % 0.075 wt % and 0.1 wt %) while keeping the nanoparticle concentration constant at 1 wt.%. Assuming a monolayer attachment of modifier on the surface and using the nanoparticle dimension and the projection area of the modifier, the degree of surface coating was theoretically estimated to be 42.2 %, 63.3 %, and 84.4 %, respectively, for these three cases. The modified nanoparticles were characterized using the Delsa™ Nano analyzer. No increments in nanoparticle diameters were observed in these samples as compared to the unmodified nanoparticle sample, indicating no aggregation, and strong aqueous stability. The particle detachment energy, E which is the amount of energy required to move the particle from the interface to the bulk solution is given by:

$$E = \pi R^2 \gamma_{aw} (1 - |\cos \theta|)^2$$

where R is the particle radius, γaw is the surface tension of the interface and θ is the contact angle. The contact angle determination is quite difficult experimentally; however, a qualitative analysis of energy can be done based on the equation. The nanoparticles used in this work are inherently hydrophilic (θ<30º). Thus, they did not show any affinity towards air-water interface and E is quite low as shown in Figure 2.12 (left). However, surface modification by anchoring modifiers on the surface rendered them partially hydrophobic. The obtained SM-NP had the positive affinity towards air-water interface and was able to stabilize foam as observed experimentally in foam shake tests. The detachment energy also increases significantly with an order of 100. Figure 2.12 (right) illustrates this mechanism, showing air bubble stabilized by nanoparticles (green spheres) which are coated with modifiers (black molecules).

4.3.5 Foam Flow Experiments

Foam flow experiments were conducted in Berea sandstone core, 1.5" diameter and 1 ft long, using (SM-NP) nanoparticles with different degrees of the surface coating as the foaming agent. The brine porosity and permeability of the core were 22% and 606 md. The flow rates in these experiments were kept at 4 ft/d. This was done to get a large enough pressure drop, which can be measured accurately. All these experiments were performed at the room temperature and with a back-pressure of 100 psi. Before each run, the SM-NP solution pre-flush was conducted to saturate the core with SM-NP and avoid any modifier adsorption issues while foam flooding. After SM-NP solution pre-flush (1 PV), nitrogen gas and SM-NP solution were coinjected into the sandpack to generate foam at 4 ft/day and with a quality of 90%. This pre-generated foam was injected from the top of the core for at least 3.5 PV to achieve a steady state pressure drop. After completion of

each run, the core was cleaned by flushing more than 15 PV of brine. The backpressure was intermittently depressurized and pressurized several times to remove the trapped gas. It was ensured that brine flow pressure drop was about the same as the initial single-phase brine pressure drop.

First, the base case was conducted in which brine and nitrogen gas were co-injected at 4 ft/d with a quality of 90%. Figure 4.8 (left) shows the pressure drop profile for the same. The pressure drop has some fluctuations, but the average pressure drop in the steady state was 0.8 psi, which is quite low. This run was then repeated using brine containing 1 wt.% unmodified nanoparticles. The pressure drop, in this case, was also about 0.8 psi, indicating no foaming tendency of unmodified nanoparticles even in the porous medium. In the subsequent runs, SM-NPs were used as foaming agents with a different degree of surface coating. Figure 4.8 (right) shows the case of SM-NP with initial surface modifier concentration of 0.05 wt % which is equivalent to 42.2 % surface coating. The average pressure drop in the steady state, in this case, was about 3.2 psi, which was 4 times the base case. This additional pressure drop over the base case indicated the formation of in-situ foam. The core was then cleaned following the aforementioned steps. Figure 4.9 shows the pressure drop profile for the case of SM-NP with initial surface modifier concentration of 0.075 wt % (equivalent to 63.3% surface coating) (left) and 0.1 wt.% (equivalent to 84.4% surface coating) (right). The average steady state pressure drop after 3.5 PV of co-injection was found out to be 6.1 psi and 11.7 psi, respectively. The large pressure drop achieved in these cases is due to finer in-situ bubble texture stabilized by partially hydrophobic SM-NP as observed in the bulk foam stability tests. To compare these results, this experiment was repeated again with a non-ionic surfactant, Triton CG-100, as the foaming agent. The concentration of the surfactant was varied (0.02 wt %, 0.2 wt %, and 0.5 wt %). The average steady state pressure drop

was found out to be 0.8 psi, 2.6 psi, and 13.6 psi, respectively. Mobility reduction factor (MRF) is defined (here) as the ratio of the pressure drop across the core due to co-injection of gas and SM-NP surfactant solution and the pressure drop due to co-injection of gas and brine at the same flow rate (4 ft/day) and quality (90 %). Figure 4.10 compares the MRF achieved in the porous medium for SM-NP with different surface coatings and a surfactant at different concentrations. This plot indicates that SM-NP has the potential to behave as a surfactant and a promising foaming agent.
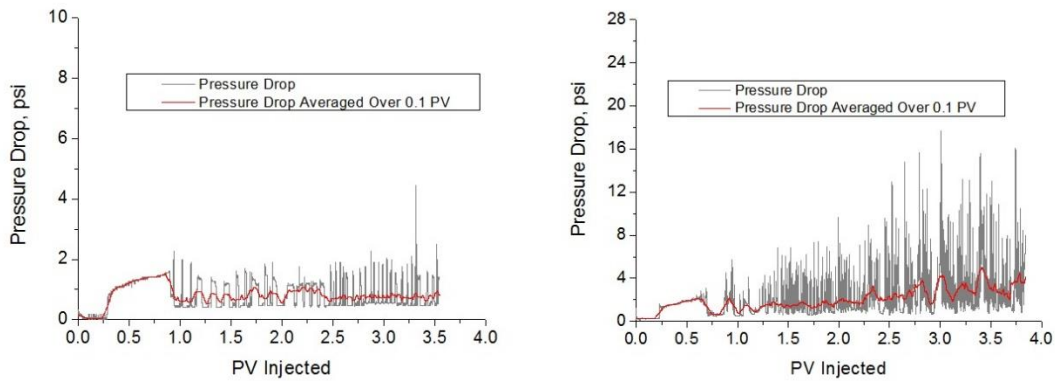
Figure 4.8: Pressure drop profile for the co-injection of nitrogen and sample at 4ft/day with the quality of 80%. Sample: Brine (left); 1 wt.% NP-0.05wt.% PG (right
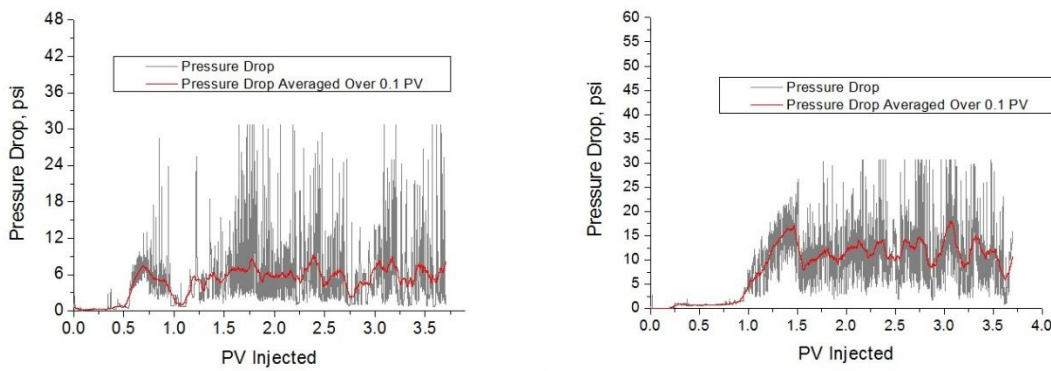
Figure 4.9: Pressure drop profile for the co-injection of nitrogen and sample at 4ft/day with quality of 80%. Sample: 1 wt.% NP-0.075wt.% PG (left); 1 wt.% NP-0.1wt.% PG (right)
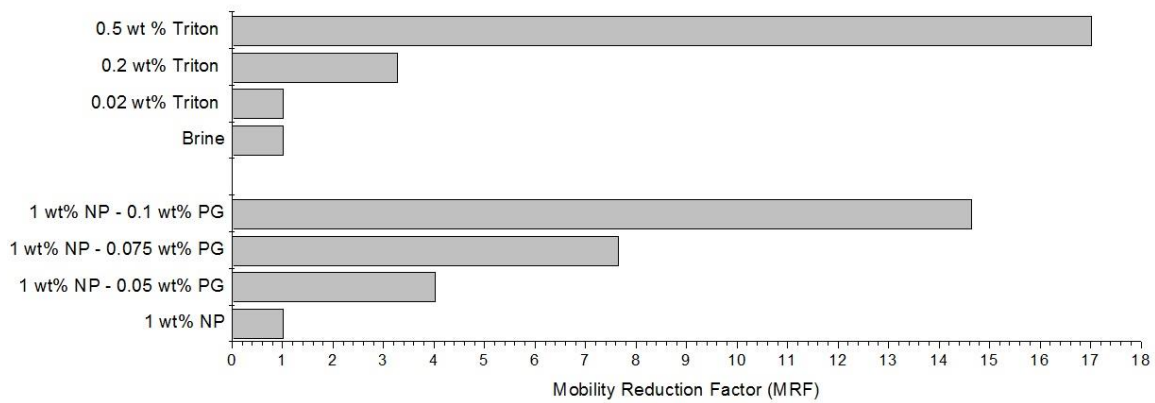
Figure 4.10: Comparison of steady state mobility reduction factor achieved for SM-NP solutions and a non-ionic surfactant

4.3.6 Oil Displacement Experiments

Core flood experiments were conducted to evaluate foam rheology in the presence of residual crude oil and microscopic sweep efficiency of the SM-NP-stabilized foam as compared to the surfactant-stabilized foam. Core Flood 1 was conducted in a Berea core with a dead crude oil and a surfactant. The core was 1" in diameter and 1 ft long with 20 % porosity and 442 md permeability. The initial oil saturation was 70 %. Figure 4.11 shows the injection procedure, cumulative oil recovery (secondary y-axis) and overall pressure drop (primary y-axis) across the core.
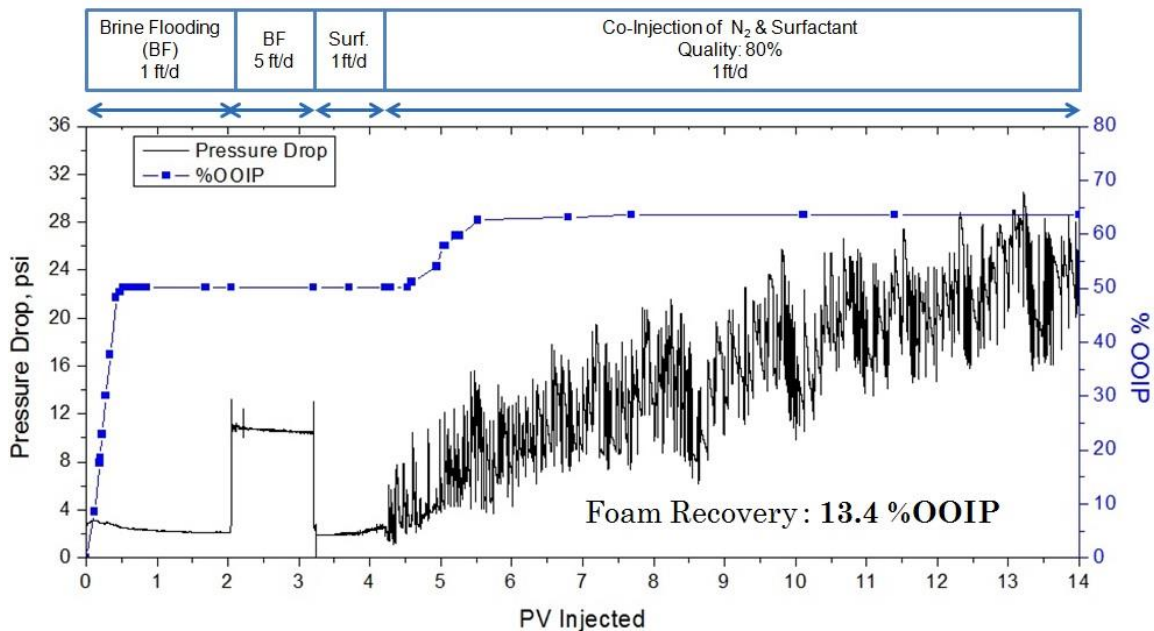
Figure 4.11: Pressure drop profile (left axis) and cumulative oil recovery (right axis) for the Core Flood 1

Brine flood was conducted at 1 ft/day to mimic waterfloods at a typical field rate. It was continued for about 2 PV until no oil was produced. The waterflood oil recovery was 50.2 %OOIP (original oil in place), and oil saturation was reduced to 34.8%. The pressure drop during water flood was between 2.1 to 2.6 psi. In order to minimize any capillary end effect, brine was then injected at 5 ft/day for another 1 PV. The pressure drop increased to 10.5 psi as the flow rate was increased 5 times. No oil was recovered during this stage implying no significant capillary end effect. Before conducting the foam flood, the core was pre-flushed with 0.5 wt% of the anionic surfactant, Bioterge AS-40 for 1 PV at 1 ft/day to avoid any surfactant adsorption during foam flooding. No oil was recovered during surfactant injection as the surfactant does not lower the IFT sufficiently

to mobilize residual oil. The pressure drop during pre-flush was about 2 psi. Then, co-injection of 0.5 wt% of surfactant solution and nitrogen gas was started with a quality of 80% at 1ft/day. The additional oil recovery for first 3.5 PV of co-injection over waterflood was 13.4 %OOIP. No significant amount of oil was produced after 3.5 PV of injection, but the co-injection was continued for another 3.5 PV to observe the foam rheology in the presence of residual oil. The average pressure drop continued to grow and reached about 25.8 psi at the end of the experiment. Steady state was not achieved during the 10 PV of foam injection. The ultimate cumulative oil recovery was 63.6 %OOIP, and final oil saturation was 25.5%.

Core Flood 2 was then conducted in another Berea core with the same procedure as the previous core flood, but with SM-NP as the foaming agent instead of the anionic surfactant. The core was 1" in diameter and 1 ft long with brine porosity and permeability of 22% and 585 md, respectively. The initial oil saturation, in this case, was also 70%. The cumulative oil recovery (%OOIP) (secondary y-axis) and overall pressure drop (primary y-axis) are shown in Figure 4.12. The core was flooded with brine for 2 PV at 1 ft/day which represents a water flood. The water flood reduced the oil saturation to 32% and resulted in 54.1 %OOIP oil recovery. The pressure drop during this water flood stage was between 1.4 psi to 2.2 psi. Then, the core was flooded with brine for 1 PV at 5 ft/day. No additional oil was recovered implying negligible capillary end effect. The pressure drop increased to about 7.4 psi at the flow rate of 5 ft/day. Then, the core was pre-flushed with SM-NP solution (1 wt% of nanoparticles modified with 0.1 wt% of surface modifiers) for 1 PV. No oil was recovered during this stage. Co-injection of SM-NP solution and nitrogen gas was then conducted at 1 ft/day with 80% quality. The additional oil recovery over water flood after 3.5 PV of injection was 19.6 %OOIP. The co-injection was continued for another 4.5 PV. The pressure drop in this core flood went to around 39.6 psi

at the end of the experiment. Steady state was not achieved during the 8 PV of foam injection. The continued increase in pressure drop indicates the continued trapping of foam and stronger in-situ foam generation due to the SM-NP. The ultimate cumulative oil recovery was 74.7 %OOIP, foam recovery over water flood was 20.6 %OOIP, and final oil saturation was reduced to 17.6%.
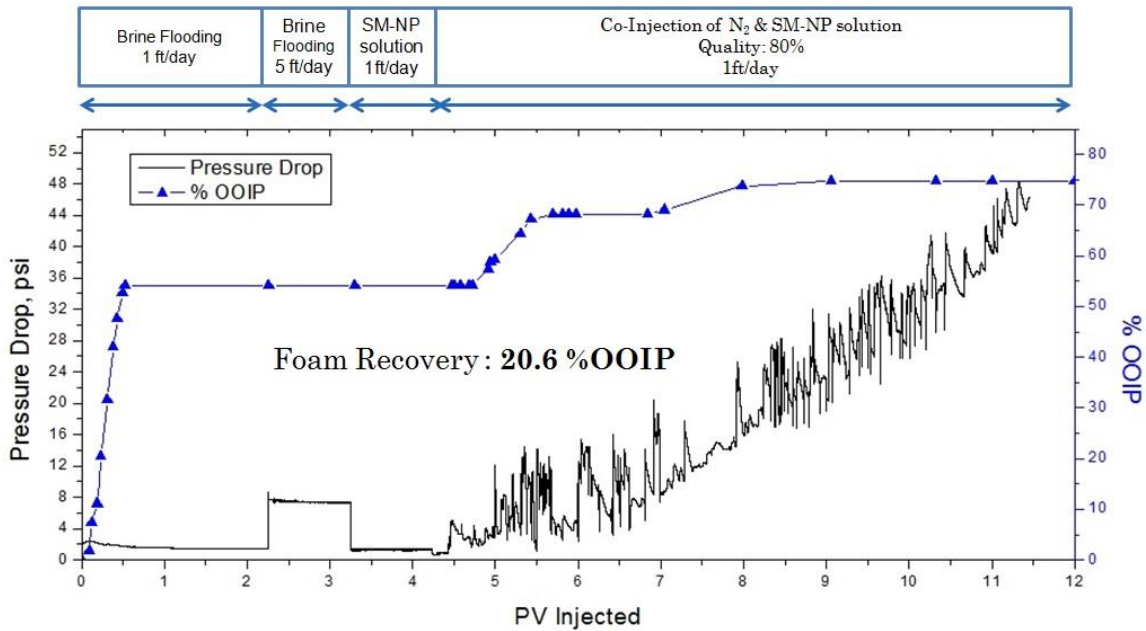
Figure 4.12: Pressure drop profile (left axis) and cumulative oil recovery (right axis) for the Core Flood 2

Core Flood 3 was then performed in another Berea core with the same injection procedure as the core flood 2, but with a reduced concentration of SM-NP (0.5 wt% of nanoparticles modified with 0.05 wt% of surface modifiers). The core was 1" in diameter and 1 ft long with brine porosity and permeability of 18% and 125 md, respectively. The initial oil saturation, in this case, was 71.8%. The cumulative oil recovery (secondary y-axis) and overall pressure drop (primary y-axis) are shown in Figure 4.13. The pressure

drop during water flood at 1 ft/day and 5 ft/day was about 4.8 psi and 23.7 psi, respectively which was relatively higher than previous cases due to lower permeability of the core. The water flood recovered 48.3 %OOIP. The core was then pre-flushed with 1 PV of SM-NP solution (0.5 wt% nanoparticles modified by 0.05 wt% of surface modifiers) at 1ft/day. No oil was recovered during this stage, and the pressure drop was about 4.3 psi. Then, SM-NP solution and nitrogen gas were co-injected at 1 ft/day with 80% quality for more than 7 PV. The additional oil recovery over water flood after 3.5 PV of foam injection was 14.8% OOIP. The pressure drop at the end of the experiment was 17.3 psi. The ultimate cumulative oil recovery was 63.1% OOIP; foam recovery over water flood was 14.8 % OOIP, and final oil saturation was reduced to 26.5%.
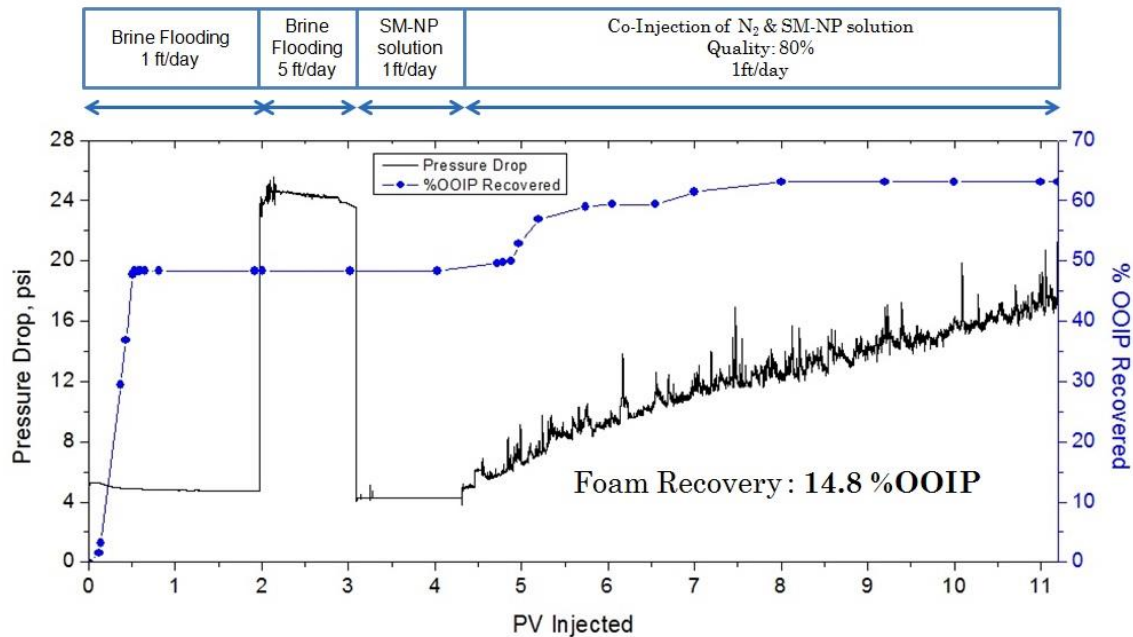
Figure 4.13: Pressure drop profile (left axis) and cumulative oil recovery (right axis) for the Core Flood 3

113

These core flood results reveal that immiscible foam can recover a significant amount of oil over waterflood. The oil recovery due to SM-NP stabilized foam (20.6% and 14.8%) was more than that by surfactant stabilized foam (13.4%). This could be due to stronger in-situ foam generation by SM-NP solution resulting in better microscopic sweep efficiency as compared to the surfactant. SM-NP stabilized foam is quite stable in the porous medium even in the presence of residual oil saturation. Further study is needed to mechanistically understand, and model transport of SM-NP stabilized foams.

4.4 CONCLUSIONS

Surface-modified nanoparticles, SM-NP were obtained by partial hydrophobization of alumina-coated silica nanoparticles using a surface modifier. Foams were then stabilized by these SM-NPs which had a tendency to adsorb at the air-water interface, in both bulk and porous media. The following conclusions can be drawn from this work:

- The attachment of the surface modifier on the nanoparticle surface occurred due to ligand-exchange reactions which are stronger than electrostatic interactions. This prevented the detachment of these anchored groups from the surface during flow through porous media. This approach of tailoring the interfacial properties of the nanoparticles is quite simple and robust, which does not require cumbersome chemical treatment as opposed to surface modification via controlled silanization.

- Bartsch shake test revealed strong foaming tendency of SM-NP even with a very low initial surface-modifier concentration (0.05 wt. %), whereas hydrophilic nanoparticles alone could not stabilize foam. The irreversible adsorption of such partially hydrophobic nanoparticles on the air-water interface results in foam stability.

114

- The optical micrographs showed that the bubble texture of foam stabilized by SM-NP solutions were finer than that obtained by a typical surfactant.

- As the degree of surface coating increased, mobility reduction factor of SM-NP foam in a Berea sandstone core increased significantly. These foam flow experiments showed that foam could be stabilized in the porous medium by in-situ surface activated nanoparticles, and they have the potential to behave as a surfactant.

- Core floods in a sandstone core with a reservoir crude oil showed that immiscible foams using SM-NP could recover a significant amount of oil over water flood. These recoveries were comparable to or higher than that obtained when a surfactant was used as the foaming agent.

Chapter 5: Foams with Wettability-Altering Capabilities for Oil-Wet Porous Media

5.1 INTRODUCTION

Chapters 3 and 4 focused on application of novel nanoparticles in improving the foam enhanced oil recovery process in sandstone porous media which are typically water-wet in nature. This chapter focuses on developing novel foam injection strategies for carbonate reservoirs which are oil-wet in nature. Additionally, these reservoirs tend to be highly heterogeneous. Foam is a potential solution to improve the sweep efficiency of these reservoirs. However, typically crude oils are highly detrimental to foam stability. An oil-wet carbonate will have a thin oil film on the surface and stabilization of foam lamellae in this condition is challenging. Wettability alteration of rock matrix toward water-wet using optimal surfactant will favor in-situ foam stability. Stronger foam can then act as an effective fluid blocking agent and can divert injectant fluid (or foam) to new lower permeability regions. Thus, wettability alteration and foaming capabilities can act in synergy to effectively improve the sweep efficiency in the oil-wet system

The goal of this work is to systematically study the effect of wettability alteration and foaming, either acting individually or synergistically, on tertiary oil recovery in oil-wet carbonate cores. Three types of anionic surfactant formulations were used: alkyl propoxy sulfate (APS), which exhibited low interfacial tension (IFT), wettability alteration (WA), and weak foaming; alpha-olefin sulfonate (AOS), which showed no WA, but good foaming; a blend of APS, AOS and a zwitterionic foam booster, which showed low IFT, WA and good foaming. Contact angle experiments, and spontaneous imbitions in a

---

This chapter is based on: (Singh and Mohanty, 2016b). Dr. Mohanty supervised the project.

microchannel were performed to evaluate the wettability-altering and IFT-lowering abilities of these formulations. Static foam tests were then performed to compare their foaming performance in bulk. The effect of adding zwitterionic surfactants to alpha olefin sulfonate (AOS) was investigated by foam flow experiments in a carbonate core in the absence of oil. Water floods and subsequent foam floods were then conducted in a carbonate core saturated with a crude oil using different surfactant formulations as the foaming agent.

5.2 METHODOLOGY

5.2.1 Materials

Table 5.1 lists the different surfactants and their properties used in this study. Anionic surfactants, APS-68 and APS-90, were chosen as they are good potential wettability altering agents (Wang and Mohanty, 2014). Anionic surfactant AOS, a C_{14-16} alpha-olefin sulfonate, was chosen as it is considered a good foaming agent (Farajzadeh et al., 2008). In the literature, betaines, a particular class of zwitterionic surfactants, are generally referred to as foam boosters (Basheva et al., 2000). In the present study, two common, commercially available zwitterionic surfactants, lauryl betaine, and Cocamidopropyl betaine were used.

Table 5.1: Surfactants used in the present study

Name	Structure	Active	Molecular weight	Type
APS-68	Alkyl 8-PO sulfate	30.6 %	~667 gm/mol	Anionic
AOS	Alpha olefin sulfonate	39 %	~324 gm/mol	Anionic
APS-90	Alkyl 7-PO sulfate	89 %	~667 gm/mol	Anionic
LB	Lauryl betaine	29 %	271.4 gm/mol	Zwitterionic
CPB	Cocoamidopropyl betaine	35 %	342.5 gm/mol	Zwitterionic

Ultrapure water with a resistivity greater than 18.2 MΩ-cm was used to prepare brine solutions. A Silurian dolomite core (1.5-inch diameter, 11.8-inch long) was used in foam flow and oil displacement experiments. The core permeability was 792 mD and porosity was 17.7%. Sandpack (0.6-inch diameter and 6-inch long) filled with Ottawa sand (40-70 Mesh) was used to pre-generate foam in foam flow and oil displacement experiments. This was done to eliminate the entrance effect and focus on foam rheology in the core. The sandpack permeability was 22.6 D, and porosity was 18%. Formation and injection brine used in these experiments are tabulated in Table 5.2. Crude oil was obtained from a reservoir, and it had a viscosity of 12.8 cp at 60 ºC, density of 0.830 g/cm^3, and an acid number equal to 4.91 mg of potassium hydroxide/gm of oil. The viscosity was measured using an ARES rheometer. The pH of the various surfactant formulations was measured using pHTestr® 20 (Oakton Instruments) which has the precision of ± 0.01. The pH electrode was calibrated with standard pH buffer solutions of pH 4, 7, and 10. Sodium chloride, calcium chloride, sodium sulfate, magnesium chloride, ethylenediaminetetraacetic (EDTA), sodium carbonate (Fisher Chemical), and methane (research grade, Matheson) were used as received. Sodium carbonate was used as an alkali to minimize surfactant adsorption in cores. EDTA was used as a chelating agent in some formulations to avoid precipitation of Ca^{2+} in the presence sodium carbonate.

118

Table 5.2: Formation and injection brine used in the study

Composition	Formation Brine	Injection Brine-I	Injection Brine-II
Na+	2.940 g/L	3.636 g/L	4.728 g/L
Ca2+	0.256 g/L	0.740 g/L	0
Mg2+	0.049 g/L	0.186 g/L	0
Cl-	4.859 g/L	7.294 g/L	7.128 g/L
SO42-	0.365 g/L	0.221 g/L	0.221 g/L
Total Salinity	8,469 ppm	12,077 ppm	12,077 ppm

5.2.2 Interfacial Tension (IFT) Measurements

Two different methods were used to measure the IFT between oil and aqueous-phase depending on its range. For high-IFT system (order of 10^{-1} dyne/cm), pendant droplet analysis was performed using Ramé-Hart goniometer. The oil droplet was held for sufficient time (>5 min) to allow it to equilibrate with the liquid phase. The axisymmetric shape analysis of the droplet was performed by DROPimage Advanced software which calculates the IFT by fitting the drop profile with Young-Laplace equation using a contour fitting algorithm. For low-IFT system (order of 10^{-2}–10^{-3}), spinning drop interfacial tensiometer (Model 510, Temco Int., USA) was used which is capable of measuring ultra-low IFTs. It calculates the IFT based on the correlation provide by Cayias et al. (1975). In both methods, first, surfactant formulation and oil were mixed and allowed to equilibrate at 60 °C. The equilibrated aqueous and oil phases were used for IFT measurement.

5.2.3 Contact Angle Experiments

Contact angle experiments were performed using mineral calcite plates as a proxy for carbonate cores as they have the similar mineralogy. First, these plates were polished by a 600-mesh diamond grinding plate to make the surface – smooth and free from any

contamination. Second, the polished plates were immersed in the formation brine for 24 hrs and then were aged in the crude oil at 80 °C for three weeks to render them oil-wet. Third, the oil-wet calcite plates were immersed in the formation brine at reservoir temperature, 60 °C to ensure its oil-wetness. Finally, the plates were placed in an optical cell and were submerged in different surfactant formulations. Zoomed images of the oil droplets on the plate were captured, and contact angles were observed. In some cases, the droplet sizes were too small (<0.5 mm) to measure the angles accurately. Therefore, after the surfactant treatment, these plates were washed with brine to remove oil. Then, these plates were placed in the brine solution, and the crude oil droplet was placed at the bottom of the plates using a U-shaped hypodermic needle, and the contact angles were measured. Several droplets were placed in random locations on the plate surface, and the average values with standard deviations are reported. This test is referred to as "post-wettability" test, and the measured contact angles give the final wettability state of the plates.

5.2.4 Spontaneous Imbibition in Microchannel

The experimental setup (Figure 5.2) consists of a cubical cell, open from the top, with four faces made of acrylic and the fifth face made of silica glass (with an etched microchannel). These faces were sealed using transparent, silicone rubber sealant to ensure leakproof connections. A rectangular, vertical microchannel (1.3 cm wide x 7 cm long) was etched in the center of the silica glass using photo-lithography and hydrogen fluoride etching method. The depth of the microchannel, measured using Dektak 6M stylus surface profilometer, was found to be 27 μm. The glass face was contacted with a hexadecyltrimethylammonium bromide (CTAB) solution (concentration = 0.5 CMC) for 1 hour to make it preferentially oil-wet. Figure 5.1 shows the contact angle of crude oil

droplet (with outer aqueous phase) on glass surface before and after the treatment with CTAB. The contact angle changes from 48.7° to 115.35° which confirms that the surface-wettability changed from water-wet to preferentially oil-wet. One of the advantages of using this technique to make glass surface oil-wet rather than using silanization is that it is a chemically reversible process and thus could be used in wettability alteration studies.
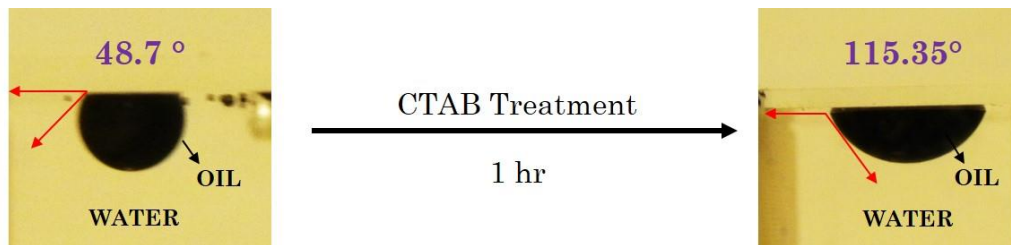
Figure 5.1: Contact angle of oil droplet on glass surface

An oil-wet calcite plate (light yellow), which was aged in the crude oil at 80 °C for three weeks, was then placed on the microchannel with crude oil trapped in-between the plate and glass via capillarity. The calcite plate had a realistic wettability (not the glass plate), and attention should be focused on the wettability alteration of the calcite plate during imbibition experiments. The plate was held firmly using a screw-bolt system. The height of microchannel was larger than the height of plate ensuring liquid contact from both top and bottom. Previous studies have also reported similar experiments such as spontaneous imbibition in two, parallel glasses system (Kumar et al., 2008) or glass-calcite system (Zhang et al., 2006). One of the technical limitations of these studies was that they used flexible spacers to maintain the gap between the plates which could change when the plates were pressed. The glass etching process in this study ensured fixed spacing in all the experiments. Different brine/surfactant formulations were then filled in the cubical cell. The displacement of oil via spontaneous imbibition was then captured

using Supereyes® microscope. The image processing was performed using the ImageJ software to calculate the oil displacement as a function of time.
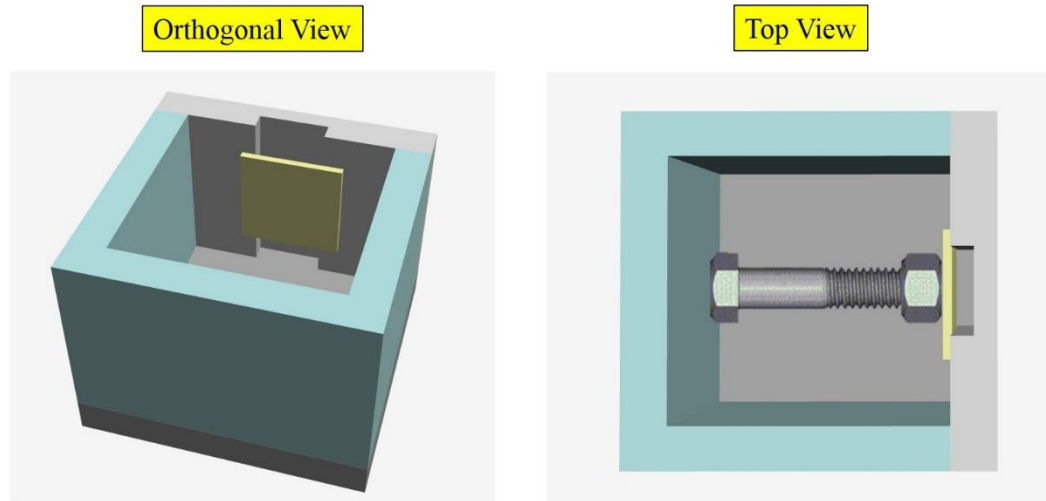
Figure 5.2: Optical cell for spontaneous imbibition experiments

5.2.5 Static Foam Tests

Static foam tests are the most common bulk foam stability analysis techniques which are typically performed to compare the bulk foaming ability of different formulations (Vikingstad et al., 2005).These experiments were performed to compare the foamability of various surfactant formulations which were used in oil-displacement experiments. It is to be noted that behavior of foam in bulk is quite different than in porous media in terms of bubble texture, bubble sizes, mechanisms of foam generation and coalescence. Therefore, bulk foam stability should not be directly correlated to foam stability in porous media. However, these tests are quite useful for screening purposes. The experiment apparatus consisted of a transparent cylinder made of acrylic (diameter: 1 cm, length: 20 cm) with a stainless steel sparging frit (pore size 2 μm) at the bottom,

which was used to disperse air. Both ends of the cylinder had Swagelok fittings which prevented evaporation. First, 20 mL of sample was then taken in the cylinder, and then air was injected at a constant pressure of 2 psi from the bottom generating static foam. These experiments were conducted at 60 ℃ (reservoir temperature in the present study). The height of the foam (above the liquid phase) was monitored as a function of time. Half-life, which is the time for the volume of foam to be reduced to half of its original volume, was calculated for each case. Each experiment was repeated two times, and the average half-lives are reported.

5.2.6 Foam Flow Experiments

Foam flow experiments were conducted to investigate potential synergism between anionic surfactant–alpha olefin sulfonate and zwitterionic surfactants–lauryl betaine, and Cocamidopropyl betaine in stabilizing foam in the absence of crude oil. The core used in these experiments was not aged with crude oil and thus was considered water-wet. Table 5.3 lists the surfactant formulations and their properties which were used in these experiments. A cylindrical, Silurian dolomite core was used for these experiments, which was 1.5" diameter and 1 ft long. The core was dried at 80 ℃ for 24 hr in an oven and was laminated with FEP shrink wrap tubing (Geophysical Supply Company, Houston, TX). It was then mounted vertically in a Hassler-type core holder (Phoenix, Houston, TX) with a confining pressure of 1200 psi. Petrophysical properties such as air porosity and permeability of the core were then determined before performing the vacuum saturation with formation brine at room temperature. Figure 5.3 shows the experimental schematic. Two series-D syringe pumps from Teledyne ISCO (Lincoln, NE) were used in the setup which are capable of low injection rates (as low as 0.001cc/min). The apparatus was built

to coinject methane gas and brine/surfactant solution through a sandpack (0.6-inch diameter and 6-inch long) to ensure proper mixing and foam generation. The pre-generated foam was then injected at the top of the core. Preforming the foam in a sandpack and injecting into a Berea core does not remove the entrance effect entirely, but lessens it (Haugen et al., 2012b). The whole setup was placed in an oven operating at reservoir temperature, 60 ℃. The downstream pressure of the experiment was maintained by a backpressure regulator (Equilibar, NC) installed after the coreholder. The pressure drop across the core was measured using Rosemount differential pressure transducers. An automated data acquisition system (LabView, National Instruments) was used to record the pressure.

Table 5.3: Surfactant formulations used as foaming agents

#	Wettability	Surfactant Formulation	Label	Viscosity, cp (60 ℃)	pH
1	Water-Wet	0.5 wt.% AOS + Injection Brine-II + 30000 ppm Na2CO3	S7	0.68	11.27
2	Water-Wet	0.25 wt.% AOS + 0.25 wt.% LB + Inj. Brine-II + 30000 ppm Na2CO3	S8	1.02	11.25
3	Water-Wet	0.25 wt.% AOS + 0.25 wt.% CPB + Inj. Brine-II + 30000 ppm Na2CO3	S9	1.01	11.25
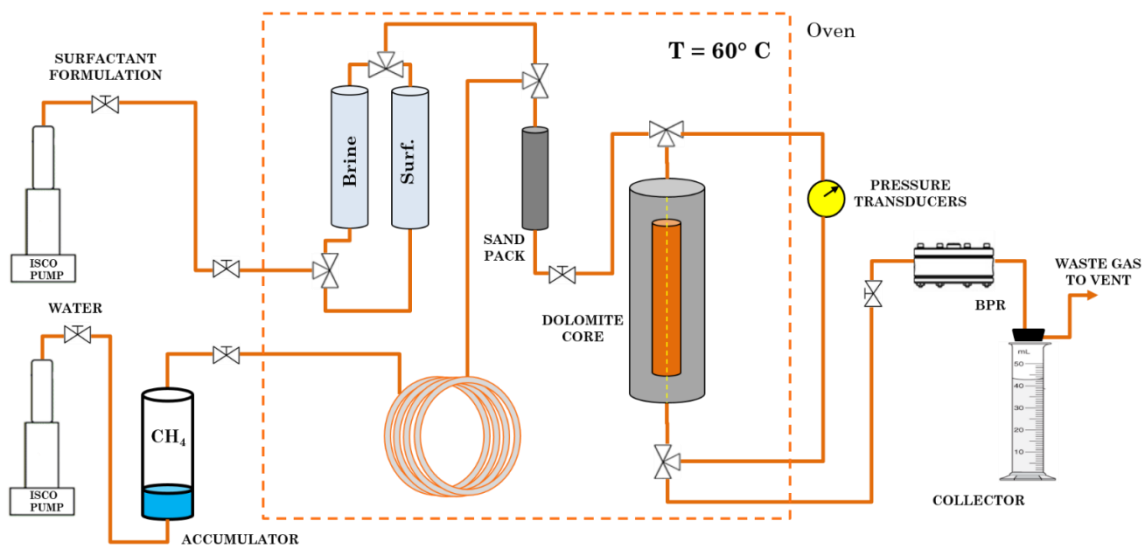
Figure 5.3: Schematic of experimental setup for foam flow and oil displacement experiments

5.2.7 Oil Displacement Experiments

In an oil-wet system, the phenomenon of foam mobility control and wettability alteration are quite complex and could be highly interdependent. In carbonate cores, which are typically heterogeneous, foam, if stable, can potentially divert injectant fluids to low-permeability regions where wettability-altering fluid can alter wettability and recover more oil. On the other hand, wettability alteration can lower the oil saturation in high permeability region by mobilizing oil and thus assisting foam stabilization, as high oil saturation is known to be detrimental to foam stability. So, the objective of performing oil displacement experiments was to study the effects of wettability alteration and foaming, acting individually or synergistically in oil-wet carbonate cores. All these experiments were done using the same Silurian dolomite core used in foam flow experiments. At the end of each experiment, the core was cleaned using the Soxhlet extraction method. Table

125

5.4 tabulates the list of experiments that were performed, initial wettability-state of the rock, surfactant formulation used and their properties. The viscosities are reported at 60 ºC and a shear rate of 10 sec^{-1}. The total weight % of surfactant in each formulation was kept constant and equal to 0.5 wt.%. The chelating agent, EDTA could also promote alkalinity, saponification, and dolomite dissolution which could result in enhanced imbibition rate and higher oil recovery (Chen and Mohanty, 2013). Thus, EDTA was not used in the S7 formulation to simplify the system and to better interpret the results. All these experiments were conducted with the core in the initial oil-wet state except Core Flood 3, which was done at the initial water-wet state. The objective, in this case, was to study the effect of surface wettability on foam rheology in the presence of oil.

Table 5.4: Surfactant formulations used in oil displacement experiments

#	Wettability	Surfactant Formulation	Label	Viscosity, cp (60 ºC)	pH	IFT dyne/cm
1	Oil-Wet	0.5 wt.% APS-68 + 1.5 wt.% EDTA + Brine-I + 30000 ppm Na2CO3	S1	0.74	11.26	0.002 ± 0.0002
2	Oil-Wet	0.5 wt.% AOS + Brine-II + 30000 ppm Na2CO3	S7	0.68	11.27	1.42 ± 0.01
3	Water-Wet	0.5 wt.% AOS + Brine-II + 30000 ppm Na2CO3	S7	0.68	11.27	1.42 ± 0.01
4	Oil-Wet	0.25 wt.% APS-90 + 0.125 wt.% AOS + 0.125 wt.% LB + 1.5 wt.% EDTA + Brine-II + 20000 ppm Na2CO3	S3	0.86	11.24	0.039 ± 0.002

The experimental setup was similar to that described in Figure 5.3. The brine porosity and permeability of the cores were determined. The cores, fully saturated with brine, were then flooded with the filtered crude oil (at least 2.5PV) from the top at a constant pressure of 750 psi at room temperature until brine production ceased. The oil-

saturated core was then aged for 1 month at 80 ℃ to make it oil-wet. Figure 5.4 shows the core when a water droplet is placed on the core before and after aging. The droplet imbibes in the former case indicating initial water-wetness but does not imbibe in the latter case confirming oil-wetness. The whole setup was pressurized with a back pressure of 100 psi. The following injection sequence was followed in each experiment. First, the brine flood was conducted at 1ft/D for 2 pore volumes (PV) until no oil was produced. This step mimicked a water flood at a typical field rate in a reservoir. Capillary end effects, which arise due to discontinuity of capillarity in the wetting fluid at the core outlet, are quite prominent in an oil-displacement process in an oil-wet system. This effect was minimized by flooding brine at a higher rate of 5ft/D for 1 PV. Second, methane gas and brine were then co-injected through the sand pack with quality (gas fraction) of 80 % until no oil was recovered. Third, methane gas and surfactant were co-injected through the sand pack at 80% quality. This pre-generated foam was then injected into the core from the top for 4 PV. Oil recovery and pressure drops were monitored at each step.

Figure 5.4: Silurian dolomite core before and after aging process

127

5.3 RESULTS AND DISCUSSION

5.3.1 Contact Angle Experiments

Contact angle, which is the angle between the solid surface and the tangent at the three-phase boundary, is the most fundamental measure of wetting. Figure 5.5 shows the oil droplet on calcite plate at t = 0 hr, t = 9 hrs and the droplet during the post-wettability test. Table 5.5 shows the average contact angles based on post-wettability tests. After aging the calcite plate, the plate was first immersed in the formation brine at the reservoir temperature of 60 ˚C. The flattened oil droplet can be seen with a contact angle of 152° confirming the oil-wetness of the calcite plate. In the subsequent runs, similar oil-wet calcite plates were submerged in different surfactant formulations at reservoir temperature, and oil droplets were observed. It can be seen that surfactant formulation, S1 with APS-68 as surfactant changed the wettability of plate from oil-wet to water-wet. The formulation, S2 containing alpha-olefin sulfonate (AOS) as a surfactant was not able to change the wettability of the plate. Remarkably, the addition of 3 wt.% sodium carbonate to S2 formulation (i.e., S7) resulted in wettability alteration of the plate from oil-wet to preferentially water-wet. The formulation S3 and S4 which contained equal wt.% of APS-90, and AOS-zwitterionic mixture (1:1) was also found to effective in wettability alteration of the plate as most of the oil droplets left the calcite plates in just 9 hrs as shown in Figure 5.5. A stream of fine oil-droplets leaving the surface was observed as soon as they were submerged in the surfactant formulations S1, S3 and S4 indicating the low-IFT behavior of the surfactant-oil system.

128

Table 5.5: Average contact angle based on post-wettability tests

#	Formulations	Label	\<Contact Angle\>
1	Brine- II	B2	$152° \pm 2°$
2	0.5 wt.% APS-68+ Brine-I +1.5 wt.% EDTA + 30000 ppm Na_2CO_3	S1	$64° \pm 3°$
3	0.5 wt.% AOS + Brine-II + 0 ppm Na2CO3	S2	$154° \pm 2°$
4	0.25 wt.% APS-90 + 0.125 wt.% AOS + 0.125 wt.% LB + 1.5 wt.% EDTA + Brine-II + 20000 ppm Na2CO3	S3	$42° \pm 6°$
5	0.25 wt.% APS-90 + 0.125 wt.% AOS + 0.125 wt.% CPB + 1.5 wt.% EDTA + Brine-II + 20000 ppm Na2CO3	S4	$40° \pm 2°$
6	0.5 wt.% AOS + Brine-II + 10000 ppm Na2CO3	S5	$131° \pm 4°$
7	0.5 wt.% AOS + Brine-II + 20000 ppm Na2CO3	S6	$131° \pm 8°$
8	0.5 wt.% AOS + Brine-II + 30000 ppm Na2CO3	S7	$45° \pm 4°$
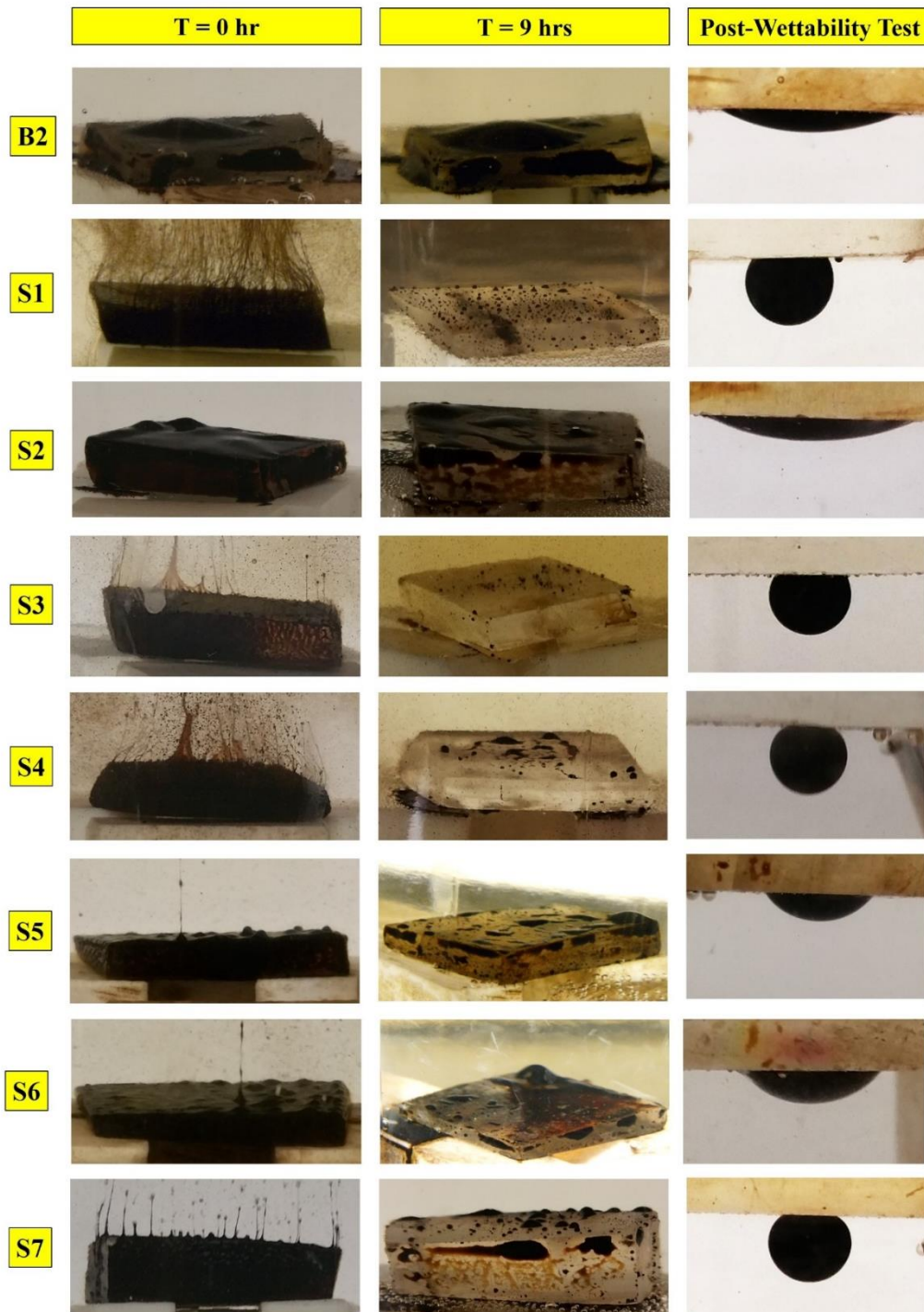
Figure 5.5: Oil droplets on calcite plate: at t = 0 hr (left), at t = 9 hrs (middle), and post-wettability test (right)

5.3.2 Spontaneous Imbibition in Microchannel

The three main factors influencing the oil-trapping in oil-wet rock matrix are wettability, interfacial tension, and capillarity. In a spontaneous imbibition process, the wetting phase is drawn in the pores/microchannel while the non-wetting phase is displaced out via capillary gradient. For an oil-wet system, water will not imbibe in the matrix unless wettability is modified to water-wet or IFT is reduced considerably. The ubiquitous buoyant forces acting along with wettability-altering and IFT-lowering processes can counter the capillary forces in an oil-wet system. These processes are studied in the following experiments. The oil-wet calcite plates, obtained by aging in crude oil at elevated temperature, were placed on the CTAB-treated glass microchannel. Different formulations were then filled in the optical cell, and oil displacement via spontaneous imbibition was monitored. Table 5.6 shows the list of these formulations. First, injection brine was filled in the cell. Figure 5.6 shows oil trapped in the microchannel at the start of the experiment and after 24 hrs. No oil displacement was observed even after 24 hrs indicating that buoyant forces were not sufficient enough to overcome the capillary forces. For the case of S1 formulation, the oil displacement via imbibition could be seen even in first few min of experiment with the recovery of more than 50% oil in first 4 hrs. The final oil recovery for this case was 92.3% after 20 hrs. The clean calcite plate and the glass surface at the end of the experiment indicated the wettability-altering capability of the formulation from oil-wet to water-wet. Moreover, fine droplets leaving the top outlet of the microchannel confirmed the low-IFT behavior of the formulation with the crude oil. For the S2 formulation, the ultimate recovery was very low (11.9%) suggesting that the formulation was neither able to imbibe effectively in the microchannel nor was able to alter wettability. Interestingly, the same formulation with added sodium carbonate (S7) was able to spontaneously imbibe in the channel with an oil recovery of 22.8% in the first

hour and ultimate oil recovery of 63.8%. This result is in line with the observation made during the contact angle experiment in which the S7 formulation shows wettability-altering behavior. A careful look at the oil-displacement process showed that most of the left-over, isolated oil is sticking to the glass surface and not the calcite plate. It shows that the formulation, S7 was able to alter the wettability of calcite plate more effectively than the glass surface. Since, the calcite surface aged with crude-oil is more representative of an oil-wet carbonate reservoir than a synthetically-modified, oil-wet glass surface; the final recovery (63.8%) is quantitatively underestimated. The surfactant formulation, S3 also showed good result in recovering oil with about 40% recovery in 4 hrs and final oil recovery of 81.3%. The ultimate oil recovery for the S4 case was found to be low (55.5%) than the S3 case. The reason for this could be that IFT of S4 was one order of magnitude larger than that of S3. These results show that S1, S3, and S7 formulation are promising candidates for oil-displacement experiments. Figure 5.7 compares the oil recovery as a function of time of these different cases.

Table 5.6: Final oil recovery via spontaneous imbibition in microchannel

#	Formulations	Label	pH	Final Recovery
1	Injection Brine-II	B2	6.90	0 %
2	0.5 wt.% APS-68+ Brine-I +1.5 wt.% EDTA + 30000 ppm Na2CO3	S1	11.26	92.3 %
3	0.5 wt.% AOS + Brine-II + 0 ppm Na2CO3	S2	8.32	11.9 %
4	0.5 wt.% AOS + Brine-II + 30000 ppm Na2CO3	S7	11.27	63.8 %
5	0.25 wt.% APS-90 + 0.125 wt.% AOS + 0.125 wt.% LB + 1.5 wt.% EDTA + Brine-II + 20000 ppm Na2CO3	S3	11.24	81.3 %
6	0.25 wt.% APS-90 + 0.125 wt.% AOS + 0.125 wt.% CPB + 1.5 wt.% EDTA + Brine-II + 20000 ppm Na2CO3	S4	11.24	55.5 %
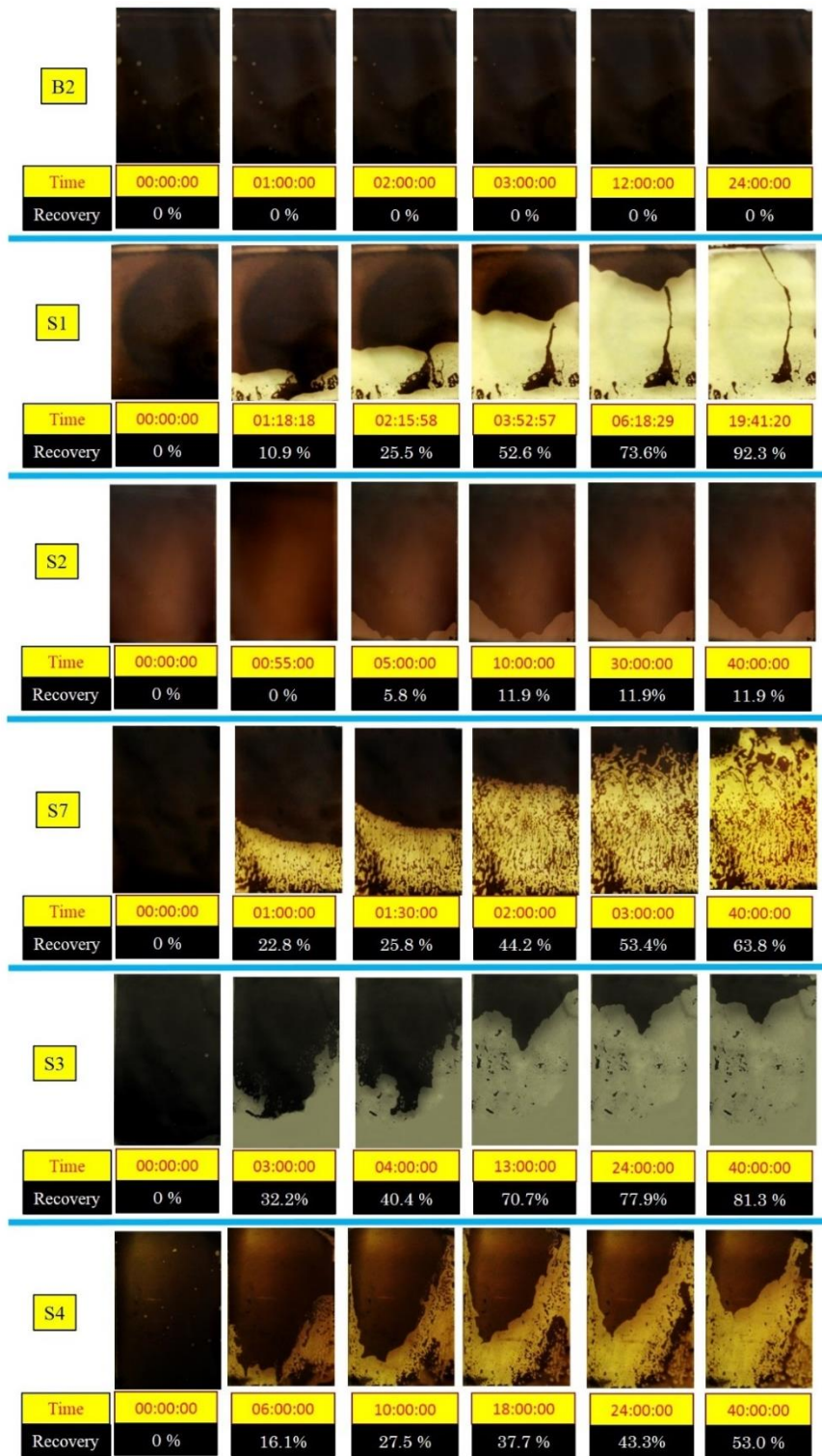
Figure 5.6: Oil displacement via spontaneous imbibition in a microchannel
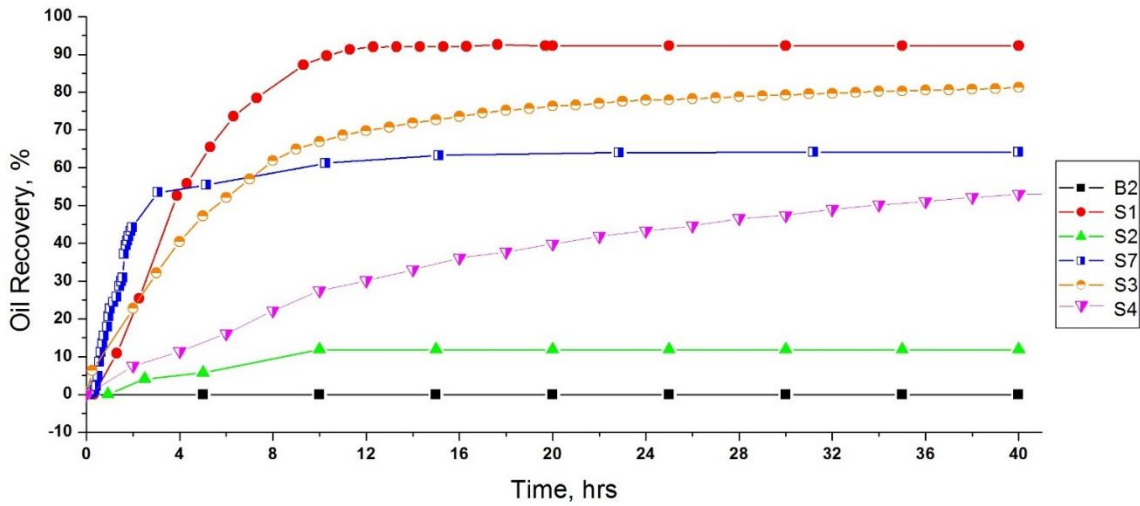
Figure 5.7: Plot of oil recovery via spontaneous imbibition as a function of time of different surfactant

5.3.3 Static Foam Tests

Static foam tests were performed to compare the bulk foam stability of the different surfactant formulations which would be used as foaming agents in the porous medium in the subsequent experiments. Figure 5.8 shows the decay of relative foam height with time for the different surfactant formulations. Average half-lives for S1 and S7 formulations were found to be 12 min and 216.5 min, respectively which suggests that alpha-olefin sulfonate (AOS) are better foaming agents than alkyl propoxy sulfate (APS). The half-life of S3 formulations, which is the blend of APS, AOS, and LB, was found to be slightly higher than that of S1. The half-life of S8 (blend of AOS and LB) and S9 (blend of AOS and CPB) was found to be 378.5 min and 447.5 min, respectively which was more than that of S7 (AOS). This increase in bulk foam stability due to the presence of zwitterionic surfactant could be due to increment in the viscosity of the solutions. Table 5.7 summarizes the average half-life of the static foam generated by different surfactant formulations.

134
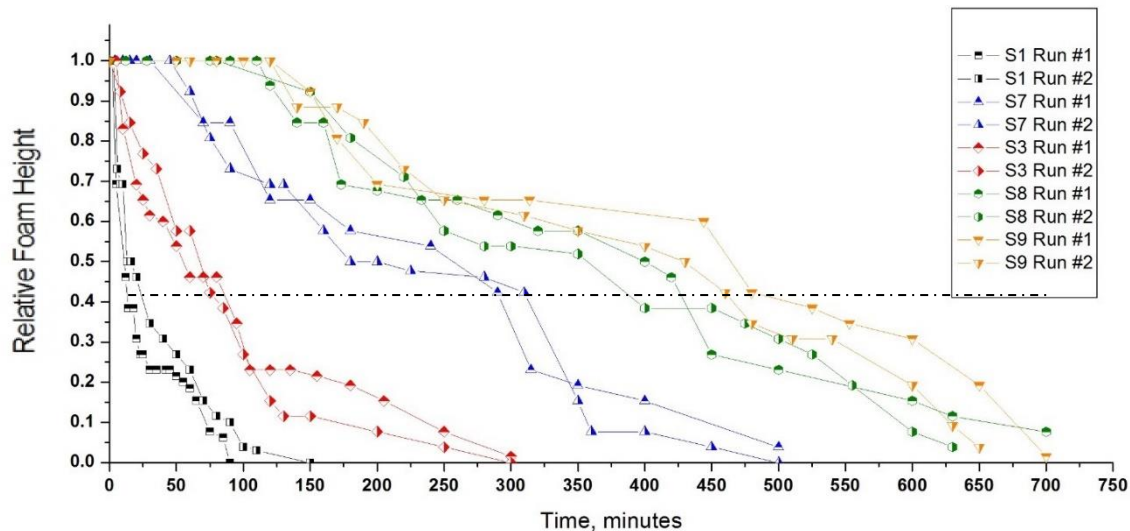
Figure 5.8: Plot of the decay of static relative foam height with time

Table 5.7: Static Foam Tests Results

S	Surfactant Formulation	Label	Viscosity, cp (60 ºC)	Half-life, min
1	0.5 wt.% APS-68+ Brine-I +1.5 wt.% EDTA + 30000 ppm Na2CO3	S1	0.74	12 ± 1.4
2	0.5 wt.% AOS + Injection Brine-II + 30000 ppm Na2CO3	S7	0.68	216.5 ± 55.9
3	0.25 wt.% APS-90 + 0.125 wt.% AOS + 0.125 wt.% LB + 1.5 wt.% EDTA + Brine-II + 20000 ppm Na2CO3	S3	0.86	60 ± 9.9
4	0.25 wt.% AOS + 0.25 wt.% LB + Inj. Brine-II + 30000 ppm Na2CO3	S8	1.02	378.5 ± 30.4
5	0.25 wt.% AOS + 0.25 wt.% CPB + Inj. Brine-II + 30000 ppm Na2CO3	S9	1.01	447.5 ± 24.7

5.3.4 Foam Flow Experiments

Foam flow experiments were conducted to investigate the effect of the addition of zwitterionic surfactants such as lauryl betaine and Cocamidopropyl betaine to anionic surfactant (alpha-olefin sulfonate) in foam stabilization in carbonate cores. The total

135

surfactant concentration was kept constant at 0.5 wt.%. These experiments were conducted in the absence of oil, and therefore, the core was not aged in crude oil after the core cleaning process and thus was water-wet. The total flow rate in these experiments was maintained at 4 ft/D. This was done to achieve sufficient pressure drop that one can measure accurately. These experiments were performed at 60 ˚C with a backpressure of 100 psi. Before each run, sufficient time (>12 hrs) was allowed to achieve isothermal conditions in the system. After each run, the core was flushed with 4 PV of methanol to break the foam and remove the surfactant from the core. Then, the core was flushed with more than 20 PV of brine to displace methanol and leftover surfactant. The backpressure was intermittently depressurized and pressurized to remove any trapped gas from the system. Finally, it was ensured that the brine-flow pressure drop was approximately equal to single-phase brine-flow pressure drop measured before the start of the experiment.

First, a base case was performed in which brine and gas were co-injected at 80% quality. The average pressure drop after 8 PV on injection was equal to 0.45 psi. In the subsequent experiments, different surfactant formulations were used as the foaming agent. Figure 5.9 shows the pressure drop profiles for the case of formulation S7, S8, and S9. S7 had 0.5 wt.% of AOS while S8 and S9 had 0.25 wt.% AOS and 0.25 wt.% of lauryl betaine and Cocamidopropyl betaine, respectively. The average steady-state pressure drop after more than 10 PV of injection was found to be 20.05 psi, 16.19 psi, and 16.02 psi, respectively for these cases. The foam resistance factor, which is the ratio of pressure drop due to foam flow to the pressure drop due to brine-gas coinjection at the same quality, was 44.6, 36 and 35.6, respectively. Thus, no synergy was observed in foam stabilization via 1:1 blend of AOS and zwitterionic surfactants.

136
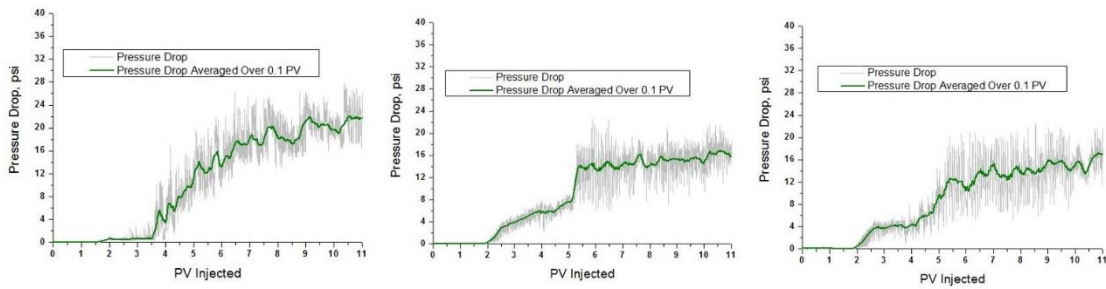
Figure 5.9: Pressure drop profile for foam flow experiments with S7 (left), S8 (middle), and S9 (right) formulations as foaming agent

5.3.5 Oil Displacement Experiments

Core flood experiments were conducted to evaluate three surfactant formulations with different properties in terms of IFT-reduction, wettability alteration, and foaming based on bulk experiments. The objectives of these experiments were two-fold: evaluate foam rheology in corefloods in the presence of oil and assess the microscopic oil displacement efficiency by the foams. The total surfactant concentration was kept constant at 0.5 wt.%. All these experiments were conducted with same Silurian dolomite core which was also used in previous foam flow experiments. The wettability-state of the core and the surfactant formulation used for each experiment is reported in Table 5.4. A dead, reservoir crude oil of viscosity 12.8 cp (at 60 ºC) was used in these experiments. These tests do not evaluate the sweep efficiency of foams because they are conducted in a core of 1.5-inch diameter. Multi-dimensional tests or layered core floods should be used to evaluate the sweep efficiency of foam formulations. However, the pressure gradient generated during these foam floods gives indications of foam stability in the presence of a crude oil and the potential for improved sweep efficiency.

Core Flood 1 was conducted on oil-wet core obtained by aging it with crude oil at an elevated temperature. The initial oil saturation was 66.3%. Figure 5.10 shows the injection procedure, cumulative oil recovery (secondary y-axis) and overall pressure drop (primary y-axis) across the core. Brine flood was conducted at 1 ft/D to mimic waterfloods at a typical field rate. It was continued for about 2 PV until no oil was produced. The waterflood oil recovery was 34.8% OOIP (original oil in place), and oil saturation was reduced to 43.2%. The pressure drop during water flood was between 0.68 psi. Capillary end effects, which arise due to discontinuity in the capillary pressure at the outlet, could lead to accumulation of wetting phase (oil in this case) at the core outlet. In order to minimize these effects, brine was injected at 5 ft/D for 1 PV. The pressure drop increased to about 1.4 psi as the flow rate was increased 5 times. Significant oil (5% OOIP) was recovered during this stage implying the presence of capillary end effects. Then, injection brine and methane gas were coinjected with a quality of 80% at 1ft/D. No oil was recovered during this stage. This is due to the fact that, in such water-flooded oil-wet system, the gas being the least wetting-phase flows only through the larger pores and could not displace any oil (most wetting-phase) which is present in the smaller pores. After this stage, surfactant formulation, S1, and methane gas were coinjected under similar conditions (80% quality, 1 ft/D) for 4 PV. The additional oil recovery over waterflood was 33% OOIP for this stage. The average pressure drop during this stage was very low (0.63 psi) suggesting only weak foam propagated through the core. Thus, wettability-alteration and IFT–reduction was the dominant mechanism for this significant recovery. Finally, methane gas flooding (100% quality, 1ft/D) was conducted for more than 1 PV. No oil was produced during this stage. The ultimate cumulative oil recovery was 72.8 %OOIP, and final oil saturation was 18%. In this case, the pressure gradient was low indicating that

138

the foam was unstable in the presence of this oil and there was low potential for sweep improvement.
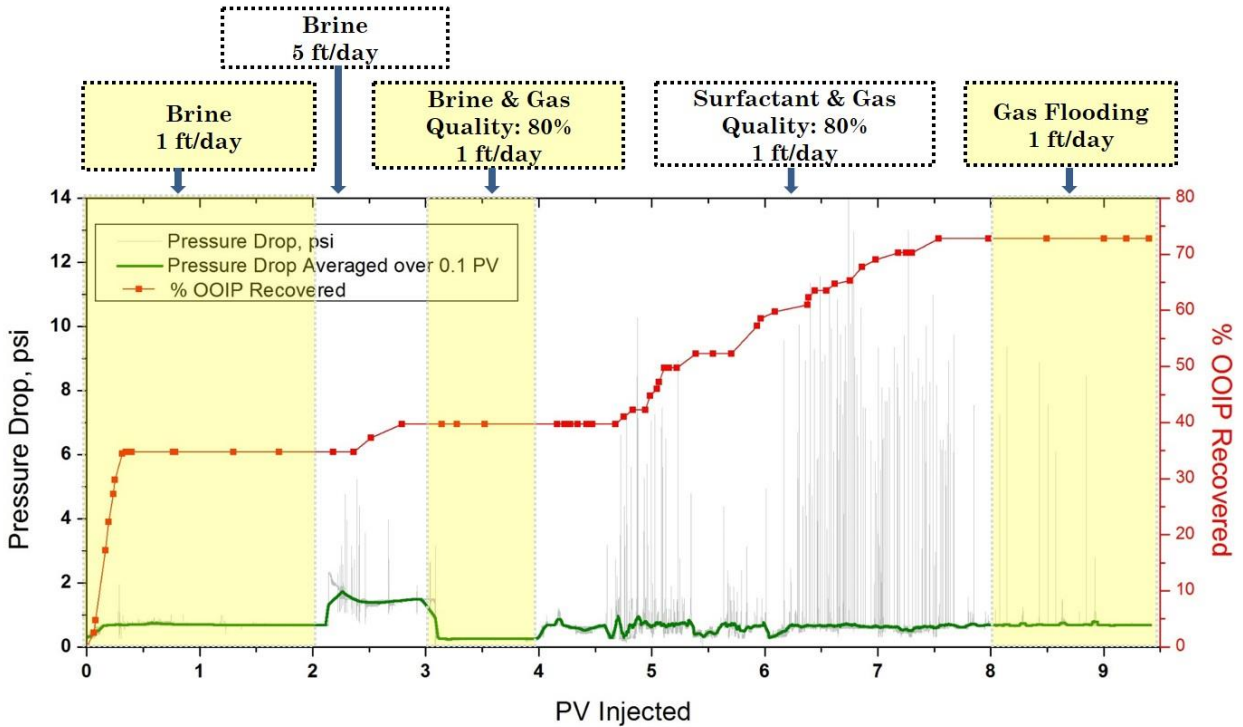
Figure 5.10: Pressure drop profile (left axis) and cumulative oil recovery (right axis) for the Core Flood 1

Core Flood 2 was again conducted on the same oil-wet core obtained after cleaning the core via Soxhlet extraction and then aging with crude oil at high temperature. The initial oil saturation, in this case, was 65%. The cumulative oil recovery (%OOIP) (secondary y-axis) and overall pressure drop (primary y-axis) are shown in Figure 5.11. The same injection sequence was followed as in Core Flood 1. The core was flooded with brine for 2 PV at 1 ft/D which represents a water flood. The water flood reduced the oil

saturation to 40.8% and resulted in 37.2% OOIP oil recovery. The pressure drop during this water flood stage was between 0.63 psi to 0.38 psi. Then, the core was flooded with brine for 1 PV at 5 ft/D resulting in 5.1% OOIP oil recovery due to capillary end effects. Then, injection brine and gas ware coinjected at 80% quality and 1 ft/D for 1 PV. No oil was recovered for this stage similar to Core Flood 1. Then, co-injection of surfactant formulation, S7, and methane gas was conducted at 1ft/D with 80% quality for 4 PV. The additional oil recovery over water flood was 16.7% OOIP for this stage. The pressure drop during this stage was very low (0.36 psi). This foam rheology in the presence of crude oil indicates that only weak foam propagated through the core. Finally, gas flooding was performed for more than 1 PV during which no oil was recovered. The ultimate cumulative oil recovery was 59% OOIP, oil recovery due to foam (over water flood) was 16.7% OOIP, and final oil saturation was reduced to 26.7%. Wettability alteration due to the synergy between AOS surfactant and alkali (sodium carbonate) seems to be the dominant mechanism for this oil recovery. The interfacial tension was not low for this formulation. The oil recovery due to foam is 16.7% in core flood 2 compared to 33% in core flood 1, primarily due to higher interfacial tension. In core flood 2, the pressure gradient was low indicating that the foam was unstable in the presence of this oil and there was low potential for sweep improvement.
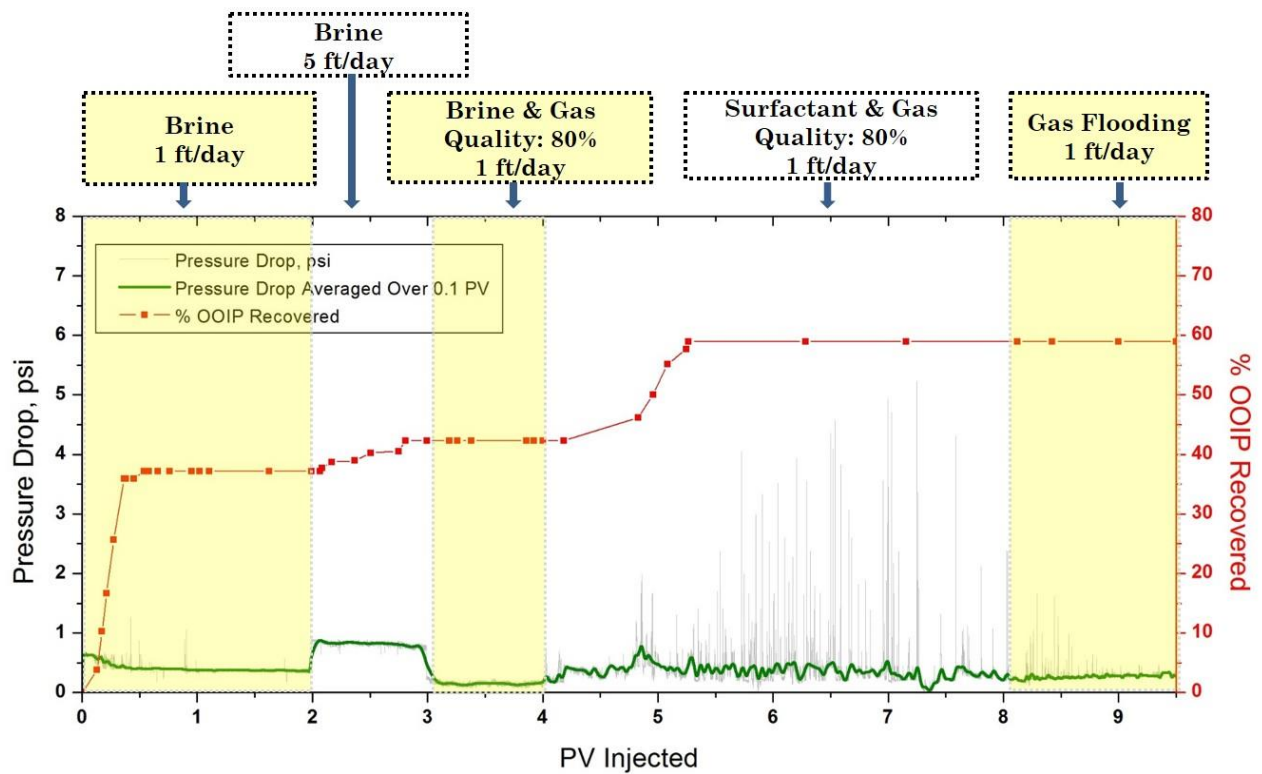
Figure 5.11: Pressure drop profile (left axis) and cumulative oil recovery (right axis) for the Core Flood 2

Anionic surfactants can adsorb to carbonates under low pH conditions. Since the core used in the present study is an outcrop core with a negligible amount of clay, and sodium carbonate was used as an alkali which can keep the system pH high, the surfactant adsorption was not a governing mechanism for foam instability. It is also known that foam strength is significantly lower in an oil-wet system as compared to water-wet systems, with rest of the parameters kept constant. This formulation changes the wettability towards water-wet; thus foam weakness is probably not due to wettability. The crude oil was quite detrimental to foam stability in this case.

141

In order to understand the underlying reason for the weak foam propagation in the present study, Core Flood 3 was conducted with the same surfactant formulation, but in a water-wet core. No aging was done after the core-cleaning process. Figure 5.12 shows the injection procedure, cumulative oil recovery (secondary y-axis) and overall pressure drop (primary y-axis) across the core. Water flood at 1 ft/D for 2 PV resulted in 51.9 %OOIP which is more than the previous cases owing to the water-wet nature of the core. Then, water flood at 5 ft/D was conducted for 1 PV. No extra oil was recovered since capillary end effects are absent at the end of waterfloods in water-wet systems. Then, brine and methane gas were coinjected at 80% quality at 1 ft/D. The injection was continued for 4 PV (as opposed to previous cases) until oil production ceased. The additional oil recovery (over the water flood) in this case was 20% OOIP. The physics of the oil-displacement by coinjection of brine-gas in this water-wet system is different than in previous oil-wet system. In a water-flooded water-wet system, water (most wetting-phase) lies in the smallest pores whereas oil (non-wetting phase) lies in the bigger pores. Therefore, the gas (least wetting-phase) injection can displace some of the oil from biggest pores in the system. Coinjection of gas with brine provides some mobility reduction to the gas phase which is equivalent to commonly applied water-alternating-gas (WAG) process. After this stage, surfactant formulation, S7 was coinjected with methane gas under similar conditions (80 % quality, 1 ft/D) for 4 PV. It resulted in an incremental oil recovery of 10.2 %OOIP with ultimate cumulative oil recovery was 82% OOIP. The pressure drop, in this case, was again very low even though the oil saturation was lower than the previous case and the rock surface was water-wet. This indicates that the main factor responsible for weak foam strength is the detrimental nature of crude oil to AOS-stabilized foam films in porous media and not the rock-surface wettability.

142
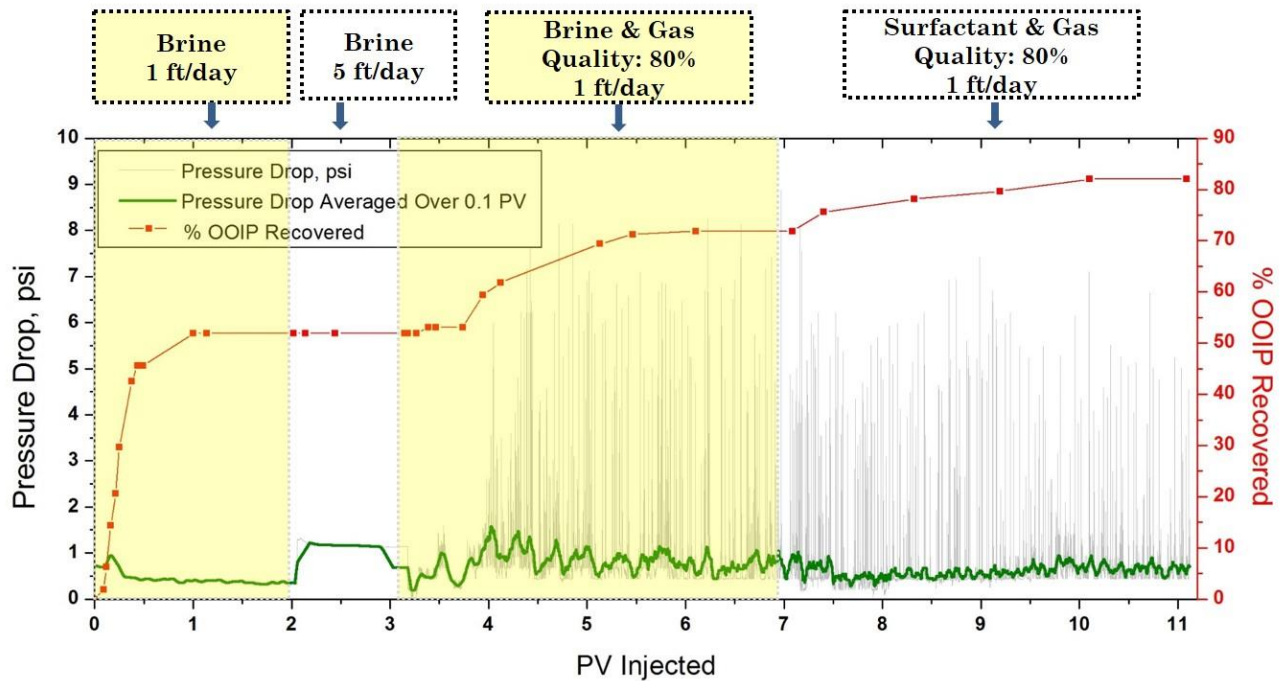
Figure 5.12: Pressure drop profile (left axis) and cumulative oil recovery (right axis) for the Core Flood 3

Core Flood 4 was conducted on the oil-wet core using surfactant formulation, S3 as the foaming agent. S3 comprises blend of 0.25 wt.% APS-90, 0.125 wt.% AOS, and 0.125 wt.% LB which offered good wettability alteration, some IFT-reduction, and foaming in the bulk experiments. The same injection sequence was followed as in previous corefloods. Figure 5.13 shows the injection procedure, cumulative oil recovery (secondary y-axis) and overall pressure drop (primary y-axis) across the core. Brine flood at 1 ft/D resulted in oil recovery of 36.6% OOIP, reducing the oil saturation from 60% to 37.9%. Brine flood at a higher rate of 5 ft/D resulted in an additional 5.1% OOIP recovery due to the capillary end effects. Then, brine and methane gas were coinjected at 80% quality for 1 PV. No oil was recovered during this stage similar to previous oil-wet

143

corefloods cases (Core Flood 1, 2). Then, surfactant formulation (S3) and methane gas were coinjected at 80% quality for 4 PV. It not only resulted in a significant oil recovery of 18.9% OOIP, but also strong in-situ foam was propagated through the core which is apparent from the foam rheology during this stage. The pressure drop rose up to 50 psi due to strong foam generation in the core. This foam is stable in the presence of oil. This stability can be attributed to the foam booster in addition to wettability alteration. The presence of foam booster (LB) in the formulation helped the foam lamellae to become more oil-tolerant. After foam flooding, methane gas was injected at 100% quality for 5 PV. It resulted in an oil recovery of 2.9 % OOIP in the initial 1.5 PV of gas injection which is due to foam propagation. Therefore, the total oil recovery due to foam flooding was 21.8% OOIP, and the ultimate cumulative oil recovery was 63.4% OOIP. The oil recovery of 21.8% is very significant, but lower than that in core flood 1. Wettability alteration, IFT reduction, and foam boosters all contribute to improved oil recovery. The IFT in core flood 4 is much higher than that in core flood 1 (Table 5.4) and may be the reason for the lower recovery. In the present study, the surfactant that could potentially lower the IFT to ultra-low values was alkyl propoxy sulfate (APS). So, one could vary the concentration of APS in the blend or the salinity of the formulations such that ultra-low IFT with crude oil is achieved. Such optimization of the formulation was not performed in the current study. It is possible to develop a system capable of ultra-low IFT, wettability alteration and strong in-situ foam propagation.

In summary, these coreflood results demonstrate the synergistic effects of wettability alteration and foaming in an originally oil-wet rock and how the addition of foam boosters can significantly improve the foam strength in the presence of crude oil. Such strong in-situ foams can help reduce permeability contrasts in a typical heterogeneous/fractured carbonate system and thus can improve volumetric sweep

efficiency significantly. These core floods do not evaluate the sweep efficiency of foams; multi-dimensional tests and layered core tests should be used to evaluate the sweep efficiency of these foam formulations. It is to be noted that foam stability is a strong function of pressure as reported in several studies (Holt et al., 1996; Liu et al., 2005). The effect of different pressures on foam stability in porous media was not investigated in the present study. Use of zwitterionic surfactants and chelating agents adds to the cost of foam formulations. A cost-benefit analysis should be conducted before field applications.
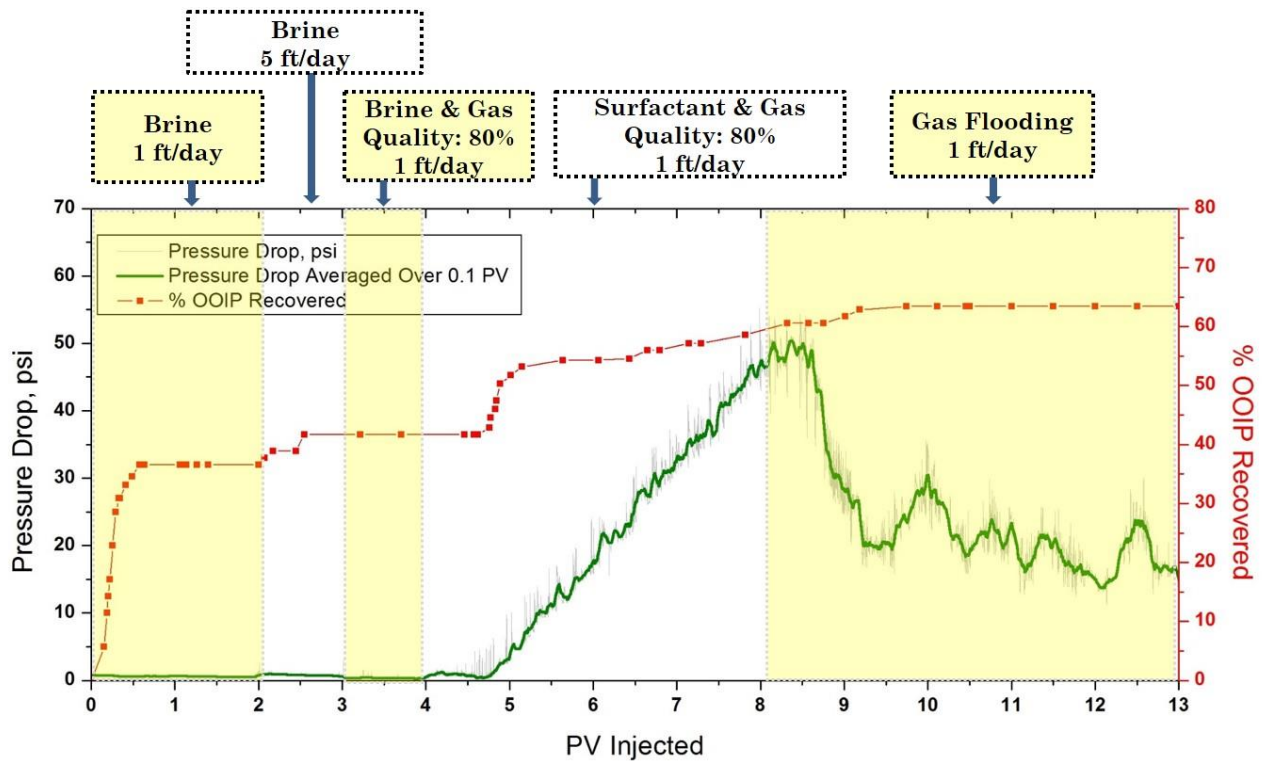
Figure 5.13: Pressure drop profile (left axis) and cumulative oil recovery (right axis) for the Core Flood 4

145

5.4 CONCLUSIONS

Secondary oil recovery in carbonates reservoirs is often very poor due to surface oil-wetness and heterogeneity. This study offers a novel systematic investigation of wettability alteration and foaming on tertiary oil recovery in an originally oil-wet carbonate core. The following conclusions were drawn from this study.

- Spontaneous imbibition in a microchannel with oil-wet calcite plates offered a visualization technique to study the role of buoyancy, IFT-reduction and wettability alteration on oil recovery. Etching of microchannel via photo-lithography on a glass surface provided a reliable method to keep the depth of the microchannel constant.

- Alpha olefin-sulfonate (AOS), a common foaming agent used in research/field applications, altered the wettability of calcite plate from oil-wet to water-wet in the presence of sodium carbonate, but was ineffective when acting alone.

- Contact angle experiments and spontaneous imbibition revealed that the blend of wettability-altering surfactant (APS-90), AOS and zwitterionic surfactant changed the wettability of the calcite from oil-wet to preferentially water-wet.

- Static foam tests showed an increase in bulk foam stability with the addition of zwitterionic surfactants to alpha-olefin sulfonate. However, in foam flow experiments, no such synergism in foam stabilization was observed via the blend of zwitterionic surfactant and alpha-olefin sulfonate (1:1) over alpha-olefin sulfonate solution alone in a water-wet carbonate core.

- Oil displacement experiment in oil-wet carbonate core revealed that tertiary oil-recovery via coinjection of wettability-altering surfactant and gas can recover a significant amount of oil (33% OOIP) over the waterflood. The foam rheology in the presence of oil suggested only weak in-situ foam in the oil-wet carbonate core.

146

- During foam flooding with AOS as a foaming agent, only the weak foam was propagated in the carbonate core, irrespective of the core wettability. Interaction with the residual oil degraded foams.

- A blend of a wettability-altering surfactant, AOS, and a zwitterionic surfactant not only altered the wettability of the carbonate core from oil-wet to water-wet but also significantly increased the foam pressure gradient in the presence of crude oil.

Chapter 6: Microencapsulation and Stimuli-Responsive Controlled Release of Particles using Water-in-Air Powders

6.1 INTRODUCTION

In this work, a facile, one-step method to encapsulate hydrophilic particles (HP) (micro- or nano- size) using water-in-air powders is reported. Hydrophobic silica nanoparticles were mixed with an aqueous phase containing HP in the presence of air under high shear. It resulted in self-assembly of silica nanoparticles on water droplets to make water-in-air powders with HP encapsulated in the aqueous phase within the silica-shell. The encapsulated HP can be released based on an external stimulus such as adding an external aqueous phase of a certain pH or a surfactant solution which alters the wettability of the encapsulating silica nanoparticles. A contact angle study was performed using surface-hydrophobized glass slides, which acted as a proxy for hydrophobic silica nanoparticles, to investigate the effect of these stimuli on surface hydrophobicity. Such encapsulation and stimuli-responsive controlled release system has promising potential in subsurface petroleum engineering such as delayed swelling of particles for conformance control and delayed acid stimulation.

6.2 METHODOLOGY

6.2.1 Materials

Commercially available fumed silica powder, Aerosil® R 202 with a primary particle size of 14 nm was supplied by Evonik Industry, USA. These particles were

---

This chapter is based on: (Panthi, Singh, and Mohanty, 2017). Panthi helped with the experiments and Dr. Mohanty supervised the project.

surface-treated with polydimethylsiloxane which makes them highly hydrophobic in nature. Hydrophilic fluorescent silica nanoparticles (FL-NP) coated with polyethylene glycol chains (PEG) were obtained from 3M (St. Paul, MN) with a nominal diameter of 10 nm. Salinity-sensitive, super-absorbing polymeric particles, LiquiBlock™ 2G-110 and LiquiBlock™ 40F were supplied by Emerging Technologies Inc, NC. These particles are the sodium salt of crosslinked polyacrylic acid and potassium salt of crosslinked polyacrylic acid/polyacrylamide copolymer, respectively. These particles are often referred to as "preformed particle gel (PPG)" in the literature and are typically used for conformance control in subsurface applications (Elsharafi and Bai, 2012; Imqam and Bai, 2015). These micro-particles are called PPG in this paper. The anionic surfactant, Amphoam (68% active) was provided by Weatherford Company. As per the supplier, it is an anionic surfactant with a sulfonate headgroup. This surfactant was chosen as it has shown to be quite robust in aqueous stability at high temperature and high salinity conditions (Xue et al., 2015). Dichlorodimethylsilane, DCMS (>99.5 %, Sigma Aldrich), anhydrous cyclohexane (>99.5 %, Sigma Aldrich) and Sodium chloride (Fisher Chemical) were used as received. Ultrapure water with a resistivity greater than 18.2 MΩ-cm was used to prepare brine solutions. The pH of the various surfactant formulations was measured using pHTestr® 20 (Oakton Instruments) which has the precision of ± 0.01. The pH electrode was calibrated with standard pH buffer solutions of pH 4, 7, and 10.

6.2.2 Encapsulation of Particles

The experiments were carried out using a Bella-Rocket blender. The volume of blending cup was 350 cc with cross blades. The hydrophilic particles (HP) (micro- or nano- size) dispersed in the aqueous phase were mixed with hydrophobic nanoparticles at

several ratios (by weight). The mixture was blended at 16,000 rpm for 1 minute. It resulted in the formation of a water-in-air powder stabilized by hydrophobic silica nanoparticles with HP dispersed inside the water droplets. Each experiment was repeated at least two times for reproducibility. Two different types of commercially available polymeric microparticles and one hydrophilic nanoparticle were encapsulated. The delayed release of one of the encapsulated micro-particle system was studied via an external stimulus in the subsequent sections.

6.2.3 Characterization of Encapsulated Particles

The surface morphology of the encapsulated micro-particles was analyzed using the FEI Quanta 650 SEM operating under high vacuum at an accelerating voltage of 5 kV. The samples were placed on double-sided carbon tapes glued on the aluminum stubs. Since these SEM measurements were performed under vacuum conditions, it may result in evaporation of water (Forny et al., 2007) which could lead to a collapsed silica shell (Carter et al., 2011). To avoid this potential issue, the use of other techniques such as freeze-fracture microscopy (Forny et al., 2007) and confocal laser scanning microscopy (CLSM) (Carter et al., 2011) has been successfully demonstrated in the literature. In this work, CLSM technique was adopted to image the encapsulated micro-particles which does not require any vacuum to perform the imaging. It was performed using a Zeiss LSM 710 Confocal Microscope with the 10X dry (EC Plan-Neofluor 10X) objective lens operating in fluorescence mode. Hydrophilic fluorescent silica nanoparticles (FL-NP) or hydrophilic dyes such as Nile Blue A and Rhodamine B were used for imaging the encapsulated micro-particles. A small amount of the sample was transferred using a dropper onto a slide with a well. A coverslip was then placed on top of the slide to seal it. The bottom of the

sample was then scanned at room temperature. The excitation wavelength of lasers used for FL-NP, Nile Blue A and Rhodamine B were 488 nm, 633 nm, and 514 nm, respectively. The image resolution was 1564 x 1564 pixels. The final image processing was performed using Fiji software. Bright-field images of the samples were obtained using a Nikon optical microscope equipped with a high-resolution camera.

6.2.4 Release from Micro-Particles

In these experiments, the PPG-encapsulating micro-particles were mixed with different aqueous solutions, and the release of the PPG (micro-particles) in the bulk solution was observed. The delayed release was triggered by addition of an external aqueous phase of a certain pH or a surfactant solution. 0.8 gm of PPG-encapsulating micro-particles was mixed with 39.2 gm of an aqueous solution (ratio 1:49 by weight) in 50-mL graduated centrifuge tubes. The tubes were capped, placed horizontally on a LabQuake® shaker (Barnstead Thermolyne) and were agitated at the room temperature. The samples were periodically centrifuged in a CRU-5000 centrifuge (Damon/IEC Division) operating at 3000 rpm for 2 min and the volume of precipitated PPG, $V_{measured}$ was measured. Note that the swelling time of the non-encapsulated PPG particles used in the present study was only 3 seconds. Therefore, the PPG particles are expected to swell instantly as soon as it breaks from the encapsulation. After centrifugation, the tubes were again mixed vigorously and were placed on the shaker for further release of PPG. To calculate the percentage release of PPG particles from the measured volume of swollen PPG ($V_{measured}$), first, the maximum volume (V_{max}) of fully-swollen PPG was calculated which would correspond to 100% release of particles. Theoretically, the initial volume of dry PPG particles and volume of saline water in 0.8 gm of PPG-encapsulating micro-

151

particles was calculated. The final salinity of the solution (mixture of 0.8 gm micro-particles and 39.2 gm aqueous solution) was calculated assuming 100% breaking of encapsulation. V_{max} was then calculated at this calculated salinity using the experimentally determined swelling ratio as reported in Table 6.1. The percentage release of particles was calculated based on the ratio of $V_{measured}$ and V_{max}.

Table 6.1: Swelling ratio of PPGs at different aqueous salinity

Particles	DI water	0.31 wt.%	2 wt.%	4 wt.%	8 wt.%	10 wt.%	20 wt.%
2G-110	>323	101	65	48	36	32	24
40F	>323	81	56	44	40	36	36

6.2.5 Contact Angle Measurement

Glass slides were made completely hydrophobic using the silane treatment described by Salter and Mohanty (1982). Briefly, glass slides were cleaned with deionized water and dried at 80 ºC. Then, they were immersed in a mixture of dichlorodimethylsilane (6% by volume) and dry cyclohexane for 24 hr at room temperature followed by drying. The sessile drop method was used to measure the water-air contact angle. The static contact angle was measured using a Ramé-Hart goniometer at 25 ºC. Water drops (10 µL) were placed on the glass slides for more than 5 min to equilibrate and then were analyzed using the DROPimage Advanced software. The contact angle of water drop changed from 29º to 103º due to the silane treatment which confirms the wettability alteration of the glass slides toward hydrophobic.

6.2.6 Surface Tension

The surface tension between air-water systems was measured via pendant droplet analysis using a Ramé-Hart goniometer. An aqueous drop (with varying surfactant concentration) was held in air from a hypodermic needle for a sufficient time (>5 min) to allow it to equilibrate with the air phase. The goniometer took a picture of the drop. The axisymmetric shape analysis of the drop was performed by DROPimage Advanced software which measures the IFT by fitting the drop profile to the Young-Laplace equation. Ten measurements were performed 5 seconds apart, and the mean and standard deviations of these measurements were calculated.

6.2.7 Particle Size Distribution

The particle hydrodynamic diameters of hydrophobic silica nanoparticles in the aqueous dispersions were characterized by dynamic light scattering (DLS) technique using the Delsa™ Nano analyzer. First, the samples were prepared by mixing 2 mg of hydrophobic nanoparticles and 10 mL of aqueous solution with varying Amphoam surfactant concentration. The samples were agitated vigorously on a MaxiMix™ Vortex Mixer (Thermo Scientific™) for 2 min and then stirred for 24 hrs using magnetic stir bars. Finally, 1 mL samples were taken in glass cuvette for DLS measurement without any pH adjustment at room temperature. It was ensured that no trapped foam bubble was present in the sample before each measurement.

6.3 RESULTS AND DISCUSSION

In this work, a facile approach to encapsulate particles is demonstrated in which encapsulation is performed by making water-in-air powder with particles dispersed in the

aqueous phase. The present approach is quite robust but limited to encapsulation of hydrophilic particles. In this work, particles of two different length scales — micro- and nano- were encapsulated to demonstrate the applicability of the proposed process. Two different types of polymeric micro-particles/PPG (LiquiBlock™ 2G-110 and LiquiBlock™ 40F) and fluorescently-tagged silica nanoparticles (FL-NP) were encapsulated. The PPG micro-particles are the sodium salt of crosslinked polyacrylic acid and potassium salt of crosslinked polyacrylic acid/polyacrylamide copolymer, respectively. These particles are superabsorbent polymers which swell in the presence of water by absorbing a large amount of water. The amount of swelling is strongly dependent on the water salinity. Table 6.1 shows the swelling ratio (volume of the swollen particle to the volume of the dry particle) of these micro-particles for the different salinity of the water. The swelling ratio of PPG (2G-110) decreases from 323 to 24 with an increase in salinity. This swelling ratio was found to be independent of change in pH or addition of surfactant in the aqueous phase. Therefore, in this work, first the PPG was encapsulated in a high salinity brine in which the PPG is only partially swollen. Then, this encapsulated PPG was mixed with a low salinity brine. The delayed breaking of encapsulation via an external stimulus allowed the partially-swollen PPG to mix with the low salinity brine allowing it to further swell by several times. Since PPG absorbs a lot of water even under high salinity conditions, the volume of free water (non-absorbed water) to PPG ratio (FW/PPG) varies as a function of total water to PPG ratio (TW/PPG). Water (20 wt.% NaCl) and PPG were mixed in the different ratios and were agitated on a LabQuake® shaker (Barnstead Thermolyne) at the room temperature for 30 min. (Note that the gelation time of these PPGs are only 3 seconds). The different samples were then centrifuged in a CRU-5000 centrifuge (Damon/IEC Division) operating at 3000 rpm for 2 min, and amount of FW/PPG was calculated. Figure 6.1 shows the plot of FW/PPG as a function of TW/PPG. The FW/PPG

is zero for LiquiBlock 2G-100 and LiquiBlock 40F for TW/PPG less than 10 and 15, respectively.
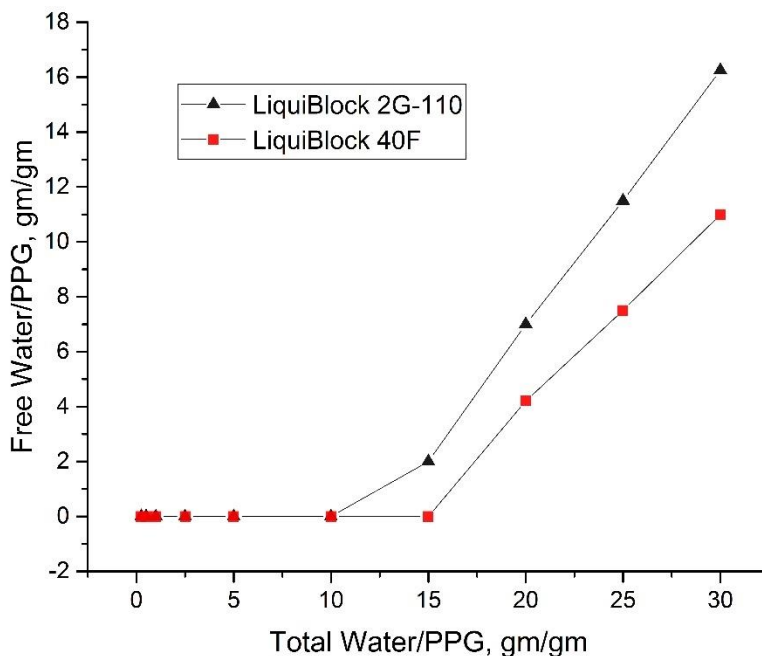
Figure 6.1: Plot of free water/PPG as a function of total water/PPG for the two different PPG used in this study

6.3.1 Encapsulation

6.3.1.1 Encapsulation of Micro-Particles

First, 5 gm of PPG (LiquiBlock^{TM} 2G-110) was dispersed in 25 gm of 20 wt.% NaCl solution. No pH adjustment was made. The PPG instantly absorbs the water and forms a gel, as shown in Figure 6.2b. This gel was placed in a blending cup and was mixed with 2.5 gm of hydrophobic silica nanoparticles (Figure 6.2a) at 16,000 rpm for 1 minute. It resulted in the formation of dry powders (Figure 6.2d) (termed encapsulated PPG powder, EPP) which flow freely through glass funnels (Figure 6.2c) as opposed to a

gel (Figure 6.2b) which does not flow without application of a shear force. Note that the weight ratio of nanoparticles to water (20 wt.% NaCl) to PPG was 1:10:2. The free water (non-absorbed water) in this case was zero (Figure 6.1). The blending of silica nanoparticles and hydrophilic gel in the presence of air resulted in water-in-air powder. The continuous-phase of this powder is the air while the discontinuous-phase is the partially-swollen PPG micro-particles with a water layer on their surface. It is interesting to note that the internal-phase is mostly gel particles with a hydrophilic surface. Figure 6.3a and 6.3b shows the SEM image showing the surface morphologies of the PPG (2G-110) and the encapsulated-PPG (2G-110), respectively. As mentioned earlier, since this SEM analysis was performed under vacuum conditions, it could lead to water evaporation and could potentially change the surface morphology of the EPP. Therefore, optical and confocal laser scanning microscopy to characterize these EPP was conducted. Figure 6.3c shows the optical micrograph of the encapsulated-PPG which was analyzed using the ImageJ software. The particle size was calculated to be 39 ± 25 microns by analyzing at least 200 particles. Figure 6.3d shows the confocal micrograph of the EPP with the aqueous phase (20 wt.% NaCl) tagged with hydrophilic dye, Nile Blue A. The irregularly shaped surface morphology of the EPP can be seen clearly from this micrograph which is similar to one observed in SEM (Figure 6.3b).

As mentioned earlier, since the amount of free water in this case was zero, the inner core of the EPP was expected to be only PPG particles. A CLSM analysis of another sample was then performed in which very less PPG particles are present. A ratio of nanoparticles to water (20 wt.% NaCl) to PPG = 1:10:0.05 was chosen. CLSM was performed using Zeiss LSM 710 Confocal Microscope with the 10X dry (EC Plan-Neofluor 10X) objective lens operating in fluorescence mode. Hydrophilic dyes, Nile Blue

156

A and Rhodamine B were used to tag the free water and PPG particles in the encapsulated
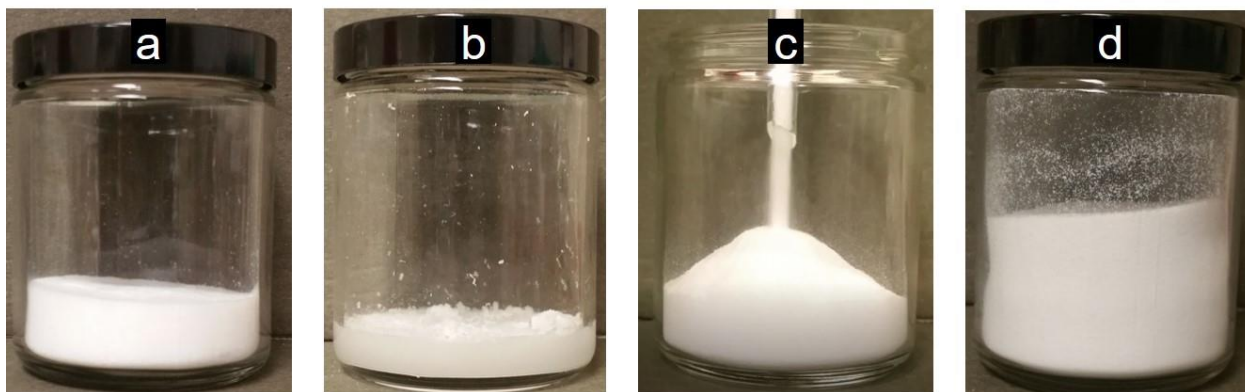
PPG powder (EPP).

Figure 6.2: (a) Hydrophobic silica nanoparticles; (b) PPG (2G-110) mixed in 20 wt.%
NaCl solution; (c) Encapsulated PPG Powder (EPP) flowing freely through
glass funnel; (d) Encapsulated PPG Powder (EPP)

First, PPG particles were mixed with excess water (20 wt.% NaCl) and few drops

of Rhodamine B stock solution (1 wt.%). The mixture was agitated on a shaker for 15 min,

and then free water (non-absorbed) was removed using centrifugation. The obtained

tagged-PPG particles were then mixed with water (20 wt.% NaCl) and few drops of Nile

Blue A stock solution (1 wt.%). The mixture was then blended with hydrophobic silica

nanoparticles (with NP: total water: PPG = 1:10:0.05.) to obtain encapsulated PPG powder

(EPP). A small amount of the EPP was transferred using a dropper onto a slide with a

well. A coverslip was then placed on top of the slide to seal it. The bottom of the sample

was then scanned at room temperature. The excitation wavelength of lasers used for Nile

Blue A and Rhodamine B were 633 nm, and 514 nm, respectively. The image resolution

was 1564 x 1564 pixels. The final image processing was performed using Fiji software.
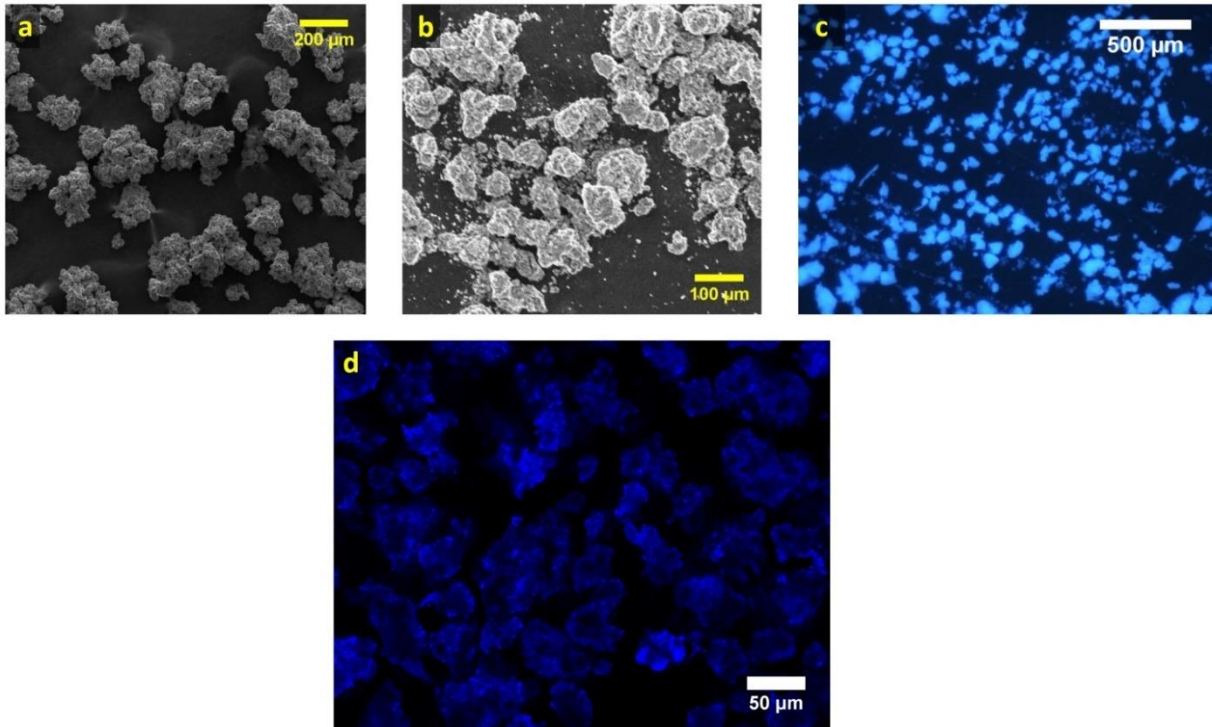
Figure 6.3: (a) SEM image of PPG (2G-110) particles (Scale Bar: 200 µm); (b) SEM image of Encapsulated PPG powder (EPP) (Scale Bar: 100 µm); (c) Optical micrograph of EPP (Scale Bar: 500 µm); (d) Confocal micrograph of EPP with aqueous phase tagged with Nile Blue A dye (Scale Bar: 50 µm)

Figure 6.4 shows the confocal micrograph of the sample. A small section (yellow box) where PPG particle was seen inside the EPP was zoomed in and was scanned along the z-axis. Figure 6.4 shows micrographs of five scans along the z-axis which were equally spaced at 8 microns. These micrographs show that how PPG particles surrounded by free water are present in the EPP. (An effective 3D- reconstruction of these slices were not possible due to availability of fewer slices) It is to be noted that since both dyes used in this case were hydrophilic, they tend to diffuse into each other slowly. Therefore, a weak fluorescent signal of Rhodamine B was detected along with Nile Blue A in the free water phase in some cases. However, the contrast between these signal and highly

158

fluorescent PPG particles was very high, which allowed effective imaging of the sample. The use of a hydrophobic dye to tag the PPG particles was avoided as it could alter the surface property of the particles.
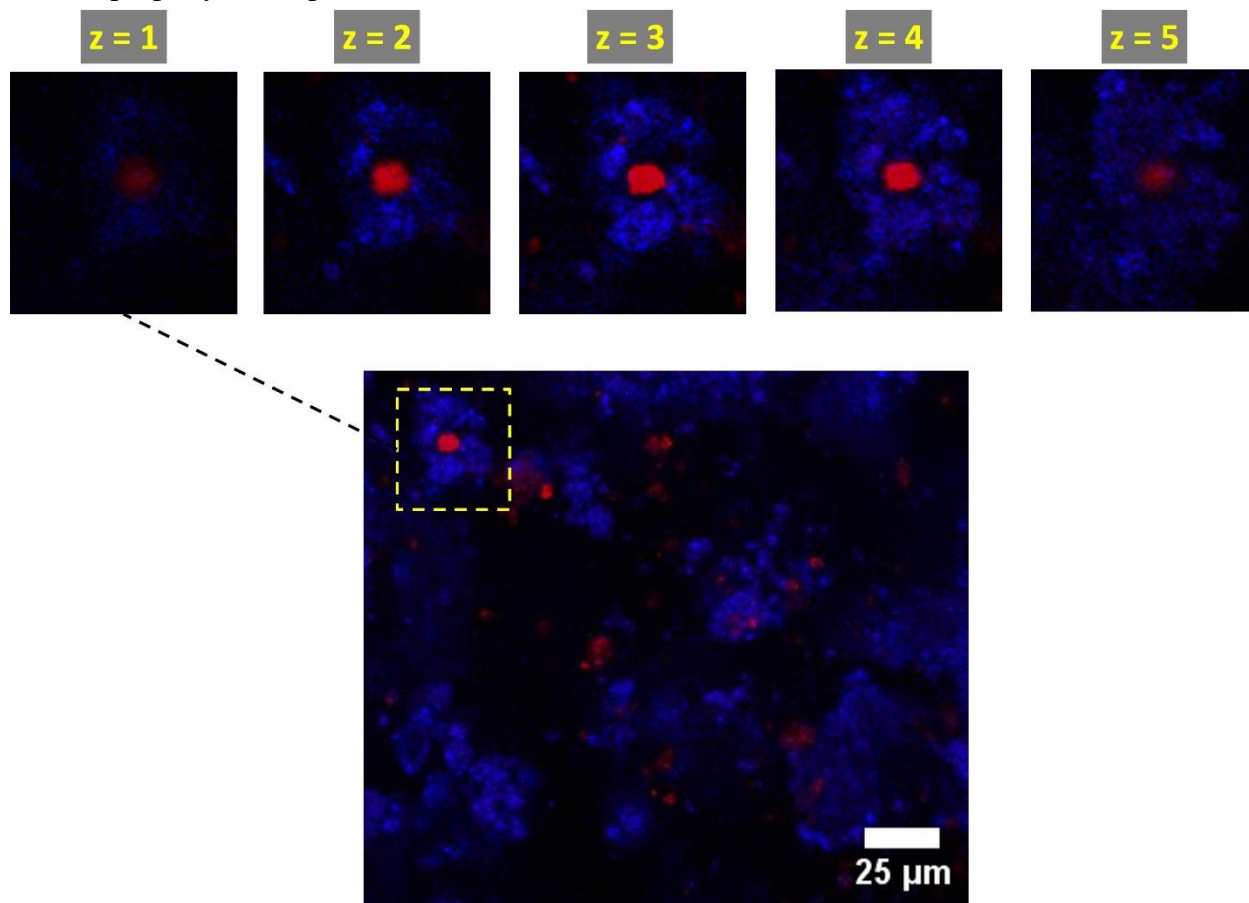
Figure 6.4: Confocal micrograph of encapsulated PPG (2G-110) powder formed using the ratio of NP: water: PPG = 1:10:0.05; free water is tagged with Nile Blue dye (blue), and PPG (2G-110) is tagged with Rhodamine B dye (red); the different z corresponds to different slices along the z-axis with a spacing of 8 microns

To validate that all the PPG (2G-110) micro-particles were completely encapsulated by the silica nanoparticles, 0.8 gm of encapsulated PPG powder (EPP) was mixed with 39.2 gm deionized (DI) water in a centrifuge tube. The sample was vigorously

hand shaken for 1 minute and then placed on LabQuake® shaker (Barnstead Thermolyne) at the room temperature for agitation for 24 hr. The sample was then centrifuged in a CRU-5000 centrifuge (Damon/IEC Division) operating at 3000 rpm for 2 min. No precipitate of PPG was observed indicating complete encapsulation of PPG micro-particles inside the silica nanoparticle protective coating. Note that PPG swells in the presence of DI water. The coating protects the PPG particles completely from the outside low-salinity water and thus preventing any swelling.

Assuming homogenous PPG (2G-110) concentration (by mass) inside the EPP powder, 0.8 gm of EPP corresponds to 0.123 gm of PPG (2G-110). If the encapsulation completely breaks, the final salinity of the solution would be 0.31 wt.%. The total expected swelling ratio at this salinity is 101 as reported in the Table 6.1. The silica nanoparticles used in the present study are highly dispersible in ethanol. To instantly break the encapsulation, 5gm of ethanol was then added to the sample and was mixed vigorously. The sample was again centrifuged, and swollen PPG was observed in the precipitate. The swelling ratio came out to be 101. This procedure was repeated several times, and the result was repeatable with an error of 0.8% which shows that PPG concentration in the EPP is quite homogenous. In a similar way, the second type of PPG (LiquiBlock^{TM} 40F) was successfully encapsulated, and a free-flowing Encapsulated PPG Powder (EPP) was obtained.

In the above cases, the weight ratio of nanoparticles to water (20 wt.% NaCl) to PPG (2G-110) was 1:10:2 by weight. The ratio of nanoparticles to water (20 wt.% NaCl) to PPG (2G-110) was then varied from 1:1:0 to 1:60:16 to fully-identify the domain of the possible ratios, where EPP can be formed. These mixtures with varying ratios were blended under the same operating condition. The final product was tested on the physical appearance, the ability to flow freely through a glass funnel and the mixing property with

deionized (DI) water (as discussed in the earlier section). Figure 6.5a shows the ternary plot indicating the final products obtained for the fifty different ratios. The three axes of the ternary plots correspond to the weight fractions of nanoparticles, total water, and PPG. The three weight fractions must add to one. Since PPG particles can absorb a lot of water, the amount of free water (non-absorbed) varies depending on the ratio of initial water to PPG ratio. In order to better interpret the results of the ternary plot, the amount of free water was calculated for all the fifty cases based on the experimentally-determined relation between total water to PPG ratio and free water to PPG ratio as shown in Figure 6.1. Figure 6.5b shows a second ternary plot with free water as one of the axes in place of total water. Several key observations can be deduced from these plots. Depending on the ratio, three different types of products were obtained – encapsulated PPG powder (EPP), mousse and PPG-nanoparticle mixture. Table 6.2 lists the product obtained for different ratios. These are discussed in detail in the following section.

Table 6.2: The final products for the different ratios of hydrophobic silica NP to water (20 wt.% NaCl) to PPG (Liquiblock 2G-110)

Sample #	Ratio of NP:Water:PPG	Final Product		
		Encapsulated PPG Powder (EPP)	Mousse	PPG-Nanoparticle Mixture
1	1:1:0	✓		
2	1:1:0.05	✓		
3	1:1:1			✓
4	1:1:2			✓
5	1:1:4			✓
6	1:1:8			✓
7	1:1:16			✓
8	1:4:0	✓		
9	1:4:0.05	✓		
10	1:4:2	✓		

Table 6.2, cont.

11	1:4:4			✓
12	1:4:8			✓
13	1:4:16			✓
14	1:10:0	✓		
15	1:10:0.05	✓		
16	1:10:1	✓		
17	1:10:2	✓		
18	1:10:4			✓
19	1:10:8			✓
20	1:10:16			✓
21	1:20:0	✓		
22	1:20:0.05	✓		
23	1:20:2	✓		
24	1:20:4	✓		
25	1:20:8			✓
26	1:20:16			✓
27	1:30:0	✓		
28	1:30:0.05	✓		
29	1:30:2		✓	
30	1:30:4	✓		
31	1:30:8			✓
32	1:30:16			✓
33	1:40:0	✓		
34	1:40:0.05	✓		
35	1:40:2		✓	
36	1:40:4		✓	
37	1:40:8	✓		
38	1:40:16			✓
39	1:50:0	✓		
40	1:50:0.05	✓		
41	1:50:2		✓	
42	1:50:4		✓	
43	1:50:8		✓	
44	1:50:16			✓

Table 6.2, cont.

45	1:60:0	✓		
46	1:60:0.05	✓		
47	1:60:2		✓	
48	1:60:4		✓	
49	1:60:8		✓	
50	1:60:16		✓	

6.3.1.2 Encapsulated PPG Powder (EPP) Formation

As mentioned earlier, the physical appearance of EPP was a dry powder which flows freely through a glass funnel. Figure 6.5a shows this product for the case of ratio = 1:10:2. In order to map the regime where EPP could be obtained, the amount of water and PPG were sequentially increased. Figure 6.6a shows the results in the ternary plot. Several key observations can be made from the plot. The range of total water to PPG (TW/PPG) varied from 2 to infinity. The value infinity corresponds to the cases with no PPG (or negligible PPG) such as the ratio of 1:60:0. The case with the maximum PPG/water ratio = 0.5 was 1:4:2 which corresponds to the case with the maximum amount of PPG that can be encapsulated for a fixed amount of silica nanoparticles. The range of free water to PPG ratio (FW/PPG) varies from 0 to infinity. (Note that for the case with no PPG particles, total water is equal to free water). It shows that for successful formation of EPP, the presence of mobile, free water is not required. However, in these cases, the PPG particles still have thin liquid films (as verified by CLSM) which assist in the formation of EPP.

163
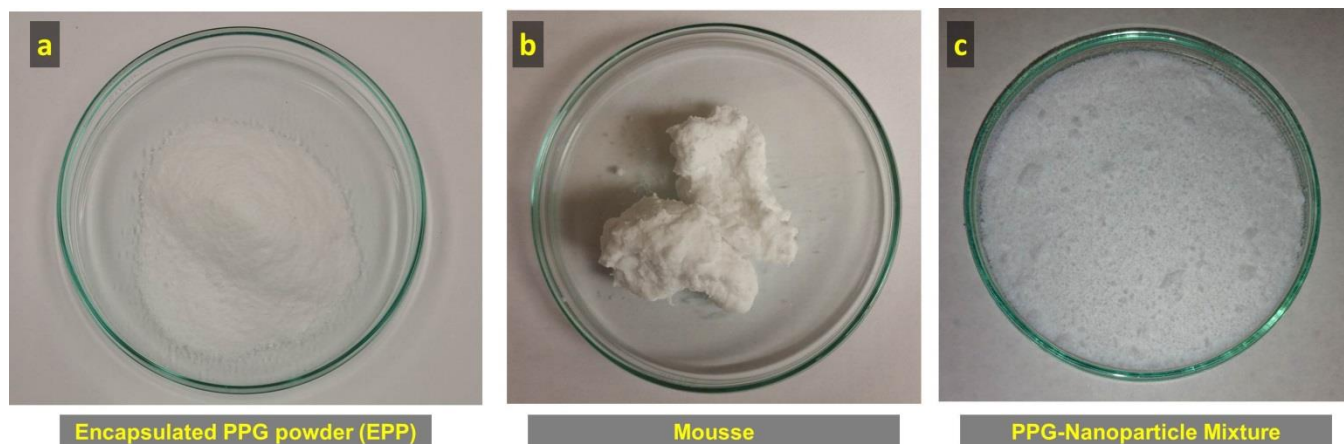
Figure 6.5: Examples of the three types of products obtained for different ratio of NP:
Water: PPG (2G-110) (a) encapsulated PPG powder (Ratio=1:10:2), (b)
Mousse (Ratio= 1:40:4), (c) PPG-Nanoparticle mixture (Ratio= 1:1:1)

6.3.1.3 Mousse Formation

A homogeneous mousse (similar to a shaving cream) was obtained for certain ratios. Figure 6.5b shows the physical appearance of the final product for one of those ratios (1:40:4). It is to be noted that when no PPG particles were present in the system and the ratio of water to nanoparticles was sequentially increased from 1:1 to 80:1, no mousse formation was obtained for any case. Water-in-air powders were obtained for 1:1 to 60:1 and for higher ratios (70:1, 80:1) two separate phases of nanoparticle and water were obtained. Mousse formation was only observed when there were PPG particles in the system. It shows that presence of PPG influences the formation of mousse. Interestingly, the mousse was only seen when the ratio of water to silica nanoparticle was ≥ 30 as shown in Figure 6.6a. The range of total water to PPG ratio (TW/PPG), where mousse formation was obtained, was 3.75 to 30. The range of free water to PPG ratio (FW/PPG) was 0 to 16.25. Another interesting observation, in this case, was that transitional inversion from mousse to water-in-air powder was obtained by increasing the amount of

164

PPG in the system while keeping the ratio of the nanoparticle to water constant. For example: for the samples with fixed nanoparticles to PPG ratios of 1:2, mousse formation was seen for the ratio of water to nanoparticles $\geq$ 30, e.g., samples corresponding to 1:30:2 and 1:40:2 ratios (Table 6.2). To obtain water-in-air powder, the amount of PPG was needed to be increased which reduced the amount of free water in the system. For example, the water-in-air powder was obtained for 1:30:4 and 1:40:8. This transitional inversion from mousse to dry-water seems to be a complex interplay of the amount of free water, ratios of NP: water: PPG. Understanding this mechanism of phase inversion is quite complex and deserves further investigations in future.

6.3.1.4 PPG-Nanoparticle Mixture Formation

The physical appearance of this product was dry powder, and it looks quite similar to EPP. One of the examples of this case is just the mixture of PPG and nanoparticles with no water or negligible water (Example: Ratio = 1:0:1). The final product in these cases is expected to be dry because of the presence of no or minimal water. Figure 6.5c shows the physical appearance of the final product for one of those ratios (1:1:1). However, in this case, PPG particles are not encapsulated by silica nanoparticles but rather form a homogenous mixture of PPG-nanoparticles. Such product does not flow freely through glass funnel. To further differentiate this product with EPP, a small amount of the sample was mixed with excess deionized water. It resulted in instant swelling of PPG particles as they were not encapsulated. The range of total water to PPG ratio (TW/PPG) for this product was found to be small and between 0.0625-4 which shows that this product was typically formed when the amount of PPG is high in the system as can be seen in the ternary plot (Figure 6.6a). Moreover, the amount of free water for all the cases for this product was zero. Figure 6.6b shows that how all the scattered points corresponding to this

PPG-Nanoparticle mixture in the ternary plot (left) with total water converge to x-axis corresponding to zero free water.
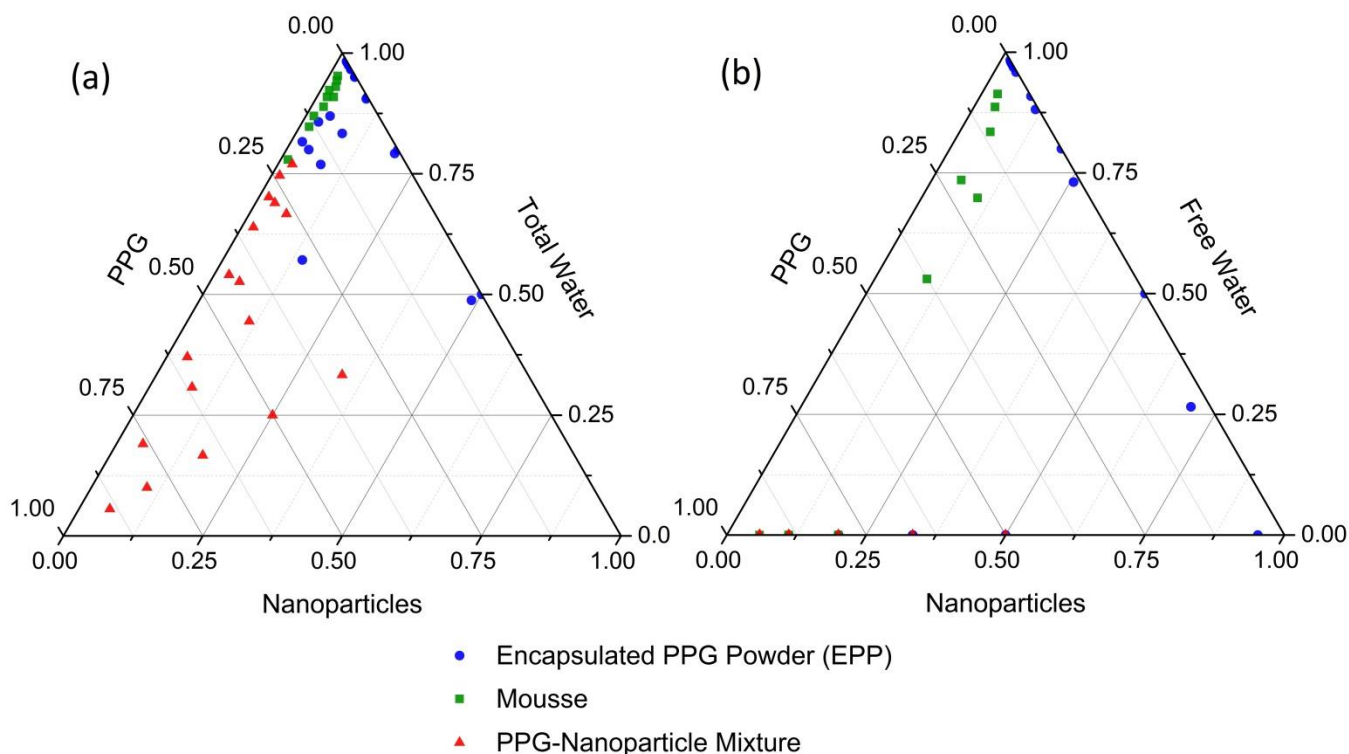
Figure 6.6: Ternary plot with three axes corresponding to weight fractions of silica nanoparticles, water (20 wt.% NaCl) and PPG (2G-110) indicating the final product formed after blending the mixtures under the same operating conditions (a: water axis corresponds to total water; b: water axis corresponds to free water)

6.3.1.5 Encapsulation of Nano-Particles (Fl-NP)

The encapsulation of particles via water-in-air powder offers a robust technique to encapsulate hydrophilic particles of different sizes ranging from microns to nanometers. In this section, encapsulation of hydrophilic nanoparticles was discussed to demonstrate this

166

concept. Fluorescently-tagged silica nanoparticles (FL-NP) of diameter 10 nm were used in this case. These nanoparticles show green fluorescence in the presence of UV light (Figure 6.7b). First, 2.5 gm of hydrophobic silica nanoparticles (Figure 6.7a) and 25 gm of 0.5 wt.% FL-NP solution was taken in a blending cup. This mixture with nanoparticles to FL-NP solution ratio of 1:10 (by weight) was blended at 16,000 rpm for 1 minute. The product resulted in a dry, white powder (Encapsulated FL-NP Powder, EFP) that flows freely through a glass funnel (Figure 6.7c). This EFP was then visualized under UV-light (Figure 6.7d). No green fluorescence was observed indicating complete encapsulation of Fl-NP particles. Figure 6.7 a,b shows the SEM images of the EFP. Figure 6.7 c, d shows the optical and confocal micrographs. No hydrophilic dye was needed to tag the aqueous phase as the FL-NPs were already fluorescent. The particle size was calculated to be 27 ± 12 microns by analyzing at least 200 particles. Note that the particle size, in this case, was smaller than the encapsulated PPG powder case (39 ± 25 microns). However, these results should not be compared quantitatively. Since the particle size of water-in-air powders is strongly governed by mixing conditions and relies on high-speed blades generating fine water droplets. For the case of EPP formation, there is an added complexity in the system due to the presence of PPG particles. The high-speed blades also cut the PPG particles to finer sizes along with generating fine water droplets (if free water is present). Thus, mixing conditions of both cases are quite different, and it is difficult to compare these two cases.

167
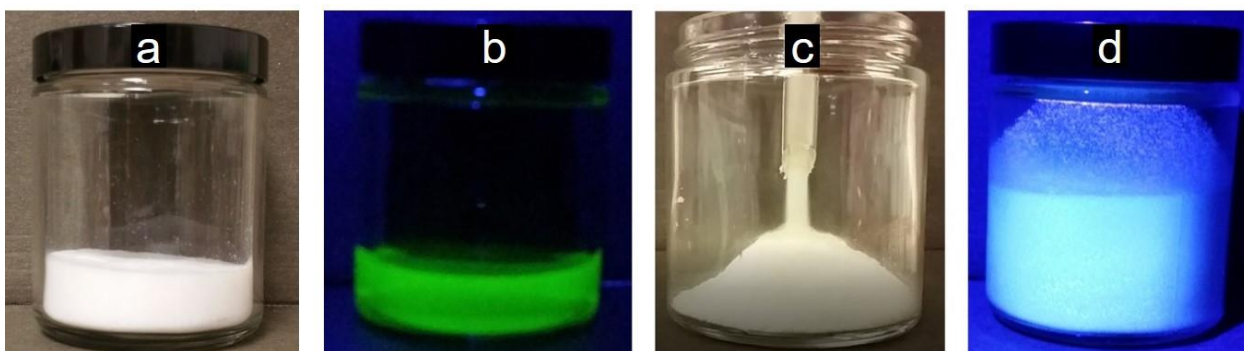
Figure 6.7: (a) Hydrophobic silica nanoparticles (2.5 gm); (b) Fluorescent silica nanoparticle (FL-NP) solution under UV light (25 gm); (c) Encapsulated FL-NP Powder (EFP) flowing freely through glass funnel; (d) EFP under UV light
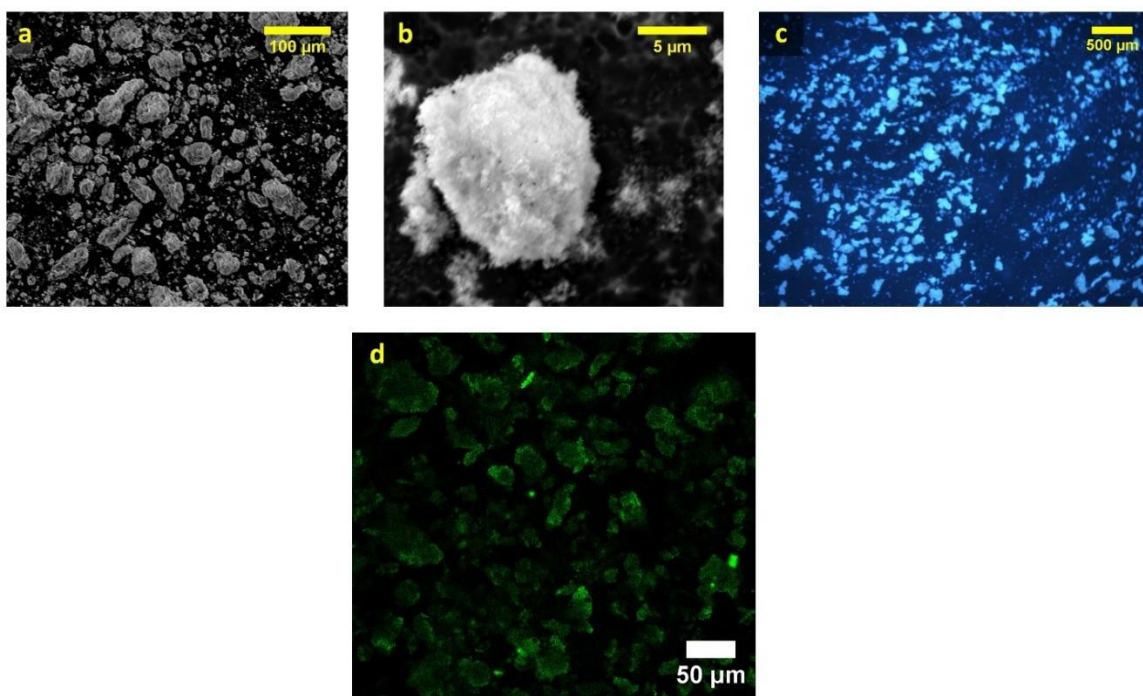
Figure 6.8. SEM image of EFP (Scale Bar: 100 μm); (b) SEM image of EFP (Scale Bar: 5 μm); (c) Optical micrograph of EFP (Scale Bar: 500 μm; (d) Confocal micrograph of EFP (Scale Bar: 50 μm)

To verify the complete encapsulation of the FL-NP, 0.4 gm of the EFP was mixed with 19.6 gm of deionized water in a glass vial. The sample was vigorously hand shaken for 1 minute and then placed on LabQuake® shaker (Barnstead Thermolyne) at room temperature for agitation for 24 hr. Figure 6.9a shows the sample under visible light, and Figure 6.9b shows the same sample under the UV light. No green fluorescence was observed in the bulk aqueous phase indicating total encapsulation of the Fl-NPs. Note that even if the EFP was completely mixed with water, it is expected that there would be thin air-film surrounding the powder. This air film would have a preferential affinity to the highly hydrophobic nanoparticles as compared to the external (hydrophilic) aqueous phase making it stable. So, the EFP should be considered as water-in-air powders rather than water-in-water emulsions. The presence of air film also increases the powder stability and delays the interaction with the external aqueous phase. A small amount of sample (1 mL) was taken from the bulk and was analyzed using UV-spectroscopy. No peak corresponding to the Fl-NP was observed confirming complete encapsulation of Fl-NP. Then, 2.5 gm of ethanol was added to the sample and was mixed vigorously to break the encapsulation. Figure 6.9c shows the sample under visible light, and Figure 6.9d shows under the fluorescent light. The green fluorescence observed under UV-light indicates release of FL-NP in the bulk solution.

In the aforementioned case, the ratio of hydrophobic silica nanoparticles to the FL-NP solution was 1:10 by weight. This ratio was then varied from 1:1 to 1:80 using two different concentration (0.5 wt.% and 1 wt.%) of FL-NP in the aqueous phase. The results are compared with the case with no FL-NP (deionized water). Figure 6.10 shows the final product obtained for the different ratios of the aqueous phase to silica nanoparticles.
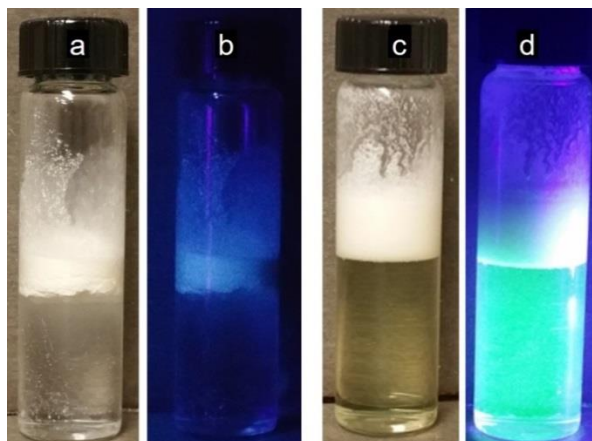
Figure 6.9: Encapsulated FL-NP powder in water (a) under visible light (b) under UV light, (c) after adding ethanol under visible light and (d) after adding ethanol under UV light
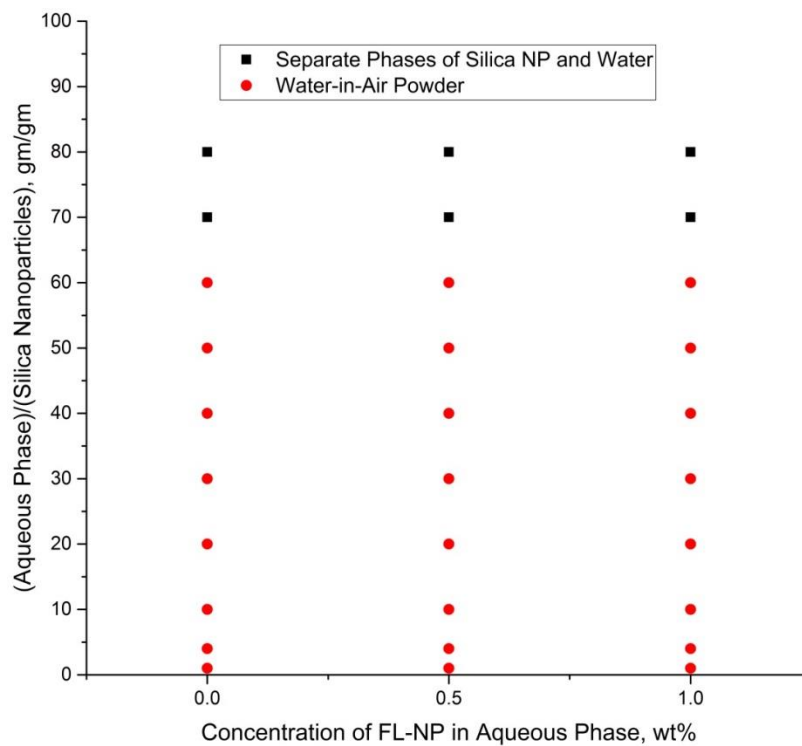
Figure 6.10: The final products for the different ratios of aqueous phase to silica nanoparticles for different concentration of FL-NP in aqueous phase

Water-in-air powders were obtained for all cases for aqueous phase/silica nanoparticles ratio ≤ 60, irrespective of the FL-NP concentrations. This shows that the presence of hydrophilic nanoparticles in the aqueous phase does not affect the water-in-air powder formation. For the higher ratios such as 1:70, a small amount of powder was formed which floated on top of the FL-NP solution indicating that only small portion of the aqueous solution was encapsulated. Interestingly, no mousse formation was observed in these cases, in contrast with the PPG encapsulation cases.

6.3.2 Temperature-Tolerance of the Encapsulation

The studies described in the last few sections were conducted at 25 ºC. The encapsulated PPG particles can be used in conformance control in oil fields. The application includes blocking high permeability channels, fractures, and thief zones in oil reservoirs to prevent channeling of injection fluids. Since most of these reservoirs are at temperatures higher than 25 ºC; it becomes vital to study the effect of high temperature on the degree of encapsulation. To study this, custom-designed borosilicate glass vessels were built which can be sealed using Teflon-threaded caps. The chemical-resistant O-rings provided a leak-proof system at high temperatures. Then, mixtures of EPP (obtained with a ratio of nanoparticles: water (20 wt.% NaCl): PPG (2G-110) = 1: 10: 2) and deionized water (1:49) (in these vessels) were placed in an oven operating at 80 ºC or 125 ºC. These samples were periodically centrifuged to measure any release of PPG (2G-110) particles. Even after one month, no PPG particles were released at both the temperatures. This shows that the encapsulation of the micro-particles is robust even at higher temperatures. This makes the proposed encapsulation technique lucrative for several applications in

subsurface oil field applications such as conformance control, delayed acid stimulation, etc.

6.3.3 Stimuli-Responsive Release

In an air-water-particle system, the wettability of the particle governs the stability and curvature of the powder. In the present case, highly hydrophobic nanoparticles ($\theta >$ 90°) stabilizes the water-in-air powder to encapsulate the hydrophilic particles. Surface-wettability alteration toward water-wetness ($\theta < 90°$) via external stimuli could weaken the powder and could result in transitional phase inversion from water-in-air powder to air-in-water foam. Such inversion will release the particles allowing them to interact with the external phase. In the present work, change in pH and addition of surfactant as external stimuli were focused to trigger the release of particles.

In the literature, there have been studies which focused on the effect of these stimuli during the water-in-air powder preparation (Binks et al., 2010, 2007). Binks et al. (2010) reported that by mixing highly hydrophobic silica nanoparticles, air and water with a surfactant (sodium dodecyl sulfate, SDS) under high shear rate, water-in-air powder was obtained for lower surfactant concentration while air-in-water foam was obtained for higher surfactant concentration. The ratio of nanoparticles (HDK-H18, Wacker-Chemie) to water (containing varying amounts of surfactant) was kept constant and equal to 1:25 in their study. They demonstrated that surfactant tends to adsorb on the silica nanoparticles and makes it hydrophilic which result in transitional inversion. In another study (Binks et al., 2007), they investigated the effect of pH on a similar phase inversion from a water-in-air powder to an air-in-water foam. The ratio of nanoparticles (HDK-H18, Wacker-Chemie) to water (of varying pH) was kept constant and equal to 1:50 in their study. They reported the formation of water-in-powder for a pH range of 6-9. For pH range 10.0-10.8,

they obtain a sticky, souffle´-like material and for pH ≥ 11, they obtain an air-in-water foam. They showed that an increase in pH increases the hydrophilicity of the nanoparticles which result in the transitional phase inversion. Such study of the effect of stimuli during water-in-air powder formation could provide interesting insight into the expected effect of these stimuli post-powder formation. Thus, in the present work, first the effect of pH and presence of surfactant on powder formation was studied in the absence of any PPG particles.

In the first case, the ratio of hydrophobic silica nanoparticles to aqueous phase was fixed to 1:10 by weight. The aqueous phase with varying pH (2 to 12) or different surfactant concentration, C_{surf} (0.01 wt.% to 1 wt %) was blended with nanoparticles at 16,000 rpm for 1 minute. It resulted in the formation of water-in-air powder for all the runs irrespective of the pH and the presence of surfactant as shown in Figure 6.11a and 6.11b, respectively. No transitional inversion was seen in this case as observed by Binks and coworkers (Binks et al., 2010, 2007). However, the ratio of nanoparticles to aqueous phase used in this case (1:10) was lower than their work (1:50 for pH study (Binks et al., 2007) and 1:25 for surfactant study (Binks et al., 2010)).

In the second case, the ratio of hydrophobic silica nanoparticles to aqueous phase was changed to 1:50 by weight and the experiment was repeated. The final products (images taken after t= 60 min of product formation) are shown in Figure 6.11c and 6.12d. For 2 ≥ pH ≥ 7, the water-in-air powder was formed which flows freely through a glass funnel. For pH≥ 10, a sticky, mousse-like material was formed which does not flow through glass funnel. Similarly, for the C_{surf} ≤ 0.1 wt.%, the water-in-air powder was obtained, and for C_{surf} ≥ 0.2 wt.%, a mousse-like material was formed. For C_{surf}= 1 wt.%, the mousse slowly separates with time, resulting in a bottom aqueous phase as shown in Figure 6.11d (image taken at t=60 min). These observations are in line with the literature

173

and show that a change in pH (close to 12) or presence of surfactant (close to 0.2 wt %) could result in transitional inversion. Since this effect was only observed for the case of a lower nanoparticles to aqueous phase ratio (1:50) and not at a higher ratio (1:10), it shows that in order to alter the surface-wettability of nanoparticles, a critical amount of aqueous phase (high pH or high surfactant concentration) is required for a fixed amount of nanoparticles.

In the subsequent sections, the effect of these stimuli on pre-formed water-in-air powders will be focused. The powders will be mixed with an excess of aqueous phase (of varying pH or surfactant concentration) on a shaker. It is interesting to note that the interaction of these stimuli, when applied after the powder formation, is different from that applied during the powder formation. There are two main differences in these two scenarios. First, when the stimulus is applied during the powder formation, the experiment is performed under high shear conditions in a blender as opposed to mixing at a low shear on a shaker. The mixing of hydrophobic silica nanoparticle (non-dispersible in water) and aqueous phase under high shear results in effective contact between the two as compared to mixing under low shear. Such effective mixing could expedite the surface-contact between the stimuli and nanoparticles. Also, since the presence of high shear and presence of excess air are the critical requirements for water-in-air powder formation, the regeneration of the powder is not possible (from any free silica nanoparticles in the system) when stimuli are applied under low shear and limited air. Second, when the stimuli are applied after the powder formation, its interaction with the pre-formed water-in-air powder is expected to be much more complex than the interaction with silica nanoparticles aggregates. Also, when water-in-air powders are mixed with external liquid under low shear rate, it is expected that there will be a small layer of air surrounding the powders even when it is fully immersed in the liquid system. The presence of this thin air

film will increase the stability of these powders and delays the interaction of silica nanoparticles with the liquid. Therefore, even in the immersed state, the powders should be considered as water-in-air powders rather than water-in-water emulsions.
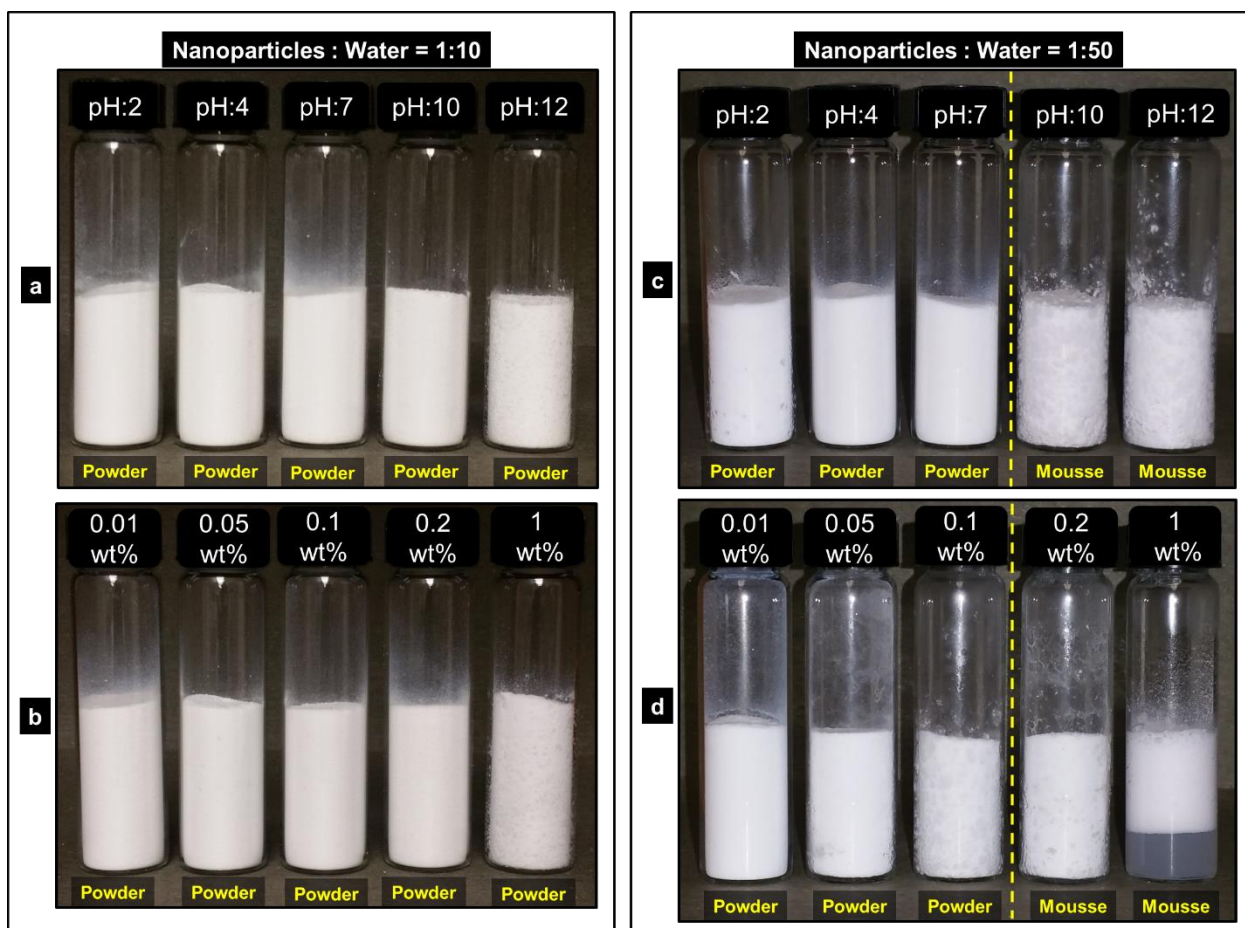
Figure 6.11: Final product obtained for (a) varying pH from 2 to 12 with nanoparticles: water ratio = 1:10; (b) varying surfactant concentration from 0.01 wt.% to 1 wt.% with nanoparticles: water ratio = 1:10; (c) varying pH from 2 to 12 with nanoparticles: water ratio = 1:50; (d) varying surfactant concentration from 0.01 wt.% to 1 wt.% with nanoparticles: water ratio = 1:50

6.3.3.1 pH-Triggered Release

Encapsulated PPG Powder, EPP obtained with a ratio of nanoparticles: water (20 wt.% NaCl): PPG (2G-110) = 1: 10: 2 was used in this experiment. This EPP was mixed with water of varying pH in the ratio of 1:49 by weight in 50-mL graduated centrifuge tubes. The pH of the deionized water was changed to 2, 4, 7, 10 and 12 by adjusting the concentration by 0.1M hydrochloric acid (HCl) and 0.1M sodium hydroxide (NaOH). The tubes were capped, placed horizontally on a LabQuake® and were agitated at 25 ºC. The samples were periodically centrifuged at 3000 rpm for 2 min to measure the amount of precipitated PPG. After centrifugation, the tubes were again mixed vigorously and were placed on the shaker.

Figure 6.12 shows the percentage release of PPG (2G-110) particles as a function of time. The reproducibility of the result was within ± 4%. The percentage release which is the ratio of the volume of precipitated, swollen PPG to the volume of fully-swollen PPG (as determined in Table 6.1) was calculated for different times. It is to be noted that swelling time of the non-encapsulated PPG particles used in the present study was only 3 seconds; hence the delayed swelling is due to delayed breaking of the encapsulation. The time required for 10% of the particles to be released (t_{10}) was 0.125, 214.6, 341.7, 355.2, and 420.5 hr corresponding to the pH of 12, 10, 7, 4, and 2. As pH increased, the EPP released the PPG faster.
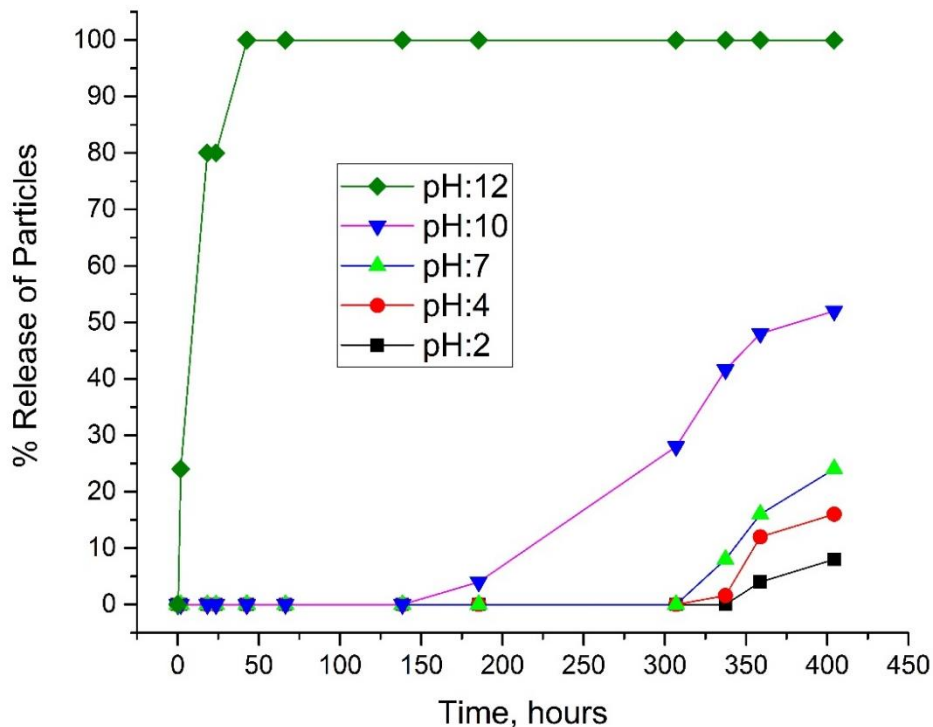
Figure 6.12: The percentage release of PPG (2G-110) particles as a function of time with an external aqueous phase of different pH

6.3.3.2 Surfactant-Triggered Release

Encapsulated PPG Powder, EPP obtained with a ratio of nanoparticles: water (20 wt.% NaCl): PPG (2G-110) = 1: 10: 2 was also used here. The EPP was mixed with deionized water with varying Amphoam surfactant concentration in the ratio of 1:49 by weight in 50-mL graduated centrifuge tubes. Samples were agitated at room temperature and periodically centrifuged to measure particle release. Figure 6.13 shows the percentage release of particles as a function of time (log-scale). For higher surfactant concentrations (e.g., 1 wt.%), the release of particles was faster as compared to lower surfactant concentrations (0.01 wt.%). The time required for 10% of the particles to be released (t_{10})

177

decreases sharply with increase in surfactant concentration. The value of t_{10} was 3 min, 5 min, 33 min, 56 min, and 600 min for 1wt.%, 0.2 wt.%, 0.1 wt.%, 0.05 wt.%, and 0.01 wt.%, respectively.
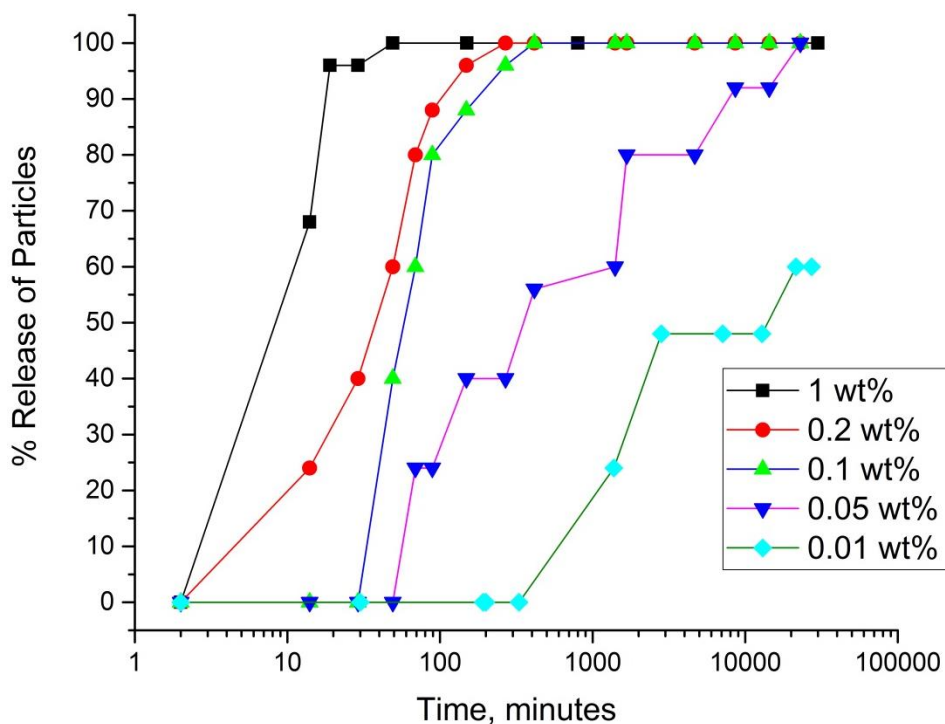
Figure 6.13: The percentage release of PPG (2G-110) particles as a function of time with external aqueous phase of varying surfactant concentration

Mechanisms of Particle Release

In the previous section, it was shown that the stimuli (such as higher pH or higher surfactant concentration), when applied during the water-in-air powder formation (as opposed to applied after powder formation), could lead to transitional inversion from water-in-air powder to mousse formation because of increased hydrophilicity of the silica nanoparticles. Similarly, it was observed that the release of PPG (2G-110) particles from

178

the encapsulated PPG powder (EPP) could be triggered depending on the pH and presence of surfactant in the external aqueous phase. The release of particles was faster for higher pH (such as pH = 12) and higher surfactant concentration (such as 1 wt.%). The increased hydrophilicity of silica nanoparticles under different stimuli assist in the weakening of the encapsulation and, finally, the release of particles. However, given the differences between the two scenarios of stimuli applied during and after the water-in-air powder formation (as discussed earlier), a direct comparison of mechanisms involved in these two scenarios is difficult. The presence of PPG particles in EPP further adds to the complexity of particle release. To decouple this effect of PPG particles and understand the effect of stimuli applied after powder formation, release-experiments without PPG particles were conducted. First, water-in-air powders were formed using a ratio of silica nanoparticles to water (20 wt.% NaCl) of 1:10. Note that all the water present in this system is free water (non-absorbed) as compared to the EPP case where there was no free water. A similar procedure (as used in the release study of EPP) was then used to investigate the effect of different stimuli. In contrast to measuring the release of PPG particles, the amount of sodium ions released into the external aqueous phase was measured using Ion-Chromatography (IC) as a function of time in these cases. To better understand the effect of different stimuli on surface-wettability of silica nanoparticles, contact angle experiments were performed. The results are discussed in the subsequent sections.

Figure 6.14 shows percentage release of sodium chloride (NaCl) as a function of time for varying pH of external aqueous phase. The time taken to release 10%, t_{10} of sodium/chloride ions was found to be 16.2 min, 220.5 min, 207.8 min, 219.1 min, 268.2 min corresponding to the pH of 12, 10, 7, 4, and 2. The release of sodium ions was faster for the case of pH = 12 compared to other pH cases. As compared to PPG release data with varying pH, the release was faster for all these cases. However, in both cases, the

release was faster at pH = 12. The two key differences in these cases were the different amount of free water and the presence of PPG particles in the system. Future studies of the release of particles with a varying ratio of PPG in the EPP could shed more light on the underlying mechanisms and effect of PPG particles on the release of particles.
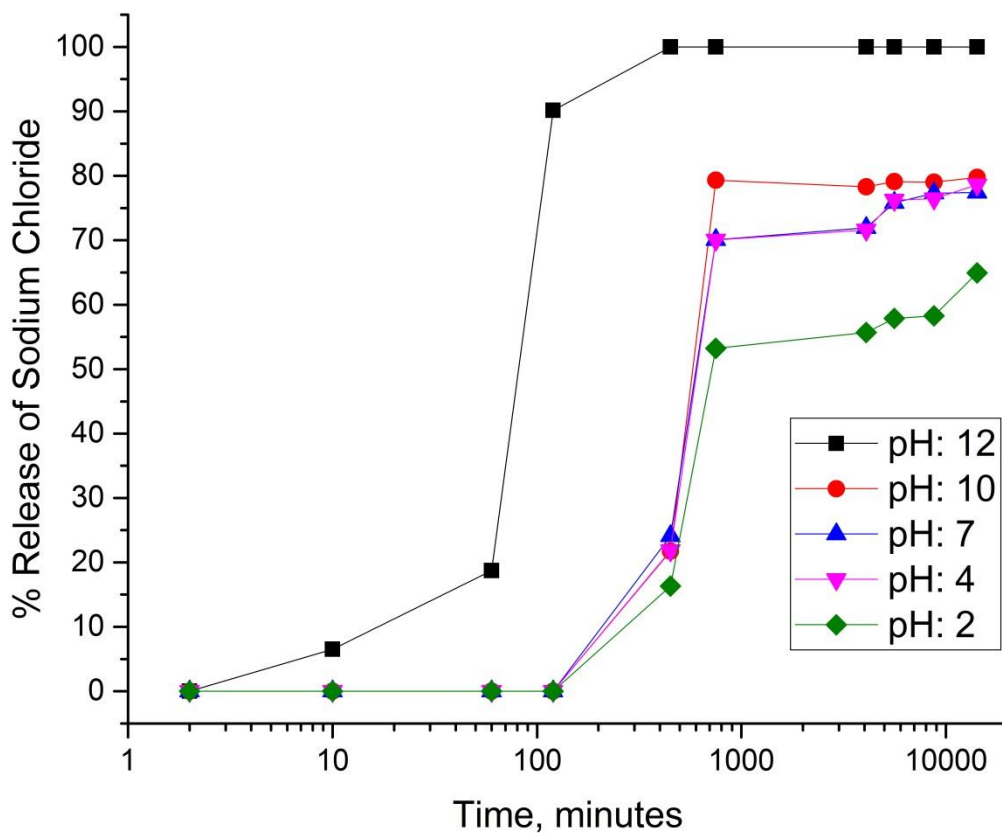
Figure 6.14: The percentage release of sodium chloride as a function of time with an external aqueous phase of different pH

To investigate the effect of different pH medium on the hydrophobicity of silica nanoparticles, contact angle experiments were performed. The silica nanoparticles used in

180

the present study are highly hydrophobic in nature. However, measuring the contact angle on these nanoparticles directly is quite complex. Contact angle measurement of a small water droplet (10 µL) on compressed nanoparticles (Aerosil R202) tablet via sessile-drop method yielded a contact angle of $143.3° ± 1.4°$. However, this method is not very accurate and typically overpredicts the contact angle owing to the high surface roughness obtained after powder compaction. Forny et al. (2010) performed a detailed study on the effect of solid/liquid contact angles of silica nanoparticles on the dry water formation. They measured the contact angles using a liquid intrusion method. They reported a contact angle of 118° for the Aerosil R812S/water system. Since the Aerosil R202 used in the present study is more hydrophobic than the Aerosil R812S (Forny et al., 2009), the contact angle is expected to be higher than 118°. Binks et al. (2007) reported a simplified, indirect method to investigate the particle wettability using hydrophobized glass slides. In this work, a similar approach was adopted. Surface-modified glass slides (which were rendered hydrophobic in a similar way as the nanoparticles) were used as a proxy to the silica nanoparticles. The advancing contact angle of deionized water on the original glass slide was 29°; it changed to 103° after the surface treatment of the glass slide indicating the surface-hydrophobization due to silanization. If a single particle is brought into contact with a liquid slowly, the advancing contact angle controls the wetting. In the process studied here, vigorous mixing is conducted, and the role of advancing contact angle would only be qualitative.

First, the effect of pH on surface hydrophobicity of the hydrophobic glass slides was investigated. A small aqueous droplet (10 µL) with varying pH (2, 4, 7, 10, and 12) was placed on the surface-hydrophobized glass slide, and the advancing contact angle was measured. Each measurement was performed three times at different locations on the

slides, and the average value is reported. Figure 6:16 shows the plot of advancing contact angle as a function of pH at the time, t= 0. The contact angle decreases slightly from 107.4 $^o \pm 1.4$ for pH = 2 to 99 $^o \pm 1.5$ for pH = 12 indicating a slight change in wettability towards water-wetness. A hydrophobized glass slide was then cut into 5 pieces which were individually immersed in different pH solutions for 24 hrs and advancing contact angle were measured again. Figure 6:16 shows the plot of contact angle versus pH of the solution at the time, t=24 hrs. All the contact angle shows decrement as compared to the angle measured at the time, t=0. The angle decreases from 95.2 $^o \pm 4$ for pH=2 to 76.6 $^o \pm 1$ for pH=12 indicating wettability alteration of slides from air-wet to water-wet at a high pH near 12. The time-dependence on contact angle could be because the hydroxyl group on the silica glass surface may not be easily accessible because of shielding by large silane functional groups. However, once the surface is in contact with water for a longer duration, it allows it to ionize to a different degree depending on the pH (Binks et al., 2007). These results are in agreement with the results of delayed release of particles and ions triggered by different pH. Figure 6:16 shows the t_{10} (secondary axis) for the different pH. It can be seen that for pH of 12, the particles and ions were released very quickly because of surface-modification of hydrophobic silica nanoparticles. The t_{10} almost remains constant for pH<10 and then decreases for external fluid pH of 12, following the trend of hydrophilicity.
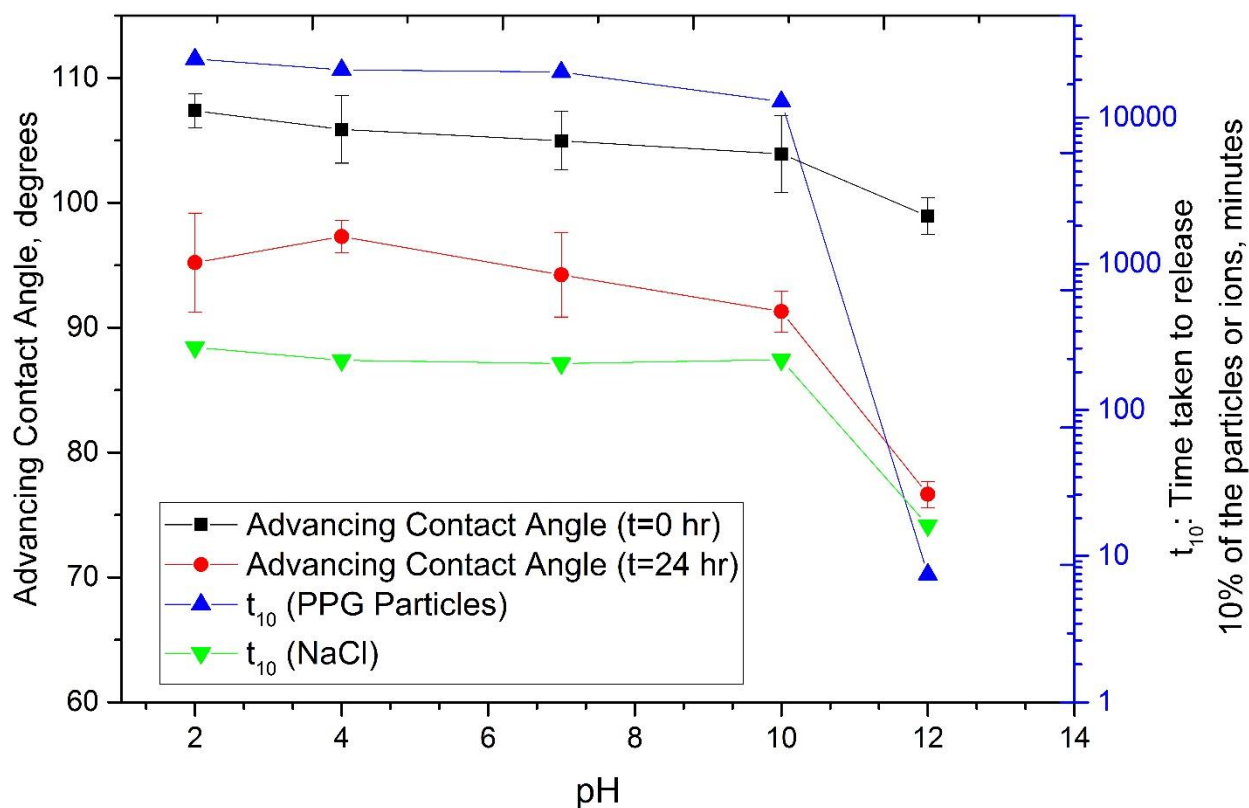
Figure 6.15: Advancing contact angle of the water droplet with varying pH on a hydrophobic glass slide for time, t = 0 and t = 24 hrs; t_{10}: time taken to release 10% of particles (2G-110) or ions for different pH cases (secondary y-axis)

To understand the mechanism of surfactant-triggered release, release-experiments using water-in-air powders without particles were performed. Figure 6.16 shows percentage release of sodium chloride (NaCl) as a function of time for varying surfactant concentration in the external aqueous phase. As observed in the EPP case, the release was faster for high surfactant concentration such as 1wt % and 0.2 wt%. The time required for 10% of the ions to be released (t_{10}) decreases with increase in surfactant concentration. The value of t_{10} was 2.3 min, 2.7 min, 5 min, 16 min, and 101 min for 1wt%, 0.2 wt%, 0.1 wt%, 0.05 wt%, and 0.01 wt%, respectively. This shows that presence of surfactant in the external aqueous phase slowly breaks the encapsulation releasing any encapsulated

183

particles or ions from water-in-air powders. Then, contact angle experiments were performed to understand the effect of surfactant concentration on surface-wettability of the hydrophobic silica surface. A small aqueous droplet (10 µL) with varying Amphoam surfactant concentration was placed on the glass slide, and the advancing (water-air) contact angle was measured. Figure 6.17 shows the advancing contact angles on the hydrophobic glass slide as a function of Amphoam concentration. Each measurement was performed three times at different locations on the slides, and the average value is reported. For lower surfactant concentrations (0 to 0.03125 wt %), the contact angle was greater than 90º indicating hydrophobic wettability of the silanized silica surface. For higher surfactant concentration, the contact angle decreased, and for concentration greater than 1 wt%, the angle was close to 38º. Hydrophobic silica nanoparticles are a critical requirement for formation and stability of water-in-air powders. The addition of surfactant solution makes the silica surface increasingly hydrophilic which causes them to break. These contact angle results are in agreement with the observed release of PPG particles and sodium ions. Figure 6.17 shows the plot of t_{10} (secondary axis) vs. surfactant concentration. The time required for 10% of the particles or ions to be released, t_{10} decreases sharply for higher surfactant concentration which corresponds to a lower contact angle (hydrophilic).
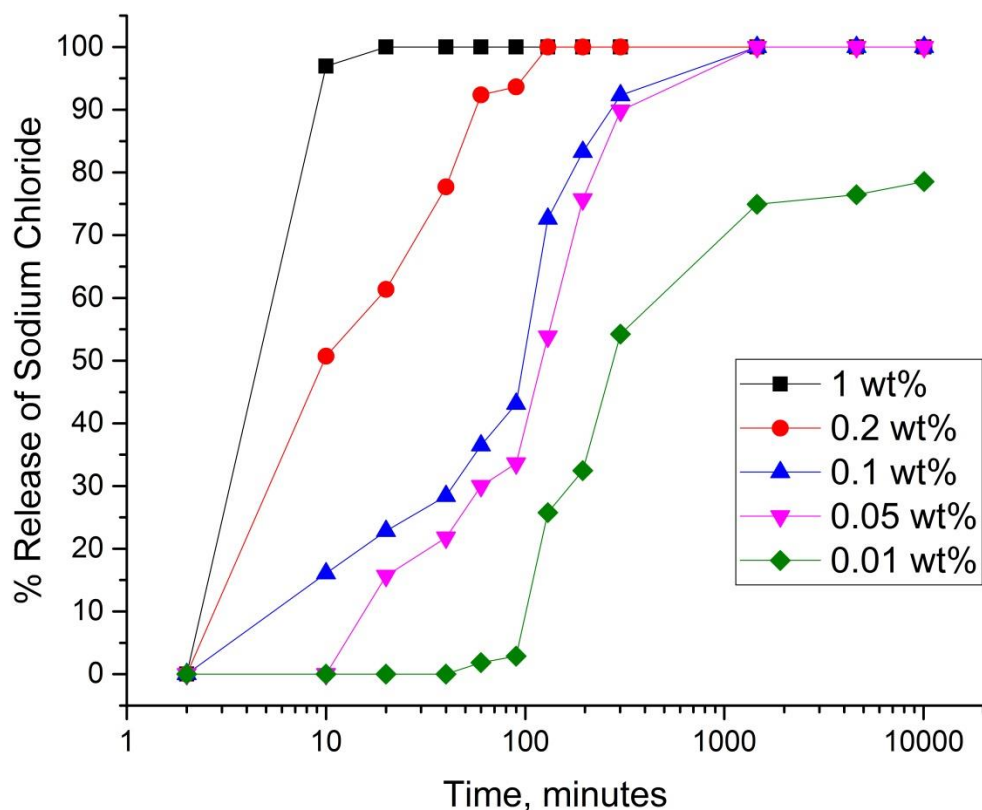
Figure 6.16: The percentage release of sodium chloride as a function of time with external aqueous phase of varying surfactant concentration

Table 6.3 shows the particle size distribution of the hydrophobic nanoparticles in aqueous solutions with varying Amphoam surfactant concentration. In the absence of any surfactant, only a small fraction of nanoparticles was dispersible in the water. The measured particle diameter using DLS technique, in this case, was 63 ± 12 nm. As the surfactant concentration increases, the diameter increases from 63 nm to 1073 nm (Table 6.3). It is to be noted that DLS analysis of pure surfactant solutions (without any particles) was not able to measure any micellar particles indicating the micelle size of Amphoam surfactant solutions to be less than 5 nm. It is to be noted that using DLS technique, we get the 'hydrodynamic' diameter and not the actual particle core-diameter. Typically, the DLS

values are higher than actual core-diameter values as DLS technique is biased towards bigger particles in the solution(Cumberland and Lead, 2009b). Surfactants are typically used as a dispersing agent for nanoparticles in the aqueous solution (Singh et al., 2015; Tigges et al., 2010). Depending on the initial particle wettability, the surfactant molecules can attach themselves (either head- or tail-on) and can render the particles either more hydrophobic or hydrophilic. In the present case, it was observed that as the surfactant concentration was increased, the nanoparticles became increasingly dispersible. Thus, the physical adsorption of Amphoam surfactant molecules on the initially hydrophobic nanoparticles altered the particle surface toward water-wet. Although the particles become more dispersible in water, counterintuitively, the particle size continuously grew with an increase in surfactant concentration. This increase in size is due to formation of three-dimensional network of particles formed by fractal-like aggregates held together by van der Waals forces, which is a typical property of hydrophobic fumed silica (Binks et al., 2010; "Wacker HDK® Pyrogenic Silica Brochure, Wacker-Chemie GmbH, Germany, 2016.," n.d.). Binks et al. (2010) reported the DLS data of a mixture of highly hydrophobic silica nanoparticles and SDS surfactant (CMC = 8mM) as a function of surfactant concentration. They also observed an increase in dispersibility of nanoparticles along with an increase in particle sizes (even above CMC) with an increase in surfactant concentration.
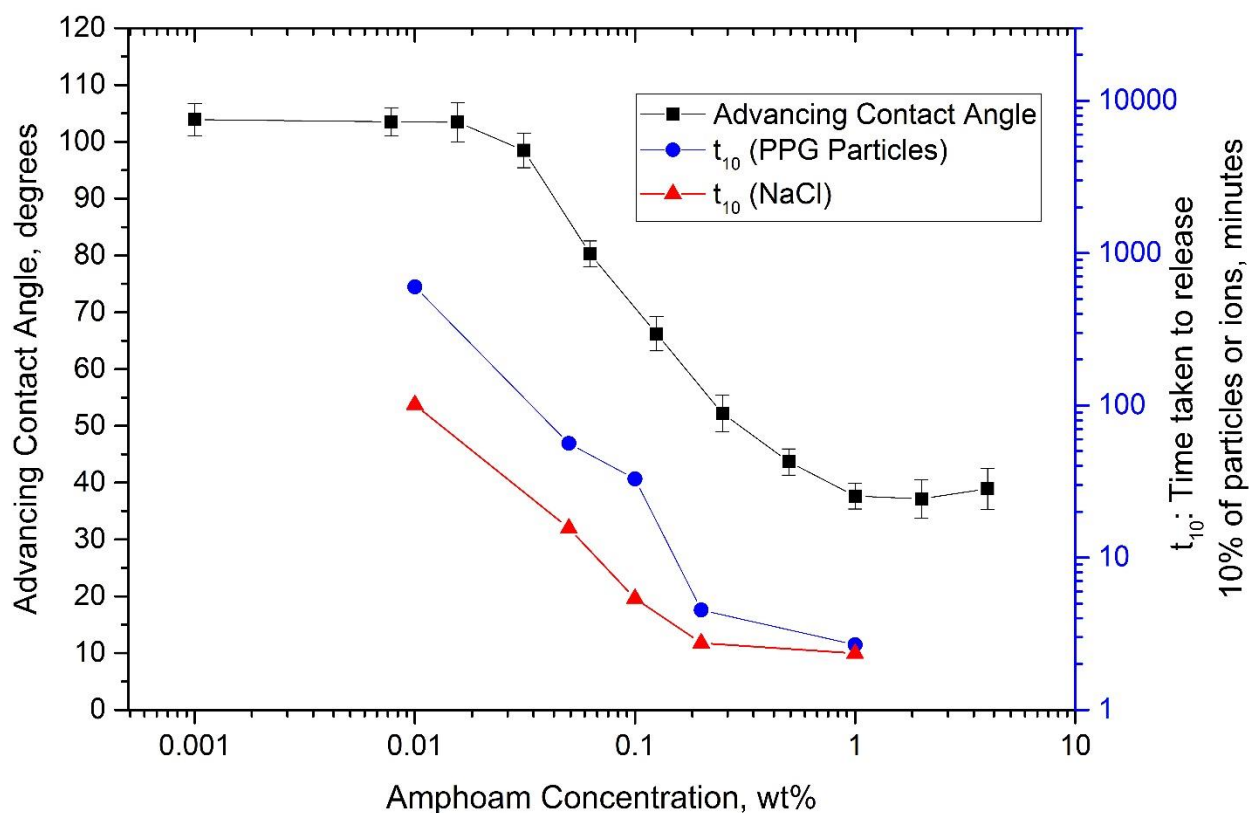
Figure 6.17: Advancing contact angle of the water droplet with varying surfactant concentration on a hydrophobic glass slide; t_{10}: time taken to release 10% of particles (2G-110) or ions for different surfactant concentration cases (secondary y-axis)

Table 6.3: Hydrodynamic diameter of hydrophobic silica nanoparticles dispersed in water with varying surfactant concentration

Amphoam surfactant concentration, wt%	Hydrodynamic diameter range, nm
0	63 ± 12
0.125	356 ± 145
0.25	405 ± 64
0.5	417 ± 28
1	454 ± 184
2	584 ± 239
4	1073 ± 62

In order to quantify the adsorption of Amphoam surfactant concentration on the silica nanoparticle surface, the method described by Lucassen-Reynders (1963) was used. Assuming negligible surfactant adsorption at the solid-air interface, the ratio of surfactant adsorption at the solid-water interface to the air-water interface is given by:

$$\frac{d(\gamma_{aw}cos\theta)}{d\gamma_{aw}} = -\frac{\tau_{sw}}{\tau_{aw}}$$

where γ_{aw} is the air-water surface tension, τ_{sw} and τ_{aw} are the surfactant adsorption at solid-water and air-water interface, respectively. Figure 6.18 shows the γ_{aw}, air-water surface tension as a function of surfactant concentration. The surface tension decreases with the increase in surfactant concentration to 33.4 ± 0.3 mN/m (corresponding to 0.125 wt%) and then almost plateaus indicating the CMC of the surfactant to be close to 0.125 wt%.
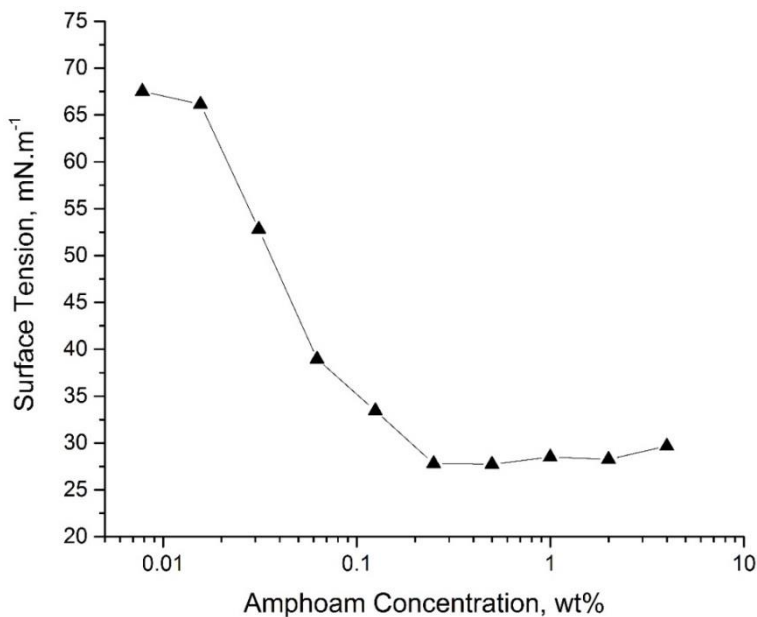
Figure 6.18: Surface tension of the water droplet with varying surfactant concentration

188

Figure 6.19 shows the plot of $\gamma_{aw} \cos\theta$ versus γ_{aw}. A linear plot was fitted to the data points with a regression, $R^2 = 0.96$. The slope of the curve, which is the ratio of τ_{sw} and τ_{aw}, was calculated to be 0.97. It implies that 97% of surfactant is adsorbed on the solid-water interface compared to air-water interface. In the literature, similar values of the ratio are reported. Binks et al. (2010) calculated a ratio of 0.6 for SDS surfactant adsorption on DCDMS-coated silica glass slides while Lucassen-Reynders reported a ratio of 0.8 for Aerosol surfactant adsorption on solid paraffin surfaces (Lucassen-Reynders, 1963).
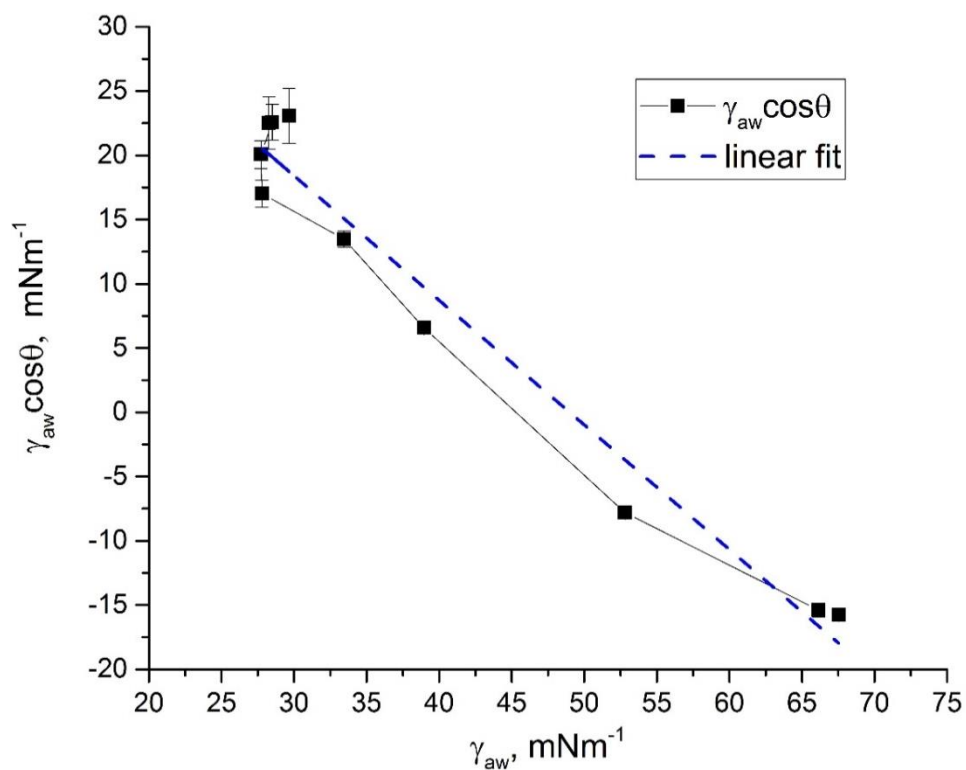
Figure 6.19: $\gamma_{aw} \cos\theta$ versus γ_{aw} for a silanized glass slide in the presence of Amphoam surfactant

6.4 CONCLUSIONS

In this study, hydrophilic particles dispersed in an aqueous phase were encapsulated using highly hydrophobic silica nanoparticles which self-assemble to form water-in-air powders under high shear mixing. It was demonstrated that these powders can be used as stimuli-responsive controlled release systems. Hydrophilic particles ranging from nanometers to micrometers scale could be encapsulated and released by external stimuli. The following conclusions can be drawn from this work:

- The compositions of silica nanoparticles, water (20 wt.% NaCl) and PPG where the encapsulated PPG powder (EPP) are obtained were determined. For a fixed amount of nanoparticles, a maximum PPG/water ratio, which could be encapsulated, was found to be 0.5 (e.g., at the weight ratio of 1:4:2). The encapsulated FL-NP powders (EFP) were formed for a wider range of aqueous phase to nanoparticle ratio from 1:1 to 1 to 60, irrespective of FL-NP concentration.

- The encapsulation of the PPG particles was robust even at high temperatures. No release of particles was observed after one month at 80 ºC and 125 ºC.

- A sequential increase in pH or increase in surfactant concentration resulted in a transitional inversion from water-in-air powders to mousse for the PPG cases with higher aqueous phase to nanoparticles ratios, when these stimuli were applied during powder formation.

- The initial surface wettability of the silica nanoparticles is highly hydrophobic which is critical for the formation of water-in-air powders. The surface modification toward water-wet due to external stimuli weakens the powders.

- The addition of surfactants to the external fluid triggers the release of PPG particles. The percentage release of particles is faster for a higher surfactant concentration.

- The percentage release of PPG particles increases with an increase in pH of the external fluid. The time taken to release 10% of particles (t10) is reduced by several orders of magnitude for pH of 12.

- The air-water contact angle study reveals that due to the presence of the surfactant or a pH of 12, the wettability of the initially hydrophobic surface changes towards water-wet.

These stimuli-responsive microencapsulated particles have potential applications in subsurface petroleum engineering such as conformance control agents with delayed swelling and delayed acidization agents.

Chapter 7: Microencapsulation of Acids by Nanoparticles for Acid Treatment of Shales

7.1 INTRODUCTION

Acid treatment is one of the common well-stimulation techniques to improve the production in tight carbonates or calcite-rich shale reservoirs. Because the reaction rates are often too large at the reservoir temperatures, retarded acid systems such as emulsified acids, foamed acids, and polymer-gelled acids are used. Retarded acids also minimize damage to the wellbore and propagate acids long-distance from the well bore in fractured shales. In this work, a novel encapsulation method of highly concentrated acid (~10 wt% HCl) is reported as an alternative retarded acid system. Microencapsulation of these acids is performed using highly hydrophobic silica nanoparticles. The mixing of these particles with acid under high shear rates results in the formation of acid-in-air powders. The release of acid from these powders could be triggered by external stimuli such as mechanical pressure or surfactant addition. The thermal stability, corrosion inhibition efficiency, and shale surface reactivity are compared with conventional acid-in-oil emulsions which are typically used for shale acidization processes.

7.2 METHODOLOGY

7.2.1 Materials

Aerosil® R 202, obtained from Evonik Industries, which is a hydrophobic, fumed silica powder surface-treated with polydimethylsiloxane was used. The nominal size of the

primary particles was 14 nm. Calcite-rich shale core samples from Eagle Ford were obtained from Kocurek Industries. An anionic surfactant, Bioterge AS-40 and a non-ionic surfactant, Tergitol 15-S-5 were obtained from Stepan and Sigma-Aldrich, respectively. n-Decane was used to form the acid-in-oil emulsions. Deionized water with a resistivity greater than 18.2 MΩ-cm was used to prepare solutions. Iron wire with diameter 1 mm (>99.9 Fe, Sigma-Aldrich, CAS Number 7439-89-6), Hydrochloric acid (37 %, Sigma-Aldrich), and Sodium Chloride (Fisher Chemical) were used as received.

7.2.2 Encapsulation of Acids

Hydrophobic silica nanoparticles and aqueous hydrochloric acid solution (different concentrations) were placed in a blender (Bella-Rocket blender) in a ratio of 1:10 by weight. The volume of the blending cup was 350 cc. The mixture was blended at constant speed of 16,000 rpm for 60 seconds using a cross-blade attachment. It resulted in the formation of water-in-air (or acid-in-air) powders with hydrochloric acid solution completely encapsulated inside the silica shell. These powders are referred as 'acid-in-air powders' or 'dry acids' (analogous to 'dry water') in this chapter.

7.2.3 Characterization of Encapsulated Particles

The acid-in-air powders were characterized using different microscopy techniques. The surface morphology of the powders was characterized using scanning electron microscopy (SEM). FEI Quanta 650 SEM operating under high vacuum at an accelerating voltage of 5 kV was used. The samples were glued onto standard aluminum stubs using double-sided carbon tape. One of the drawbacks of using SEM technique to characterize water-in-air powders is that it requires vacuum during the measurement. It could lead to

193

water evaporation (Forny et al., 2007) which could potentially collapse the silica shell (Carter et al., 2011). In previous chapter, it was demonstrated that confocal laser scanning microscopy (CLSM) technique which does not require any vacuum conditions could be performed to characterize these powders. Zeiss LSM 710 Confocal Microscope with the 10X dry (EC Plan-Neofluor 10X) objective lens operating in fluorescence mode was used. The aqueous hydrochloric acid phase was tagged with fluorescent Nile Blue A dye. The excitation wavelength for this dye was 633 nm. A small of amount of sample was placed in a chambered slide using a dropper. The coverslip was placed on top to prevent any contamination and minimize evaporation. The sample was scanned from the bottom at room temperature. The image resolution was 1564 x 1564 pixels. The image processing was done using the open-source Fiji software (Schindelin et al., 2012). Optical microscopy was performed to measure the average particle size of the powders. Bright-field images of the samples were captured using a Nikon optical microscope equipped with a high-resolution camera.

7.2.4 Bulk Thermal Stability

Acid-in-oil emulsions are typically used as acid delivery agents for stimulation of tight rocks such as shale or carbonate reservoirs. The stability of these conventional emulsions was compared with the acid-in-air powders formed in this work. To form acid-in-oil emulsions, first, varying ratio of oil and acid solution containing 1 wt% Tergitol 15-S-5 surfactant were taken in glass vials. The mixtures were mixed at high shear using a rotor-stator homogenizer (Ultra Turrax, T25, IKA Werke, Germany) operating at 10,000 rpm for 30 seconds. The samples were then placed in ovens operating at 60, 80 and 125 ºC. The emulsion stability was monitored in terms of the emulsion height (or volume) as a

function of time. Similarly, the acid-in-air powders were also taken in glass vials and were placed under different temperature conditions. The vials were intermittently centrifuged in CRU-5000 centrifuge (Damon, Needham, MA) operating at 3000 rpm for 2 min, and the volume of the powder and the released acid solution were measured to quantify the thermal stability. Note that typically dry powders are kept in plastic containers (and not glass vials) to avoid spontaneous release of aqueous phase. However, in this test glass vials were used for visualization purpose.

7.2.5 Corrosion Rate

A gravimetric measurement technique was adopted to investigate the potential corrosion inhibition benefit of encapsulating the acids (Salarvand et al., 2017). An iron wire of 1 mm diameter was cut into small pieces of length about 2.54 cm each. These pieces were cleaned with acetone to remove any grease and then washed with deionized water. Finally, the pieces were dried in an oven operating at 80 ºC. After drying, the weight of each piece was measured using a sensitive weighing machine which has a precision of ± 0.0001 gm. The pieces were immersed in different acid systems for a specified amount of time, t (hr). Corrosion rate was calculated based on ASTM standard (ASTM, 2004). The corrosion rate was calculated using the following equation.

$$Corrosion\ Rate\ (CR) = \frac{K * W}{A * t * \rho}$$

where corrosion rate (CR) is in mm per year (mm y^{-1}), K is a constant equal to 8.76 x10^4, W is mass loss in gm, A is the initial surface area in cm^2, t is the time of immersion in hr, and ρ is the density of the iron in 7.87 gm cm^{-3}.

195

7.2.6 Bulk Shale Acidization

Semi-disc shaped samples were cut in similar shape and sizes to ensure similar surface area. These samples were dried in an oven at 60 ºC overnight, and dry weight of the samples was measured. The samples were then placed in different acid systems such as non-encapsulated acid, acid-in-air powders, and acid-in-oil emulsions. (Further details about these systems will be discussed in the results section.) The samples were then placed in an oven operating at 60 ºC for 24 hr. The samples were then washed with brine (4 wt% NaCl) and again dried at 80º C for 48 hr. The difference in the dry weight (ΔM) before and after the acid treatment was then calculated. This ΔM gives a measure of the degree of reaction of the acid with shale samples for the different cases. Note that in these experiments, 4 wt% NaCl was added to the acid solutions to prevent any clay swelling in the shale.

7.2.7 Shale Surface Topology

The objective of the experiment was to investigate the interaction of shale surface with the acid-in-air powders. When concentrated acid interacts with shale surface, which is typically enriched with minerals such as calcite, it leads to surface etching which could be characterized using the surface roughness. In this work, the shale surface roughness was quantified using the Wyko NT9100 optical profilometer (Veeco Instruments Inc.). Disk-shaped shale samples were obtained by cutting shale cores (diameter: 1 inch) into pieces of 1 cm height. These samples were initially polished using a 600-mesh diamond-grinding plate. 2-gm dry acid powders were placed on the shale sample. It was ensured that the initial mean surface roughness was less than 1.1 microns. These samples were

contacted with acid (non-encapsulated or encapsulated) for 24 hr at 60 ℃. (Note that in these experiments, 4 wt% NaCl was always added to the acid solutions to prevent any clay swelling in the shale) Then, the samples were then dried in the oven overnight. These samples were placed on a vibration-free platform of the profilometer and were scanned in the vertical scanning interferometry mode in a non-contact manner.

7.2.8 Surfactant-Triggered Release

In the previous chapter, it is reported that micro- or nanosized particles could be encapsulated using water-in-air powders. It was showed that these encapsulated particles could be released using different stimuli such as a change in surfactant concentration or change of the pH medium of the external carrier fluid. Following a similar approach, the delayed release of acid from acid-in-air powders using a surfactant was studied in this work. 1 gm of dry acid powders was mixed with 4 gm of deionized water in centrifuge tubes. These tubes were placed in the oven operating at 60 ℃. A small amount of sample was collected from the vials and was analyzed using ion chromatography (IC) for chloride ion to quantify the release of acids from the powders.

7.3 RESULTS

7.3.1 Formation of Acid-in-Air Powders

First, 25 gm of concentrated hydrochloric acid (5 wt%) was taken in the blending cup. The aqueous solution was mixed with a small amount of hydrophilic, fluorescent Nile Blue A dye (3 drops of 1 wt% stock dye), as shown in Figure 7.1a. The aqueous solution was mixed with 2.5 gm hydrophobic silica nanoparticles (Figure 7.1b) in the cup. The mixture was blended at 16,000 rpm for 60 seconds. It resulted in the formation of acid-in-air powders. The appearance of this powder is completely dry (Figure 7.1d), and it flows

freely through a glass funnel (Figure 7.1c) indicating a dry powder-like behavior, albeit it is a 90% aqueous solution by weight. The final product, termed here as dry acids, looked white in color (Figure 7.1d) indicating the complete encapsulation of blue acid solution, as shown in schematic Figure 7.1e.
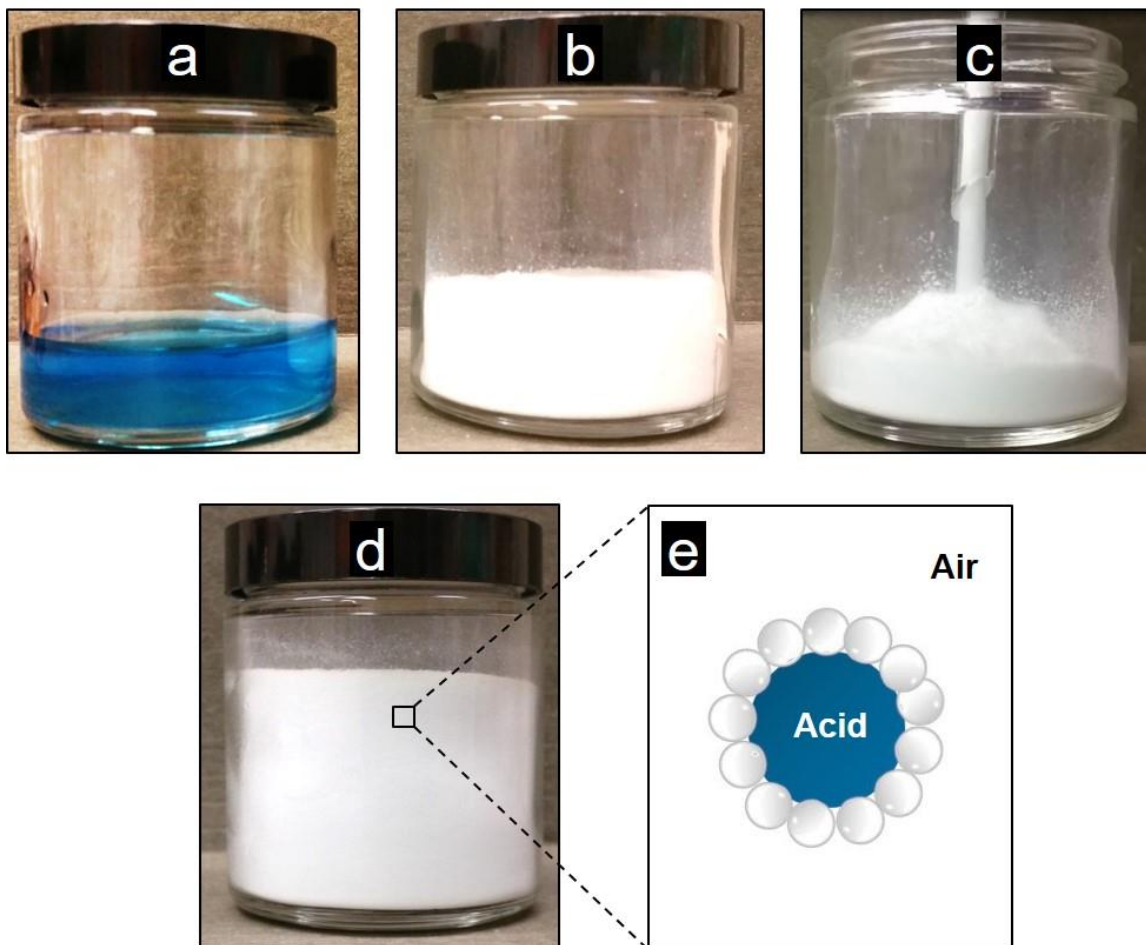
Figure 7.1: (a) 5 wt% hydrochloric acid dyed with Nile Blue A (25 gm); (b) hydrophobic silica nanoparticles (2.5 gm); (c) dry acid powder flowing freely through glass funnel; (d) dry acid powder (total product weight = 27.5 gm); (e) schematic of acid-in-air powder (white sphere represents the silica nanoparticles)

The obtained dry acid powder was characterized using several analytical techniques. First, the external morphology of the powder was characterized using scanning electron microscopy (SEM). Figure 7.2a shows the SEM image of the dry acid (5 wt%wt.% HCl). The irregular shaped structure of these water-in-air powders is due to jamming of particles at the interfaces. One of the technical limitations of the performing imaging via SEM, in this case, is that it requires vacuum conditions during measurement which can result in evaporation of aqueous phase and potential changes in the particle morphology. To address this concern, imaging analysis using confocal laser scanning microscope and an optical microscope was performed which does not require any vacuum conditions. As mentioned above, the acid phase was tagged with a fluorescent dye (Nile Blue A) before the dry acid formation. Although, post-encapsulation, the acid phase in enclosed within the silica shell, the CLSM technique could still image the encapsulated fluorescent material. Carter et al. (2010) first demonstrated this technique to image the 'dry water emulsion' formed in their study. Figure 7.2b shows the confocal micrograph of the dry acid powder with fluorescent acid phase shown in magenta (pseudo-color). Figure 7.2c shows the optical micrograph of the same sample. The average particle size of the powder was measured to be 27 ± 12 μm.
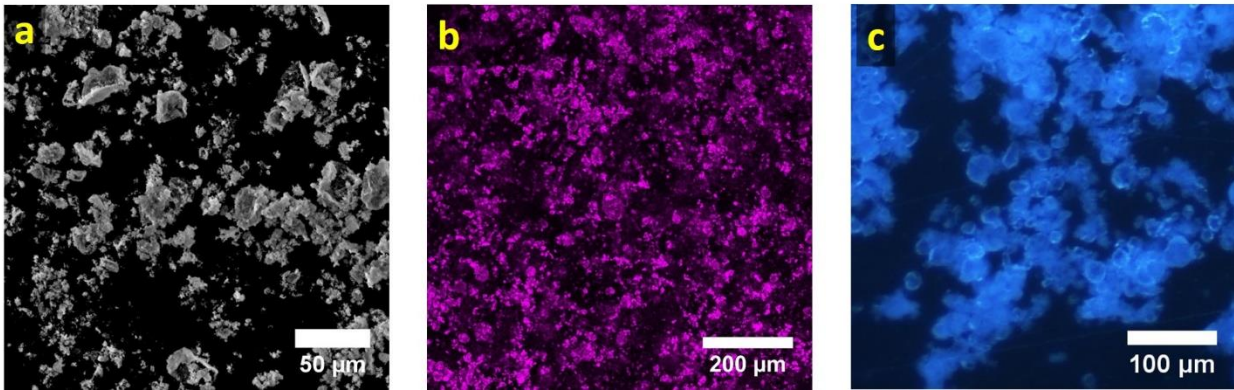
Figure 7.2: (a) SEM image of the acid-in-air powders (scale bar is 50 μm); (b) confocal micrograph of acid-in-air powders with acid phase dyed using Nile Blue A dye (scale bar is 200 μm); (c) optical micrograph of acid-in-air powder (scale bar is 100 μm)

7.3.2 Formation of Acid-in-Oil Emulsions

Injection of a strong acid into a reservoir has two disadvantages: unwanted interaction with the wellbore and too fast reaction with the rock matrix. To minimize these two issues, acid-in-oil emulsions are typically used as delivery vehicles. The slow breaking of these water-in-oil type emulsions ensures long distance propagation of acids. The first step in obtaining acid-in-oil emulsions is to choose a suitable surfactant. The radius of the curvature of oil-water interface is governed by head and tail components of the surfactant stabilizing the interface (Williams, 1991). The HLB (hydrophile-lipophile balance) of surfactant determines the tendency of the surfactant monolayers to curve towards either water or oil phase resulting in water-in-oil emulsions or oil-in-water emulsions (Aveyard et al., 1986; Boyd et al., 1972). Typically, a surfactant with HLB range of 7-11 acts as water-in-oil emulsifier while an HLB range of 12-16 acts as an oil-in-water emulsifier. Therefore, in this work, Tergitol 15-S-5 was chosen whose HLB is 10.5 per the vendor. Decane was used as the oil phase in this work, but most oils would work as well. Concentrated acid (5 wt.% HCl) with 1 wt.% Tergitol surfactant and decane

were taken in a vial in the ratio of 70:30 as shown in Figure 7.3a. A small amount of hydrophilic dye, Nile Blue A was added to the aqueous acid phase for visualization. The acid-oil mixture was mixed vigorously using a homogenizer (Ultra-Turrax T25) operating at 10,000 rpm for 30 seconds. It resulted in the formation of the acid-in-oil emulsion, as shown in Figure 7.3b. The emulsion texture was white in color (as opposed to blue) indicating the complete encapsulation of blue aqueous phase as shown in the schematic in Figure 7.3b. For visual comparison, another surfactant, Bioterge, was chosen whose HLB was >12. As in the previous case, the concentrated acid (5 wt.% HCl) with 1 wt.% Bioterge surfactant and decane were taken in a vial in the ratio of 70:30 (Figure 7.3c). The same amount of dye was added to the aqueous phase. Figure 7.3d shows the emulsion texture after homogenization at 10,000 rpm for 30 seconds. The emulsion is blue in color indicating oil-in-acid type emulsion as shown in the schematic. Therefore, Tergitol surfactant was chosen to form acid-in-oil emulsions in the subsequent experiments.

7.3.3 Thermal Stability

The thermal stability of the encapsulated acid system is critical for the successful implementation of the shale acidization process. A stable system will ensure long distance propagation of the acid in the fractures and avoid localized dissolution. Moreover, it will minimize corrosion damage to surface equipment and the wellbore. The thermal stability of both acid-in-oil emulsion and the acid-in-air powder was conducted at 25, 60, and 80 ºC. The acid concentration was kept constant at 5 wt.%. For the case of an acid-in-oil emulsion, three different quality (volume fraction of acid) – 50, 70, and 90% were investigated. The acid-oil mixture was mixed using homogenizer at 10,000 rpm for 30 seconds. The stability of the emulsion was measured in terms of relative emulsion height as a function of time. Relative emulsion height is the ratio of height (or volume) to the

initial emulsion height just after mixing. A higher emulsion height indicates slower release of acid via bubble coalescence.
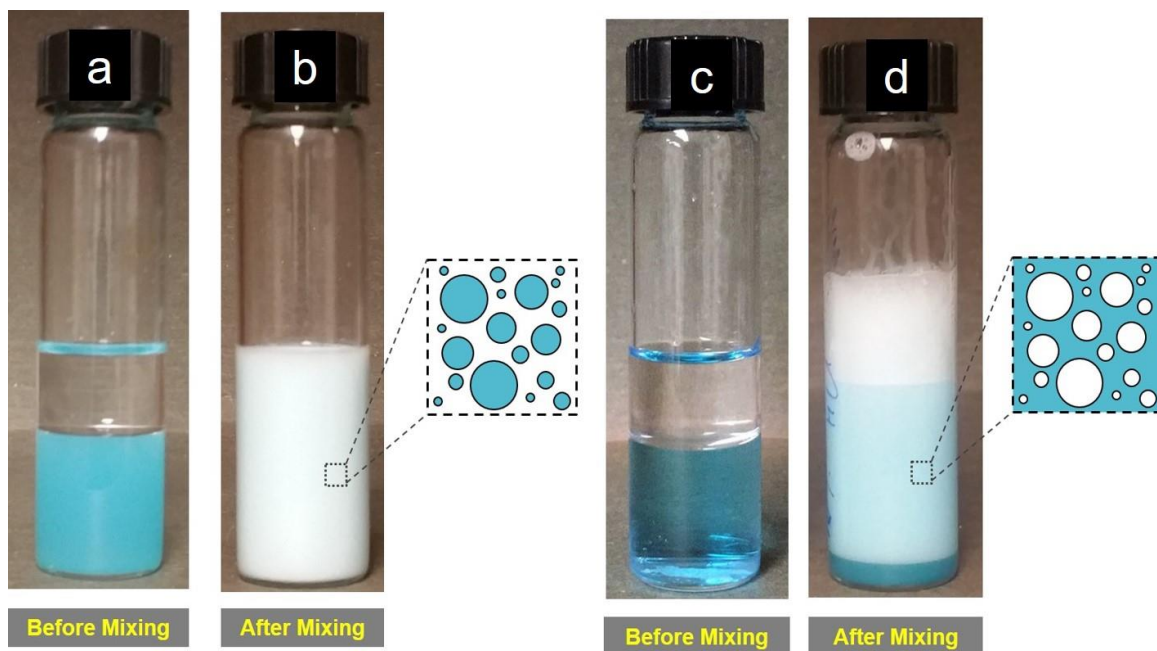
Figure 7.3: (a) Vial containing acid solution (5 wt.% HCl) containing 1 wt.% Tergitol surfactant dyed with Nile Blue A and decane before mixing; (b) texture of acid-in-oil emulsions after mixing; (c) Vial containing acid solution (5 wt.% HCl) containing 1 wt.% Bioterge surfactant dyed with Nile Blue A and decane before mixing (d) texture of oil-in-acid emulsions after mixing. Some foam is also present on the top of the emulsion.

Figure 7.4a, b, c shows the plot of decay of emulsion height with time for the three temperatures. The half-life of the emulsion, a measure of bulk emulsion stability, defined as the time taken for the emulsion to break to half of its original height can be calculated corresponding to relative emulsion height of 0.5 from the plot. The half-life was more than 180 hr for 50% quality (volume fraction of acid) at 25 ºC indicating a stable emulsion. The half-life was < 2.5 hr for the 70% and 90% cases at 25 ºC. As expected, the emulsion stability decreases with an increase in temperature. The half-lives were 1.3, 2.7 and 0.5 hr

202

corresponding to 50, 70, and 90% quality at 60 ℃. They were 0.9, 1.16, and 0.4 hr corresponding to 50, 70, and 90% quality at 80 ℃. The lower half-lives at higher temperature indicate a weaker emulsion. The outer liquid (oil here) drainage process increases with an increase in temperature due to a reduction in viscosity which results in a thinning of the lamellae and an increase in coalescence tendency of the emulsion.

Similarly, the bulk thermal stability of the acid-in-air powders was studied. The acid concentration was kept the same as the previous case and equal to 5 wt.%. The powder was prepared by mixing nanoparticles and acid solution in the ratio of 1:10 by weight and was kept in ovens operating at three different temperatures. Analogous to the emulsion case, the stability of these powders was evaluated based on the relative powder height (or volume) with time. To quantify the released acid accurately and ensure there is no trapped released acid in the powders, the vials were taken out of the ovens periodically and were centrifuged at 3000 rpm for 3 min. Figure 7.4d shows the decay of powder height with time. Interestingly, the acid-in-air powders were found to be quite stable at all the temperature. The half-lives were greater than 200 hr for the three temperatures. The powder height was only reduced to 94.5, 83.5, and 84.0% (from 100% initial volume) in 200 hr corresponding to 25, 60, and 80 ℃ indicating minimal release of acid from the system and relatively stable acid system as compared to acid-in-oil emulsions. Note that the half-lives were increased from a few hr for emulsions to more than 200 hr for acid-in-air powders at 60 ℃ and 80 ℃. The higher stability of these particle-stabilized emulsions (powders) is due to the irreversibly adsorbed nanoparticles at the air-water interface which act as a physical barrier between two acid droplets and thus retarding the droplet coalescence process.
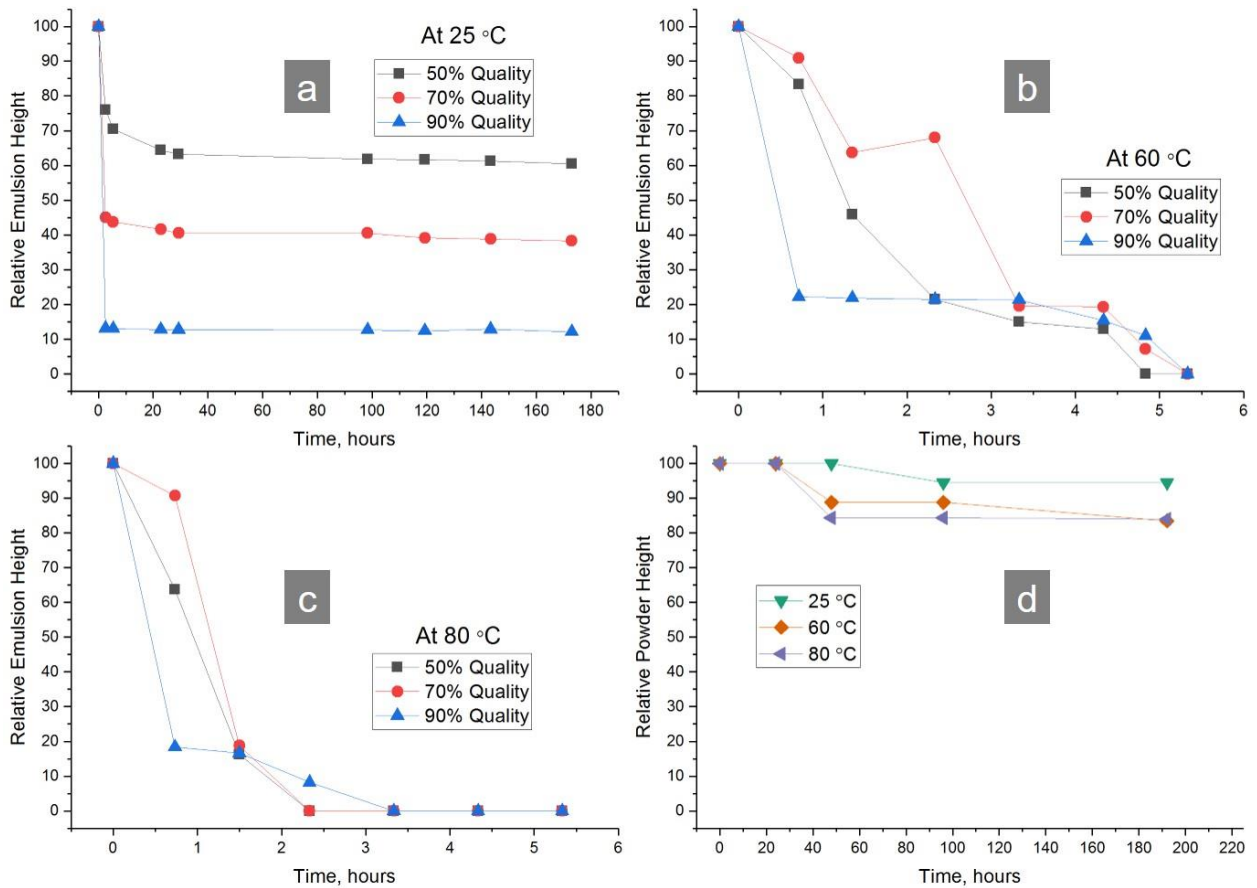
Figure 7.4: Relative emulsion height of the acid-in-oil emulsions as a function time at (a) 25 ºC, (b) 60 ºC, (c) 80 ºC; (d) Relative powder height of acid-in-air powders as a function of time for three temperatures

7.3.4 Corrosion Rate

One of the challenges associated with acid stimulation is to prevent corrosion of wellbore and surface equipment due to contact with the acid. Emulsification of the acid in oil helps reduce this reaction. Different types of acids are used for stimulation purposes in carbonates and shales. These include HCl, HF, nitric acid, acetic acid, and formic acids (Finšgar and Jackson, 2014). However, the most common acidizing agent is HCl with high concentrations of 5-28% (Smith et al., 1978). Therefore, in this work, HCl was chosen to

evaluate the corrosion of iron. The degree of corrosion of an iron wire due to HCl acid, conventional acid-in-oil emulsions, and acid-in-air powders was investigated.

The compartmentalization of acids in either powder or emulsion forms reduces the direct contact of the acid with the external solid surface which could reduce the corrosive effect of acid. This experiment was conducted at 60 ℃. The chosen acid concentrations were 1, 5, and 10 wt.%. Three different cases were studied. In the first case, iron samples were submerged in acid directly (referred here as non-encapsulated acid) and were placed in the oven for a fixed amount of time. In the second case, the iron samples were placed in the acid-in-oil emulsions. The quality of emulsion was kept constant at 50%. Finally, in the third case, the iron samples were placed in the acid-in-air powders. The total amount of acids was kept constant in all three cases. Figure 7.5a, b, c shows the corrosion rate for the three different acid concentrations at three different temperatures. At every temperature, highest corrosion rate was found for the non-encapsulated acid case for all the acid concentrations. The corrosion rate was relatively reduced for the case of acid-in-oil emulsions for all the cases. For example: it was reduced from 3121.9 mm.y^{-1} to 136.8 mm.y^{-1} (reduction factor of 22.82) for the case of 5 wt% acid concentration at 60 ℃. In all the cases, the acid-in-air powder outperformed the acid-in-oil emulsion with a reduction in corrosion rate. For example: the corrosion rate for 5 wt% acid case at 60 ℃ was only 31.6 mm.y^{-1} which is a reduction from 136.8 mm.y^{-1} for the emulsion. These data showcase the potential of acid-in-air powders to minimize corrosion damage to the wellbore equipment.

205
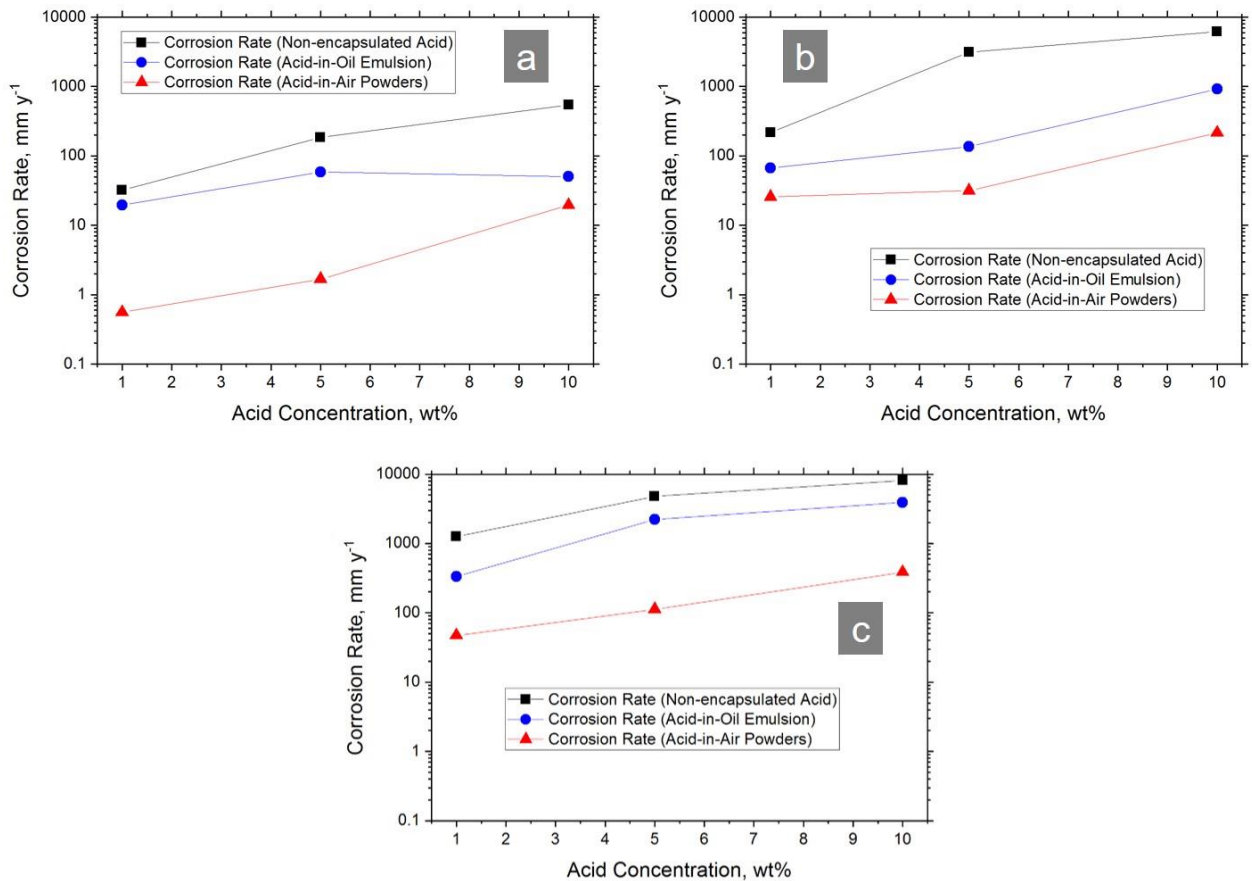
Figure 7.5: Corrosion rate for different acid systems at (a) 25 ºC, (b) 60 ºC, and (c) 80 ºC

7.3.5 Bulk Shale Acidization

The goal of this experiment was to understand the degree of interaction between the acid and the mineral present in shale samples. It was quantified by measuring the weight loss of the shale sample. Four different cases were studied. These include direct reaction with HCl acid (referred here as non-encapsulated acid), acid-in-air powders (crushed and uncrushed), and acid-in-oil emulsions. These experiments were performed at 60 ºC and reaction period was 24 hr for each case. Three different HCl acid concentrations- 1, 5, 10 wt% were used. Since the permeability of the shale samples is very low, the acid reaction is strongly controlled by the exposed surface area. Therefore,

all the shale samples were cut in similar size and shape to ensure similar surface areas. In the first case, the shale samples were submerged in concentrated acid (1,5, and 10 wt%) at 60 ºC for 24 hr. The shale samples were then taken out and were dried in an oven at 80º C overnight. The % mass loss in the shale sample was calculated and is plotted in Figure 7.6. As expected, the percentage mass loss increases with an increase in acid concentration. It was 3.8, 18.0, 21.7% corresponding to 1, 5, and 10 wt% acid concentrations. In the second case, shale samples were submerged in the acid-in-oil emulsions with acid concentrations 1, 5, and 10 wt%. The quality of emulsion was kept constant at 50%. The percentage mass loss, in this case, was very close to the non-encapsulated acid case as shown in Figure 7.6. It is due to the poor stability of the acid-in-oil emulsion as observed in the bulk stability experiments. In the third case, shale samples were placed in three different acid-in-air powder system. The concentrations of encapsulated acid were 1, 5, and 10 wt%. No external pressure or stimuli were applied to release the encapsulated acid in this case. The objective was to investigate the interaction between shale samples and any spontaneously released acids. Figure 7.6 shows that the mass loss was only 0.4, 1.1 and 4.6 wt% corresponding to 1, 5, and 10 wt% encapsulated acid concentrations. This shows that, as observed in the cases of corrosion study, the acid encapsulation via the acid-in-air powders is quite robust and the interaction between the acid and the shale surface is small. Finally, in the fourth case, the shale samples were again placed in acid-in-air powders with varying acid concentrations (1, 5, 10 wt%). However, in this case, the whole system was pressed using a Teflon-coated plate to crush the acid powders (to mimic the fracture closure) and release the encapsulated acid. The system was placed in an oven at 60 ºC for 24 hr. The mechanical pressure released the concentrated acid which reacted with the shale surfaces. The mass loss, in this case, was quite similar to the non-encapsulated acid case (Figure 7.6) indicating that the silica nanoparticles did not interfere with the reaction

and most of the acid was released. This experiment shows that how acid-in-air powders can act as carrier agents for concentrated acid. The reaction of acids with shale surface would be considerably retarded when no external stimuli such as mechanical pressure were applied. The fracture closure will result in the instant release of acid which will result in surface-etching and increased fracture conductivity after fracture closure. In the present study, the crushing pressure was not quantified. It would be interesting to study the release of acids from these powders as a function of crushing pressure in the future studies.
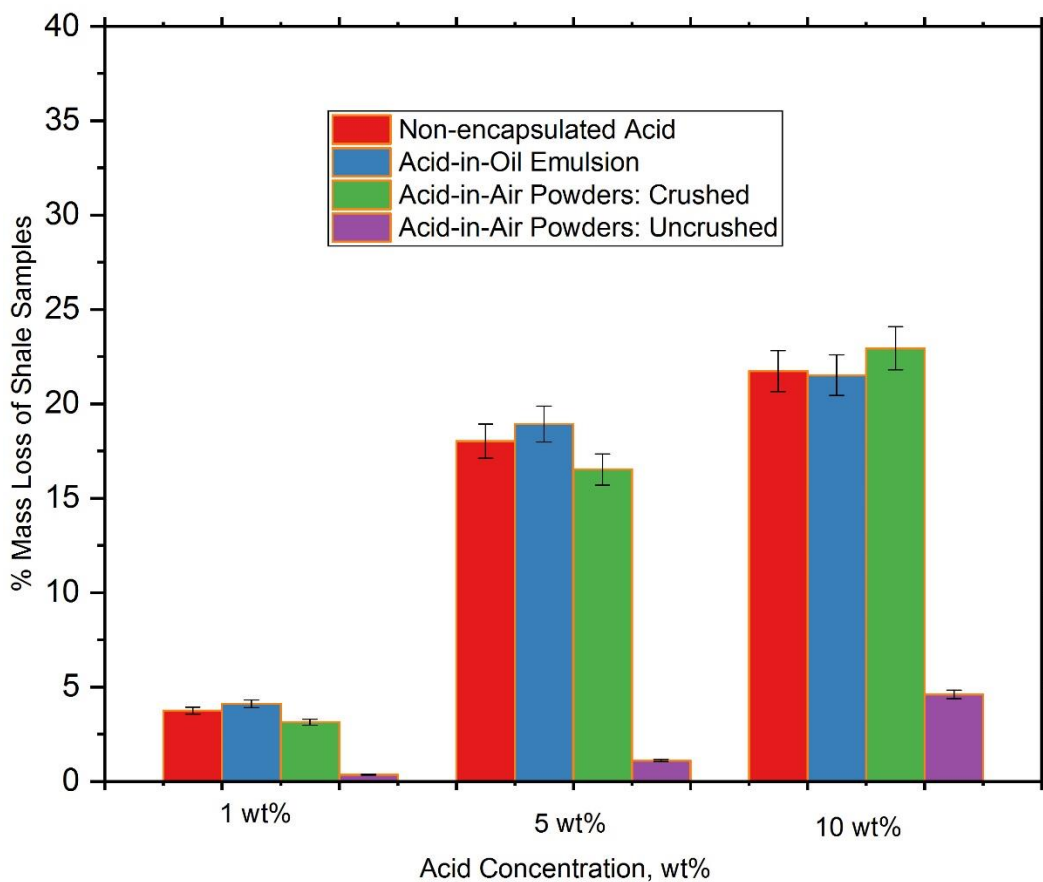
Figure 7.6: The percentage mass loss of the shale samples for acid systems with varying concentrations

7.3.6 Shale Surface Topology

The parameters, average roughness (R_a) and root mean square roughness (R_{rms}), are typically used to quantify the roughness of any surface. The original surfaces of these samples were quite rough due to scratches from the cutting saw, as shown in Figure 7.7a. The blue regions represent the valley regions whereas the red regions represent the elevated regions. The average and root mean square roughness was 4.76 ± 1.18 μm and 6.10 ± 1.37 μm, respectively. Therefore, all the samples were first polished using a 600-mesh diamond-grinding plate to smoothen the surfaces to ensure repeatability of the experiments. The average roughness of the samples was reduced to 1.02 ± 0.22 μm. Figure 7.7a and 7b shows a direct comparison between the same shale sample before and after the polishing. Four different cases were investigated. An acid resistant O-ring was first placed on the shale samples, and different acid samples were placed on the shale. In the first case, (nonencapsulated) acid (5 wt%) HCl was placed on the shale sample. It was pressed with a Teflon sheet using a steel clamp. The O-ring prevented any leakage of acids and evaporation. The system was placed in an oven operating at 60 ºC for 24 hr. The shale samples were then washed with brine (4 wt% NaCl) and were dried at 60 ºC overnight. The surface topography was then performed. Figure 7.7c shows the result of one of the scan. The average roughness of the shale sample increased to 4.32 ± 1.37 μm. A comparison between Figure 7.7b and 7c shows the etching of the shale surfaces with blue regions indicating the valleys / etched regions in the acid treated shale (Figure 7.7c).
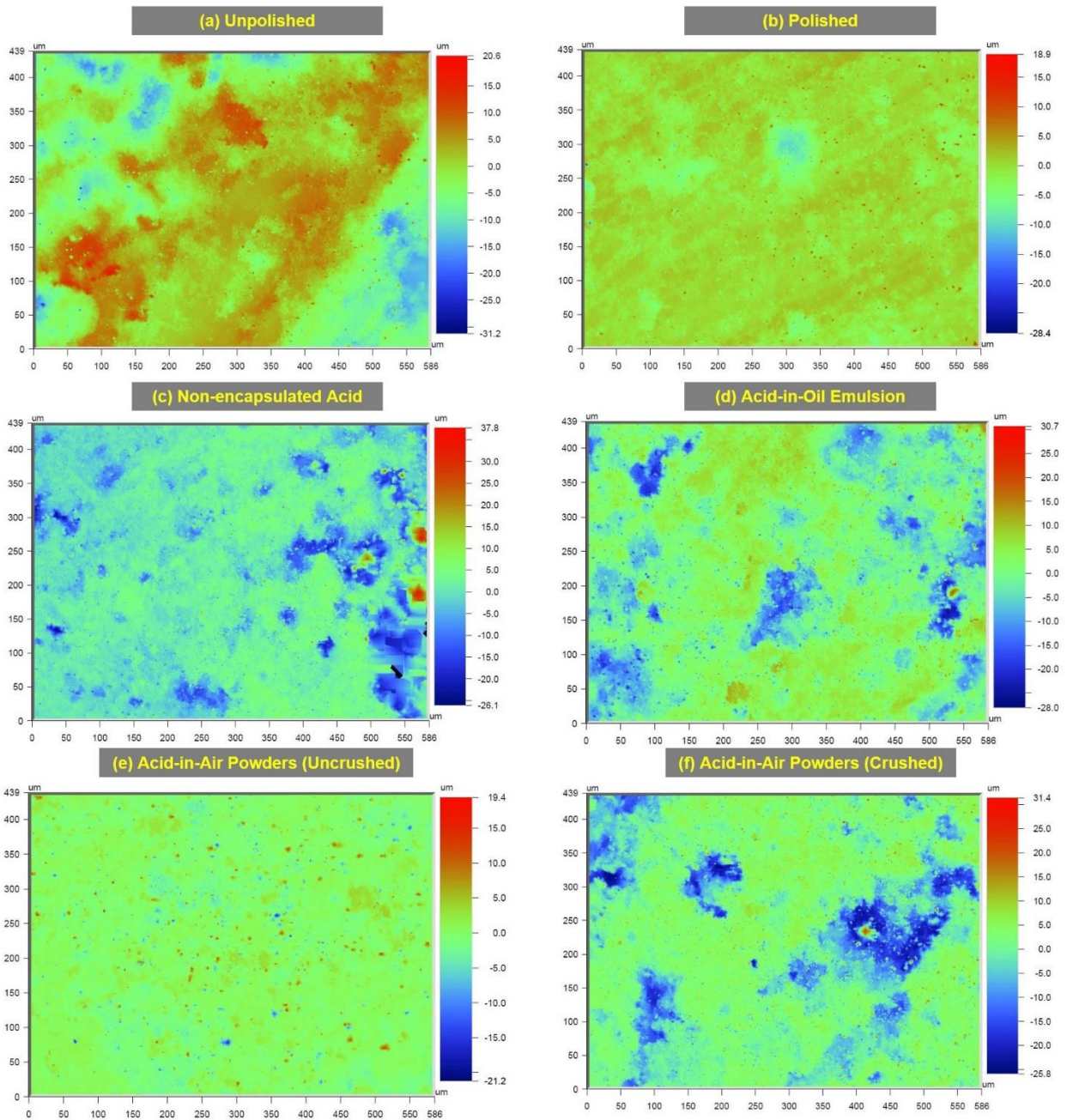
Figure 7.7: Shale surface topology (a) of the original shale sample; (b) polished shale sample; and after treatment with (c) non-encapsulated acids, (d) acid-in-oil emulsions, (e) acid-in-air powders (uncrushed), (f) acid-in-air powders (crushed)

In the second case, a small amount of acid-in-air emulsion was placed on the shale sample with the help of acid-resistant o-ring, and Teflon plate was placed on it and system was slightly tightened using a clamp to prevent any leak of the emulsion. s 7.7d shows the shale topography for this case. The average roughness, in this case, was 3.77 ± 0.60 µm much higher than the base case indicating release of acid from emulsions. Similarly, a small amount of acid-in-air powder was placed on the shale samples using the O-ring and Teflon sheet was clamped to prevent any leakage. However, the system was not fully tightened in this case. The system was placed in an oven at 60 ºC for 24 hr. Figure 7.7e shows the surface topography of the shale sample. The average surface roughness was measured to be 1.19 ± 0.05 µm which is close to the initial average surface roughness of the polished plates indicating no spontaneous release of acid at 60 ºC. This result is in line with the thermal stability results which showed that the acid-in-air powders show excellent stability even at temperatures as high as 80 ºC. In the fourth case, the same procedure was repeated, and acid-in-air powders were placed on the sample. However, in this case, the clamp was fully tightened which resulted in crushing of the powders and thus releasing the acid. The presence of O-ring prevented the leak of the released acid. Figure 7.7f shows the surface topology of the shale sample for this case. The surface etching is clearly visible on the shale surface confirming the release of the acid. The surface roughness, in this instance, was 3.72 ± 0.87 µm. All the roughness results are listed in Table 7.1. Both average roughness and RMS roughness followed a similar trend. Table 7.1 summarizes the average and RMS roughness for all the cases studied.

Table 7.1: The average and RMS (root mean square) roughness of the shale samples

Label	Cases	Average Roughness, R_a in μm	RMS Roughness, R_{rms} in μm
a	Unpolished	4.76 ± 1.18	6.10 ± 1.37
b	Polished	1.02 ± 0.22	1.52 ± 0.24
c	Non-encapsulated Acid	4.32 ± 1.37	6.17 ± 1.90
d	Acid-in-Oil Emulsion	3.77 ± 0.60	5.00 ± 0.57
e	Acid-in-Air Powders (Uncrushed)	1.19 ± 0.05	1.64 ± 0.09
f	Acid-in-Air Powders (Crushed)	3.72 ± 0.87	5.06 ± 0.98

7.3.7 Surfactant-Triggered Release

In the previous section, the acid release from acid-in-air powders was triggered using mechanical pressure. During the acid treatment process, the fracture closure pressure is typically very high (order of 1000s of psi) which will result in mechanical crushing of powders and complete release of encapsulated acids. An additional strategy for the controlled-release of acids before the fracture-closure can be the achieved by the addition of surfactants to the aqueous-based carrier fluid transporting the powders. The formation of acid-in-powders relies on hydrophobic wetting nature of the silica nanoparticles. Any external stimuli such as an increase in pH that can alter the surface wettability of these particles towards hydrophilicity can weaken the acid-in-air powder. A surfactant molecule, which comprises of the hydrophilic tail and hydrophobic chain, can physically adsorb on the silica nanoparticles to make the surface water-wet. In this work, acid-in-air powders were mixed with an aqueous solution of an anionic surfactant, and the vials were placed in the oven operating at 60 ℃. A small amount of aqueous sample was taken intermittently to measure the amount of released chloride ions using ion chromatography which gives

the measure of the amount of acid released with time. Figure 7.8 shows the plot of the percentage release of acids with time. The total amount of acid released was normalized using the maximum amount of acid present in the system. For the case of 1 wt% surfactant, all the encapsulated acid was released within 10 min. The t_{50}, time taken for the 50% of acid release, was 3.5, 438.2, 3625.6, and 4146.7 min for 1 wt%, 0.1 wt%, 0.05 wt% and 0.01 wt% surfactant solutions, respectively. The degree of acid release was reduced with a reduction in the surfactant concentration. In previous chapter, a contact angle study was reported using highly hydrophobic glass slides as a proxy for hydrophobic silica nanoparticles. It was shown that an increase in the concentration of surfactant in the aqueous solution reduces the air-water contact angle (measured through water phase) making the surface increasingly hydrophilic. Thus, by selecting the concentration of surfactant in the external aqueous carrier fluid, a delayed release of acid can be achieved before the fracture closure. Since the physical adsorption of surfactant on nanoparticles' surface governs the emulsions-breaking process and the release of acids, the surfactant-type will play a major role in controlling this release rate. The future studies will explore the effect of different surfactant-types on the rate of release of acids. Nevertheless, it is to be noted that post-fracture closure, mechanical crushing is expected to be the dominating mechanism for the complete release of acids.
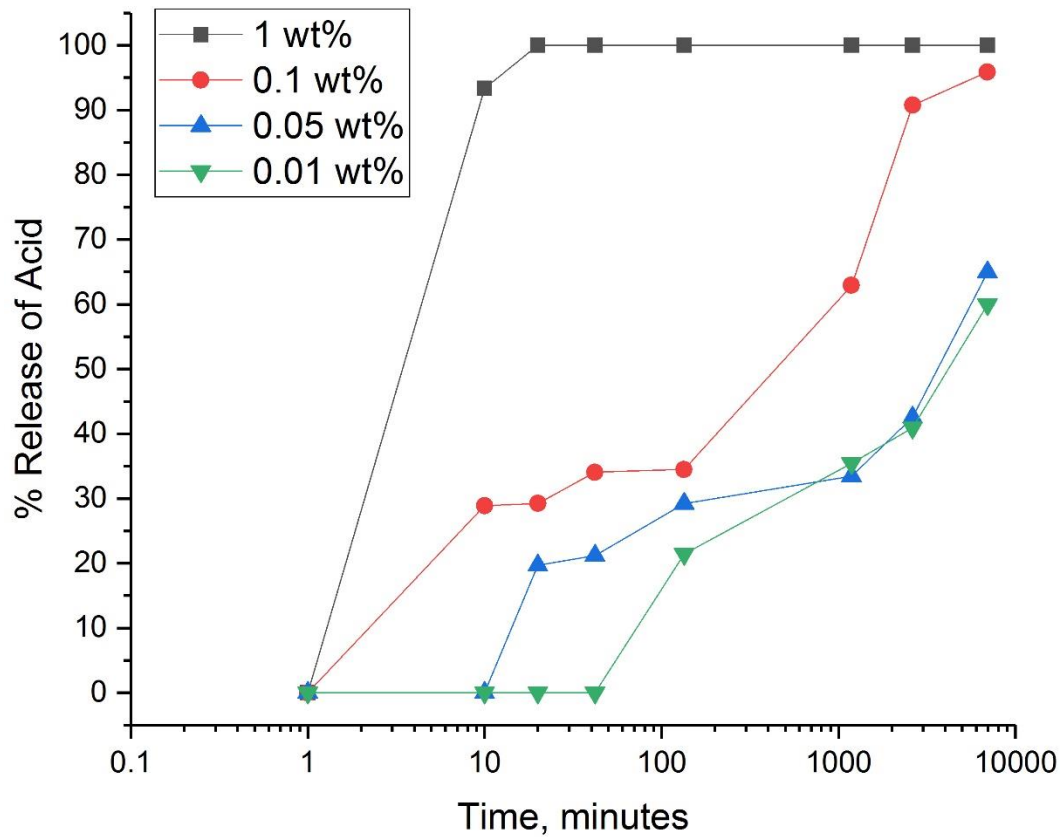
Figure 7.8: The percentage release of the encapsulated acid from the acid-in-air powders with external aqueous fluid with surfactant concentrations 1, 0.1, 0.05 and 0.01 wt.%

7.3.8 Comparison with Other Acid Treatment Processes

In acid treatment, direct injection of acids is avoided as it can cause several operational issues. Notably, it leads to corrosion of wellbore and results in precipitation of iron-containing compounds which will require the addition of corrosion inhibitor and iron-sequestering agents. Moreover, it will lead to excessive reaction near wellbore regions. To avoid these issues, retarded acid systems such as emulsified acid system or solid encapsulated acid system are typically used. Both these systems have their own

drawbacks. Although emulsified acids have been successfully used in some fields, robust emulsion stability is still a challenge, and it requires additional additives and specialized equipment and expertise (Still et al., 2007). In this chapter, the key advantages of proposed acid powders over acid-in-oil emulsions were illustrated in terms of stability tests and corrosion tests.

The solid encapsulated system relies on physical or chemical degradation of the surface coating for the release of acid. The precise control of required chemical conditions in the reservoir is difficult. Moreover, bulk scale production of these coated systems is prone to physical defects which will lead to early release of acids. For example: Burgos et al. (2004) reported a field trial of acid fracturing using encapsulated citric acid. The acid was coated with vegetable oil which prevented mixing with aqueous carrier fluids. The system relied on melting of coating above 180 °F in reservoir and crushing during fracture closure. Similarly, Nasr-El-Din et al. (2009) reported the injection of the precursor of lactic acid in the form of solid beads. These beads hydrolyze in the presence of water and produce in-situ lactic acid. One of the reported operational challenge encountered during the implementation was that not all the beads were hydrolyzed due to an insufficient amount of water as most of the water was leak-offed in the formation after the fracture closure. The proposed acid powders technique does not need any such reaction conditions for the release of acids and thus are more robust. Also, as opposed to a reaction-based coating, the coating in the acid powders relies on self-assembly of silica nanoparticles at the air-water interface and therefore are not susceptible to physical coating defects. Moreover, the one-step method of formation of acid powders offers a facile route for bulk scale production of these powders.

The dry acid powder used in this study were formed using a nanoparticle to acid solution mass ratio of 1:10. Thus 1 lb of dry acid powder will require 0.091 lb of

nanoparticles. Assuming a nanoparticle cost of about $5 per lb, the additional nanoparticle cost would be $0.45 per lb of dry powder. These preliminary results for the acid powder systems are quite promising. In future, detailed reservoir specific studies must be performed to fully understand the technical, operational, and financial challenges.
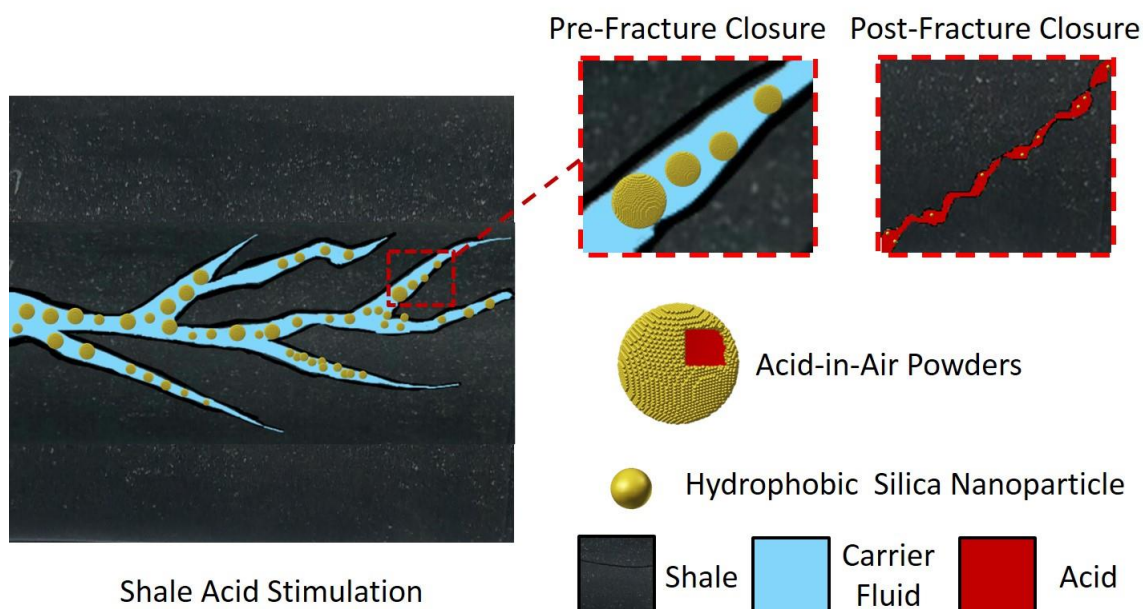
Figure 7.9: Sketch of a possible application of acid-in-air powders in shale fractures

7.4 CONCLUSIONS

A simple one-step approach for encapsulation of concentrated acids was reported using nanoparticles. Highly hydrophobic silica nanoparticles were mixed with concentrated HCl acid at high shear rates to obtain acid-in-air powders. These powders can act as robust acid encapsulating agents, and the acid-release could be triggered using external stimuli such as mechanical pressure or surfactant addition. Figure 7.9 shows a

sketch of a possible application of acid-in-air powders in shale fractures. In the field conditions, the air can be substituted by any aqueous (brine) or non-aqueous fluids (e.g., diesel, crude oil, NGL, natural gas). Thermal stability, corrosion inhibition efficiency, and shale surface reactivity were compared with conventional acid-in-oil emulsions which are typically used for shale acid treatments. The following conclusions can be drawn from this work:

- Microencapsulation of concentrated HCl acid (1, 5, 10 wt%) was successfully performed by forming acid-in-air powders using highly hydrophobic silica nanoparticles.
- Acid-in-oil emulsions were formed by choosing a surfactant with HLB of 10.5 with the inner phase of concentrated acid (1-10 wt%) and a continuous external phase of Decane oil.
- The acid-in-air powders show excellent thermal stability as compared to acid-in-oil emulsions with two orders of magnitude higher half-lives (time taken to release 50% encapsulated acid) at 60 ºC and 80 ºC.
- The corrosion inhibition capability of these powders was superior to acid-in-oil emulsions or non-encapsulated acid. It makes them lucrative to use in subsurface applications as it will reduce corrosion damage to surface equipment and wellbores.
- Shale topography study reveals release of acid from the acid-in-air powders when the external stimulus of external pressure was applied. The released acid resulted in surface etching and increase in average surface roughness of the sample. Such roughness in the walls of primary fractures or microfractures could potentially enhance the productivity of shale reservoirs.

217

The release of acid from the acid-in-air powders could be triggered by adding a small amount of surfactant in the carrier fluid. The percentage release increases with an increase in the surfactant concentration.

Chapter 8: Conclusions and Recommendations

8.1 CONCLUSION

Foam is a promising tool to improve sweep efficiency in gas floods. It can reduce the mobility of gas by several orders of magnitude by increasing the apparent viscosity of gas while the liquid phase mobility remains unchanged. Chapters 3, 4, and 5 are focused on developing novel foams to improve oil recovery in water-wet sandstone and oil-wet carbonate reservoirs.

For the case of sandstones, which are typically water-wet in nature, two different approaches of foam stabilization using nanoparticles were developed. In the first approach, synergistic stabilization of foams using a mixture of hydrophilic nanoparticles and an anionic surfactant in bulk and porous media was investigated. Static foam test showed that the foam half-lives increase with the addition of nanoparticles to surfactant formulations. Vertical foam film test and confocal laser scanning microscopy revealed the mechanisms of how the nanoparticles are trapped in the lamellae as well as Gibbs-Plateau borders. These nanoparticles act as a physical barrier and retard the liquid drainage and Ostwald ripening process. Oil-free foam flow experiments in Berea cores demonstrated that as the concentration of nanoparticles increased, the mobility reduction factor, a measure of foam strength, of surfactant-nanoparticle foam in a Berea core increased up to a factor of two. To fundamentally understand the role of nanoparticles in altering the foam dynamics in porous media, a high-pressure visualization study was performed in a 2D layered, heterogeneous porous media. The permeability contrast between the layers was 6:1 which was favorable for channeling of gas through high-permeability regions. Foam flood in these 2D sandpacks with a reservoir crude oil showed incremental oil recovery of

219

25% to 34% OOIP (over waterflood) using immiscible foams. The surfactant-nanoparticle blend outperformed surfactant-stabilized foam by 9% OOIP. Two different cross-flow mechanisms of foam were identified which governs the displacement in these heterogeneous porous media.

In the second approach, foam stabilization via in-situ surface activated nanoparticles without the presence of surfactants was investigated. Hydrophilic nanoparticles were made partially hydrophobic by anchoring small-chain amphiphiles (surface-modifier) to obtain surface-modified nanoparticles (SM-NPs). These SM-NPs could stabilize foams even in the absence of surfactant molecules. Bulk foam stability experiments such as Bartsch shake test, static foam test, bubble morphology visualization showed that initially hydrophilic nanoparticles modified by the even low concentration of surface-modifier (~0.05 wt%) could stabilize strong bulk foams. Oil-free foam flow experiments in cores showed that as the concentration of surface-modifier increases the in-situ foam stability increases. Core floods in a sandstone core with a reservoir crude oil showed that immiscible foams using these SM-NP can recover a significant amount of oil over water flood. Both these approaches show that nanoparticles with optimal surface coating have the potential to stabilize robust foams in both bulk and porous media and thus could act as effective foam EOR agents in sandstone reservoirs.

For the case of carbonates, which are typically oil-wet in nature, the emphasis was laid on developing surfactant formulations which can simultaneously act as wettability altering agents as well as in-situ foaming agent. Crude oils are typically detrimental to foam stability. The presence of oil-film on the rock surface due to the inherent oil-wet nature of carbonates presents a challenge to form strong in-situ foams. In such case, adopting a synergistic approach where surfactant formulation can perform both wettability alteration and generate strong foam was shown to be beneficial. Surfactant screening was

performed by conducting bulk experiments such as spontaneous imbibitions in a microchannel, static foam tests, and contact angle studies on calcite plates. Optimized surfactant formulation comprising a blend of a wettability-altering surfactant (APS), AOS, and a zwitterionic surfactant not only altered the wettability of the carbonate core from oil-wet to water-wet but also significantly increased the foam pressure gradient in the presence of crude oil.

Chapters 6 and 7 are focused on developing techniques of microencapsulation using nanoparticles by forming water-in-air type emulsion (powders). Hydrophilic particles ranging from micrometers to nanometers dispersed in an aqueous phase were encapsulated using highly hydrophobic silica nanoparticles which self-assemble to form water-in-air powders under high shear mixing. The encapsulation of particles was shown to be quite robust even at high temperatures of 80 °C and 125 °C. The release of particles could be triggered by external stimuli such change in pH or addition of surfactant in the external fluid. A contact angle study was conducted using surface-hydrophobized glass slides, which acted as a proxy for hydrophobic silica nanoparticles, to investigate the effect of these stimuli on surface hydrophobicity and understand the release mechanisms. This microencapsulation system could potentially be used for targeted delivery of PPG microparticles for conformance control applications.

Retarded acid systems such as emulsified acids, foamed acids, and polymer-gelled acids are often used for acid treatments in calcite-rich shale reservoir to improve the conductivity. In this dissertation, microencapsulated acids were proposed as an alternative robust acid carrier system. Hydrophobic silica nanoparticles were used to encapsulate concentrated acids (10 wt% HCl) to obtain acid-in-air powders. The key advantages of using these powders over conventional acid-in-oil emulsions were illustrated in terms of thermal stability, corrosion inhibition efficiency, and shale surface reactivity.

8.2 RECOMMENDATIONS

Based on the experience and the technical knowledge gained from this work, the following future work is recommended.

1. In this work, silica nanoparticles grafted with polyethylene glycol (PEG) were used as a foam stabilizer in the water-wet system. The coating resulted in enhanced aqueous stability and minimal retention during flow in porous media. The grafting of other low-molecular-weight ligands such as (3-Glycidyloxypropyl)trimethoxysilane, (GLYMO) could further improve the steric stabilization especially under low pH conditions which are typically expected during CO_2 floods (Singh and Mohanty, 2017b). Future studies should explore the foam stabilization using such nanoparticles grafted with different ligands and perform a detail comparative study.

2. Foams stabilization by in-situ surface activated nanoparticles (SM-NP) was shown as one of the potential routes to generate foams in the absence of surfactant. It would be interesting to visualize and compare the foam dynamics of SM-NPs with conventional surfactant in a 2D layered, heterogeneous sandpacks.

3. In Chapters 3 and 4, nitrogen gas was used to make foam at low-pressure conditions. The rheology of N_2 foam is not very sensitive to pressure conditions. It would be interesting to conduct the nanoparticle-stabilized foam studies using CO_2 gas as CO_2 foam rheology could significantly change under high-pressure conditions.

4. In this work, surfactants were used for wettability alteration of the oil-wet carbonates. Recent studies have shown certain nanoparticles as effective wettability-altering agents (Al-Anssari et al., 2016; Giraldo et al., 2013; Karimi et al., 2012b). It would be interesting to develop hybrid nanoparticle formulations which could perform wettability alteration as well produce strong in-situ foams without using nanoparticles.

5. Stimuli-responsive water-in-air powders were studied in this work. These powders were characterized using different techniques such as SEM, optical microscopy, confocal laser and scanning microscopy. Future studies can focus on characterizing these powders using cryo-SEM. It will help to study the surface morphology of these powders in detail. It will allow one to mechanistically understand the mechanism involved in dynamic formation or coalescence due to external stimuli.

6. Future studies should focus on using these powders under reservoir-specific conditions to better understand the technical challenges associated with the field-scale implementation.

Nomenclature

B	bridging coefficient
CLSM	confocal laser scanning microscopy
θ	contact angle
CR	corrosion rate
CMC	critical micelle concentration
d	days
ρ	density
EFP	encapsulated FL-NP Powder
EPP	encapsulated PPG powders
E	entering coefficient
FL-NP	fluorescent nanoparticles
hr	hours
HP	hydrophilic particles
γ_{aw}	interfacial tension between air-water
L	lamella number
μ	micron or cp
mD	milli Darcy
mL	milliliter
min	minutes
MRF	mobility reduction factor
OOIP	original-oil-in-place
PV	pore volume
$M\Omega$-cm	resistivity
S	spreading coefficient
SM-NP	surface-modified nanoparticles
τ_{aw}	surfactant adsorption at air-water interface
τ_{sw}	surfactant adsorption at solid-water interface

References

Adibhatla, B., Mohanty, K.K., 2008. Oil Recovery From Fractured Carbonates by Surfactant-Aided Gravity Drainage: Laboratory Experiments and Mechanistic Simulations. SPE Reserv. Eval. Eng. 11, 119–130. https://doi.org/10.2118/99773-PA

Al-Anssari, S., Barifcani, A., Wang, S., Maxim, L., Iglauer, S., 2016. Wettability alteration of oil-wet carbonate by silica nanofluid. J. Colloid Interface Sci. 461, 435–442. https://doi.org/10.1016/j.jcis.2015.09.051

Alargova, R.G., Warhadpande, D.S., Paunov, V.N., Velev, O.D., 2004. Foam Superstabilization by Polymer Microrods. Langmuir 20, 10371–10374. https://doi.org/10.1021/la048647a

Almajid, M.M., Kovscek, A.R., 2016. Pore-level mechanics of foam generation and coalescence in the presence of oil. Adv. Colloid Interface Sci., Clayton Radke Festschrift 233, 65–82. https://doi.org/10.1016/j.cis.2015.10.008

Alvarez, J.O., Neog, A., Jais, A., Schechter, D.S., 2014. Impact of Surfactants for Wettability Alteration in Stimulation Fluids and the Potential for Surfactant EOR in Unconventional Liquid Reservoirs. Presented at the SPE Unconventional Resources Conference, Society of Petroleum Engineers. https://doi.org/10.2118/169001-MS

Alzobaidi, S., Da, C., Tran, V., Prodanović, M., Johnston, K.P., 2017a. High temperature ultralow water content carbon dioxide-in-water foam stabilized with viscoelastic zwitterionic surfactants. J. Colloid Interface Sci. 488, 79–91. https://doi.org/10.1016/j.jcis.2016.10.054

Alzobaidi, S., Lotfollahi, M., Kim, I., Johnston, K.P., DiCarlo, D.A., 2017b. Carbon dioxide-in-brine foams at high temperatures and extreme salinities stabilized with silica nanoparticles. Energy Fuels. https://doi.org/10.1021/acs.energyfuels.7b01814

Anderson, W.G., 1987. Wettability Literature Survey- Part 4: Effects of Wettability on Capillary Pressure. J. Pet. Technol. 39, 1,283-1,300. https://doi.org/10.2118/15271-PA

Aronson, A.S., Bergeron, V., Fagan, M.E., Radke, C.J., 1994. The influence of disjoining pressure on foam stability and flow in porous media. Colloids Surf. Physicochem. Eng. Asp. 83, 109–120.

ASTM, A., 2004. G31–72: Standard Practice for Laboratory Immersion Corrosion Testing of Metals, Annual Book of ASTM Standards. Phila. PA Am. Soc. Test. Mater.

Austad, T., Matre, B., Milter, J., Sævareid, A., Øyno, L., 1998. Chemical flooding of oil reservoirs 8. Spontaneous oil expulsion from oil- and water-wet low permeable chalk material by imbibition of aqueous surfactant solutions. Colloids Surf. Physicochem. Eng. Asp. 137, 117–129. https://doi.org/10.1016/S0927-7757(97)00378-6

Aveyard, R., Binks, B.P., Clint, J.H., 2003. Emulsions stabilised solely by colloidal particles. Adv. Colloid Interface Sci. 100–102, 503–546. https://doi.org/10.1016/S0001-8686(02)00069-6

Aveyard, R., Binks, B.P., Mead, J., 1986. Interfacial tension minima in oil–water–surfactant systems. Effects of alkane chain length and presence of n-alkanols in systems containing aerosol OT. J. Chem. Soc. Faraday Trans. 1 Phys. Chem. Condens. Phases 82, 1755–1770. https://doi.org/10.1039/F19868201755

Bai, B., Liu, Y., Coste, J.-P., Li, L., 2007. Preformed Particle Gel for Conformance Control: Transport Mechanism Through Porous Media. SPE Reserv. Eval. Eng. 10, 176–184. https://doi.org/10.2118/89468-PA

Bale, A., Smith, M.B., Klein, H.H., 2010. Stimulation of Carbonates Combining Acid Fracturing With Proppant (CAPF): A Revolutionary Approach for Enhancement of Final Fracture Conductivity and Effective Fracture Half-Length, in: SPE Annual Technical Conference and Exhibition, SPE-134307. https://doi.org/10.2118/134307-MS

Barati, R., Johnson, S.J., McCool, S., Green, D.W., Willhite, G.P., Liang, J.-T., 2012. Polyelectrolyte complex nanoparticles for protection and delayed release of enzymes in alkaline pH and at elevated temperature during hydraulic fracturing of oil wells. J. Appl. Polym. Sci. 126, 587–592. https://doi.org/10.1002/app.36845

Basheva, E.S., Ganchev, D., Denkov, N.D., Kasuga, K., Satoh, N., Tsujii, K., 2000. Role of Betaine as Foam Booster in the Presence of Silicone Oil Drops. Langmuir 16, 1000–1013. https://doi.org/10.1021/la990777+

Bergeron, V., 1997. Disjoining Pressures and Film Stability of Alkyltrimethylammonium Bromide Foam Films. Langmuir 13, 3474–3482. https://doi.org/10.1021/la970004q

Bernard, G.G., Jacobs, W.L., 1965. Effect of foam on trapped gas saturation and on permeability of porous media to water. Soc. Pet. Eng. J. 5, 295–300.

Bertin, H.J., Apaydin, O.G., Castanier, L.M., Kovscek, A.R., 1999. Foam Flow in Heterogeneous Porous Media: Effect of Cross Flow. SPE J. 4, 75–82. https://doi.org/10.2118/56009-PA

Binks, B., Kirkland, M., A. Rodrigues, J., 2008. Origin of stabilisation of aqueous foams in nanoparticle – surfactant mixtures. Soft Matter 4, 2373–2382. https://doi.org/10.1039/B811291F

Binks, B.P., 2002. Particles as surfactants—similarities and differences. Curr. Opin. Colloid Interface Sci. 7, 21–41. https://doi.org/10.1016/S1359-0294(02)00008-0

Binks, B.P., Desforges, A., 2007. Synergistic Stabilization of Emulsions by a Mixture of Surface-Active Nanoparticles and Surfactant. Langmuir 23, 1098–1106. https://doi.org/10.1021/la062510y

Binks, B.P., Duncumb, B., Murakami, R., 2007. Effect of pH and salt concentration on the phase inversion of particle-stabilized foams. Langmuir 23, 9143–9146. https://doi.org/10.1021/la701393w

Binks, B.P., Horozov, T.S., 2005a. Aqueous foams stabilized solely by silica nanoparticles. Angew. Chem. 117, 3788–3791. https://doi.org/10.1002/ange.200462470

Binks, B.P., Horozov, T.S., 2005b. Aqueous Foams Stabilized Solely by Silica Nanoparticles. Angew. Chem. Int. Ed. 44, 3722–3725. https://doi.org/10.1002/anie.200462470

Binks, B.P., Johnson, A.J., Rodrigues, J.A., 2010. Inversion of 'dry water' to aqueous foam on addition of surfactant. Soft Matter 6, 126–135. https://doi.org/10.1039/B914706C

Binks, B.P., Lumsdon, S.O., 2001. Pickering emulsions stabilized by monodisperse latex particles: effects of particle size. Langmuir 17, 4540–4547. https://doi.org/10.1021/la0103822

Binks, B.P., Muijlwijk, K., Koman, H., Poortinga, A.T., 2017. Food-grade Pickering stabilisation of foams by in situ hydrophobisation of calcium carbonate particles. Food Hydrocoll. 63, 585–592. https://doi.org/10.1016/j.foodhyd.2016.10.002

Binks, B.P., Murakami, R., 2006. Phase inversion of particle-stabilized materials from foams to dry water. Nat. Mater. 5, 865–869. https://doi.org/10.1038/nmat1757

Binks, B.P., Rodrigues, J.A., 2007. Synergistic Interaction in Emulsions Stabilized by a Mixture of Silica Nanoparticles and Cationic Surfactant. Langmuir 23, 3626–3636. https://doi.org/10.1021/la0634600

Blaker, T., Aarra, M.G., Skauge, A., Rasmussen, L., Celius, H.K., Martinsen, H.A., Vassenden, F., 2002. Foam for gas mobility control in the Snorre field: the FAWAG project. SPE Reserv. Eval. Eng. 5, 317–323.

Boud, D.C., Holbrook, O.C., 1958. Gas drive oil recovery process. US2866507 A.

Boyd, J., Parkinson, C., Sherman, P., 1972. Factors affecting emulsion stability, and the HLB concept. J. Colloid Interface Sci. 41, 359–370. https://doi.org/10.1016/0021-9797(72)90122-1

Brown, E.N., Kessler, M.R., Sottos, N.R., White, S.R., 2003. In situ poly(urea-formaldehyde) microencapsulation of dicyclopentadiene. J. Microencapsul. 20, 719–730. https://doi.org/10.3109/02652040309178083

Brown, R.J.S., Fatt, I., 1956. Measurements Of Fractional Wettability Of Oil Fields' Rocks By The Nuclear Magnetic Relaxation Method. Presented at the Fall Meeting of the Petroleum Branch of AIME, Society of Petroleum Engineers. https://doi.org/10.2118/743-G

Burgos, G., Birch, G., Buijse, M., 2004. Acid Fracturing With Encapsulated Citric Acid, in: SPE International Symposium and Exhibition on Formation Damage Control, SPE-86484-MS. https://doi.org/10.2118/86484-MS

Cairns, A.J., Al-Muntasheri, G.A., Sayed, M., Fu, L., Giannelis, E.P., 2016. Targeting Enhanced Production through Deep Carbonate Stimulation: Stabilized Acid Emulsions, in: SPE International Conference and Exhibition on Formation Damage Control, SPE-178967. https://doi.org/10.2118/178967-MS

Caldelas, F.M., Murphy, M., Huh, C., Bryant, S.L., 2011. Factors governing distance of nanoparticle propagation in porous media, in: SPE Production and Operations Symposium, 27-29 March, Oklahoma City, Oklahoma, USA, SPE-142305.

Carn, F., Colin, A., Pitois, O., Vignes-Adler, M., Backov, R., 2009. Foam Drainage in the Presence of Nanoparticle−Surfactant Mixtures. Langmuir 25, 7847–7856. https://doi.org/10.1021/la900414q

Carter, B.O., Adams, D.J., Cooper, A.I., 2010. Pausing a stir: heterogeneous catalysis in "dry water." Green Chem. 12, 783–785. https://doi.org/10.1039/B922508K

Carter, B.O., Weaver, J.V.M., Wang, W., Spiller, D.G., Adams, D.J., Cooper, A.I., 2011. Microencapsulation using an oil-in-water-in-air 'dry water emulsion.' Chem. Commun. 47, 8253–8255. https://doi.org/10.1039/C1CC12698A

Casteel, J.F., Djabbarah, N.F., 1988. Sweep Improvement in CO2 Flooding by Use of Foaming Agents. SPE Reserv. Eng. 3, 1,186-1,192. https://doi.org/10.2118/14392-PA

Cayias, J.L., SCHECHTER, R.S., WADE, W.H., 1975. The Measurement of Low Interfacial Tension via the Spinning Drop Technique, in: Adsorption at Interfaces, ACS Symposium Series. AMERICAN CHEMICAL SOCIETY, pp. 234–247. https://doi.org/10.1021/bk-1975-0008.ch017

Chambers, K.T., Radke, C.J., 1990. Capillary phenomena in foam flow through porous media. Interfacial Phenom. Oil Recovery.

Chen, P., Mohanty, K., 2013. Surfactant-Mediated Spontaneous Imbibition in Carbonate Rocks at Harsh Reservoir Conditions. SPE J. 18, 124–133. https://doi.org/10.2118/153960-PA

Chen, Y., Elhag, A.S., Cui, L., Worthen, A.J., Reddy, P.P., Noguera, J.A., Ou, A.M., Ma, K., Puerto, M., Hirasaki, G.J., Nguyen, Q.P., Biswal, S.L., Johnston, K.P., 2015. CO2-in-Water Foam at Elevated Temperature and Salinity Stabilized with a Nonionic Surfactant with a High Degree of Ethoxylation. Ind. Eng. Chem. Res. 54, 4252–4263. https://doi.org/10.1021/ie503674m

Chilingar, G.V., Yen, T.F., 1983. Some Notes on Wettability and Relative Permeabilities of Carbonate Reservoir Rocks, II. Energy Sources 7, 67–75. https://doi.org/10.1080/00908318308908076

Chou, S.I., Vasicek, S.L., Pisio, D.L., Jasek, D.E., Goodgame, J.A., 1992. CO2 foam field trial at north ward-estes, in: SPE Annual Technical Conference and Exhibition, 4-7 October, Washington, D.C., SPE-24643. https://doi.org/10.2118/24643-MS

Cui, H., Zhao, Y., Ren, W., Liu, Y., Wang, M., 2013. Aqueous foams stabilized solely by CoOOH nanoparticles and the resulting construction of hierarchically hollow structure. J. Nanoparticle Res. 15, 1851. https://doi.org/10.1007/s11051-013-1851-7

Cui, L., Ma, K., Puerto, M., Abdala, A.A., Tanakov, I., Lu, L.J., Chen, Y., Elhag, A., Johnston, K.P., Biswal, S.L., Hirasaki, G., 2016. Mobility of Ethomeen C12 and Carbon Dioxide (CO_2) Foam at High Temperature/High Salinity and in Carbonate Cores. SPE J. 21, 1,151-1,163. https://doi.org/10.2118/179726-PA

Cui, Z.-G., Cui, Y.-Z., Cui, C.-F., Chen, Z., Binks, B.P., 2010. Aqueous Foams Stabilized by in Situ Surface Activation of CaCO3 Nanoparticles via Adsorption of Anionic Surfactant. Langmuir 26, 12567–12574. https://doi.org/10.1021/la1016559

Cumberland, S.A., Lead, J.R., 2009a. Particle size distributions of silver nanoparticles at environmentally relevant conditions. J. Chromatogr. A 1216, 9099–9105. https://doi.org/10.1016/j.chroma.2009.07.021

Cumberland, S.A., Lead, J.R., 2009b. Particle size distributions of silver nanoparticles at environmentally relevant conditions. J. Chromatogr. A 1216, 9099–9105.

Denkov, N.D., 2004a. Mechanisms of Foam Destruction by Oil-Based Antifoams. Langmuir 20, 9463–9505. https://doi.org/10.1021/la049676o

229

Denkov, N.D., 2004b. Mechanisms of Foam Destruction by Oil-Based Antifoams. Langmuir 20, 9463–9505. https://doi.org/10.1021/la049676o

Denkov, N.D., Ivanov, I.B., Kralchevsky, P.A., Wasan, D.T., 1992. A possible mechanism of stabilization of emulsions by solid particles. J. Colloid Interface Sci. 150, 589–593. https://doi.org/10.1016/0021-9797(92)90228-E

Derjaguin, B., 1940. On the repulsive forces between charged colloid particles and on the theory of slow coagulation and stability of lyophobe sols. Trans. Faraday Soc. 35, 203–215. https://doi.org/10.1039/TF9403500203

DiCarlo, D.A., Aminzadeh, B., Roberts, M., Chung, D.H., Bryant, S.L., Huh, C., 2011. Mobility control through spontaneous formation of nanoparticle stabilized emulsions. Geophys. Res. Lett. 38, L24404. https://doi.org/10.1029/2011GL050147

Dicksen, T., Hirasaki, G.J., Miller, C.A., 2002. Conditions for Foam Generation in Homogeneous Porous Media. Presented at the SPE/DOE Improved Oil Recovery Symposium, Society of Petroleum Engineers. https://doi.org/10.2118/75176-MS

Diegoli, S., Manciulea, A.L., Begum, S., Jones, I.P., Lead, J.R., Preece, J.A., 2008. Interaction between manufactured gold nanoparticles and naturally occurring organic macromolecules. Sci. Total Environ. 402, 51–61. https://doi.org/10.1016/j.scitotenv.2008.04.023

Dieter, S., Franz-Theo, S., Helmut, B., 1968. Predominantly aqueous compositions in a fluffy powdery form approximating powdered solids behavior and process for forming same. US3393155 A.

Donaldson, E.C., Alam, W., 2013. Wettability. Elsevier.

Doorwar, S., 2015. Understanding unstable immiscible displacement in porous media (Thesis). https://doi.org/10.15781/T25G6Q

Du, Z., Bilbao-Montoya, M.P., Binks, B.P., Dickinson, E., Ettelaie, R., Murray, B.S., 2003. Outstanding stability of particle-stabilized bubbles. Langmuir 19, 3106–3108.

Eastoe, J., Dalton, J.S., 2000. Dynamic surface tension and adsorption mechanisms of surfactants at the air–water interface. Adv. Colloid Interface Sci. 85, 103–144. https://doi.org/10.1016/S0001-8686(99)00017-2

Ehrlich, R., Wygal, R.J.J., 1977. Interrelation of Crude Oil and Rock Properties With the Recovery of Oil by Caustic Waterflooding. Soc. Pet. Eng. J. 17, 263–270. https://doi.org/10.2118/5830-PA

Elimelech, M., Gregory, J., Jia, X., 2013. Particle Deposition and Aggregation: Measurement, Modelling and Simulation. Butterworth-Heinemann.

Elsharafi, M.O., Bai, B., 2012. Effect of weak preformed particle gel on unswept oil zones/areas during conformance control treatments. Ind. Eng. Chem. Res. 51, 11547–11554. https://doi.org/10.1021/ie3007227

Emrani, A.S., Ibrahim, A.F., Nasr-El-Din, H.A., 2017. Evaluation of Mobility Control with Nanoparticle-Stabilized CO_2 Foam. Presented at the SPE Latin America and Caribbean Petroleum Engineering Conference, SPE-185551-MS. https://doi.org/10.2118/185551-MS

Enick, R.M., Olsen, D.K., Ammer, J.R., Schuller, W., 2012. Mobility and Conformance Control for CO2 EOR via Thickeners, Foams, and Gels -- A Literature Review of 40 Years of Research and Pilot Tests. Presented at the SPE Improved Oil Recovery Symposium, Society of Petroleum Engineers. https://doi.org/10.2118/154122-MS

Eskandar, N.G., Simovic, S., Prestidge, C.A., 2007. Synergistic effect of silica nanoparticles and charged surfactants in the formation and stability of submicron oil-in-water emulsions. Phys. Chem. Chem. Phys. 9, 6426–6434. https://doi.org/10.1039/B710256A

Eslahian, K.A., Lang, T., Bantz, C., Keller, R., Sperling, R., Docter, D., Stauber, R., Maskos, M., 2014. Characterization of Nanoparticles Under Physiological Conditions, in: Wegener, J. (Ed.), Measuring Biological Impacts of Nanomaterials, Bioanalytical Reviews. Springer International Publishing, pp. 1–29. https://doi.org/10.1007/11663_2014_10

Espinoza, D.A., Caldelas, F.M., Johnston, K.P., Bryant, S.L., Huh, C., 2010. Nanoparticle-Stabilized Supercritical CO2 Foams for Potential Mobility Control Applications. Presented at the SPE Improved Oil Recovery Symposium, Society of Petroleum Engineers. https://doi.org/10.2118/129925-MS

Ettinger, R.A., Radke, C.J., 1992. Influence of Texture on Steady Foam Flow in Berea Sandstone. SPE Reserv. Eng. 7, 83–90. https://doi.org/10.2118/19688-PA

Falls, A.H., Hirasaki, G.J., Patzek, T.W., Gauglitz, D.A., Miller, D.D., Ratulowski, T., 1988. Development of a Mechanistic Foam Simulator: The Population Balance and Generation by Snap-Off. SPE Reserv. Eng. 3, 884–892. https://doi.org/10.2118/14961-PA

Farajzadeh, R., Krastev, R., Zitha, P.L.J., 2008. Foam films stabilized with alpha olefin sulfonate (AOS). Colloids Surf. Physicochem. Eng. Asp. 324, 35–40. https://doi.org/10.1016/j.colsurfa.2008.03.024

Farajzadeh, R., Lotfollahi, M., Eftekhari, A.A., Rossen, W.R., Hirasaki, G.J.H., 2015. Effect of Permeability on Implicit-Texture Foam Model Parameters and the Limiting Capillary Pressure. Energy Fuels 29, 3011–3018. https://doi.org/10.1021/acs.energyfuels.5b00248

Finšgar, M., Jackson, J., 2014. Application of corrosion inhibitors for steels in acidic media for the oil and gas industry: A review. Corros. Sci. 86, 17–41. https://doi.org/10.1016/j.corsci.2014.04.044

Forny, L., Pezron, I., Saleh, K., Guigon, P., Komunjer, L., 2007. Storing water in powder form by self-assembling hydrophobic silica nanoparticles. Powder Technol. 171, 15–24. https://doi.org/10.1016/j.powtec.2006.09.006

Forny, L., Saleh, K., Denoyel, R., Pezron, I., 2010. Contact Angle Assessment of Hydrophobic Silica Nanoparticles Related to the Mechanisms of Dry Water Formation. Langmuir 26, 2333–2338. https://doi.org/10.1021/la902759s

Forny, L., Saleh, K., Pezron, I., Komunjer, L., Guigon, P., 2009. Influence of mixing characteristics for water encapsulation by self-assembling hydrophobic silica nanoparticles. Powder Technol., Special Issue: 3rd International Workshop on Granulation: Granulation across the Length Scales3rd International Workshop on Granulation across the Length Scales 189, 263–269. https://doi.org/10.1016/j.powtec.2008.04.030

Frelichowska, J., Bolzinger, M.-A., Valour, J.-P., Mouaziz, H., Pelletier, J., Chevalier, Y., 2009. Pickering w/o emulsions: Drug release and topical delivery. Int. J. Pharm. 368, 7–15. https://doi.org/10.1016/j.ijpharm.2008.09.057

Friedmann, F., Jensen, J.A., 1986. Some Parameters Influencing the Formation and Propagation of Foams in Porous Media. Presented at the SPE California Regional Meeting, Society of Petroleum Engineers. https://doi.org/10.2118/15087-MS

Gauglitz, P., Friedmann, F., I. Kam, S., R. Rossen, W., 2002. Foam generation in homogeneous porous media. Chem. Eng. Sci. 57, 4037–4052. https://doi.org/10.1016/S0009-2509(02)00340-8

Giraldo, J., Benjumea, P., Lopera, S., Cortés, F.B., Ruiz, M.A., 2013. Wettability Alteration of Sandstone Cores by Alumina-Based Nanofluids. Energy Fuels 27, 3659–3665. https://doi.org/10.1021/ef4002956

Gonzenbach, U.T., Studart, A.R., Tervoort, E., Gauckler, L.J., 2006a. Ultrastable Particle-Stabilized Foams. Angew. Chem. Int. Ed. 45, 3526–3530. https://doi.org/10.1002/anie.200503676

Gonzenbach, U.T., Studart, A.R., Tervoort, E., Gauckler, L.J., 2006b. Stabilization of Foams with Inorganic Colloidal Particles. Langmuir 22, 10983–10988. https://doi.org/10.1021/la061825a

Goudarzi, A., Zhang, H., Varavei, A., Taksaudom, P., Hu, Y., Delshad, M., Bai, B., Sepehrnoori, K., 2015. A laboratory and simulation study of preformed particle gels for water conformance control. Fuel 140, 502–513. https://doi.org/10.1016/j.fuel.2014.09.081

Grieser, W.V., Wheaton, W.E., Magness, W.D., Blauch, M.E., Loghry, R., 2007. Surface Reactive Fluid's Effect on Shale, in: Production and Operations Symposium, SPE-106815-MS. https://doi.org/10.2118/106815-MS

Griffith, C., Daigle, H., 2017. Stability of polyvinyl alcohol-coated biochar nanoparticles in brine. J. Nanoparticle Res. 19, 23. https://doi.org/10.1007/s11051-016-3705-6

Guo, F., Aryana, S., 2016. An experimental investigation of nanoparticle-stabilized CO2 foam used in enhanced oil recovery. Fuel 186, 430–442. https://doi.org/10.1016/j.fuel.2016.08.058

Guo, F., He, J., Johnson, P.A., Aryana, S.A., 2017. Stabilization of CO2 foam using by-product fly ash and recyclable iron oxide nanoparticles to improve carbon utilization in EOR processes. Sustain. Energy Fuels 1, 814–822. https://doi.org/10.1039/C7SE00098G

Guo, T., Zhang, S., Qu, Z., Zhou, T., Xiao, Y., Gao, J., 2014. Experimental study of hydraulic fracturing for shale by stimulated reservoir volume. Fuel 128, 373–380. https://doi.org/10.1016/j.fuel.2014.03.029

Gupta, D.V.S., Kirk, J.W., 2009. Well treating compositions for slow release of treatment agents and methods of using the same, U.S. Patent No. 7,493,955. US7493955 B2.

Gupta, R., Mohanty, K., 2010. Temperature Effects on Surfactant-Aided Imbibition Into Fractured Carbonates. SPE J. 15, 588–597. https://doi.org/10.2118/110204-PA

Harkins, W.D., 1941. A General Thermodynamic Theory of the Spreading of Liquids to Form Duplex Films and of Liquids or Solids to Form Monolayers. J. Chem. Phys. 9, 552–568. https://doi.org/10.1063/1.1750953

Haugen, Å., Fernø, M.A., Graue, A., Bertin, H.J., 2012a. Experimental Study of Foam Flow in Fractured Oil-Wet Limestone for Enhanced Oil Recovery. SPE Reserv. Eval. Eng. 15, 218–228. https://doi.org/10.2118/129763-PA

Haugen, Å., Fernø, M.A., Graue, A., Bertin, H.J., 2012b. Experimental Study of Foam Flow in Fractured Oil-Wet Limestone for Enhanced Oil Recovery. SPE Reserv. Eval. Eng. 15, 218–228. https://doi.org/10.2118/129763-PA

Heller, J.P., 1994. CO~ 2 Foams in Enhanced Oil Recovery. Adv. Chem. Ser. 242, 201–201.

Hendraningrat, L., Li, S., Torsæter, O., 2013. A coreflood investigation of nanofluid enhanced oil recovery. J. Pet. Sci. Eng. 111, 128–138. https://doi.org/10.1016/j.petrol.2013.07.003

Hidber, P.C., Graule, T.J., Gauckler, L.J., 1997. Influence of the dispersant structure on properties of electrostatically stabilized aqueous alumina suspensions. J. Eur. Ceram. Soc. 17, 239–249. https://doi.org/10.1016/S0955-2219(96)00151-3

Hirasaki, G.J., 1989. Supplement to SPE 19505, The Steam-Foam Process--Review of Steam-Foam Process Mechanisms.

Hirasaki, G.J., Lawson, J.B., 1985. Mechanisms of Foam Flow in Porous Media: Apparent Viscosity in Smooth Capillaries. Soc. Pet. Eng. J. 25, 176–190. https://doi.org/10.2118/12129-PA

Holm, L.W., 1968. The Mechanism of Gas and Liquid Flow Through Porous Media in the Presence of Foam. Soc. Pet. Eng. J. 8, 359–369. https://doi.org/10.2118/1848-PA

Holt, T., Vassenden, F., Svorstol, I., 1996. Effects of Pressure on Foam Stability; Implications for Foam Screening. Presented at the SPE/DOE Improved Oil Recovery Symposium, Society of Petroleum Engineers. https://doi.org/10.2118/35398-MS

Horozov, T.S., 2008. Foams and foam films stabilised by solid particles. Curr. Opin. Colloid Interface Sci. 13, 134–140. https://doi.org/10.1016/j.cocis.2007.11.009

Hunter, T.N., Wanless, E.J., Jameson, G.J., Pugh, R.J., 2009. Non-ionic surfactant interactions with hydrophobic nanoparticles: Impact on foam stability. Colloids Surf. Physicochem. Eng. Asp., Interfaces Against Pollution 347, 81–89. https://doi.org/10.1016/j.colsurfa.2008.12.027

Ikem, V.O., Menner, A., Bismarck, A., 2008. High internal phase emulsions stabilized solely by functionalized silica particles. Angew. Chem. Int. Ed. 47, 8277–8279. https://doi.org/10.1002/anie.200802244

Imqam, A., Bai, B., 2015. Optimizing the strength and size of preformed particle gels for better conformance control treatment. Fuel 148, 178–185. https://doi.org/10.1016/j.fuel.2015.01.022

Imqam, A., Bai, B., Al Ramadan, M., Wei, M., Delshad, M., Sepehrnoori, K., 2015. Preformed-Particle-Gel Extrusion Through Open Conduits During Conformance-Control Treatments. SPE J. 20, 1,083-1,093. https://doi.org/10.2118/169107-PA

Irani, C.A., Solomon, C.J., 1986. Slim-Tube Investigation Of CO2 Foams. Presented at the SPE Enhanced Oil Recovery Symposium, Society of Petroleum Engineers. https://doi.org/10.2118/14962-MS

Israelachvili, J.N., 1985. Intermolecular and Surface Forces: With Applications to Colloidal and Biological Systems. Academic Press.

Jensen, J.A., Friedmann, F., 1987. Physical and Chemical Effects of an Oil phase on the Propagation of Foam in Porous Media, in: SPE California Regional Meeting, 8-10 April, Ventura, California, SPE-16375.

Jiang, J., Oberdörster, G., Biswas, P., 2009. Characterization of size, surface charge, and agglomeration state of nanoparticle dispersions for toxicological studies. J. Nanoparticle Res. 11, 77–89. https://doi.org/10.1007/s11051-008-9446-4

Jiang, L., Li, S., Yu, W., Wang, J., Sun, Q., Li, Z., 2016. Interfacial study on the interaction between hydrophobic nanoparticles and ionic surfactants. Colloids Surf. Physicochem. Eng. Asp. 488, 20–27. https://doi.org/10.1016/j.colsurfa.2015.10.007

Johonnott, E.S.J., 1906. LXVIII. The black spot in thin liquid films. Philos. Mag. 11, 746–753. https://doi.org/10.1080/14786440609463494

Kalfayan, L.J., 2007. Fracture Acidizing: History, Present State, and Future, in: SPE Hydraulic Fracturing Technology Conference, SPE-106371-MS. https://doi.org/10.2118/106371-MS

Kalyanaraman, N., Arnold, C., Gupta, A., Tsau, J.S., Ghahfarokhi, R.B., 2017. Stability improvement of CO2 foam for enhanced oil-recovery applications using polyelectrolytes and polyelectrolyte complex nanoparticles. J. Appl. Polym. Sci. 134, n/a-n/a. https://doi.org/10.1002/app.44491

Kam, S.I., Rossen, W.R., 1999. Anomalous Capillary Pressure, Stress, and Stability of Solids-Coated Bubbles. J. Colloid Interface Sci. 213, 329–339. https://doi.org/10.1006/jcis.1999.6107

Kaptay, G., 2006. On the equation of the maximum capillary pressure induced by solid particles to stabilize emulsions and foams and on the emulsion stability diagrams. Colloids Surf. Physicochem. Eng. Asp. 282, 387–401. https://doi.org/10.1016/j.colsurfa.2005.12.021

Karimi, A., Fakhroueian, Z., Bahramian, A., Pour Khiabani, N., Darabad, J.B., Azin, R., Arya, S., 2012a. Wettability Alteration in Carbonates using Zirconium Oxide Nanofluids: EOR Implications. Energy Fuels 26, 1028–1036. https://doi.org/10.1021/ef201475u

Karimi, A., Fakhroueian, Z., Bahramian, A., Pour Khiabani, N., Darabad, J.B., Azin, R., Arya, S., 2012b. Wettability Alteration in Carbonates using Zirconium Oxide Nanofluids: EOR Implications. Energy Fuels 26, 1028–1036. https://doi.org/10.1021/ef201475u

Khatib, Z.I., Hirasaki, G.J., Falls, A.H., 1988a. Effects of capillary pressure on coalescence and phase mobilities in foams flowing through porous media. SPE Reserv. Eng. 3, 919–926.

Khatib, Z.I., Hirasaki, G.J., Falls, A.H., 1988b. Effects of capillary pressure on coalescence and phase mobilities in foams flowing through porous media. SPE Reserv. Eng. 3, 919–926.

Kim, I., Worthen, A.J., Johnston, K.P., DiCarlo, D.A., Huh, C., 2016. Size-dependent properties of silica nanoparticles for Pickering stabilization of emulsions and foams. J. Nanoparticle Res. 18, 82. https://doi.org/10.1007/s11051-016-3395-0

Kim, T.W., Kovscek, A.R., 2013. Wettability Alteration of a Heavy Oil/Brine/Carbonate System with Temperature. Energy Fuels 27, 2984–2998. https://doi.org/10.1021/ef400204k

Kostakis, T., Ettelaie, R., Murray, B.S., 2007. Enhancement of stability of bubbles to disproportionation using hydrophilic silica particles mixed with surfactants or proteins, in: Food Colloids. pp. 357–368.

Koval, E.J., 1963. A Method for Predicting the Performance of Unstable Miscible Displacement in Heterogeneous Media. Soc. Pet. Eng. J. 3, 145–154. https://doi.org/10.2118/450-PA

Kovscek, A.R., Patzek, T.W., Radke, C.J., 1994. Mechanistic Prediction of Foam Displacement in Multidimensions: A Population Balance Approach. Presented at the SPE/DOE Improved Oil Recovery Symposium, Society of Petroleum Engineers. https://doi.org/10.2118/27789-MS

Kovscek, A.R., Radke, C.J., 1996. Gas bubble snap-off under pressure-driven flow in constricted noncircular capillaries. Colloids Surf. Physicochem. Eng. Asp. 117, 55–76. https://doi.org/10.1016/0927-7757(96)03637-0

Kovscek, A.R., Radke, C.J., 1994. Fundamentals of Foam Transport in Porous Media, in: Foams: Fundamentals and Applications in the Petroleum Industry, Advances in Chemistry. American Chemical Society, pp. 115–163. https://doi.org/10.1021/ba-1994-0242.ch003

Kovscek, A.R., Tadeusz, W.P., Radke, C.J., 1997. Mechanistic foam flow simulation in heterogeneous and multidimensional porous media. SPE J. 2, 511–526.

Kralchevski, P., Nikolov, A., Wasan, D.T., Ivanov, I., 1990. Formation and expansion of dark spots in stratifying foam films. Langmuir 6, 1180–1189. https://doi.org/10.1021/la00096a026

Kuhlman, M.I., 1990. Visualizing the Effect of Light Oil on CO2 Foams. J. Pet. Technol. 42, 902–908. https://doi.org/10.2118/17356-PA

Kumar, K., Dao, E.K., Mohanty, K.K., 2008. Atomic Force Microscopy Study of Wettability Alteration by Surfactants. SPE J. 13, 137–145. https://doi.org/10.2118/93009-PA

Lake, L.W., 1989. Enhanced oil recovery. Prentice Hall, Englewood Cliffs, NJ.

Lake, L.W., Venuto, P.B., 1990. A niche for enhanced oil recovery in the 1990s. Oil Gas J. 88, 62–67.

Leach, R.O., Wagner, O.R., Wood, H.W., Harpke, C.F., 1962. A Laboratory and Field Study of Wettability Adjustment in Water Flooding. J. Pet. Technol. 14, 206–212. https://doi.org/10.2118/119-PA

Lee, D., Cho, H., Lee, J., Huh, C., Mohanty, K., 2015. Fly ash nanoparticles as a CO2 foam stabilizer. Powder Technol. 283, 77–84. https://doi.org/10.1016/j.powtec.2015.05.010

Lee, M.-H., Oh, S.-G., Moon, S.-K., Bae, S.-Y., 2001. Preparation of Silica Particles Encapsulating Retinol Using O/W/O Multiple Emulsions. J. Colloid Interface Sci. 240, 83–89. https://doi.org/10.1006/jcis.2001.7699

Li, N., Dai, J., Li, J., Bai, F., Liu, P., Luo, Z., 2016. Application status and research progress of shale reservoirs acid treatment technology. Nat. Gas Ind. B 3, 165–172. https://doi.org/10.1016/j.ngib.2016.06.001

Li, R.F., Hirasaki, G., Miller, C.A., Masalmeh, S.K., 2012. Wettability Alteration and Foam Mobility Control in a Layered, 2D Heterogeneous Sandpack. SPE J. 17, 1,207-1,220. https://doi.org/10.2118/141462-PA

Li, S., Li, Z., Wang, P., 2016. Experimental Study of the Stabilization of CO2 Foam by Sodium Dodecyl Sulfate and Hydrophobic Nanoparticles. Ind. Eng. Chem. Res. 55, 1243–1253. https://doi.org/10.1021/acs.iecr.5b04443

Li, S., Qiao, C., Li, Z., Wanambwa, S., 2017. Properties of Carbon Dioxide Foam Stabilized by Hydrophilic Nanoparticles and Hexadecyltrimethylammonium Bromide. Energy Fuels 31, 1478–1488. https://doi.org/10.1021/acs.energyfuels.6b03130

237

Li, W., Oliveira, H.A., Maxey, J.E., 2013. Invert Emulsion Acid for Simultaneous Acid and Proppant Fracturing, in: Offshore Technology Conference, SPE-24332-MS. Presented at the OTC Brasil. https://doi.org/10.4043/24332-MS

Liontas, R., Ma, K., Hirasaki, G.J., Biswal, S.L., 2013. Neighbor-induced bubble pinch-off: novel mechanisms of in situ foam generation in microfluidic channels. Soft Matter 9, 10971–10984. https://doi.org/10.1039/C3SM51605A

Liu, K., Jiang, J., Cui, Z., Binks, B.P., 2017. pH-Responsive Pickering Emulsions Stabilized by Silica Nanoparticles in Combination with a Conventional Zwitterionic Surfactant. Langmuir 33, 2296–2305. https://doi.org/10.1021/acs.langmuir.6b04459

Liu, Q., Zhang, S., Sun, D., Xu, J., 2009. Aqueous foams stabilized by hexylamine-modified Laponite particles. Colloids Surf. Physicochem. Eng. Asp. 338, 40–46. https://doi.org/10.1016/j.colsurfa.2008.12.035

Liu, Y., Bai, B., Shuler, P.J., 2006. Application and Development of Chemical-Based Conformance Control Treatments in China Oilfields. Presented at the SPE/DOE Symposium on Improved Oil Recovery, Society of Petroleum Engineers. https://doi.org/10.2118/99641-MS

Liu, Y., Grigg, R.B., Svec, R.K., 2005. CO2 Foam Behavior: Influence of Temperature, Pressure, and Concentration of Surfactant. Presented at the SPE Production Operations Symposium, Society of Petroleum Engineers. https://doi.org/10.2118/94307-MS

Lucassen-Reynders, E.H., 1963. Contact Angles and Adsorption on Solids. J. Phys. Chem. 67, 969–972. https://doi.org/10.1021/j100799a005

Maestro, A., Rio, E., Drenckhan, W., Langevin, D., Salonen, A., 2014. Foams stabilised by mixtures of nanoparticles and oppositely charged surfactants: relationship between bubble shrinkage and foam coarsening. Soft Matter 10, 6975–6983. https://doi.org/10.1039/C4SM00047A

Mahani, H., Keya, A.L., Berg, S., Bartels, W.-B., Nasralla, R., Rossen, W.R., 2015. Insights into the Mechanism of Wettability Alteration by Low-Salinity Flooding (LSF) in Carbonates. Energy Fuels 29, 1352–1367. https://doi.org/10.1021/ef5023847

Martinez, A.C., Rio, E., Delon, G., Saint-Jalmes, A., Langevin, D., Binks, B.P., 2008. On the origin of the remarkable stability of aqueous foams stabilised by nanoparticles: link with microscopic surface properties. Soft Matter 4, 1531–1535. https://doi.org/10.1039/B804177F

Mast, R.F., 1972. Microscopic Behavior of Foam in Porous Media. Presented at the Fall Meeting of the Society of Petroleum Engineers of AIME, Society of Petroleum Engineers. https://doi.org/10.2118/3997-MS

Miller, C.A., Neogi, P., 1985. Interfacial phenomena. Marcel Dekker, New York.

Mo, D., Yu, J., Liu, N., Lee, R.L., 2012. Study of the Effect of Different Factors on Nanoparticle-Stablized CO_2 Foam for Mobility Control. Presented at the SPE Annual Technical Conference and Exhibition, Society of Petroleum Engineers. https://doi.org/10.2118/159282-MS

Mohan, K., Gupta, R., Mohanty, K.K., 2011. Wettability Altering Secondary Oil Recovery in Carbonate Rocks. Energy Fuels 25, 3966–3973. https://doi.org/10.1021/ef200449y

Morita, T., Sakamura, Y., Horikiri, Y., Suzuki, T., Yoshino, H., 2000. Protein encapsulation into biodegradable microspheres by a novel S/O/W emulsion method using poly(ethylene glycol) as a protein micronization adjuvant. J. Controlled Release 69, 435–444. https://doi.org/10.1016/S0168-3659(00)00326-6

Morrow, N.R., 1990. Interfacial Phenomena in Petroleum Recovery. CRC Press.

Mukherjee, J., Nguyen, Q.P., Scherlin, J., Vanderwal, P., Rozowski, P., 2016. CO_2 Foam Pilot in Salt Creek Field, Natrona County, WY: Phase III: Analysis of Pilot Performance, in: SPE Improved Oil Recovery Conference, 11-13 April, Tulsa, Oklahoma, USA, SPE-179635. Society of Petroleum Engineers. https://doi.org/10.2118/179635-MS

Murphy, M.J., 2012. Experimental analysis of electrostatic and hydrodynamic forces affecting nanoparticle retention in porous media (thesis).

Murray, B.S., Durga, K., Yusoff, A., Stoyanov, S.D., 2011. Stabilization of foams and emulsions by mixtures of surface active food-grade particles and proteins. Food Hydrocoll. 25, 627–638. https://doi.org/10.1016/j.foodhyd.2010.07.025

Najafabadi, N.F., Delshad, M., Sepehrnoori, K., Nguyen, Q.P., Zhang, J., 2008. Chemical Flooding of Fractured Carbonates Using Wettability Modifiers. Presented at the SPE Symposium on Improved Oil Recovery, Society of Petroleum Engineers. https://doi.org/10.2118/113369-MS

Napper, D.H., 1983. Polymeric stabilization of colloidal dispersions. Academic Press.

Nasr-El-Din, H.A., Al-Anazi, H.A., Mohamed, S.K., 2000. Stimulation of Water-Disposal Wells Using Acid-in-Diesel Emulsions: Case Histories. SPE Prod. Facil. 15, 176–182. https://doi.org/10.2118/65069-PA

Nasr-El-Din, H.A., Al-Zahrani, A.A., Garzon, F.O., Giraldo, C.A.F., Al-Hakami, I.M., Al-Marri, H.M., 2009. Acid Fracturing of Gas Wells by Use of an Acid Precursor in the Form of Solid Beads: Lessons Learned From First Field Application. SPE Prod. Oper. 24, 320–335. https://doi.org/10.2118/110895-PA

Nazzaro, F., Orlando, P., Fratianni, F., Coppola, R., 2012. Microencapsulation in food science and biotechnology. Curr. Opin. Biotechnol., Food biotechnology - Plant biotechnology 23, 182–186. https://doi.org/10.1016/j.copbio.2011.10.001

Nguyen, P., Fadaei, H., Sinton, D., 2014. Nanoparticle Stabilized CO_2 in Water Foam for Mobility Control in Enhanced Oil Recovery via Microfluidic Method. Presented at the SPE Heavy Oil Conference-Canada, Society of Petroleum Engineers. https://doi.org/10.2118/170167-MS

Orr, F.M., Heller, J.P., Taber, J.J., 1982. Carbon dioxide flooding for enhanced oil recovery: Promise and problems. J. Am. Oil Chem. Soc. 59, 810A–817A. https://doi.org/10.1007/BF02634446

Outlook, A.E., 2001. DOE/EIA-0383; Department of Energy. Energy Inf. Adm. Wash. DC.

Panthi, K., Singh, R., Mohanty, K.K., 2017. Microencapsulation and Stimuli-Responsive Controlled Release of Particles Using Water-in-Air Powders. Langmuir 33, 3998–4010. https://doi.org/10.1021/acs.langmuir.7b00149

Patzek, T.W., 1996a. Field applications of steam foam for mobility improvement and profile control. SPE Reserv. Eng. 11, 79–86.

Patzek, T.W., 1996b. Field Applications of Steam Foam for Mobility Improvement and Profile Control. SPE Reserv. Eng. 11, 79–86. https://doi.org/10.2118/29612-PA

Pei, H., Zhang, G., Ge, J., Wang, J., Ding, B., Liu, X., 2010. Investigation of Polymer-Enhanced Foam Flooding with Low Gas/Liquid Ratio for Improving Heavy Oil Recovery, in: Canadian Unconventional Resources and International Petroleum Conference, 19-21 October, Calgary, Alberta, Canada, SPE-137171. https://doi.org/10.2118/137171-MS

Peters, E.J., 2012. Advanced Petrophysics: Volume 1: Geology, Porosity, Absolute Permeability, Heterogeneity and Geostatistics. Live Oak Book Co Austin Tex.

Pickering, S.U., 1907. CXCVI.—Emulsions. J. Chem. Soc., Trans. 91, 2001–2021. https://doi.org/10.1039/CT9079102001

Ponnapati, R., Karazincir, O., Dao, E., Ng, R., Mohanty, K.K., Krishnamoorti, R., 2011. Polymer-Functionalized Nanoparticles for Improving Waterflood Sweep Efficiency:

Characterization and Transport Properties. Ind. Eng. Chem. Res. 50, 13030–13036. https://doi.org/10.1021/ie2019257

Pritchett, J., Frampton, H., Brinkman, J., Cheung, S., Morgan, J., Chang, K.T., Williams, D., Goodgame, J., 2003. Field Application of a New In-Depth Waterflood Conformance Improvement Tool. Presented at the SPE International Improved Oil Recovery Conference in Asia Pacific, Society of Petroleum Engineers. https://doi.org/10.2118/84897-MS

Pugh, R.J., 1996. Foaming, foam films, antifoaming and defoaming. Adv. Colloid Interface Sci. 64, 67–142. https://doi.org/10.1016/0001-8686(95)00280-4

Ramsden, W., 1903. Separation of Solids in the Surface-Layers of Solutions and'Suspensions'(Observations on Surface-Membranes, Bubbles, Emulsions, and Mechanical Coagulation).–Preliminary Account. Proc. R. Soc. Lond. 72, 156–164.

Ransohoff, T.C., Radke, C.J., 1988. Mechanisms of Foam Generation in Glass-Bead Packs. SPE Reserv. Eng. 3, 573–585. https://doi.org/10.2118/15441-PA

Roberts, M., Aminzadeh, B., DiCarlo, D.A., Bryant, S.L., Huh, C., 2012. Generation of Nanoparticle-Stabilized Emulsions in Fractures. Presented at the SPE Improved Oil Recovery Symposium, Society of Petroleum Engineers. https://doi.org/10.2118/154228-MS

Robinson, J.V., Woods, W.W., 1948. A method of selecting foam inhibitors. J. Soc. Chem. Ind. 67, 361–365. https://doi.org/10.1002/jctb.5000670908

Roehl, P.O., Choquette, P.W., 2012. Carbonate petroleum reservoirs. Springer Science & Business Media.

Roof, J.G., 1970. Snap-Off of Oil Droplets in Water-Wet Pores. Soc. Pet. Eng. J. 10, 85–90. https://doi.org/10.2118/2504-PA

Rosen, M.J., Zhu, B.Y., 1984. Synergism in binary mixtures of surfactants. J. Colloid Interface Sci. 99, 427–434. https://doi.org/10.1016/0021-9797(84)90129-2

Rossen, W.R., 1996. Foams in enhanced oil recovery. Surfactant Sci. Ser. 413–464.

Rossen, W.R., Lu, Q., 1997. Effect of Capillary Crossflow on Foam Improved Oil Recovery. Presented at the SPE Western Regional Meeting, 25-27 June, Long Beach, California, SPE-38319. https://doi.org/10.2118/38319-MS

Rossen, W.R., Van Duijn, C.J., Nguyen, Q.P., Shen, C., Vikingstad, A.K., 2010a. Injection strategies to overcome gravity segregation in simultaneous gas and water injection into homogeneous reservoirs. SPE J. 15, 76–90.

Rossen, W.R., van Duijn, C.J., Nguyen, Q.P., Shen, C., Vikingstad, A.K., 2010b. Injection Strategies To Overcome Gravity Segregation in Simultaneous Gas and Water Injection Into Homogeneous Reservoirs. SPE J. 15, 76–90. https://doi.org/10.2118/99794-PA

Salarvand, Z., Amirnasr, M., Talebian, M., Raeissi, K., Meghdadi, S., 2017. Enhanced corrosion resistance of mild steel in 1 M HCl solution by trace amount of 2-phenyl-benzothiazole derivatives: Experimental, quantum chemical calculations and molecular dynamics (MD) simulation studies. Corros. Sci. 114, 133–145. https://doi.org/10.1016/j.corsci.2016.11.002

Salathiel, R.A., 1973. Oil Recovery by Surface Film Drainage In Mixed-Wettability Rocks. J. Pet. Technol. 25, 1,216-1,224. https://doi.org/10.2118/4104-PA

Saleh, K., Forny, L., Guigon, P., Pezron, I., 2011. Dry water: From physico-chemical aspects to process-related parameters. Chem. Eng. Res. Des., Special Issue on Agglomeration 89, 537–544. https://doi.org/10.1016/j.cherd.2010.06.005

Saleh, N., Sarbu, T., Sirk, K., Lowry, G.V., Matyjaszewski, K., Tilton, R.D., 2005. Oil-in-Water Emulsions Stabilized by Highly Charged Polyelectrolyte-Grafted Silica Nanoparticles. Langmuir 21, 9873–9878. https://doi.org/10.1021/la050654r

Salter, S.J., Mohanty, K.K., 1982. Multiphase Flow in Porous Media: I. Macroscopic Observations and Modeling, in: SPE Annual Technical Conference and Exhibition. New Orleans, Louisiana. SPE-11017. https://doi.org/10.2118/11017-MS

Sanchez, J.M., Hazlett, R.D., 1992. Foam Flow Through an Oil-Wet Porous Medium: A Laboratory Study. SPE Reserv. Eng. 7, 91–97. https://doi.org/10.2118/19687-PA

Schembre, J.M., Tang, G.-Q., Kovscek, A.R., 2006. Interrelationship of Temperature and Wettability on the Relative Permeability of Heavy Oil in Diatomaceous Rocks (includes associated discussion and reply). SPE Reserv. Eval. Eng. 9, 239–250. https://doi.org/10.2118/93831-PA

Schindelin, J., Arganda-Carreras, I., Frise, E., Kaynig, V., Longair, M., Pietzsch, T., Preibisch, S., Rueden, C., Saalfeld, S., Schmid, B., others, 2012. Fiji: an open-source platform for biological-image analysis. Nat. Methods 9, 676–682.

Schramm, L.L., Mannhardt, K., 1996. The effect of wettability on foam sensitivity to crude oil in porous media. J. Pet. Sci. Eng. 15, 101–113. https://doi.org/10.1016/0920-4105(95)00068-2

Schramm, L.L., Novosad, J.J., 1990. Micro-visualization of foam interactions with a crude oil. Colloids Surf. 46, 21–43. https://doi.org/10.1016/0166-6622(90)80046-7

Schramm, L.L., Wassmuth, F., 1994. Foams: Basic Principles, in: Foams: Fundamentals and Applications in the Petroleum Industry, Advances in Chemistry. American Chemical Society, pp. 3–45. https://doi.org/10.1021/ba-1994-0242.ch001

Schulze-Zachau, F., Braunschweig, B., 2017. Structure of Polystyrenesulfonate/Surfactant Mixtures at Air–Water Interfaces and Their Role as Building Blocks for Macroscopic Foam. Langmuir 33, 3499–3508. https://doi.org/10.1021/acs.langmuir.7b00400

Seethepalli, A., Adibhatla, B., Mohanty, K.K., 2004. Physicochemical Interactions During Surfactant Flooding of Fractured Carbonate Reservoirs. SPE J. 9, 411–418. https://doi.org/10.2118/89423-PA

Sethumadhavan, G., Nikolov, A., Wasan, D., 2004. Stability of films with nanoparticles. J. Colloid Interface Sci. 272, 167–171. https://doi.org/10.1016/j.jcis.2003.11.024

Sethumadhavan, G.N., Nikolov, A.D., Wasan, D.T., 2001. Stability of Liquid Films Containing Monodisperse Colloidal Particles. J. Colloid Interface Sci. 240, 105–112. https://doi.org/10.1006/jcis.2001.7628

Shariatpanahi, S.F., Strand, S., Austad, T., 2011. Initial Wetting Properties of Carbonate Oil Reservoirs: Effect of the Temperature and Presence of Sulfate in Formation Water. Energy Fuels 25, 3021–3028. https://doi.org/10.1021/ef200033h

Sharma, G., Mohanty, K., 2013. Wettability Alteration in High-Temperature and High-Salinity Carbonate Reservoirs. SPE J. 18, 646–655. https://doi.org/10.2118/147306-PA

Sharma, H., Dufour, S., Arachchilage, G.W.P., Weerasooriya, U., Pope, G.A., Mohanty, K., 2015. Alternative alkalis for ASP flooding in anhydrite containing oil reservoirs. Fuel 140, 407–420.

Shi, J., Varavei, A., Huh, C., Delshad, M., Sepehrnoori, K., Li, X., 2011. Transport Model Implementation and Simulation of Microgel Processes for Conformance and Mobility Control Purposes. Energy Fuels 25, 5063–5075. https://doi.org/10.1021/ef200835c

Simjoo, M., Nguyen, Q.P., Zitha, P.L.J., 2012. Rheological Transition during Foam Flow in Porous Media. Ind. Eng. Chem. Res. 51, 10225–10231. https://doi.org/10.1021/ie202218z

Simovic, S., Prestidge, C.A., 2007. Nanoparticle layers controlling drug release from emulsions. Eur. J. Pharm. Biopharm. 67, 39–47. https://doi.org/10.1016/j.ejpb.2007.01.011

Singh, R., Gupta, A., Mohanty, K.K., Huh, C., Lee, D., Cho, H., 2015. Fly Ash Nanoparticle-Stabilized CO2-in-Water Foams for Gas Mobility Control Applications, in:

SPE Annual Technical Conference and Exhibition, Houston, Texas, USA, SPE-175057. https://doi.org/10.2118/175057-MS

Singh, R., Mohanty, K.K., 2017a. Foam flow in a layered, heterogeneous porous medium: A visualization study. Fuel 197, 58–69. https://doi.org/10.1016/j.fuel.2017.02.019

Singh, R., Mohanty, K.K., 2017b. Nanoparticle-Stabilized Foams for High-Temperature, High-Salinity Oil Reservoirs, in: SPE Annual Technical Conference and Exhibition, San Antonio, Texas, SPE-187165.

Singh, R., Mohanty, K.K., 2016a. Foams Stabilized by In-Situ Surface-Activated Nanoparticles in Bulk and Porous Media. SPE J. 21, 121–130. https://doi.org/10.2118/170942-PA

Singh, R., Mohanty, K.K., 2016b. Foams with Wettability-Altering Capabilities for Oil-Wet Carbonates: A Synergistic Approach. SPE J. 21, 1126–1139. https://doi.org/10.2118/175027-PA

Singh, R., Mohanty, K.K., 2015. Synergy between nanoparticles and surfactants in stabilizing foams for oil recovery. Energy Fuels 29, 467–479. https://doi.org/10.1021/ef5015007

Singh, R., Panthi, K., Mohanty, K.K., 2017. Microencapsulation of Acids by Nanoparticles for Acid Treatment of Shales. Energy Fuels 31, 11755–11764. https://doi.org/10.1021/acs.energyfuels.7b02003

Smith, C.F., Dollarhide, F.E., Byth, N.J., 1978. Acid Corrosion Inhibitors - Are We Getting What We Need? J. Pet. Technol. 30, 737–746. https://doi.org/10.2118/5644-PA

Still, J.W., Dismuke, K., Frenier, W.W., 2007. Generating Acid Downhole in Acid Fracturing. US7166560 B2.

Stocco, A., Drenckhan, W., Rio, E., Langevin, D., Binks, B.P., 2009. Particle-stabilised foams: an interfacial study. Soft Matter 5, 2215–2222. https://doi.org/10.1039/B901180C

Stocco, A., Rio, E., Binks, B.P., Langevin, D., 2011. Aqueous foams stabilized solely by particles. Soft Matter 7, 1260–1267. https://doi.org/10.1039/C0SM01290D

Strand, S., Standnes, D.C., Austad, T., 2003. Spontaneous Imbibition of Aqueous Surfactant Solutions into Neutral to Oil-Wet Carbonate Cores: Effects of Brine Salinity and Composition. Energy Fuels 17, 1133–1144. https://doi.org/10.1021/ef030051s

Subramaniam, A.B., Mejean, C., Abkarian, M., Stone, H.A., 2006. Microstructure, morphology, and lifetime of armored bubbles exposed to surfactants. Langmuir 22, 5986–5990.

Sun, Q., Li, Z., Li, S., Jiang, L., Wang, J., Wang, P., 2014a. Utilization of Surfactant-Stabilized Foam for Enhanced Oil Recovery by Adding Nanoparticles. Energy Fuels 28, 2384–2394. https://doi.org/10.1021/ef402453b

Sun, Q., Li, Z., Li, S., Jiang, L., Wang, J., Wang, P., 2014b. Utilization of surfactant-stabilized foam for enhanced oil recovery by adding nanoparticles. Energy Fuels 28, 2384–2394.

Sun, Q., Li, Z., Wang, J., Li, S., Li, B., Jiang, L., Wang, H., Lü, Q., Zhang, C., Liu, W., 2015. Aqueous foam stabilized by partially hydrophobic nanoparticles in the presence of surfactant. Colloids Surf. Physicochem. Eng. Asp. 471, 54–64. https://doi.org/10.1016/j.colsurfa.2015.02.007

Taber, J.J., Martin, F.D., Seright, R.S., 1997. EOR Screening Criteria Revisited - Part 1: Introduction to Screening Criteria and Enhanced Recovery Field Projects. SPE Reserv. Eng. 12, 189–198. https://doi.org/10.2118/35385-PA

Tang, G.Q., Morrow, N.R., 1997. Salinity, Temperature, Oil Composition, and Oil Recovery by Waterflooding. SPE Reserv. Eng. 12, 269–276. https://doi.org/10.2118/36680-PA

Taylor, K.C., Nasr-El-Din, H.A., 2003. Laboratory Evaluation of In-Situ Gelled Acids for Carbonate Reservoirs. SPE J. 8, 426–434. https://doi.org/10.2118/87331-PA

Tcholakova, S., Mitrinova, Z., Golemanov, K., Denkov, N.D., Vethamuthu, M., Ananthapadmanabhan, K.P., 2011. Control of Ostwald Ripening by Using Surfactants with High Surface Modulus. Langmuir 27, 14807–14819. https://doi.org/10.1021/la203952p

Tigges, B., Dederichs, T., Möller, M., Liu, T., Richtering, W., Weichold, O., 2010. Interfacial Properties of Emulsions Stabilized with Surfactant and Nonsurfactant Coated Boehmite Nanoparticles. Langmuir 26, 17913–17918. https://doi.org/10.1021/la102761k

Tikekar, R.V., Pan, Y., Nitin, N., 2013. Fate of curcumin encapsulated in silica nanoparticle stabilized Pickering emulsion during storage and simulated digestion. Food Res. Int. 51, 370–377. https://doi.org/10.1016/j.foodres.2012.12.027

Tong, S., Mohanty, K.K., 2016. Proppant transport study in fractures with intersections. Fuel 181, 463–477. https://doi.org/10.1016/j.fuel.2016.04.144

Tong, S., Singh, R., Mohanty, K.K., 2017. Proppant Transport in Fractures with Foam-Based Fracturing Fluids, in: SPE Annual Technical Conference and Exhibition, San Antonio, Texas, SPE-187376-MS.

Treiber, L.E., Owens, W.W., 1972. A Laboratory Evaluation of the Wettability of Fifty Oil-Producing Reservoirs. Soc. Pet. Eng. J. 12, 531–540. https://doi.org/10.2118/3526-PA

Vatanparast, H., Samiee, A., Bahramian, A., Javadi, A., 2017. Surface behavior of hydrophilic silica nanoparticle-SDS surfactant solutions: I. Effect of nanoparticle concentration on foamability and foam stability. Colloids Surf. Physicochem. Eng. Asp. 513, 430–441. https://doi.org/10.1016/j.colsurfa.2016.11.012

Vikingstad, A.K., Aarra, M.G., Skauge, A., 2006. Effect of surfactant structure on foam–oil interactions. Colloids Surf. Physicochem. Eng. Asp. 279, 105–112. https://doi.org/10.1016/j.colsurfa.2005.12.047

Vikingstad, A.K., Skauge, A., Høiland, H., Aarra, M., 2005. Foam–oil interactions analyzed by static foam tests. Colloids Surf. Physicochem. Eng. Asp. 260, 189–198. https://doi.org/10.1016/j.colsurfa.2005.02.034

Wacker HDK® Pyrogenic Silica Brochure, Wacker-Chemie GmbH, Germany, 2016., n.d.

Wang, C., Bobba, A.D., Attinti, R., Shen, C., Lazouskaya, V., Wang, L.-P., Jin, Y., 2012. Retention and Transport of Silica Nanoparticles in Saturated Porous Media: Effect of Concentration and Particle Size. Environ. Sci. Technol. 46, 7151–7158. https://doi.org/10.1021/es300314n

Wang, J., Xue, G., Tian, B., Li, S., Chen, K., Wang, D., Sun, Y., Xu, H., Petkov, J.T., Li, Z., 2017. Interaction between Surfactants and SiO2 Nanoparticles in Multiphase Foam and Its Plugging Ability. Energy Fuels 31, 408–417. https://doi.org/10.1021/acs.energyfuels.6b02592

Wang, L., Mohanty, K., 2014. Enhanced Oil Recovery in Gasflooded Carbonate Reservoirs by Wettability-Altering Surfactants. SPE J. 20, 60–69. https://doi.org/10.2118/166283-PA

Wang, W., Bray, C.L., Adams, D.J., Cooper, A.I., 2008. Methane Storage in Dry Water Gas Hydrates. J. Am. Chem. Soc. 130, 11608–11609. https://doi.org/10.1021/ja8048173

Wang, W., Liu, X., Xie, Y., Zhang, H., Yu, W., Xiong, Y., Xie, W., Ma, X., 2006. Microencapsulation using natural polysaccharides for drug delivery and cell implantation. J. Mater. Chem. 16, 3252–3267. https://doi.org/10.1039/B603595G

Wang, Y., Ge, J., Zhang, W., Zhang, G., Lin, Y., Song, K., 2016. Surface property and enhanced oil recovery study of foam aqueous dispersions comprised of surfactants–organic acids–nanoparticles. RSC Adv. 6, 113478–113486. https://doi.org/10.1039/C6RA22988C

Wang, Z., Wille, U., Juaristi, E., 2017. Encyclopedia of Physical Organic Chemistry, , 6 Volume Set. John Wiley & Sons.

Wei, W., Varavei, A., Sepehrnoori, K., 2017. Modeling and Analysis on the Effect of Two-Phase Flow on Wormhole Propagation in Carbonate Acidizing. SPE J. https://doi.org/10.2118/186111-PA

Williams, B.B., Gidley, J.L., Schechter, R.S., 1979. Acidizing fundamentals. Henry L. Doherty Memorial Fund of AIME, Society of Petroleum Engineers of AIME.

Williams, J.M., 1991. High internal phase water-in-oil emulsions: influence of surfactants and cosurfactants on emulsion stability and foam quality. Langmuir 7, 1370–1377.

World energy outlook, 2006. . OECD/IEA.

Worldwide EOR survey, 2014. . Oil Gas J. 112.

Worthen, A., Tran, V., A. Cornell, K., M. Truskett, T., P. Johnston, K., 2016. Steric stabilization of nanoparticles with grafted low molecular weight ligands in highly concentrated brines including divalent ions. Soft Matter 12, 2025–2039. https://doi.org/10.1039/C5SM02787J

Worthen, A.J., Bagaria, H.G., Chen, Y., Bryant, S.L., Huh, C., Johnston, K.P., 2013a. Nanoparticle-stabilized carbon dioxide-in-water foams with fine texture. J. Colloid Interface Sci. 391, 142–151.

Worthen, A.J., Bryant, S.L., Huh, C., Johnston, K.P., 2013b. Carbon dioxide-in-water foams stabilized with nanoparticles and surfactant acting in synergy. AIChE J. 59, 3490–3501. https://doi.org/10.1002/aic.14124

Wuelfing, W.P., Zamborini, F.P., Templeton, A.C., Wen, X., Yoon, H., Murray, R.W., 2001. Monolayer-Protected Clusters: Molecular Precursors to Metal Films. Chem. Mater. 13, 87–95. https://doi.org/10.1021/cm0005440

Xu, K., Zhu, P., Colon, T., Huh, C., Balhoff, M., 2017. A Microfluidic Investigation of the Synergistic Effect of Nanoparticles and Surfactants in Macro-Emulsion-Based Enhanced Oil Recovery. SPE J. 22, 459–469. https://doi.org/10.2118/179691-PA

Xu, M., Zhang, W., Pei, X., Jiang, J., Cui, Z., P. Binks, B., 2017. CO 2 /N 2 triggered switchable Pickering emulsions stabilized by alumina nanoparticles in combination with a conventional anionic surfactant. RSC Adv. 7, 29742–29751. https://doi.org/10.1039/C7RA03722H

Xue, Z., Panthi, K., Fei, Y., Johnston, K.P., Mohanty, K.K., 2015. CO2-Soluble Ionic Surfactants and CO2 Foams for High-Temperature and High-Salinity Sandstone Reservoirs. Energy Fuels 29, 5750–5760. https://doi.org/10.1021/acs.energyfuels.5b01568

Xue, Z., Worthen, A., Qajar, A., Robert, I., Bryant, S.L., Huh, C., Prodanović, M., Johnston, K.P., 2016. Viscosity and stability of ultra-high internal phase CO2-in-water foams stabilized with surfactants and nanoparticles with or without polyelectrolytes. J. Colloid Interface Sci. 461, 383–395. https://doi.org/10.1016/j.jcis.2015.08.031

Yang, W., Wang, T., Fan, Z., Miao, Q., Deng, Z., Zhu, Y., 2017. Foams Stabilized by In Situ-Modified Nanoparticles and Anionic Surfactants for Enhanced Oil Recovery. Energy Fuels 31, 4721–4730. https://doi.org/10.1021/acs.energyfuels.6b03217

Yang, X., Liu, Z., 2010. A Kind of Nanofluid Consisting of Surface-Functionalized Nanoparticles. Nanoscale Res. Lett. 5, 1324. https://doi.org/10.1007/s11671-010-9646-6

Yu, J., An, C., Mo, D., Liu, N., Lee, R.L., 2012. Foam Mobility Control for Nanoparticle-Stabilized Supercritical CO2 Foam. Presented at the SPE Improved Oil Recovery Symposium, Society of Petroleum Engineers. https://doi.org/10.2118/153336-MS

Yu, L., Wardlaw, N.C., 1986. The influence of wettability and critical pore-throat size ratio on snap—off. J. Colloid Interface Sci. 109, 461–472. https://doi.org/10.1016/0021-9797(86)90324-3

Zakaria, M., Husein, M.M., Harland, G., 2012. Novel Nanoparticle-Based Drilling Fluid with Improved Characteristics. Presented at the SPE International Oilfield Nanotechnology Conference and Exhibition, SPE-156992-MS. https://doi.org/10.2118/156992-MS

Zhang, C., Li, Z., Sun, Q., Wang, P., Wang, S., Liu, W., 2016. CO2 foam properties and the stabilizing mechanism of sodium bis(2-ethylhexyl)sulfosuccinate and hydrophobic nanoparticle mixtures. Soft Matter 12, 946–956. https://doi.org/10.1039/C5SM01408E

Zhang, D., Liu, S., Puerto, M., Miller, C.A., Hirasaki, G.J., 2006. Wettability alteration and spontaneous imbibition in oil-wet carbonate formations. J. Pet. Sci. Eng., Reservoir Wettability 52, 213–226. https://doi.org/10.1016/j.petrol.2006.03.009

Zhang, H., 2004. Effect of oils, soap and hardness on the stability of foams (Thesis). Rice University.

Zhang, H., Nikolov, A., Wasan, D., 2014. Enhanced Oil Recovery (EOR) Using Nanoparticle Dispersions: Underlying Mechanism and Imbibition Experiments. Energy Fuels 28, 3002–3009. https://doi.org/10.1021/ef500272r

Zhao, L., Luo, J., Wang, H., Song, G., Tang, G., 2016. Self-assembly fabrication of microencapsulated n-octadecane with natural silk fibroin shell for thermal-regulating textiles. Appl. Therm. Eng. 99, 495–501. https://doi.org/10.1016/j.applthermaleng.2015.12.111

Zhu, Y., Fu, T., Liu, K., Lin, Q., Pei, X., Jiang, J., Cui, Z., Binks, B.P., 2017. Thermoresponsive Pickering Emulsions Stabilized by Silica Nanoparticles in Combination with Alkyl Polyoxyethylene Ether Nonionic Surfactant. Langmuir 33, 5724–5733. https://doi.org/10.1021/acs.langmuir.7b00273

Ziegler, V.M., Handy, L.L., 1981. Effect of temperature on surfactant adsorption in porous media. Soc. Pet. Eng. J. 21, 218–228.

Zou, S., Yang, Y., Liu, H., Wang, C., 2013. Synergistic stabilization and tunable structures of Pickering high internal phase emulsions by nanoparticles and surfactants. Colloids Surf. Physicochem. Eng. Asp. 436, 1–9. https://doi.org/10.1016/j.colsurfa.2013.06.013